Universidad del País Vasco
Euskal Herriko Unibertsitatea

University of the Basque Country
Universidad del Pais Vasco (UPV)
Euskal Herriko Unibertsitatea (EHU)

Modeling and Analysis of Thermoelectric Energy Conversion Efficiency in Nanostructures

by

Kaike Yang

Supervisors:
Prof. Roberto D'Agosta
Prof. Angel Rubio

A thesis submitted in partial fulfillment for the
degree of Doctor of Philosophy

in the
Faculty of Physics and Materials Science

May 2016

(c)2016 KAIKE YANG

Abstract

Recently, nanostructured materials are received tremendous research interests because of their exceptional properties and great potential in applications. In this thesis, we investigated the thermoelectric transport properties of Si and Ge nanomembranes and nanowires as well as silica nanoclusters by using density functional theory calculations combined with Landauer-Büttiker formalism in the linear response regime. We also investigated the thermoelectric coefficients for quantum devices in the Coulomb blockade regime. The thesis is organized as follows.

We firstly investigated the thermoelectric properties in one- and two-dimensional Si and Ge nanomembranes, *i.e.*, silicene and germanene. We found that the figure of merit ZT in the one-dimensional zigzag-edged silicene and germanene nanoribbons decreases monotonously when the width of the nanoribbons increases. The decreasing figure of merit can be attributed to the rapid rising of the thermal conductance. Broader nanoribbons have more phonon modes contributing to the transport than those of the narrow nanoribbons, while electron conduction does not change so much. For armchair-edged silicene and germanene nanoribbons, ZT as a function of ribbon width shows an oscillating behavior. To improve the thermoelectric performance, we mixed the Si and Ge in the nanoribbons to enhance the lattice scattering. We found that the figure of merit at room temperature for hybrid narrow silicene and germanene nanoribbons is remarkably high, up to 2.5.

Secondly we investigated the thermoelectric energy conversion efficiency of Si and Ge nanowires, and in particular, that of SiGe core-shell nanowires. We showed how the presence of a thin Ge shell on a Si core nanowire increases the overall figure of merit. We found the optimal thickness of the Ge shell to provide the largest figure of merit for the devices. We also considered the Ge-core/Si-shell nanowires. We found that an optimal thickness of the Si shell does not exist, since the figure of merit is a monotonically decreasing function of the radius of the nanowire. Moreover, we considered the nanowire in which the shell is an alloy of Si and Ge. We verified the empirical law relating the electron energy gap to the optimal working temperature, at which the efficiency of the device is maximized.

Thirdly we investigated the heat transfer between two silica nanoclusters. We found that when the gap between two neighboring clusters is in the range 4 Å to 3 times the cluster size, the thermal conductance decreases due to the surface charge-charge interaction. When the gap is further increased to 5 times the cluster size, the volume dipole-dipole interaction dominates. On the other hand, when the gap is smaller than 4 Å, a quantum interaction dominates, where electrons of both clusters are shared. This quantum interaction leads to the dramatic increase of thermal coupling between neighboring clusters when the gap distance decreases. This study provides a description of the transition between radiation and heat conduction in gaps smaller than a few nanometers.

Finally we investigated the thermoelectric coefficients, in particular the Seebeck efficient, for strongly interacting electrons in the Coulomb blockade regime. The Seebeck coefficient plays a fundamental role in identifying the efficiency of a thermoelectric device. Its theoretical evaluation for atomistic models is routinely based on density functional theory calculations combined with the Landauer-Büttiker approach to quantum transport.

This combination, however, suffers from serious drawbacks for devices in the Coulomb blockade regime. We showed how to cure the theory through a simple correction in terms of the *temperature derivative* of the exchange-correlation potential. We also showed the comparison of our results with those obtained from both rate equations and experimental measurements on carbon nanotubes, and we found good qualitative agreement in all cases.

Our results are expected to be beneficial for the understanding of material performance and for designing future nanodevices.

Resumen

Recientemente, los materiales nanoestructurados han recibido un gran interés por sus excepcionales propiedades y su enorme potencial para aplicaciones. En esta tesis investigamos las propiedades de transporte termoeléctrico de nanomembranas y nanohilos de Si y el Ge así como nanoclusters de silicio utilizando cálculos de teoría del funcional de la densidad combinados con el formalismo Landauer-Büttiker en régimen de respuesta lineal. También investigamos los coeficientes termoeléctricos para dispositivos cuánticos en régimen Coulomb blockade. La tesis se organiza como sigue.

Primero analizamos las propiedades termoeléctricas en nanomembranas de Si y Ge unidimensionales y bidimensionales, es decir, siliceno y germaneno. Encontramos que el factor de mérito ZT en nanocintas unidimensionales terminadas en zigzag de siliceno y germaneno decrece monótonamente cuando el ancho de las nanocintas aumenta. El factor de mérito decreciente puede atribuirse al rápido aumento de la conductancia térmica. Las nanocintas más anchas tienen más modos fonónicos contribuyendo al transporte que las nanocintas más estrechas, mientras que la conducción de electrones no cambia mucho. Para nanocintas de siliceno y germaneno con borde armchair, ZT como función del ancho de la cinta muestra un comportamiento oscilatorio. Para mejorar el rendimiento termoeléctrico mezclamos Si y Ge en las nanocintas para mejorar el lattice scattering. Encontramos que el factor de mérito a temperatura ambiente para nanocinas estrechas híbridas de siliceno y germano es destacablemente alto, hasta 2.5.

En segundo lugar analizamos la eficiencia de conversión termoeléctrica de nanohilos de Si y Ge, y en particular, la de nanohilos de núcleo-capa SiGe. Mostramos cómo la presencia de una fina capa de Ge sobre un núcleo de nanohilo de Si incrementa el factor de mérito general. Encontramos el ancho óptimo para la capa de Ge para obtener el máximo factor de mérito para los dispositivos. También consideramos los nanohilos núcleo de Ge/capa de Si. Encontramos que el ancho óptimo de la capa de Si no existe, ya que el factor de mérito es una función monótonamente decreciente del radio del nanohilo. Es más, analizamos también nanohilos en los que la capa en una aleación de Si y Ge. Verificamos la ley empírica que relaciona el gap de energía electrónico a la temperatura óptima de trabajo, a la que la eficiencia del dispositivo es máxima.

En tercer lugar analizamos la transferencia de calor entre dos nanoclusters de silicio. Encontramos que cuando el gap entre dos clusters vecinos está en el rango de 4 Å a 3 veces el tamaño del cluster, la conductancia térmica decrece debido a la interacción carga-superficie. Cuando el gap es aumentado a 5 veces el tamaño del cluster, la interacción en volumen dipolo-dipolo domina. Por otro lado, cuando el gap es menor que 4 Å, una interacción cuántica domina, en la que los electrones de ambos clusters son compartidos. Esta interacción cuántica provoca un incremento dramático del acoplamiento térmico entre los clusters vecinos cuando la distancia de gap disminuye. Este estudio proporciona una descripción de la transición entre la conducción por radiación y por calor en gaps menores que unos pocos nanómetros.

Por último, investigamos los coeficientes termoeléctricos, en particular el coeficiente de Seebeck, para electrones interaccionando fuertemente en régimen de Coulomb blockade. El coeficiente de Seebeck juega un papel fundamental en identificar la eficiencia de un dispositivo termoeléctrico. Su evaluación teórica para modelos atomísticos está basada de la manera corriente en cálculos de teoría del funcional de la densidad combinados con con el método de Landauer-Büttiker para transporte cuántico. Esta combinación, sin embargo, sufre serios inconvenientes para dispositivos en el régimen Coulomb blockade. Mostramos cómo subsanar la teoría mediante una simple corrección en términos de *derivadad de la temperatura* del potencial de correlación-intercambio. También mostramos la comparación de nuestros resultados con lo obtenidos tanto de ecuaciones de ritmo como de medidas experimentales en nanotubos de carbono, y encontramos un buen acuerdo cualitativo en todos los casos.

Se espera que nuestros resultados sean beneficiosos para el entendimiento del rendimiento de los materiales y para diseñar futuros nanodispositivos.

Acknowledgements

The almost four-years' PhD studies are not only to gain an honorable academic degree but also to strengthen the personal research ability because in this process one could learn new skills and solve problems to achieve the scientific research project. My PhD training was an unforgettable experience, and during it I benefited richly from the generosity of many self-giving people. At this special time, I sincerely thank all of them.

First of all, I thank my supervisors, Profs. Roberto D'Agosta and Angel Rubio, from the bottom of my heart. Discussion and communication with them in the past 4-years have endowed me knowledge and wisdom. Their kindness and enthusiasm are impressive and I have many opportunities to attend the international conferences and to discover the frontier of science. This thesis could not have been finished without their help.

Secondly, I thank all of my collaborators. At the early stage of my PhD study, Dr S. Cahangirov helped me to do the density functional theory calculations and provided some ideas on how to set the VASP parameters. Prof. A. Cantarero, one of the collaborators of the project of silicon and germanium nanomembranes and nanowires, taught me how to calculate the phonon dispersions based on the empirical potential model. Prof. S. Kurth, Prof. G. Stefanucci, and Dr E. Perfetto are the collaborators of the Coulomb blockade project. I learned the density functional theory from them. Dr S. Xiong and Prof. S. Volz are the collaborators of the project of heat transfer. We did the calculations of thermal conductance using the Green's function method.

Thirdly, I thank all my workmates in the nano-bio spectroscopy group and my classmates in the department of material physics of UPV/EHU. They helped me live a happy life in San Sebastian, and we had some pleasant meetings on the weekend. Some of them are remain in the group or the university, while some have been graduated or moved to other places. Also, I could not forget to acknowledge our secretary Ms. Cecilia. B. B. Cortabitarte who helped me with paperwork. I would also like to thank the financial support of the consolider nanoTHERM project, the ERC project, the GC Grupos Consolidados project, the AIRFORCE project, and the Basque government.

Finally, I thank my parents who always support and encourage me unconditionally at any time.

List of Publications

- Density functional theory for the calculation of Seebeck coefficient in the Coulomb blockade regime,
  K. Yang, E. Perfetto, S. Kurth, G. Stefanucci, and R. D'Agosta,
  Phys. Rev. Lett., (2016) (in review).

- Optimal thermoelectric figure of merit of Si/Ge core-shell nanowires,
  K. Yang, A. Cantarero, A. Rubio, and R. D'Agosta,
  Nano Res. 8, 2611 (2015).

- Classical to quantum transition of heat transfer between two silica clusters,
  S. Xiong, K. Yang, Y. A Kosevich, Y. Chalopin, R. D'Agosta, P. Cortona, and S. Volz,
  Phys. Rev. Lett. 112, 114301 (2014).

- Thermoelectric properties of atomically thin silicene and germanene nanostructures,
  K. Yang, S. Cahangirov, A. Cantarero, A. Rubio, and R. D'Agosta,
  Phys. Rev. B 89, 125403 (2014).

Contents

Abstract iii

Resumen v

Acknowledgements vii

List of Publications viii

List of Figures xiii

List of Tables xix

Abbreviations xxi

Physical Constants and Symbols xxiii

1 Introduction to thermoelectricity **1**
- 1.1 Three significant physical effects . . . 1
  - 1.1.1 Seebeck effect . . . 1
  - 1.1.2 Peltier effect . . . 2
  - 1.1.3 Thomson effect . . . 2
- 1.2 Thermoelectric efficiency . . . 4
  - 1.2.1 Maximizing the efficiency . . . 4
  - 1.2.2 Performance analysis . . . 6
- 1.3 Research on this thesis . . . 7

2 Density functional and thermoelectric transport theory **11**
- 2.1 Many body problem . . . 11
  - 2.1.1 Many particle Schrödinger equation . . . 11
  - 2.1.2 Born-Oppenheimer approximation . . . 12
- 2.2 Hartree-Fock approximation . . . 14
  - 2.2.1 Hartree equation . . . 14
  - 2.2.2 Fock equation . . . 15
- 2.3 Density functional theory . . . 16
  - 2.3.1 Hohenberg-Kohn theorem . . . 16
  - 2.3.2 Kohn-Sham equations . . . 18

2.3.3 Approximate functionals . . . 19
    2.3.3.1 Local density approximation . . . 19
    2.3.3.2 Generalized gradient approximation . . . 21
2.4 Fermionic Green's function . . . 22
    2.4.1 Modeling electronic Hamiltonian . . . 22
    2.4.2 General expression of currents . . . 23
    2.4.3 Landauer theory for electron transport . . . 28
2.5 Bosonic Green's function . . . 29
    2.5.1 Modeling Hamiltonian of phonons . . . 29
    2.5.2 General expression of lattice heat current . . . 30
    2.5.3 Landauer-like formula for phonon transport . . . 34
2.6 Boltzmann transport equation . . . 35
2.7 Rate equation . . . 37

3 Modeling and analysis of thermoelectric properties in nanostructures 39
3.1 Modeling of thermoelectric coefficients in SiGe nanomembranes . . . 39
    3.1.1 Introduction . . . 39
    3.1.2 Computational details . . . 41
    3.1.3 Two-dimensional silicon and germanium . . . 41
        3.1.3.1 Geometrical structures of two-dimensional Si and Ge nanomembranes . . . 41
        3.1.3.2 Energy Bands and electronic figure of merit . . . 42
    3.1.4 Quasi-one-dimensional nanoribbons . . . 45
        3.1.4.1 Germanene nanoribbons . . . 45
        3.1.4.2 Silicene nanoribbons . . . 52
    3.1.5 Silicon-germanium heterostructures . . . 53
        3.1.5.1 Thermoelectric properties of hybrid silicene-germanene nanoribbons . . . 54
        3.1.5.2 Component modulation on the figure of merit of hybrid silicene-germanene nanoribbons . . . 57
        3.1.5.3 Disorder effect on the figure of merit of hybrid silicene-germanene nanoribbons . . . 58
3.2 Optimal figure of merit of SiGe core-shell nanowires . . . 61
    3.2.1 Introduction . . . 61
    3.2.2 Details of electronic structure calculations . . . 62
    3.2.3 Results and discussions . . . 62
        3.2.3.1 Geometries of SiGe nanowires . . . 62
        3.2.3.2 Thermoelectric coefficients of pure Si and Ge nanowires . 63
        3.2.3.3 Figure of merit of clean SiGe core-shell nanowires . . . 64
        3.2.3.4 Shell-disordered SiGe nanowires . . . 66
        3.2.3.5 Temperature effect on the figure of merit . . . 68
3.3 Classical to quantum transition of heat transfer between silica nanoclusters 71
    3.3.1 Introduction . . . 71
    3.3.2 Silica nanoclusters and computational details . . . 72
    3.3.3 Thermal conductance calculations and analyses . . . 74
        3.3.3.1 Lattice thermal conductance . . . 74
        3.3.3.2 Electronic density analysis . . . 76

3.3.3.3 Phonon transmission coefficient 77

4 Theory of thermoelectric coefficients and its application in the Coulomb blockade regime 79

4.1 Introduction 79
4.2 Hamiltonian of the interacting system 80
4.3 Theory of thermoelectric coefficients for single level system 80
4.3.1 Analytical properties for quantum dot weakly coupled to leads . . 81
4.3.2 Hxc-potential of a single-site model 84
4.3.3 Dynamical xc-correction to the Kohn-Sham conductance 86
4.3.4 Dynamical xc-correction to the Kohn-Sham Seebeck coefficient . . 88
4.4 Numerical calculations of thermoelectric coefficients for single impurity Anderson model 89
4.5 Generalization to multiple levels 91
4.6 Application to carbon nanotubes 93

5 Conclusions 97

A Relations of Seebeck, Peltier and Thomson coefficients 99

B Time-ordered Green's functions 101

B.1 Fermionic Green's function 101
B.1.1 Equation of motion of time-ordered Green's function 101
B.1.2 Spectral function of many body interacting system with single level 103
B.2 Time-ordered bosonic Green's function 104

Bibliography 107

List of Figures

1.1 (Color) Diagram of the circuit on which Seebeck discovered the thermoelectric effect. a and b are two different metals with n-type and p-type, respectively. The interfaces A and B have temperatures T_1 and T_2. We assume $T_2 > T_1$ so that carriers will move from B to A. 2

1.2 (Color) A schematic illustration of the Peltier effect, where heat absorption and generation are shown at the left and right sides of the interface. . 3

1.3 (Color) A schematic illustration of the Thomson effect, where a current flows through the conductor and inside the conductor there exists temperature gradient. 3

1.4 (Color) A two-element thermoelectric generator. The p-type and n-type materials with different temperatures, T_h and T_c, at the interfaces are connected. The current is generated due to the moving of carriers from the hot terminal to the cold terminal. 5

1.5 (Color) Thermoelectric efficiency η versus temperature difference ΔT for figure of merit ZT ranging from 1 to 10, where the temperature in the cold side is $T_c = 200$ K and hot side is $T_h = T_c + \Delta T$. 7

2.1 (Color) A schematic picture of real system and KS system, where in both cases ground state densities are the same. 20

2.2 (Color) A schematic illustration of the modelling system including left and right leads and central interacting region, where μ_L and μ_R are the chemical potentials, T_L and T_R are the temperatures of the left and right leads, respectively. 23

3.1 (Color) A schematics of 2D free-standing silicene. In contrast to graphene, silicene is not flat. 40

3.2 (Color) Geometrical structures of one-layer 3×3 silicene (yellow) (a) (top view) and (b) (side view) on top of five-layers 4×4 Ag(111) (white). Geometrical structures of one-layer 3×3 germanene (green) (c) (top view) and (d) (side view) on top of five-layers 4×4 Ag(111). The buckling distances for supported silicene and germanene are 0.79 Å and 1.42 Å, respectively. 42

3.3 (Color) Electronic energy bands corresponding to the distorted (a) silicene and (b) germanene by removing the Ag substrate, respectively, where the dashed blue line denotes the Fermi energy position. (c) and (d) Dimensionless electronic figure of merit ZT_e at room temperature as a function of chemical potential μ corresponding to the distorted silicene and germanene, respectively. The black continuous and red dashed lines represent ZT_e evaluated at constant relaxation time approximation and $1/\tau_e \propto E$, respectively. 43

3.4 (Color) Electron energy bands of the free-standing (a) silicene and (b) germanene, respectively, where the dotted blue line denotes the Fermi energy. (c) and (d) Dimensionless electronic figure of merit ZT_e at room temperature as a function of chemical potential μ for the free-standing silicene and germanene, respectively. The black and red curves in (c) and (d) represent two different approximations of relaxation time. 44

3.5 (Color) Optimized geometrical structures of (a) Z-GeNRs and (c) A-GeNRs and their lateral views. For the atoms at the edges, we passivate the unsaturated bonds with hydrogen atoms. W_Z and W_A denote the width of the nanoribbons for the zigzag and armchair terminated nanoribbons, respectively. 46

3.6 (Color) Phonon dispersions for (a) Z-GeNRs with $W_Z = 6$ and (b) A-GeNRs with $W_A = 6$, respectively. 47

3.7 (Color) (a) Electron energy band of Z-GeNRs with $W_Z = 6$ for the AFM state: Notice the presence of a small electronic gap. (b) Electron energy band of Z-GeNRs with $W_Z = 6$ for the FM state. (c) Electron energy band of A-GeNRs with $W_A = 6$ corresponding to the NM state. In (a-c) the Fermi energy is chosen as the reference energy and set to 0. 47

3.8 Band gap of (a) Z-GeNRs and (b) A-GeNRs as a function of the ribbon width W_Z and W_A, respectively. 48

3.9 (Color) Electron transmission coefficient as a function of energy for (a) Z-GeNRs and (b) A-GeNRs with various ribbon widths, respectively. (c) and (d) Electrical conductance, (e) and (f) Seebeck coefficient, (g) and (h) electron and phonon thermal conductances for Z-GeNRs and A-GeNRs versus chemical potential μ, where the temperature is set to 300K. 48

3.10 (Color) Density of states as a function of chemical potential μ for Z-GeNR with ribbon width $W_Z = 3$ and for A-GeNRs with ribbon width $W_A = 3,\ 4$ and 5. 49

3.11 (Color) Phonon thermal conductance κ_{ph} of (a) Z-GeNRs and (b) A-GeNRs with different ribbon width as a function of temperature. (c) The logarithm of κ_{ph} for A-GeNRs as a function of logarithm of T, where the linear behavior is shown as we expect according to Eq. (3.3). 50

3.12 (Color) Figure of merit ZT at room temperature for (a) Z-GeNRs and (b) A-GeNRs as a function of chemical potential μ for different ribbon width W_Z and W_A, respectively. In (c) we report the peak value of ZT for Z-GeNRs at negative values of the chemical potential μ associated with the hole transport (square hollow points) and positive values μ associated with the electron transport (square full points). In (d) we pick out the peak value of ZT in (b) for A-GeNRs around $\mu = 0$ for both electron and hole transport. 51

3.13 (Color) Phonon thermal conductance κ_{ph} of (a) Z-SiNRs and (b) A-SiNRs as a function of temperature, respectively. 53

3.14 (Color) Figure of merit ZT at room temperature for (a) Z-SiNRs and (b) A-SiNRs as a function of ribbon width W_Z and W_A, where the black square hollow points and the red square full points correspond to the hole and electron transport, respectively. 53

3.15 (Color) Geometrical structures of (a) Z-SiGeNRs and (b) A-SiGeNRs, where the red line encloses a supercell along the ribbon axis and L_{Si} and L_{Ge} are the lengths of silicene and germanene stripes in the supercell, respectively. We have chosen $L_{\mathrm{Si}} = L_{\mathrm{Ge}} = 3$ for this particular case and used the hydrogen to passivate the ribbon edges. 54

3.16 (a) and (b) Energy band gap as a function of ribbon width W_Z and W_A for Z-SiGeNRs and A-SiGeNRs, respectively. 55

3.17 (Color) Electronic transmission coefficient as a function of energy for (a) Z-SiGeNRs and (b) A-SiGeNRs, respectively. (c) and (d) Electrical conductance, (e) and (f) Seebeck coefficient, (g) and (h) electron and phonon thermal conductances as a function of chemical potential μ for Z-SiGeNRs and A-SiGeNRs, respectively, where we have set the temperature $T = 300$ K. 56

3.18 (Color) Phonon thermal conductance κ_{ph} of (a) Z-SiGeNRs and (b) A-SiGeNRs as a function of temperature, respectively. 56

3.19 (Color) Figure of merit ZT at room temperature for (a) Z-SiGeNRs and (b) A-SiGeNRs as a function of nanoribbon with width W_Z and W_A, where the hollow and full points correspond to the hole and electron transport, respectively. 57

3.20 (Color) Figure of merit ZT at T=300K for Z-SiGeNRs and A-SiGeNRs as a function of ribbon width W_Z and W_A under different component lengths of silicene and germanene stripes: (a) and (b) $L_{\mathrm{Si}} = L_{\mathrm{Ge}} = 2$, (c) and (d) $L_{\mathrm{Si}} = L_{\mathrm{Ge}} = 3$, (e) and (f) $L_{\mathrm{Si}} = L_{\mathrm{Ge}} = 4$, respectively. (g) and (h) Figure of merit as a function of temperature for Z-SiGeNRs and A-SiGeNRs with the corresponding ribbon width 3 and 4, where the lengths of silicene and germanene stripes in the supercell are $L_{\mathrm{Si}} = L_{\mathrm{Ge}} = 3$. The hollow and full points correspond to the hole and electron transport, respectively 58

3.21 (Color) Figure of merit ZT at $T = 300$ K for A-GeNRs, A-SiNRs, A-SiGeNRs and disordered A-SiGeNRs with ribbon width (a) $W_A = 3$ and (b) $W_A = 4$ as a function of chemical potential μ, where we have taken the supercell length $L_S = 6$, respectively. 59

3.22 (Color) Phonon thermal conductance of various armchair nanoribbons with the ribbon width $W_A = 3$, where the supercell lengths L_S for A-SiGeNRs and disordered A-SiGeNRs are (a) $L_S = 6$ and (b) $L_S = 20$, respectively. The curves in color are calculated from *ab-initio* and the other curves in gray are calculated from tight-binding. 60

3.23 Phonon thermal conductance κ_{ph} at $T = 300$ K calculated from tight-binding as a function of supercell length L_S corresponding to the ribbon width (a) $W_A = 3$ and (b) $W_A = 4$, respectively. 60

3.24 (Color) Schematic illustrations of (a) clean SiGe core-shell NW (top view) and (b) clean Si- or Ge-core but disordered SiGe-shell NW (tilted view). The yellow and green colors could represent either Si or Ge atoms. The grey atoms are hydrogen atoms used to saturate the dangling atomic-bonds at the surface. We have used N_C (or N'_C) and N_S (or N'_S) to indicate the thickness of core and shell layers, respectively, where for this particular case we have set $N_C = N_S = 3$. 63

3.25 (a) Figure of merit, (b) Seebeck coefficient, (c) electrical conductance, and (d) total thermal conductance for pure Si NWs as a function of atomic layers N_S. . . . 63

3.26 (a) Figure of merit, (b) Seebeck coefficient, (c) electrical conductance, and (d) total thermal conductance for pure Ge NWs as a function of atomic layers N_S'. . . . 64

3.27 (Color) Thermoelectric figure of merit as a function of the number of atomic layers in the shell, N_S for (a) clean Si/Ge and N_S' for (b) clean Ge/Si NWs with different core sizes N_C and N_C', respectively. . . . 65

3.28 (Color) Thermoelectric figure of merit as a function of number of layers in the shell, (a-c) N_S for Si/disordered SiGe and (d-f) N_S' for Ge/disordered SiGe NWs at different core size N_C and N_C', respectively. The vertical bars represent the range of variation of the figure of merit we have obtained from our calculations, and the solid lines represent the fitted curves [see Eqs. (3.7) for reference]. For each value of N_S or N_S' at least 5 different random structures have been calculated. . . . 67

3.29 (Color) Thermoelectric figure of merit ZT as a function of temperature. (a) The ellipse in black and rectangle in red represent ZT of clean Si/Ge NWs with $N_C = 5$, $N_S = 3$ and $N_C = 4$, $N_S = 3$; the hexagon in green and star in blue represent ZT of clean Ge/Si NWs with $N_C' = 5$, $N_S' = 3$ and $N_C' = 4$, $N_S' = 3$, respectively. (b) The hollow ellipse and rectangle represent ZT of clean Si/disordered SiGe NWs with $N_C = 2$, $N_S = 5$ and $N_C = 1$, $N_S = 5$; the hollow hexagon and star represent ZT of clean Ge/disordered SiGe NWs with $N_C' = 2$, $N_S' = 5$ and $N_C' = 1$, $N_S' = 5$, respectively. . . . 69

3.30 (Color) (a) Electrical conductance G, (b) Seebeck coefficient S and (c) total thermal conductance κ_{e-ph} as a function of temperature. The inset in (c) shows the corresponding phonon thermal conductance κ_{ph}. The curves with different symbols share the same structures as those in Fig. 3.29 70

3.31 (Color) The electronic energy gap E_g versus the critical temperature $k_B T_C$ for clean Si/Ge (rectangle) and Ge/Si NWs (star), Si/disordered SiGe (ellipse) and Ge/disordered SiGe NWs (hexagon). The red, blue, black and green lines are the linearly fitted curves. . . . 71

3.32 (Color) Schematics of the silica nanoclusters considered in the Greens function (top) and in the *ab-initio* (bottom) calculations. For the Greens function calculation, we use a cubic SiO_2 cluster with size $N \times N \times N$. For the *ab-initio* calculation, we use two parallel silica planes separated by a gap distance l. The lattice constant of SiO_2 is 4.52 Å. . . . 73

3.33 (Color) Thermal conductance κ_{ph} between two neighboring nanoclusters at $T = 300$ K for different cluster sizes versus the distance d indicated in Fig. 3.32. In our calculations, the cluster is a cube $N \times N \times N$ unit cells in volume. The diameter D is set in such a way that the sphere volume is equivalent to that of the simulated cube. The distance d is used as the abscissa instead of the gap distance l in order to discriminate the curves otherwise superimposed. The molecular dynamics (MD) results are taken from Ref. [1], where the same BKS potential parameters as those adopted in this work were used. . . . 75

3.34 (Color) *Ab initio* computation of the electronic density ρ generated by two parallel silica films separated by different gap widths. . . . 76

3.35 (Color) Angular frequency dependent cumulative phonon transmission coefficient $\mathcal{T}_{ph}$ for different gap distance l in the cluster of diameter D=1.3 nm. Inset: phonon transmission function versus angular frequency at low frequencies. 78

4.1 (Color) A schematic illustration of a finite-sized QD weakly coupled to two metallic leads, where the band width of the two leads are assumed to be much larger than the energy scale of the QD. 81
4.2 (Color) Hxc potential of single site impurity model for different temperatures as a function of density, where energies are give in units of U. . . . 85
4.3 (Color) Density ρ versus gate v for our xc corrected DFT (black), MB (blue), and RE (red). The parameters are $T = 0.1$ and $\gamma = 0.01$, where energies are given in units of U. 90
4.4 (Color) (a) Conductance G and (b) Seebeck coefficient S versus gate v for our xc corrected DFT (black), MB (blue) and RE (red). The G_S, S_S (KS, green) and the xc correction $\partial v_{\mathrm{Hxc}}/\partial T$ (cyan) of the Seebeck coefficient are also displayed. The parameters are $T = 0.1$ and $\gamma = 0.01$, where energies are given in units of U. 90
4.5 (Color) (a) Conductance, (b) Seebeck coefficient and (c) density of CIM with two spin-degenerate levels computed from RE and DFT using the approximate functional of Eq. (4.63). The KS conductance and Seebeck coefficient are also shown. 92
4.6 (Color) Seeebeck coefficient for the Anderson model with non-degenerate single-particle levels (left) and for three spin-degenerate levels (right). The parameters are $\varepsilon^0_\uparrow = 0$, $\varepsilon^0_\downarrow = 0.3$ (left panel) and $\varepsilon^0_1 = 0$, $\varepsilon^0_2 = 0.3$, $\varepsilon^0_3 = 0.6$ (right panel). In both panels $T = 0.03$ and $\gamma = 0.001$ (all energies in units of U). 93
4.7 (Color) Conductance (a) and Seebeck coefficient (b) of a single-wall carbon nanotube from our DFT (black) and experiment (red, data from Ref. [2]). Also shown is the KS Seebeck coefficient (dashed green). The single particle and charging energies are given in table 4.1. The other parameters are $T = 4.5$ K and $\gamma = 0.02$ meV. 94

List of Tables

3.1 Carrier density for the Z-GeNRs as a function of the ribbon width calculated at the chemical potential that gives the maximum figure of merit, at $T = 300$ K. The e and h subscripts refer to the electrons or holes transport, respectively. 51
3.2 Carrier density for the A-GeNRs as a function of the width calculated at the chemical potential that gives the maximum figure of merit, at $T = 300$ K. The e and h subscripts refer to the electrons or holes transport, respectively. 52
3.3 Electrical and thermal transport coefficients at the chemical potential for optimal ZT of the clean Si/Ge NWs with $N_C = 3$ for N_S between 1 and 5. 65
3.4 Fitted parameters of figure of merit ZT for both pure Si- and Ge-core with disordered SiGe shell NWs [explicit formula is presented in the text as Eq. (3.7)]. 67
3.5 Fitted parameters of linear relation between E_g and $k_B T_C$ in Fig. 3.31. . . 70
3.6 Fitted parameters of BKS potential in Eq. (3.13). 74

4.1 Single-particle energies ε_K^0 and charging energies U_K (in meV), for modelling the calculation of Fig. 4.7. 94

Abbreviations

DFT	**D**ensity **F**unctional **T**heory
KS	**K**ohn **S**ham
Hxc	**H**artree E**x**change **C**orrelation
NEGF	**N**on-**e**quilibrium **G**reen's **F**unction
LB	**L**andauer **B**üttiker
MB	**M**any **B**ody
RE	**R**ate **E**quation
BTE	**B**oltzmann **T**ransport **E**quation
CB	**C**oulomb **B**lockade

Physical Constants and Symbols

Boltzmann Constant	k_B	=	$1.380\ 658 \times 10^{-23}$ J/K
Electron Charge	e	=	$1.602\ 177\ 33 \times 10^{-19}$ C
Electron Mass	m_e	=	$9.109\ 389\ 7 \times 10^{-31}$ kg
Planck Constant	h	=	$6.626\ 075\ 5 \times 10^{-34}$ J s
Reduced Planck Constant	$\hbar$	=	$1.054\ 572\ 66 \times 10^{-34}$ J s

Particle Density	ρ
Electrical Conductance	G
Electrical Conductivity	σ
Electronic Thermal Conductance	κ_e
Electronic Thermal Conductivity	λ_e
Phononic Thermal Conductance	κ_{ph}
Phononic Thermal Conductivity	λ_{ph}
Seebeck Coefficient	S
Dimensionless Figure of Merit	ZT
Electronic Figure of Merit	ZT_e
Electronic Transmission Coefficient	$\mathcal{T}_e$
Phononic Transmission Coefficient	$\mathcal{T}_{ph}$

Chapter 1

Introduction to thermoelectricity

1.1 Three significant physical effects

Thermoelectric materials that convert waste heat into electricity or electrical power into cooling have been studied for a long time due to the technological applications in developing alternative energy sources to reduce our dependence on fossil fuels and accordingly reduce greenhouse gas emissions [3–5]. The first discovered physical phenomena of the thermoelectric conversion are the Seebeck, Peltier and Thomson effects. In the following we introduce these three effects briefly.

1.1.1 Seebeck effect

In 1821, T. J. Seebeck first discovered that when two different metals a and b are connected to form a ring, a current can be generated if the two metals have different temperatures. The arrangement is shown in Fig. 1.1. This is a thermocouple and the electromotive force produced by the temperature difference is called thermovoltage, V_T. The magnitude of the thermovoltage is proportional to the difference of the temperature of the thermocouple junctions, and the Seebeck coefficient S_{ab} is therefore defined as

$$S_{ab} = -\left(\frac{V_T}{\Delta T}\right)\bigg|_{J=0} = \left(\frac{V}{\Delta T}\right)\bigg|_{J=0}, \tag{1.1}$$

where $S_{ab} = S_b - S_a$ with S_a and S_b the Seebeck coefficients of metals a and b, and $\Delta T = T_2 - T_1$ is the temperature difference between the two metals at the interfaces, V is the external bias which is applied to balance the thermovoltage V_T so that the current $J = 0$. The minus sign before V_T comes from the fact that we define the Seebeck coefficient for hole transport as positive and for electron transport as negative. Assuming a is a n-type material in which electrons are the dominant carriers and b is a p-type material in which holes are the dominant carriers, if the temperature T_2 is larger than T_1, carriers will move from the high temperature region to the low temperature region, *i.e.*, electrons and holes will move from interface B to A. In this case a current is created, flowing from interface A to B carried by electrons in the left-hand-side (l.h.s.) of Fig. 1.1 with material a and flowing from interface B to A carried by holes in the right-hand-side (r.h.s.) of Fig. 1.1 with material b. Therefore, the temperature gradient induced potential at the r.h.s. of interface A is higher than that at the r.h.s.

of interface B because at the r.h.s., A accumulates the positive charges and B keeps the negative charges. However, the situation for the l.h.s. of Fig. 1.1 is completely reversed. Consequently S is positive for p-type materials and negative for n-type materials.

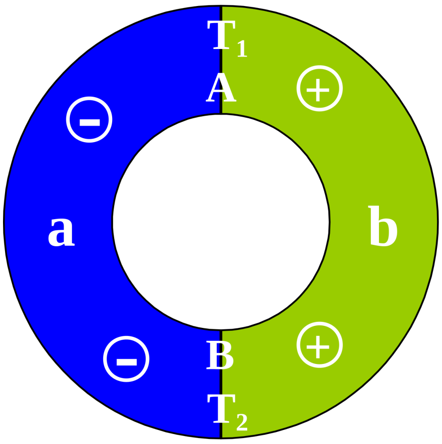

FIGURE 1.1: (Color) Diagram of the circuit on which Seebeck discovered the thermoelectric effect. a and b are two different metals with n-type and p-type, respectively. The interfaces A and B have temperatures T_1 and T_2. We assume $T_2 > T_1$ so that carriers will move from B to A.

1.1.2 Peltier effect

Conversely to the Seebeck effect, in 1834 J. Peltier found that when a current is made to flow through a junction composed of materials a and b, at the interface there exist heat generation and absorption phenomena. A schematic picture of this effect is shown in Fig. 1.2. If we take the absorbed heat as positive and released heat as negative, then the Peltier heat Q per unit time is equal to

$$\frac{dQ}{dt} = J\Pi_{ab}, \tag{1.2}$$

where $\Pi_{ab} = \Pi_b - \Pi_a$ is the Peltier coefficient which depends on the temperature of the interface and the materials composition. When a current flows from material a to b, heat absorption happens at the l.h.s of the interface since we take a as a n-type material and heat generation happens at the r.h.s. of the interface because b is a p-type material (see Fig. 1.2). In this case the Peltier coefficient Π_a is negative and Π_b is positive. The sign of the Peltier coefficient we defined here is consistent with the sign of Seebeck coefficient. Actually these two thermoelectric coefficients are not independent and we will show their relation later. The Peltier effect is reversible. If one changes the current direction in Fig. 1.2, equivalent heat energy will be generated and absorbed corresponding to the left and the right sides of the interface.

1.1.3 Thomson effect

After the discovery of the Seebeck and Peltier effects, in 1855 W. Thomson found that there is another heating or cooling process. When a current flows through a conductor and inside the conductor there exists temperature gradient, in addition to form the

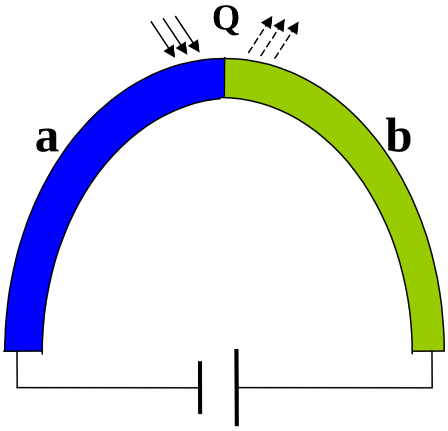

FIGURE 1.2: (Color) A schematic illustration of the Peltier effect, where heat absorption and generation are shown at the left and right sides of the interface.

Joule heat that is related to the conductor resistance, there is another heat generated or absorbed. A schematic illustration of this phenomenon is shown in Fig. 1.3. The absorbed or released heat per unit time is proportional to the current and temperature gradient, which is given by

$$\frac{dQ}{dt} = \Theta_a J \frac{dT}{dx}, \tag{1.3}$$

where Θ_a is the Thomson coefficient with unit V/K which depends on the material properties and temperature gradient, dx is the distance that current flows through the conductor per unit time. The Thomson effect is also reversible. The Thomson coefficient is positive for p-type materials and negative for n-type materials. If the current flows from low temperature region to high temperature region, it will absorb heat energy in conductors with positive Θ and release heat energy with negative Θ.

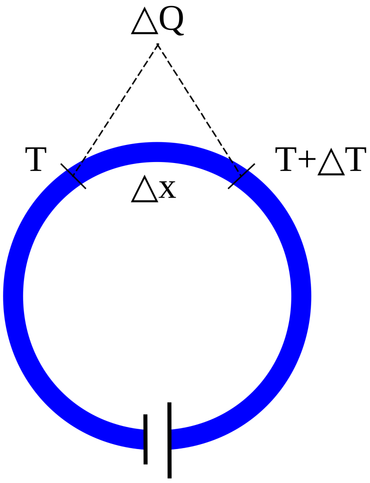

FIGURE 1.3: (Color) A schematic illustration of the Thomson effect, where a current flows through the conductor and inside the conductor there exists temperature gradient.

The above Seebeck, Peltier and Thomson coefficients are not independent. They have the relations:

$$\Pi_{ab} = TS_{ab}, \tag{1.4}$$

$$\Theta_{ab} = T\frac{dS_{ab}}{dT}, \tag{1.5}$$

where the temperature $T = (T_1 + T_2)/2$. The proof of these relations can be found in appendix A. In the above discussion, we have assumed the materials a and b are metallic. For semiconductors, the relations of the three coefficients still exist. More detailed information can be found in the book edited by H. J. Goldsmid [6]. Considering the mutual dependence of the three parameters, in the rest of this thesis, we will only focus on the Seebeck coefficient and omit the discussion of Peltier and Thomson coefficients.

Very recently, a novel thermoelectric phenomenon, spin Seebeck effect, is found in ferro- and antiferro-magnetic materials experimentally, which refers to the generation of a spin voltage caused by a temperature gradient. However, the discussion on this topic is beyond the scope of the present thesis [7–10].

1.2 Thermoelectric efficiency

1.2.1 Maximizing the efficiency

We determine the performance of thermoelectric devices using the model shown in Fig. 1.4 for a single thermocouple. Practical devices usually make use of modules that contain a number of thermocouples connected electrically in series and thermally in parallel. This enable the cooler or heat pump to be operated from a power source that delivers a manageable current with a reasonable voltage drop. It is a simple matter to extend the equations we derive below for a single couple to a multi-couple arrangement [6].

We first make the following assumptions for simplicity to calculate the thermoelectric efficiency over the temperature range $T_c \leq T \leq T_h$:
(1) $\sigma_p = \sigma_n = \sigma$ is the electrical conductivity and $G_p = G_n = G$ is the electrical conductance;
(2) $\lambda_p = \lambda_n = \lambda_e$ is the electric thermal conductivity and $\kappa_p = \kappa_n = \kappa_e$ is the electric thermal conductance;
(3) $S_p = -S_n = S$ is the Seebeck coefficient;
(4) $A_p = A_n = A$ is the cross-sectional area of the thermoelements and $l_p = l_n = l$ is the length of the thermoelements.

For the thermoelements, half of which are n-type and half of which are p-type, both electrical and thermal conductivities have the relations with their corresponding conductances:

$$G = \frac{A\sigma}{l}, \tag{1.6}$$

$$\kappa_e = \frac{A\lambda_e}{l}. \tag{1.7}$$

The total internal electrical resistance r and theremovoltage V_T are

$$r = \frac{l}{A\sigma}, \tag{1.8}$$
$$V_T = -S_n(T_h - T_c) = S\Delta T, \tag{1.9}$$

respectively. In the thermoelectric generator, the electrical current J and power W delivered to the external load R are

$$J = \frac{S\Delta T}{r + R}, \tag{1.10}$$
$$W = J^2 R = \frac{S^2 \Delta T^2 R}{(r+R)^2}, \tag{1.11}$$

where the load R can be chosen freely according to the device requirement.

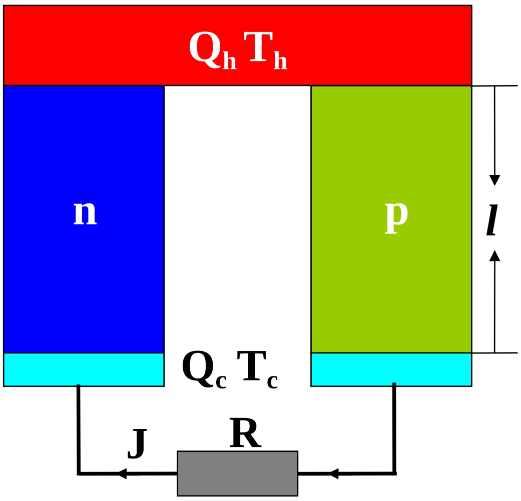

FIGURE 1.4: (Color) A two-element thermoelectric generator. The p-type and n-type materials with different temperatures, T_h and T_c, at the interfaces are connected. The current is generated due to the moving of carriers from the hot terminal to the cold terminal.

We now derive the efficiency of the device shown in Fig. 1.4. The input energy is the heat energy entering the hot junction and is given by [11]

$$Q_h = \kappa_{e-ph}\Delta T + ST_h J - \frac{J^2 r}{2}, \tag{1.12}$$

where $\kappa_{e-ph} = \kappa_e + \kappa_{ph}$ and κ_{ph} can be the phonon or lattice thermal conductance. If we define

$$y = \frac{R}{r}, \tag{1.13}$$

and use the expressions of J and W as shown in Eqs. (1.11), the efficiency can be written as

$$\eta = \frac{W}{Q_h} = \frac{\Delta T}{T_h} \frac{y/(y+1)}{1 + \kappa_{e-ph}(y+1)r/(S^2 T_h) - \Delta T/(2T_h(y+1))}. \tag{1.14}$$

By defining

$$Z = \frac{S^2}{r\kappa_{e-ph}}, \tag{1.15}$$

we can rewrite Eq. (1.14) as

$$\eta = \frac{\Delta T}{T_h} \frac{y/(y+1)}{1 + (y+1)/ZT_h - \Delta T/(2T_h(y+1))}. \tag{1.16}$$

So this formulation expresses the efficiency as a function of the parameters T_h and T_c and the parameters y and Z. As mentioned previously, the load resistance R is a free variable and may be chosen as desired to achieve any specific $y = R/r$.

There are two choices for the load resistance, R, that are particularly important. The first choice is to take $R = r$, which yields maximum power output W. The second choice is the one that yields maximum efficiency by maximizing Eq. (1.16) with respect to y, *i.e.*,

$$\frac{\partial \eta}{\partial y} = 0. \tag{1.17}$$

After some algebra, one can get

$$R_{\eta_{max}} = ry = r\sqrt{1 + ZT}, \tag{1.18}$$

where $T = (T_h + T_c)/2$. The product ZT is a dimensionless figure of merit and is often used instead of Z for thermoelectric materials. Substituting Eq. (1.18) into (1.16) yields the maximum possible efficiency for any thermoelectric generator:

$$\eta_{max} = \frac{\Delta T}{T_h} \frac{\sqrt{1 + ZT} - 1}{\sqrt{1 + ZT} + T_c/T_h}. \tag{1.19}$$

This formula provides a guideline on how to improve the thermoelectric energy conversion efficiency. The key quantity in Eq. (1.19) is the figure of merit ZT. In many situations we also use the definition:

$$ZT = \frac{\sigma S^2 T}{\lambda_{e-ph}} = \frac{G S^2 T}{\kappa_{e-ph}}, \tag{1.20}$$

where $\lambda_{e-ph} = \lambda_e + \lambda_{ph}$ and λ_{ph} is the phonon thermal conductivity. To achieve Eq. (1.20), we have used the relations shown in Eqs. (1.6)-(1.8) and also $\kappa_{ph} = A\lambda_{ph}/l$. The r.h.s. of the above Eq. (1.20) in many cases is more popular because the conductivity is not well defined for some materials such as the nanostructured atomic layered membranes where the cross-section area is not easy to estimate. And we will have more discussions on this in chapter 3 for calculating the figure of merit of two- and one-dimensional silicon and germanium nanosystems.

1.2.2 Performance analysis

After the theoretical derivation, we discuss here the performance of the Eq. (1.19). Figure 1.5 shows the thermoelectric energy conversion efficiency η as a function of temperature difference ΔT. In the calculations we define the temperatures $T_h = T_c + \Delta T$ and $T_c = 200$ K. It can be seen that the efficiency increases monotonously with the temperature difference. For a given ΔT, the larger the figure of merit ZT, the higher the efficiency η. At $\Delta T = 300$ K or $T_h = 500$ K, we find that $\eta \approx 13.7\%$ even at $ZT = 1$. As ZT increases to 2, the efficiency reaches 20.6% approximately. The current efficiency of Si-based solar cell is just about 20%.

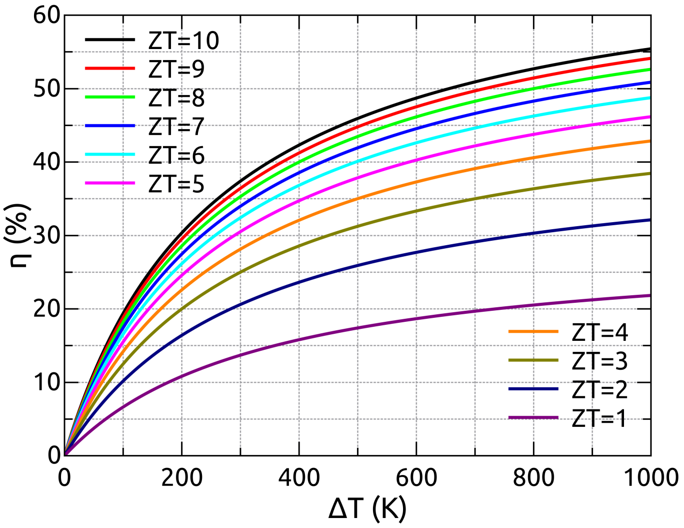

FIGURE 1.5: (Color) Thermoelectric efficiency η versus temperature difference ΔT for figure of merit ZT ranging from 1 to 10, where the temperature in the cold side is $T_c = 200$ K and hot side is $T_h = T_c + \Delta T$.

So far the best value for the figure of merit achieved with state-of-the-art technique is about 1. Although higher values have been reported in the literature for particular materials, those materials have been proven difficult to be integrated into our technologies presently, or to be produced industrially in a reliable way [12]. Indeed, the optimization of the figure of merit is a difficult problem. From the definition of ZT, we can see that an ideal thermoelectric material should hold an electrical conductivity and Seebeck coefficient as high as possible, while keeping the thermal conductivity as low as possible. Unfortunately, because the semi-empirical Wiedemann-Franz law, *i.e.*, $\lambda_e/\sigma = (k_B\pi)^2T/3e^2$, where k_B and e are the Boltzmann constant and electron charge, respectively, is valid in a great extent for metals, the two conductivities are locked together and the increase of the first leads to the increase of the second [13].

1.3 Research on this thesis

To achieve a high thermoelectric energy conversion efficiency, a large ZT value is required. In the literature, many different approaches have been tried, for example, introducing impurity atoms, superlattice modulation, stress effect and so on [14]. Nevertheless due to the mutual dependence of the quantities in ZT, the task becomes difficult. Usually increasing the electrical conductance, meanwhile, increases the thermal conductance. As far as I know the current highest ZT value reported by Zhao *et al.* is about 2.6 for a working temperature ($T = 923$ K) in SnSe crystal along a certain lattice direction [15], but it remains to be checked how efficiently these devices can be integrated within our actual Si-based technology.

In this thesis we work on the thermoelectric transport in nanostructured materials aiming to gain a considerable figure of merit. Our theoretical tools are based on DFT calculations and NEGF technique in the linear response regime. DFT combined with NEGF provides a standard way to calculate the electrical conductance, Seebeck coefficient and thermal conductance which are the quantities included in ZT and we will discuss more about this approach in the next chapter. Our studies are mainly focused on nanomaterials since they have been predicted to exhibit a promising figure of merit due to the quantum confinement effect. Furthermore we are interested in nanomaterials because they have exceptional properties, such as high electron conduction and outstanding optical characteristics, which make them have great potential in applications in future power generation and thermoelectric devices.

In chapter 2 we introduce the basics of DFT in detail. We start from the MB interacting Hamiltonian. Because of the complexity of directly solving the MB Schrödinger equation, the Born-Oppenheimer approximation (BOA) is introduced to separate the electrons and nuclei motion. Based on BOA, the Hartree-Fock equations are then proposed. DFT is another theory within BOA to solve the many-particle problem, and its starting point is the Hohenberg-Kohn theorem. For KS-DFT, the MB interacting density is effectively mapped into the density of a non-interacting system in which single particle wave functions are used. The particle-particle interaction for KS-DFT is included in a potential called xc potential. Although KS-DFT turns the complicated MB problem into a single particle problem, the xc potential remains unknown. In nowaday practical calculations, the most popular approximations for the xc potential are the local density approximation and the generalized gradient approximation. On the other hand, besides DFT, NEGF is also a powerful theory for the study of material properties. We will introduce NEGF for both fermionic and bosonic systems. Using the theory we derive the heat and electric current formulas based on the canonical Hamiltonian. Then the electrical conductance, Seebeck coefficient, thermal conductance and accordingly ZT can be calculated in terms of the Green's functions. Finally we introduce briefly the BTE and RE which are used for the calculations partially in chapters 3 and 4.

In chapter 3 we first implement the theory we have described above for silicene and germanene nanomembranes. Silicene and germanene are atomically thin materials of Si and Ge, respectively, which have similar honeycomb lattice structure as graphene. We use DFT and Landauer theory to calculate their electronic structural and transport properties. For the two-dimensional systems, we find some interesting properties, such as there is a Dirac-cone with linear dispersion in the band structure for free-standing both silicene and germanene at the K point of the first-Brillouin zone. We also study the properties of one-dimensional nanoribbons. We find that silicene and germanene nanoribbons exhibit a high figure of merit with narrow widths. When the width of the nanoribbons increases, the figure of merit decreases due to the rapidly increased phonon thermal conductance. Finally we explore the behavior of hybrid structures by mixing silicene and germanene in the growth direction of the nanoribbons. We find these hybrid structures can have better thermoelectric performance than that of pure silicene and germanene due to the increase of lattice scattering.

We then investigate the thermoelectric figure of merit of SiGe nanowires, and in particular, that of SiGe core-shell nanowires. We find the figure of merit of SiGe core-shell nanowires can be effectively improved in contrast to that of pure Si and Ge nanowires. We show that the figure of merit of Si-core/Ge-shell nanowires undergoes a transition when the diameter of the nanowires increases. An optimal thickness of Ge-shell to provide the largest ZT is observed. However, in the case of Ge-core/Si-shell nanowires, the figure of merit as a function of diameter decreases monotonously. We also investigate the disorder effect on the figure of merit by mixing Si and Ge compositions in the shell layers. In addition, we investigate the figure of merit as a function of temperature. We verify an empirical law relating the band gap to the working temperature, at which the figure of merit ZT is maximized.

We also investigate in chapter 3 the heat transfer between two silica nanoclusters by using NEGF method. We find a significant phase transition of heat transfer from classical to quantum regime. When the gap between two neighboring clusters is lesser than 4 Å, quantum interaction dominates. However, when the gap is larger than 4 Å but still lesser than 3 times the size of the nanoclusters, classical surface charge-charge interaction determines the behavior of thermal conductance. When the gap is further increased to be larger than 5 times the cluster size, classical volume dipole-dipole interaction plays a crucial role in determining the heat conduction. We compared these results with those obtained from molecular dynamics which is based on the Kubo theory. Unsurprisingly the classical molecular dynamics simulation fails to capture the quantum effect, although it shows a good agreement with NEGF calculation in the classical regime.

In chapter 4 we investigate the thermoelectric coefficients, in particular the Seebeck coefficient, for strongly interacting electrons in the CB regime. We first show the derivation of the theory of the dynamical xc correction to the KS conductance and Seebeck coefficient. Afterwards we evaluate the performance of the formulas we derived by implementing numerical calculations. We apply the theory to single impurity Anderson model and calculate the corresponding electrical conductance and Seebeck coefficient. We find that the dynamical xc correction plays a crucial role in evaluating the conductance and Seebeck coefficient. We also apply the theory to HOMO-LUMO model and multiple level systems to check the validity of the theory. Finally we compare our results with those obtained from MB and RE calculations and those obtained from experimental measurements on carbon nanotubes, and we find good qualitative agreement in all cases.

In chapter 5 we show a global conclusion of this thesis. We expect the results presented in this thesis are beneficial for future applications in the design of thermoelectric devices and other nanocircuits.

Chapter 2

Density functional and thermoelectric transport theory

2.1 Many body problem

One of the basic problems in theoretical physics and chemistry is the description of the structural and dynamical properties of many particle systems. The many particle system includes single atoms comprised of electrons and nuclei and all kinds of molecules ranging from dimers to proteins. It is complicated to solve the MB problem directly because of the particle-particle interactions. In this chapter we will discuss DFT and NEGF approaches which are widely used in calculating the electronic structures, energy bands, and transport properties of solid state materials [16–21]. We will introduce DFT in detail and derive the general expressions of electric and heat currents using the Green's functions based on the interaction Hamiltonian. At the end of this chapter we will also introduce BTE and RE, which will be used for the calculations in chapters 3 and 4.

2.1.1 Many particle Schrödinger equation

The starting point of exploring the electronic and structural properties of materials is the many particle Schrödinger equation [22, 23], which is given by

$$\hat{H}\Psi(\mathbf{r},\mathbf{R}) = E\Psi(\mathbf{r},\mathbf{R}), \tag{2.1}$$

where $\hat{H}$ is the MB Hamiltonian operator, Ψ is the eigenfunction, and E is the eigenvalue. $\mathbf{r} = (\mathbf{r}_1, \mathbf{r}_2, \cdots)$ represents all the coordinates of electrons and $\mathbf{R} = (\mathbf{R}_1, \mathbf{R}_2, \cdots)$ represents all the coordinates of nuclei. Without taking into account the electric or magnetic fields, the MB Hamiltonian $\hat{H}$ can be split into

$$\hat{H} = \hat{H}_e + \hat{H}_N + \hat{H}_{e-N}, \tag{2.2}$$

where the electronic Hamiltonian is

$$\hat{H}_e = \hat{T}_e(\mathbf{r}) + \hat{V}_e(\mathbf{r}) = -\sum_i \frac{\hbar^2}{2m_e}\nabla^2_{\mathbf{r}_i} + \frac{1}{2}\sum_{\substack{i,i' \\ i\neq i'}} \frac{e^2}{|\mathbf{r}_i - \mathbf{r}_{i'}|}, \tag{2.3}$$

where the Gaussian units are used. In the above equation, $\hat{T}_e$ is the kinetic energy of electrons, $\hat{V}_e$ describes the electron-electron interactions, and m_e is the mass of electrons. The Hamiltonian of nuclei is

$$\hat{H}_N = \hat{T}_N(\mathbf{R}) + \hat{V}_N(\mathbf{R}) = -\sum_j \frac{\hbar^2}{2M_j}\nabla^2_{\mathbf{R}_j} + \frac{1}{2}\sum_{\substack{j,j' \\ j\neq j'}} V_N(\mathbf{R}_j - \mathbf{R}_{j'}), \tag{2.4}$$

where the first term is the kinetic energy of nuclei, the second term describes the nucleus-nucleus interaction, and M_j is the j-th nuclear mass. The electron-nucleus interaction in Eq. (2.2) can be written as

$$\hat{H}_{e-N}(\mathbf{r},\mathbf{R}) = \sum_{i,j} V_{e-N}(\mathbf{r}_i - \mathbf{R}_j). \tag{2.5}$$

Equations (2.1) to (2.5) are the elementary building blocks of non-relativistic quantum mechanics in solid state physics. Once solving these equations, one can obtain in principle all the information of materials such as density, total energy and so on. However, in every cubic metre there are nearly 2.7×10^{25} particles. This huge number of particles leads to the impossibility of solving the equations directly with our current computer sources. We have to find an effective way to simplify the problem without changing the physics.

2.1.2 Born-Oppenheimer approximation

It is noticed that the Hamiltonian $\hat{H}_e$ only includes the electronic coordinates $\mathbf{r}$ and $\hat{H}_N$ is merely a function of the nuclear coordinates $\mathbf{R}$. For the electron-nucleus interaction $\hat{H}_{e-N}$, both electronic and nuclear coordinates appear. It is not reasonable if we simply ignore the electron-nucleus interaction. But we still have the possibility to separate the nuclear and electronic motions. The reason is that the mass of nuclei M_j is much larger than that of electrons m_e. The nuclear mass is about 1836 times of the electronic mass. This leads to the mobility of nuclei much less than that of electrons. Electrons can move at a very high speed, while nuclei just vibrate around their own equilibrium positions. Thus we can divide the problem into two parts. When we consider the electronic motion, the nuclei stay on particular positions. When we consider the nuclear motion, the electrons keep in their ground state positions. This approach was first proposed by Born-Oppenheimer.

Within this approximation, the many particle wave function shown in Eq. (2.1) can be written as

$$\Psi(\mathbf{r},\mathbf{R}) = \sum_k \chi_k(\mathbf{R})\Phi_k(\mathbf{r},\mathbf{R}), \tag{2.6}$$

where $\Phi_k(\mathbf{r},\mathbf{R})$ satisfies the following equation:

$$\hat{H}_0(\mathbf{r},\mathbf{R})\Phi_k(\mathbf{r},\mathbf{R}) = E_k(\mathbf{R})\Phi_k(\mathbf{r},\mathbf{R}), \tag{2.7}$$

with

$$\hat{H}_0(\mathbf{r},\mathbf{R}) = \hat{H}_e(\mathbf{r}) + \hat{H}_{e-N}(\mathbf{r},\mathbf{R}) + \hat{V}_N(\mathbf{R}). \tag{2.8}$$

Here $\chi_k(\mathbf{R})$ is a wave function that contains only the coordinates of nuclei, $\Phi_k(\mathbf{r},\mathbf{R})$ is a wave function that contains both electronic and nuclear coordinates $\mathbf{r}$ and $\mathbf{R}$, and k is a quantum number of electronic states. We notice that the nuclear coordinate $\mathbf{R}$ shown in the electronic wave function appears just as a parameter.

To understand the effect of nuclear kinetic energy operator $\hat{T}_N(\mathbf{R})$ on the electronic Hamiltonian $\hat{H}_0$, we introduce a small quantity:

$$\zeta = \left(\frac{m_e}{M_0}\right)^{1/4}, \tag{2.9}$$

where M_0 is the average value of all nuclear masses. We use $\zeta\mathbf{u} = (\mathbf{R}-\mathbf{R}_0)$ to denote the renormalized vibrational displacement of nuclei in contrast to its equilibrium position $\mathbf{R}_0$. In this case the kinetic energy operator for nuclei can be expressed as

$$\hat{T}_N(\mathbf{R}) = -\zeta^2 \sum_j \frac{M_0}{M_j}\frac{\hbar^2}{2m_e}\nabla^2_{\mathbf{u}_j}. \tag{2.10}$$

On the other hand, the wave function $\Phi_k(\mathbf{r},\mathbf{R})$ can be expanded order by order as

$$\Phi_k(\mathbf{r},\mathbf{R}) = \Phi_k(\mathbf{r},\mathbf{R}_0+\zeta\mathbf{u}) = \Phi_k^{(0)} + \mathbf{u}\Phi_k^{(1)} + \frac{\mathbf{u}^2}{2!}\Phi_k^{(2)} + \frac{\mathbf{u}^3}{3!}\Phi_k^{(3)} + \cdots, \tag{2.11}$$

where $\Phi_k^{(\nu)}$ is the ν-th derivative of Φ_k with respect to $\mathbf{u}$.

We now substitute Eq. (2.6) into Eq. (2.1) and multiply $\Phi_{k'}(\mathbf{r},\mathbf{R})$ on the left side of Eq. (2.1), and we can then obtain after an integral over $\mathbf{r}$ [19]

$$[\hat{T}_N(\mathbf{R}) + \hat{E}_k(\mathbf{R}) + \hat{C}_k(\mathbf{u})]\chi_k(\mathbf{R}) + \sum_{k'(\neq k)} \hat{C}_{kk'}(\mathbf{u})\chi_{k'}(\mathbf{R}) = E\chi_k(\mathbf{R}), \tag{2.12}$$

where

$$\hat{C}_{kk'}(\mathbf{u}) = -\zeta^2 \sum_i \frac{M_0}{M_i}\frac{\hbar^2}{2m_e}\int_{-\infty}^{\infty} d\mathbf{r}\Phi_k^*(\mathbf{r},\mathbf{u})[\nabla_{\mathbf{u}_i}\Phi_{k'}(\mathbf{r},\mathbf{u})\nabla_{\mathbf{u}_i} + \nabla^2_{\mathbf{u}_i}\Phi_{k'}(\mathbf{r},\mathbf{u})], \tag{2.13}$$

$$\hat{C}_k(\mathbf{u}) = -\zeta^2 \sum_i \frac{M_0}{M_i}\frac{\hbar^2}{2m_e}\int_{-\infty}^{\infty} d\mathbf{r}\Phi_k^*(\mathbf{r},\mathbf{u})\nabla^2_{\mathbf{u}_i}\Phi_k(\mathbf{r},\mathbf{u}). \tag{2.14}$$

In the above equations, the first term of the operator $\hat{C}_{kk'}(\mathbf{u})$ is a third-order small quantity of ζ. The second term of $\hat{C}_{kk'}(\mathbf{u})$ and the $\hat{C}_k(\mathbf{u})$ are the forth-order small quantities of ζ, while the nuclear kinetic energy operator $\hat{T}_N$ is a second-order small quantity with respect to ζ. Considering $\Phi^{(\nu)}$ is the ν-th order small quantity, we use the perturbation approach and neglect the higher order term. By setting the operator $\hat{C}_{kk'}(\mathbf{u}) = 0$, we can rewrite Eq. (2.12) as

$$[\hat{T}_N(\mathbf{R}) + \hat{E}_k(\mathbf{R}) + \hat{C}_k(\mathbf{u})]\chi_{kK}(\mathbf{R}) = E_{kK}\chi_{kK}(\mathbf{R}), \tag{2.15}$$

where E_{kK} and $\chi_{kK}(\mathbf{R})$ are the solutions of the above equation, K is a quantum number of the vibrational states. The wave function $\chi_{kK}(\mathbf{R})$ for describing the nuclei is only related to the k-th quantum state of the electronic system. The wave function corresponding to the eigenvalue E_{kK} is

$$\Psi_{kK}(\mathbf{r},\mathbf{R}) = \chi_{kK}(\mathbf{R})\Phi_k(\mathbf{r},\mathbf{R}), \tag{2.16}$$

where the first factor $\chi_{kK}(\mathbf{R})$ describes the nuclear motion. The nuclei look like moving in a potential well $E_k(\mathbf{R})+C_k(\mathbf{u})$. The second factor $\Phi_k(\mathbf{r},\mathbf{R})$ describes the electronic motion. The nuclei are fixed in their instantaneous positions when electrons move, and the nuclear motion does not influence the electronic motion.

2.2 Hartree-Fock approximation

Through the Born-Oppenheimer adiabatic approximation, the electronic and nuclear motions are separated. In the following we introduce briefly the Hartree-Fock equations.

2.2.1 Hartree equation

The many-electron Schrödinger equation can be rewritten as

$$\Big[-\sum_i \frac{\hbar^2}{2m_e}\nabla^2_{\mathbf{r}_i}+\sum_i V(\mathbf{r}_i,\mathbf{R})+\frac{1}{2}\sum_{\substack{i,i'\\ i\neq i'}}\frac{e^2}{|\mathbf{r}_i-\mathbf{r}_{i'}|}\Big]\Phi=\Big[\sum_i \hat{H}_i+\sum_{i,i'}\hat{H}_{i,i'}\Big]\Phi=E\Phi, \tag{2.17}$$

where $V(\mathbf{r}_i,\mathbf{R})$ is the external potential. This equation is still not easy to solve due to the interaction term $\hat{H}_{i,i'}$. If the interaction term equals zero, the equation turns out to be a single particle equation. In this case, the Schrödinger Eq. (2.17) becomes

$$\sum_i \hat{H}_i\Phi=E\Phi, \tag{2.18}$$

where

$$\Phi(\mathbf{r})=\varphi_1(\mathbf{r}_1)\varphi_2(\mathbf{r}_2)\cdots\varphi_n(\mathbf{r}_n) \tag{2.19}$$

is called the Hartree wave function. Inserting Eq. (2.19) into Eq. (2.18) and taking $E=\sum_i E_i$, we have

$$\hat{H}_i\varphi_i(\mathbf{r}_i)=E_i\varphi_i(\mathbf{r}_i). \tag{2.20}$$

The single particle Hartree wave function is a solution of the Eq. (2.17) if the interaction is zero, although this is not possible in reality. We now calculate the expectation value of energy, *i.e.*, $E=\langle\Phi|\hat{H}|\Phi\rangle$. Assuming φ satisfies $\langle\varphi_i|\varphi_j\rangle=\delta_{ij}$, we have

$$E=\langle\Phi|\hat{H}|\Phi\rangle=\sum_i\langle\varphi_i|\hat{H}_i|\varphi_i\rangle+\frac{1}{2}\sum_{i,i'}\langle\varphi_i\varphi_{i'}|\hat{H}_{i,i'}|\varphi_i\varphi_{i'}\rangle. \tag{2.21}$$

According to the variational principle, we have

$$\delta[E-\sum_i E_i\langle\varphi_i|\varphi_i\rangle]=0, \tag{2.22}$$

and

$$\begin{aligned}&\langle\delta\varphi_i|\hat{H}_i|\varphi_i\rangle+\sum_{i'(\neq i)}\left\langle\delta\varphi_i\varphi_{i'}\middle|\frac{e^2}{\mathbf{r}_i-\mathbf{r}_{i'}}\middle|\varphi_i\varphi_{i'}\right\rangle-E_i\langle\delta\varphi_i|\varphi_i\rangle\\ &=\left\langle\delta\varphi_i\middle|\hat{H}_i+\sum_{i'(\neq i)}\left\langle\varphi_{i'}\middle|\frac{e^2}{\mathbf{r}_i-\mathbf{r}_{i'}}\middle|\varphi_{i'}\right\rangle-E_i\middle|\varphi_i\right\rangle,\end{aligned} \tag{2.23}$$

where the equation is independent on the $\delta\varphi_i^*$. Thus

$$\left[-\frac{\hbar^2}{2m_e}\nabla^2_{\mathbf{r}_i} + V(\mathbf{r}_i,\mathbf{R}) + \sum_{i'(\neq i)}\int_{-\infty}^{\infty} d\mathbf{r}_{i'}\frac{e^2|\varphi_{i'}(\mathbf{r}_{i'})|^2}{|\mathbf{r}_i-\mathbf{r}_{i'}|}\right]\varphi_i(\mathbf{r}_i) = E_i\varphi_i(\mathbf{r}_i). \tag{2.24}$$

Eq. (2.24) is the single particle Hartree equation, describing an electron at position $\mathbf{r}_i$ moving in a mean field potential of all other electrons.

2.2.2 Fock equation

For the Hartree equation, although the Pauli exclusion principle is included, the wave function is not antisymmetric in the electron coordinates. There are $N!$ different arrangements if there are N electrons located at the positions $\mathbf{r}_1, \mathbf{r}_2, \cdots, \mathbf{r}_N$. And these N arrangements are equivalent because electrons are identical. If we denote the i-th electron's wave function as $\varphi_i(\mathbf{r}_i)$, where we assume $\mathbf{r}_i$ includes also the spin, then the Slater determinant

$$\Phi = \frac{1}{\sqrt{N!}}\begin{vmatrix} \varphi_1(\mathbf{r}_1) & \varphi_2(\mathbf{r}_1) & \dots & \varphi_N(\mathbf{r}_1) \\ \varphi_1(\mathbf{r}_2) & \varphi_2(\mathbf{r}_2) & \dots & \varphi_N(\mathbf{r}_2) \\ \vdots & \vdots & & \vdots \\ \varphi_1(\mathbf{r}_N) & \varphi_2(\mathbf{r}_N) & \dots & \varphi_N(\mathbf{r}_N) \end{vmatrix} \tag{2.25}$$

satisfies the exchange anti-symmetric properties. We now calculate the expectation value of energy again by using Eq. (2.25):

$$\begin{aligned} E = \langle\Phi|\hat{H}|\Phi\rangle = &\sum_i \int_{-\infty}^{\infty} d\mathbf{r}_i \varphi_i^*(\mathbf{r}_j)\hat{H}_i\varphi_i(\mathbf{r}_j) + \frac{1}{2}\sum_{i,i'}\sum_{\substack{j,j'\\ j\neq j'}} d\mathbf{r}_j d\mathbf{r}_{j'}\frac{|\varphi_i(\mathbf{r}_j)|^2 e^2|\varphi_{i'}(\mathbf{r}_{j'})|^2}{|\mathbf{r}_j-\mathbf{r}_{j'}|} \\ &-\frac{1}{2}\sum_{i,i'}\sum_{\substack{j,j'\\ j\neq j'}}\int_{-\infty}^{\infty} d\mathbf{r}_j d\mathbf{r}_{j'}\frac{\varphi_i^*(\mathbf{r}_j)\varphi_i(\mathbf{r}_{j'})e^2\varphi_{i'}^*(\mathbf{r}_{j'})\varphi_{i'}(\mathbf{r}_j)}{|\mathbf{r}_j-\mathbf{r}_{j'}|}. \end{aligned} \tag{2.26}$$

Comparing Eq. (2.26) with Eq. (2.21), there is an additional term shown in Eq. (2.26). Accordingly, the variation becomes

$$\delta[E - \sum_{i,i'}\lambda_{i,i'}(\langle\varphi_i|\varphi_{i'}\rangle - \delta_{i,i'})] = 0, \tag{2.27}$$

and so we have

$$\begin{aligned} &\left[-\frac{\hbar^2}{2m_e}\nabla^2_{\mathbf{r}_j} + V(\mathbf{r}_j,\mathbf{R})\right]\varphi_i(\mathbf{r}_j) + \sum_{\substack{i',j'\\ j\neq j'}}\int_{-\infty}^{\infty} d\mathbf{r}_{j'}\frac{e^2|\varphi_{i'}(\mathbf{r}_{j'})|^2}{|\mathbf{r}_j-\mathbf{r}_{j'}|}\varphi_i(\mathbf{r}_j) \\ &-\sum_{\substack{i',j'\\ j\neq j'}}\int_{-\infty}^{\infty} d\mathbf{r}_{j'}\frac{e^2\varphi_{i'}^*(\mathbf{r}_{j'})\varphi_i(\mathbf{r}_{j'})}{|\mathbf{r}_j-\mathbf{r}_{j'}|}\varphi_{i'}(\mathbf{r}_j) = \sum_{i'}\lambda_{i,i'}\varphi_{i'}(\mathbf{r}_j). \end{aligned} \tag{2.28}$$

On the right side, we can always find a transformation for $\varphi_{i'}(\mathbf{r}_j)$ so that the $\lambda_{i,i'}$ becomes diagonal, *i.e.*, $\lambda_{i,i'} = E_i\delta_{i,i'}$. Finally, we can obtain

$$\begin{aligned}\left[-\frac{\hbar^2}{2m_e}\nabla^2_{\mathbf{r}_j} + V(\mathbf{r}_j,\mathbf{R})\right]\varphi_i(\mathbf{r}_j) + \sum_{\substack{i',j'\\ j\neq j'}}\int_{-\infty}^{\infty} d\mathbf{r}_{j'}\frac{e^2|\varphi_{i'}(\mathbf{r}_{j'})|^2}{|\mathbf{r}_j-\mathbf{r}_{j'}|}\varphi_i(\mathbf{r}_j)\\ -\sum_{\substack{i',j'\\ j\neq j'}}\int_{-\infty}^{\infty} d\mathbf{r}_{j'}\frac{e^2\varphi^*_{i'}(\mathbf{r}_{j'})\varphi_i(\mathbf{r}_{j'})}{|\mathbf{r}_j-\mathbf{r}_{j'}|}\varphi_{i'}(\mathbf{r}_j) = E_i\varphi_i(\mathbf{r}_j).\end{aligned} \tag{2.29}$$

This is the Hartree-Fock equation. By comparing with the Eq. (2.24), we find that there is an additional term, *i.e.*, the 4th-term on the r.h.s. of Eq. (2.29), which is due to the exchange interaction.

2.3 Density functional theory

2.3.1 Hohenberg-Kohn theorem

In this section we introduce the density functional theory. The basic idea of DFT is that the ground state physical properties of atoms, molecules and solid states can be described by its density, originating from the work of H. Thomas and E. Fermi in 1927 [24, 25]. The starting point of DFT is the Hohenberg-Kohn theorem [20], which can be summarized as:
(1) The ground state energy of a fermionic (electronic) system is a unique functional of the density $\rho(\mathbf{r})$;
(2) Energy functional $E[\rho]$ at constant particle number takes the minimum value for correct electronic density, and moreover it equals the ground state energy of the system.

In the theorem the case for spin-degeneracy is not included. We now prove the Hohenberg -Kohn theorem. The central point of item (1) is that particle density is a basic quantity that determines the ground state physical properties of the system. Let us first define the particle density as

$$\rho(\mathbf{r}) = \langle\Phi|\hat{\psi}^\dagger(\mathbf{r})\hat{\psi}(\mathbf{r})|\Phi\rangle, \tag{2.30}$$

where Φ is the ground state wave function. $\hat{\psi}^\dagger(\mathbf{r})$ and $\hat{\psi}(\mathbf{r})$ are the field operators of creating and annihilating a particle at position $\mathbf{r}$. Then the Hamiltonian of the identical fermionic (electronic) system becomes

$$\hat{H} = \hat{T} + \hat{U} + \hat{V}, \tag{2.31}$$

with

$$\hat{T} = -\frac{\hbar}{2m_e}\int_{-\infty}^{\infty}\nabla\hat{\psi}^\dagger(\mathbf{r})\cdot\nabla\hat{\psi}(\mathbf{r})d\mathbf{r}, \tag{2.32}$$

$$\hat{U} = \frac{1}{2}\int_{-\infty}^{\infty}\frac{e^2}{|\mathbf{r}-\mathbf{r}'|}\hat{\psi}^\dagger(\mathbf{r})\hat{\psi}^\dagger(\mathbf{r}')\hat{\psi}(\mathbf{r})\hat{\psi}(\mathbf{r}')d\mathbf{r}d\mathbf{r}', \tag{2.33}$$

$$\hat{V} = \int_{-\infty}^{\infty}v(\mathbf{r})\hat{\psi}^\dagger(\mathbf{r})\hat{\psi}(\mathbf{r})d\mathbf{r}, \tag{2.34}$$

where $\hat{T}$ is the kinetic energy operator, $\hat{U}$ is the Coulomb repulsion, and $\hat{V}$ is the external potential.

We use an indirect method to prove that $v(\mathbf{r})$ is the unique functional of $\rho(\mathbf{r})$ up to a constant. We assume that there is another potential $v'(\mathbf{r})$ which gives the same particle density $\rho'(\mathbf{r}) = \rho(\mathbf{r})$. Taking $\hat{H}$ as the Hamiltonian including $v(\mathbf{r})$, its ground state is Φ and energy expectation value is E. Taking $\hat{H}'$ as the Hamiltonian including $v'(\mathbf{r})$, its ground state is Φ' and energy expectation value is E'. According to the variational principle, in the case of spin non-degeneracy, for a true ground state Φ it always has

$$\begin{aligned} E' &= \langle \Phi' | \hat{H}' | \Phi' \rangle < \langle \Phi | \hat{H}' | \Phi \rangle \\ &= \langle \Phi | \hat{H} + \hat{V}' - \hat{V} | \Phi \rangle = E + \int_{-\infty}^{\infty} \rho(\mathbf{r})[v'(\mathbf{r}) - v(\mathbf{r})] d\mathbf{r}. \end{aligned} \tag{2.35}$$

Accordingly we have

$$E' < E + \int_{-\infty}^{\infty} \rho(\mathbf{r})[v'(\mathbf{r}) - v(\mathbf{r})] d\mathbf{r}. \tag{2.36}$$

Using the same manipulation but starting from $\hat{H}$, we can get

$$\begin{aligned} E &= \langle \Phi | \hat{H} | \Phi \rangle < \langle \Phi' | \hat{H} | \Phi' \rangle \\ &= \langle \Phi' | \hat{H}' + \hat{V} - \hat{V}' | \Phi' \rangle = E' + \int_{-\infty}^{\infty} \rho(\mathbf{r})[v(\mathbf{r}) - v'(\mathbf{r})] d\mathbf{r}, \end{aligned} \tag{2.37}$$

and we have

$$E < E' + \int_{-\infty}^{\infty} \rho(\mathbf{r})[v(\mathbf{r}) - v'(\mathbf{r})] d\mathbf{r}. \tag{2.38}$$

The combination of Eqs. (2.36) and (2.38) yields

$$E + E' < E' + E. \tag{2.39}$$

This turns out to be absurd. So $\rho(\mathbf{r}) \neq \rho'(\mathbf{r})$, *i.e.*, $v(\mathbf{r})$ is the unique functional of $\rho(\mathbf{r})$. Therefore, the ground state energy is a unique functional of the density.

As to the second item of the Hohenberg-Kohn theorem, the key point is that the variation of the energy functional with respect to the particle density gives the ground state energy of the system $E_G[\rho]$. For a given potential $v(\mathbf{r})$, the energy functional $E_G[\rho]$ is defined as

$$E_G[\rho] \equiv \int_{-\infty}^{\infty} d\mathbf{r} v(\mathbf{r}) \rho(\mathbf{r}) + \langle \Phi | \hat{T} + \hat{U} | \Phi \rangle. \tag{2.40}$$

By defining

$$F[\rho] \equiv \langle \Phi | \hat{T} + \hat{U} | \Phi \rangle, \tag{2.41}$$

we have

$$E_G[\rho] \equiv \int_{-\infty}^{\infty} d\mathbf{r} v(\mathbf{r}) \rho(\mathbf{r}) + F[\rho]. \tag{2.42}$$

According to the variational principle at a constant particle number, for an arbitrary state Φ', the energy functional $E_G[\Phi']$ is

$$E_G[\Phi'] \equiv \langle \Phi' | \hat{T} + \hat{U} | \Phi' \rangle + \langle \Phi' | \hat{V} | \Phi' \rangle. \tag{2.43}$$

The minimum of $E_G[\Phi']$ happens when $\Phi' = \Phi$. Taking Φ' and ρ' as the ground state and the density corresponding to the potential $v'(\mathbf{r})$, so $E_G[\Phi']$ could also be a functional of ρ'. Then we have

$$\begin{aligned} E_G[\Phi'] = E_G[\rho'] &= F[\rho'] + \int_{-\infty}^{\infty} \rho'(\mathbf{r}) v'(\mathbf{r}) d\mathbf{r} > E_G[\Phi] \\ &= F[\rho] + \int_{-\infty}^{\infty} \rho(\mathbf{r}) v(\mathbf{r}) d\mathbf{r} = E_G[\rho]. \end{aligned} \tag{2.44}$$

For all the other densities $\rho'(\mathbf{r})$ relating to $v'(\mathbf{r})$, $E_G[\Phi]$ is the minimum value. In other words if one obtains the ground state particle density, one can know the minimum of the energy functional, and this energy functional equals the ground state energy.

In the above expressions we have not taken into account the spin factor. With spin and relativistic effect, the Hohenberg-Kohn theorem can be found elsewhere [26]. The functional $F[\rho]$ can be rewritten in the form of

$$F[\rho] = T[\rho] + \frac{1}{2} \int_{-\infty}^{\infty} \int_{-\infty}^{\infty} d\mathbf{r} d\mathbf{r}' \frac{\rho(\mathbf{r})\rho(\mathbf{r}')}{|\mathbf{r} - \mathbf{r}'|} + E_{xc}[\rho], \tag{2.45}$$

where the first and second terms are respectively the kinetic energy and Hartree term of non-interacting particles, the third term $E_{xc}[\rho]$ is called exchange-correlation (xc) interaction and is also a functional of ρ. The Hohenberg-Kohn theorem shows that the particle density ρ is a basic variable for calculating the ground state physical properties. However, there are still three unsolved questions:
(1) how to obtain the particle density ρ;
(2) how to obtain the kinetic energy functional $T[\rho]$;
(3) how to obtain the exchange correlation functional $E_{xc}[\rho]$.
The first and second questions are solved by W. Kohn and L. J. Sham [27]. The third question can be answered by doing approximations. In the following we will introduce them.

2.3.2 Kohn-Sham equations

According to the Hohenberg-Kohn theorem, ground state energy and ground state particle density can be obtained from the variation of energy functional with respect to density, *i.e.*,

$$\int_{-\infty}^{\infty} d\mathbf{r} \delta\rho(\mathbf{r}) \left[\frac{\delta T[\rho(\mathbf{r})]}{\delta\rho(\mathbf{r})} + v(\mathbf{r}) + \int_{-\infty}^{\infty} d\mathbf{r}' \frac{\rho(\mathbf{r}')}{|\mathbf{r} - \mathbf{r}'|} + \frac{\delta E_{xc}[\rho(\mathbf{r})]}{\delta\rho(\mathbf{r})} \right] = 0. \tag{2.46}$$

Taking into account the condition that the particle number is constant:

$$\int_{-\infty}^{\infty} d\mathbf{r} \delta\rho(\mathbf{r}) = 0, \tag{2.47}$$

we have

$$\frac{\delta T[\rho(\mathbf{r})]}{\delta\rho(\mathbf{r})} + v(\mathbf{r}) + \int_{-\infty}^{\infty} d\mathbf{r}' \frac{\rho(\mathbf{r}')}{|\mathbf{r} - \mathbf{r}'|} + \frac{\delta E_{xc}[\rho(\mathbf{r})]}{\delta\rho(\mathbf{r})} = \mu, \tag{2.48}$$

where the Lagrange multiplier μ is the chemical potential. Equation (2.48) expresses the particles moving in an effective potential which has the form:

$$V_{eff}(\mathbf{r}) = v(\mathbf{r}) + \int_{-\infty}^{\infty} d\mathbf{r}' \frac{\rho(\mathbf{r}')}{|\mathbf{r} - \mathbf{r}'|} + \frac{\delta E_{xc}[\rho(\mathbf{r})]}{\delta\rho(\mathbf{r})}, \tag{2.49}$$

though the kinetic energy $T[\rho]$ in Eq. (2.46) is still unknown.

Because the kinetic energy of the interacting system is unknown, W. Kohn and L. J. Sham proposed that the interacting kinetic energy functional $T[\rho]$ can be replaced by a functional $T_S[\rho]$ of a non-interacting system, where the non-interacting system has the same density as the interacting system. In this case the difference between $T[\rho]$ and $T_S[\rho]$ is added to the exchange correlation $E_{xc}[\rho]$. In order to realize the single particle picture, Kohn and Sham used the single particle wave function $\varphi_i(\mathbf{r})$ to construct the density, which is given by

$$\rho(\mathbf{r}) = \sum_{i=1} |\varphi_i(\mathbf{r})|^2, \tag{2.50}$$

where $\phi_i(\mathbf{r})$ satisfies the following Schrödinger equation:

$$(\hat{T}_S[\rho] + \hat{V}_S[\rho])\varphi_i(\mathbf{r}) = \left(-\frac{\hbar^2}{2m}\nabla^2 + v_s(\mathbf{r})\right)\varphi_i(\mathbf{r}) = \varepsilon_i\varphi_i(\mathbf{r}). \tag{2.51}$$

The $T_S[\rho]$ and $V_S[\rho]$ are the single particle kinetic and potential energies of the non-interacting system. Accordingly the total energy functional is

$$E_S[\rho] = T_S[\rho] + \int_{-\infty}^{\infty} d\mathbf{r}\rho(\mathbf{r})v_s(\mathbf{r}). \tag{2.52}$$

The variation of Eq. (2.52) with respect to density gives

$$\frac{\delta E_S[\rho]}{\delta\rho(\mathbf{r})} = \frac{T_S[\rho]}{\delta\rho(\mathbf{r})} + v_s(\mathbf{r}) = \mu. \tag{2.53}$$

By comparing Eq. (2.53) with Eq. (2.48), we have

$$\begin{aligned} v_s(\mathbf{r}) &= \frac{\delta T[\rho(\mathbf{r})]}{\delta\rho(\mathbf{r})} - \frac{T_S[\rho]}{\delta\rho(\mathbf{r})} + v(\mathbf{r}) + \int_{-\infty}^{\infty} d\mathbf{r}' \frac{\rho(\mathbf{r}')}{|\mathbf{r}-\mathbf{r}'|} + \frac{\delta E_{xc}[\rho(\mathbf{r})]}{\delta\rho(\mathbf{r})} \\ &= v(\mathbf{r}) + \int_{-\infty}^{\infty} d\mathbf{r}' \frac{\rho(\mathbf{r}')}{|\mathbf{r}-\mathbf{r}'|} + \frac{\delta E^s_{xc}[\rho(\mathbf{r})]}{\delta\rho(\mathbf{r})}, \end{aligned} \tag{2.54}$$

and

$$v^s_{xc}[\rho](\mathbf{r}) = \frac{\delta E^s_{xc}[\rho(\mathbf{r})]}{\delta\rho(\mathbf{r})}, \tag{2.55}$$

where we have put the difference between the two kinetic energies into the exchange correction potential $E^s_{xc}[\rho(\mathbf{r})]$. Equations (2.50), (2.51), (2.54), and (2.55) are together called the KS equations. Figure 2.1 shows clearly the difference between the KS and real systems. For practical calculations, we still need to know the explicit formula of the potential v^s_{xc}. For simplicity in the rest part of this thesis, we omit the superscript s in $v^s_{xc}[\rho](\mathbf{r})$ and $E^s_{xc}[\rho(\mathbf{r})]$.

2.3.3 Approximate functionals

2.3.3.1 Local density approximation

The oldest approximation of DFT, the local density functional (LDA), was originally proposed by Kohn and Sham in 1965 [27]. It expresses the xc energy of an inhomogeneous system as the integral over the xc energy density of a homogeneous electron

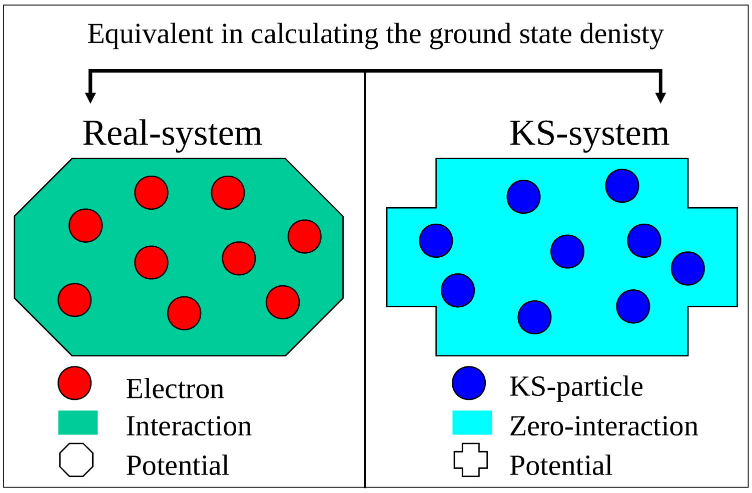

FIGURE 2.1: (Color) A schematic picture of real system and KS system, where in both cases ground state densities are the same.

liquid, evaluated at the local density. To better understand the concept of LDA, let me first recall how the non-interacting kinetic energy $T_S[\rho]$ is treated in the Thomas-Fermi approximation. In a homogeneous system one knows that the kinetic energy density is [17, 28]

$$t_s^{hom}(\rho) = \frac{3\hbar^2}{10m_e}(3\pi^2)^{2/3}\rho^{5/3}, \tag{2.56}$$

where the density ρ is constant. In an inhomogeneous system, one approximates

$$t_s(\mathbf{r}) \approx t_s^{hom}(\rho(\mathbf{r})) = \frac{3\hbar^2}{10m_e}(3\pi^2)^{2/3}\rho(\mathbf{r})^{5/3}, \tag{2.57}$$

where the density ρ is a functional of the local coordinate $\mathbf{r}$, *i.e.*, $\rho = \rho(\mathbf{r})$. Then the total kinetic energy is obtained by integration over all space

$$T_S^{LDA}[\rho] = \int_{-\infty}^{\infty} d\mathbf{r} t_s^{hom}(\rho(\mathbf{r})) = \frac{3\hbar^2}{10m_e}(3\pi^2)^{2/3}\int_{-\infty}^{\infty} d\mathbf{r}\rho(\mathbf{r})^{5/3}. \tag{2.58}$$

For the kinetic energy, the approximation $T_S[\rho] \approx T_S^{LDA}[\rho]$ is much inferior to the exact treatment of T_S in terms of orbitals, offered by the KS equations. However the LDA concept turns out to be a highly useful for the exchange-correlation potential $E_{xc}[\rho]$. For the exchange energy $E_x[\rho]$ the procedure is very simple, since the exchange energy density of homogeneous electron liquid is known exactly [29],

$$e_x^{hom}(\rho) = -\frac{3e^2}{4}\left(\frac{3}{\pi}\right)^{1/3}\rho^{4/3}. \tag{2.59}$$

Thus we have

$$E_x^{LDA}[\rho] = -\frac{3e^2}{4}\left(\frac{3}{\pi}\right)^{1/3}\int_{-\infty}^{\infty} d\mathbf{r}\rho(\mathbf{r})^{4/3}. \tag{2.60}$$

For the correlation energy $E_c[\rho]$, the situation is more complicated since $e_c^{hom}(\rho)$ is not known exactly: The determination of the correlation energy of a homogeneous interacting electron system is already a difficult many-body problem on its own. Early approximate expressions for $e_c^{hom}(\rho)$ were based on applying perturbation theory. Modern expressions for $e_c^{hom}(\rho)$ are parametrizations of the obtained data from quantum Monte Carlo calculations. These expressions are implemented in most standard DFT program packages. Independently of the parametrization, the LDA for $E_{xc}[\rho]$ formally is [26]

$$E_{xc}[\rho] \approx E_{xc}^{LDA}[\rho] = \int_{-\infty}^{\infty} d\mathbf{r} e_{xc}^{hom}(\rho)\Big|_{\rho\to\rho(\mathbf{r})} = \int_{-\infty}^{\infty} d\mathbf{r} e_{xc}^{hom}(\rho(\mathbf{r})), \tag{2.61}$$

where $e_{xc}^{hom} = e_x^{hom} + e_c^{hom}$. The corresponding xc potential is

$$v_{xc}^{LDA}[\rho](\mathbf{r}) = \frac{\partial e_{xc}^{hom}(\rho)}{\partial \rho}\Bigg|_{\rho\to\rho(\mathbf{r})}. \tag{2.62}$$

The physical meaning of LDA is: At each point $\mathbf{r}$ in space, the xc energy density e_{xc} is approximated by that which one would obtain from a homogeneous electron liquid that has a density $\rho(r)$ everywhere. This approximation for $E_{xc}[n]$ has proved amazingly successful numerically, even when applied to systems that are quite different from the electron liquid that forms the reference system for the LDA. In the next calculations of this thesis, we will adopt this approximation in our considered nanosystems.

2.3.3.2 Generalized gradient approximation

The idea of improving the LDA by constructing xc functionals which depend not only on the local density itself but also on its gradients has a long history, going back to the original work by Hohenberg and Kohn in 1964. In the LDA one exploits knowledge of the density at point $\mathbf{r}$. Any real system is spatially inhomogeneous, *i.e.*, it has a spatially varying density $\rho(\mathbf{r})$, and it would be clearly useful to also include information on the rate of this variation in the functional. A first attempt at doing this was the so-called gradient expansion approximation. In this approximation, one tries to systematically calculate the gradient correlations of the form $|\nabla\rho(\mathbf{r})|$, $|\nabla\rho(\mathbf{r})|^2$, $|\nabla^2\rho(\mathbf{r})|$, *etc.*, to the LDA. A famous example is the lowest-order gradient correction to the Thomas-Fermi approximation for $T_S[\rho]$,

$$T_S[\rho] \approx T_S^W[\rho] = T_S^{LDA}[\rho] + \frac{\hbar^2}{8m_e}\int_{\infty}^{\infty} d\mathbf{r}\frac{\nabla\rho(\mathbf{r})|^2}{\rho(\mathbf{r})}, \tag{2.63}$$

where the second term on the right hand side is called the Weizsäker term [29]. Similarly,

$$E_x[\rho] \approx E_x^{GEA(2)}[\rho] = E_x^{LDA}[\rho] - \frac{10e^2}{432\pi(3\pi^2)^{1/3}}\int_{-\infty}^{\infty} d\mathbf{r}\frac{|\nabla\rho(\mathbf{r})|^2}{\rho(\mathbf{r})^{4/3}}, \tag{2.64}$$

where the second term on the right hand side is the lowest-order gradient correction to $E_x^{LDA}[\rho]$. In practice, the inclusion of lowest-order gradient corrections almost never improves on the LDA, and often even worsens it. Higher-order corrections, on the other hand, are exceedingly difficult to calculate and little is known on them. In this situation it was a major breakthrough in the early stage to get a more general functionals which need not proceed order by order. Generalized gradient approximations (GGA) are a class of xc functionals which have the following structure [26]:

$$E_{xc}^{GGA}[\rho] = \int_{-\infty}^{\infty} d\mathbf{r} e_{xc}^{GGA}(\rho(\mathbf{r}), \nabla\rho(\mathbf{r})). \tag{2.65}$$

GGA does not arise from systematic order-by-order expansions in terms of the density gradients. Instead, the key idea is to construct explicit mathematical expressions for e_{xc}^{GGA} which satisfy as many of the known exact properties of e_{xc} as possible. In a way this can be viewed as attempting to find a proper method for the gradient expansion series.

2.4 Fermionic Green's function

2.4.1 Modeling electronic Hamiltonian

In this section, we derive the electric and energy current formulas for electron transport in terms of the Green's functions. The modelled system is schematically shown in Fig. 2.2, which is divided into three parts: left lead (L), central interacting region (C) and right lead (R). The Hamiltonian of the systems is

$$\hat{H} = \sum_{\alpha=L,R} \hat{H}_\alpha + \hat{H}_C + \hat{H}_{LC} + \hat{H}_{RC} + \hat{H}_U, \tag{2.66}$$

where $\hat{H}_\alpha$ describes the Hamiltonian of the left and right leads, $\hat{H}_C$ models the Hamiltonian of the central scattering region, $\hat{H}_{LC}$ or $\hat{H}_{RC}$ is the coupling between the left or right lead and the central scattering region, and $\hat{H}_U$ describes the inelastic interaction in the device. The interaction between the two leads is not considered. Guided by the typical experimental geometry in which the leads rapidly broaden into metallic contacts, we assume electrons in the two leads are non-interacting particles. Thus the Hamiltonian of the lead is

$$\hat{H}_\alpha = \sum_{\mathbf{k}} \varepsilon_{\mathbf{k}\alpha} \hat{c}^\dagger_{\mathbf{k}\alpha} \hat{c}_{\mathbf{k}\alpha}, \tag{2.67}$$

where $\hat{c}^\dagger_{\mathbf{k}\alpha}$ and $\hat{c}_{\mathbf{k}\alpha}$ are respectively the creation and annihilation operators for electrons in the lead α with momentum $\mathbf{k}$ in reciprocal space, $\varepsilon_{\mathbf{k}\alpha}$ is the electron energy in the lead. The coupling between the lead and the central region is

$$\hat{H}_{\alpha C} = \sum_{\mathbf{k},n} [V_{\mathbf{k}\alpha,n} \hat{c}^\dagger_{\mathbf{k}\alpha} \hat{d}_n + h.c.], \tag{2.68}$$

where $\hat{d}_n$ and $\hat{d}^\dagger_n$ are the annihilation and creation operators for electrons in the central region, respectively, $V_{\mathbf{k}\alpha,n}$ is the coupling matrix element, and $h.c.$ indicates the corresponding Hermitian conjugate. The Hamiltonian of the central region is given by

$$\hat{H}_C = \sum_m \varepsilon_m \hat{d}^\dagger_m \hat{d}_m, \tag{2.69}$$

where we have used m and n to denote the quantum number of the central region. The interaction Hamiltonian in Eq. (2.66) can be written as

$$\hat{H}_U = \frac{1}{2} \sum_{mn} U_{mn} \hat{d}^\dagger_m \hat{d}^\dagger_n \hat{d}_m \hat{d}_n, \tag{2.70}$$

where U_{mn} describes the interacting strength of electrons. The above Hamiltonian from Eq. (2.67) to (2.70) does not include the spin explicitly, while the spin factor can be added easily at any time as an additional quantum number.

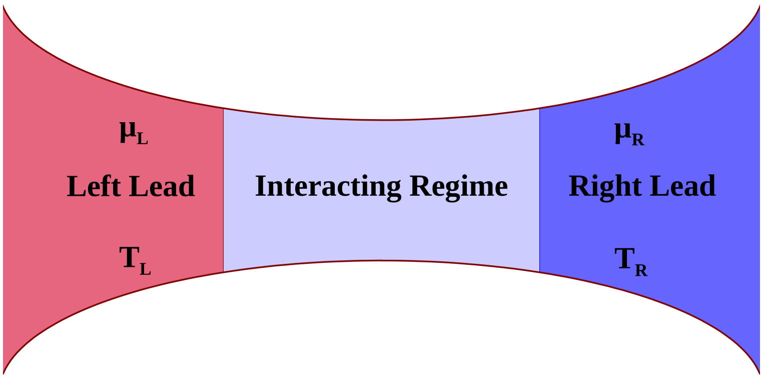

FIGURE 2.2: (Color) A schematic illustration of the modelling system including left and right leads and central interacting region, where μ_L and μ_R are the chemical potentials, T_L and T_R are the temperatures of the left and right leads, respectively.

2.4.2 General expression of currents

Based on the Hamiltonian shown in Eq. (2.66), the energy current flowing from the left lead to the central region can be calculated from the time evolution of the Hamiltonian operator of the left lead:

$$I_L^E(t) = -\langle \dot{\hat{H}}_L \rangle = -\frac{i}{\hbar}\langle [\hat{H}, \hat{H}_L] \rangle, \tag{2.71}$$

where the expectation value is taken with respect to the ground state of the interacting system. Since $\hat{H}_L$, $\hat{H}_C + \hat{H}_U$, $\hat{H}_R$ and $\hat{H}_{RC}$ commutate with $\hat{H}_L$, one finds

$$I_L^E = -\frac{i}{\hbar}\langle [\hat{H}_{LC}, \hat{H}_L] \rangle = \frac{i}{\hbar}\sum_{\mathbf{k},n} \varepsilon_{\mathbf{k}L}[V_{\mathbf{k}L,n}\langle \hat{c}^\dagger_{\mathbf{k}L}\hat{d}_n\rangle - V^*_{\mathbf{k}L,n}\langle \hat{d}^\dagger_n \hat{c}_{\mathbf{k}L}\rangle], \tag{2.72}$$

where the following relations have been used:

$$[\hat{A}\hat{B}, \hat{C}] = \hat{A}\{\hat{B}, \hat{C}\} - \{\hat{A}, \hat{C}\}\hat{B}, \tag{2.73}$$
$$[\hat{A}, \hat{B}\hat{C}] = \{\hat{A}, \hat{B}\}\hat{C} - \hat{B}\{\hat{A}, \hat{C}\}, \tag{2.74}$$

where the square brackets $[\hat{A}, \hat{B}] = \hat{A}\hat{B} - \hat{B}\hat{A}$ denote the commutator and curly brackets $\{\hat{A}, \hat{B}\} = \hat{A}\hat{B} + \hat{B}\hat{A}$ denote the anti-commutator.

To derive the expression of energy current, we first define six Green's functions for fermionic system in a general way:

$$\mathcal{G}^r_{\mathbf{x}\mathbf{x}'}(t,t') = -\frac{i}{\hbar}\theta(t-t')\langle\{\psi_{\mathbf{x}}(t), \psi^\dagger_{\mathbf{x}'}(t')\}\rangle, \tag{2.75}$$
$$\mathcal{G}^a_{\mathbf{x}\mathbf{x}'}(t,t') = \frac{i}{\hbar}\theta(t'-t)\langle\{\psi_{\mathbf{x}}(t), \psi^\dagger_{\mathbf{x}'}(t')\}\rangle, \tag{2.76}$$
$$\mathcal{G}^<_{\mathbf{x}\mathbf{x}'}(t,t') = \frac{i}{\hbar}\langle\psi^\dagger_{\mathbf{x}'}(t')\psi_{\mathbf{x}}(t)\rangle, \quad \mathcal{G}^>_{\mathbf{x}\mathbf{x}'}(t,t') = -\frac{i}{\hbar}\langle\psi_{\mathbf{x}}(t)\psi^\dagger_{\mathbf{x}'}(t')\rangle, \tag{2.77}$$
$$\mathcal{G}^t_{\mathbf{x}\mathbf{x}'}(t,t') = -\frac{i}{\hbar}\theta(t-t')\langle\psi_{\mathbf{x}}(t)\psi^\dagger_{\mathbf{x}'}(t')\rangle + \frac{i}{\hbar}\theta(t'-t)\langle\psi^\dagger_{\mathbf{x}'}(t')\psi_{\mathbf{x}}(t)\rangle, \tag{2.78}$$
$$\mathcal{G}^{\bar{t}}_{\mathbf{x}\mathbf{x}'}(t,t') = -\frac{i}{\hbar}\theta(t'-t)\langle\psi_{\mathbf{x}}(t)\psi^\dagger_{\mathbf{x}'}(t')\rangle + \frac{i}{\hbar}\theta(t-t')\langle\psi^\dagger_{\mathbf{x}'}(t')\psi_{\mathbf{x}}(t)\rangle, \tag{2.79}$$

where $\psi_{\mathbf{x}}(t)$ and $\psi^{\dagger}_{\mathbf{x}'}(t')$ are the annihilation and creation operators for the leads or for the central interacting region with respect to the degrees of freedom of $\mathbf{x}$ and t. $\mathbf{x}$ could represent either the quantum state $\mathbf{k}\alpha$ of the lead or the state mn of the central region as we shall see later. The step function satisfies the properties: $\theta(t-t') = 1$ if $(t-t') \geq 0$ and 0 if $(t-t') < 0$. The above six Green's functions are respectively named as retarded, advanced, lesser, greater, time-ordered and anti-time ordered Green's functions. The physical meaning of the Green's function can be understood as a propagator, such as $\mathcal{G}^{<}_{\mathbf{x}\mathbf{x}'}$ represents the transmission probability of a particle moving from $\mathbf{x}$ to $\mathbf{x}'$. And for more detailed introduction about the Green's function, one can find in the book edited by G. Stefanucci and R. van Leeuwen [30]. From the definitions, we find the following relations:

$$\mathcal{G}^{r}_{\mathbf{x}\mathbf{x}'}(t,t') = \theta(t-t')[\mathcal{G}^{>}_{\mathbf{x}\mathbf{x}'}(t,t') - \mathcal{G}^{<}_{\mathbf{x}\mathbf{x}'}(t,t')], \tag{2.80}$$

$$\mathcal{G}^{a}_{\mathbf{x}\mathbf{x}'}(t,t') = -\theta(t'-t)[\mathcal{G}^{>}_{\mathbf{x}\mathbf{x}'}(t,t') - \mathcal{G}^{<}_{\mathbf{x}\mathbf{x}'}(t,t')], \tag{2.81}$$

$$\mathcal{G}^{t}_{\mathbf{x}\mathbf{x}'}(t,t') = \theta(t-t')\mathcal{G}^{>}_{\mathbf{x}\mathbf{x}'}(t,t') + \theta(t'-t)\mathcal{G}^{<}_{\mathbf{x}\mathbf{x}'}(t,t'), \tag{2.82}$$

$$\mathcal{G}^{\bar{t}}_{\mathbf{x}\mathbf{x}'}(t,t') = \theta(t'-')\mathcal{G}^{>}_{\mathbf{x}\mathbf{x}'}(t,t') + \theta(t-t')\mathcal{G}^{<}_{\mathbf{x}\mathbf{x}'}(t,t'). \tag{2.83}$$

So the above six fermionic Green's functions are not independent. Moreover in equilibrium or in steady state, the six Green's functions only depend on the time difference $(t-t')$. In this thesis we will mainly focus on the retarded and lesser Green's functions and our calculations in the next chapter are also limited in steady state. In terms of the Green's functions, the energy current at long time limit can be rewritten as

$$I^{E}_{L} = 2\big\{\mathrm{Re}\big[\sum_{\mathbf{k},n} \varepsilon_{\mathbf{k}L} V_{\mathbf{k}L,n} \mathcal{G}^{<}_{n,\mathbf{k}L}(t,t)\big]\big\}, \tag{2.84}$$

where

$$\mathcal{G}^{<}_{n,\mathbf{k}\alpha}(t,t') = \frac{i}{\hbar}\langle \hat{c}^{\dagger}_{\mathbf{k}\alpha}(t')\hat{d}_{n}(t)\rangle, \tag{2.85}$$

$$\mathcal{G}^{<}_{\mathbf{k}\alpha,n}(t,t') = \frac{i}{\hbar}\langle \hat{d}^{\dagger}_{n}(t')\hat{c}_{\mathbf{k}\alpha}(t)\rangle, \tag{2.86}$$

are the lesser Green's functions relating to the lead and the central region and having the property: $\mathcal{G}^{<}_{\mathbf{k}\alpha,n}(t,t) = -[\mathcal{G}^{<}_{n,\mathbf{k}\alpha}(t,t)]^{*}$. We note that the energy current is calculated by taking the time-diagonal components of the lesser Green's function.

For the next step we need to derive the expression of $\mathcal{G}^{<}_{n,\mathbf{k}\alpha}(t,t')$. As to the non-interacting lead, a general relation for the time-ordered Green's function $\mathcal{G}^{t}_{n,\mathbf{k}\alpha}(t,t')$ can be derived from the equation of motion (see appendix B), and we obtain

$$\mathcal{G}^{t}_{n,\mathbf{k}\alpha}(t,t') = \sum_{m}\int_{-\infty}^{\infty} dt_1 \mathcal{G}^{t}_{nm}(t,t_1) V^{*}_{\mathbf{k}\alpha,m} g^{t}_{\mathbf{k}\alpha}(t_1,t'), \tag{2.87}$$

where $\mathcal{G}^{t}_{nm}(t,t_1)$ is the time-ordered Green's function of the central region, and $g^{t}_{\mathbf{k}\alpha}(t_1,t')$ is the time-ordered Green's function of the lead α. Then according to the Langreth theorem [31], we have

$$\mathcal{G}^{<}_{n,\mathbf{k}\alpha}(t,t') = \sum_{m}\int_{-\infty}^{\infty} dt_1 [\mathcal{G}^{r}_{nm}(t,t_1) V^{*}_{\mathbf{k}\alpha,m} g^{<}_{\mathbf{k}\alpha}(t_1,t') + \mathcal{G}^{<}_{nm}(t,t_1) V^{*}_{\mathbf{k}\alpha,m} g^{a}_{\mathbf{k}\alpha}(t_1,t')], \tag{2.88}$$

where $g^{<}_{\mathbf{k}\alpha}$ and $g^{a}_{\mathbf{k}\alpha}$ are the lesser and advanced Green's functions of the lead, respectively. The Fourier transform [1] of Eq. (2.88) is

$$\mathcal{G}^{<}_{n,\mathbf{k}\alpha}(\varepsilon) = \sum_{m} [\mathcal{G}^{r}_{nm}(\varepsilon) V^{*}_{\mathbf{k}\alpha,m} g^{<}_{\mathbf{k}\alpha}(\varepsilon) + \mathcal{G}^{<}_{nm}(\varepsilon) V^{*}_{\mathbf{k}\alpha,m} g^{a}_{\mathbf{k}\alpha}(\varepsilon)]. \tag{2.89}$$

Whereby the energy current becomes

$$\begin{aligned} I^{E}_{L} &= 2\Big\{\mathrm{Re}\sum_{\mathbf{k},n} \varepsilon_{\mathbf{k}L} V_{\mathbf{k}L,n}\Big[\frac{1}{2\pi}\int_{-\infty}^{\infty} \mathcal{G}^{<}_{n,\mathbf{k}L}(\varepsilon) e^{-i\varepsilon(t-t)} d\varepsilon\Big]\Big\} \\ &= 2\int_{-\infty}^{\infty} \frac{d\varepsilon}{2\pi}\Big\{\mathrm{Re}\Big[\sum_{\mathbf{k},nm} V_{\mathbf{k}L,n} V^{*}_{\mathbf{k}L,m}(\mathcal{G}^{r}_{nm}(\varepsilon) g^{<}_{\mathbf{k}L}(\varepsilon) + \mathcal{G}^{<}_{nm}(\varepsilon) g^{a}_{\mathbf{k}L}(\varepsilon))\Big]\Big\}, \end{aligned} \tag{2.90}$$

where the first and the second terms relate to $g^{<}_{\mathbf{k}\alpha}(\varepsilon)$ and $g^{a}_{\mathbf{k}\alpha}(\varepsilon)$ in the energy current formula. As to the lesser Green's function of the lead, using the definition of Eq. (2.77), we have

$$g^{<}_{\mathbf{k}\alpha}(t,t') = \frac{i}{\hbar}\langle \hat{c}^{\dagger}_{\mathbf{k}\alpha}(t')\hat{c}_{\mathbf{k}\alpha}(t)\rangle = \frac{i}{\hbar} f(\varepsilon_{\mathbf{k}\alpha}) e^{-i\varepsilon_{\mathbf{k}\alpha}(t-t')}, \tag{2.91}$$

where we have used $\hat{c}^{\dagger}_{\mathbf{k}\alpha}(t') = \hat{c}^{\dagger}_{\mathbf{k}\alpha} e^{i\varepsilon_{\mathbf{k}\alpha}t'}$, $\hat{c}_{\mathbf{k}\alpha}(t) = \hat{c}_{\mathbf{k}\alpha} e^{-i\varepsilon_{\mathbf{k}\alpha}t}$, $\langle \hat{c}^{\dagger}_{\mathbf{k}\alpha}\hat{c}_{\mathbf{k}\alpha}\rangle = f(\varepsilon_{\mathbf{k}\alpha}) = 1/[e^{(\varepsilon_{\mathbf{k}\alpha}-\mu_{\alpha})/k_B T_{\alpha}} + 1]$ is the Fermi-Dirac distribution function at temperature T_{α}, and k_B is the Boltzmann constant.

Fourier transform of Eq. (2.91) gives

$$g^{<}_{\mathbf{k}\alpha}(\varepsilon) = \frac{2\pi i}{\hbar} f(\varepsilon_{\mathbf{k}\alpha})\delta(\varepsilon - \varepsilon_{\mathbf{k}\alpha}). \tag{2.92}$$

In a similar process, the retarded Green's function for the lead can be derived, using the definition of Eq. (2.75), as

$$\begin{aligned} g^{r}_{\mathbf{k}\alpha}(t,t') &= -\frac{i}{\hbar}\theta(t-t')\langle\{\hat{c}_{\mathbf{k}\alpha}(t), \hat{c}^{\dagger}_{\mathbf{k}\alpha}(t')\}\rangle \\ &= -\frac{1}{\hbar}\int_{-\infty}^{\infty} \frac{d\epsilon}{2\pi}\frac{1}{\epsilon - i\zeta} e^{-i(\varepsilon_{\mathbf{k}\alpha}-\epsilon)(t-t')}, \end{aligned} \tag{2.93}$$

where we have replaced the step function with $\theta(t-t') = \int_{-\infty}^{\infty} \frac{d\epsilon}{2\pi i}\frac{e^{i\epsilon(t-t')}}{\epsilon - i\zeta}$. After a Fourier transform, we have

$$g^{r}_{\mathbf{k}\alpha}(\varepsilon) = \frac{1}{\hbar}\frac{1}{\varepsilon - \varepsilon_{\mathbf{k}\alpha} + i\zeta}. \tag{2.94}$$

where ζ is an infinite positive small quantity. Therefore the advanced Green's function for the lead is

$$\begin{aligned} g^{a}_{\mathbf{k}\alpha}(\varepsilon) &= \frac{1}{\hbar}\frac{1}{\varepsilon - \varepsilon_{\mathbf{k}\alpha} - i\zeta} \\ &= \frac{1}{\hbar}\mathrm{P}\Big(\frac{1}{\varepsilon - \varepsilon_{\mathbf{k}\alpha}}\Big) + \frac{i\pi}{\hbar}\delta(\varepsilon - \varepsilon_{\mathbf{k}\alpha}), \end{aligned} \tag{2.95}$$

where the first term is the principal value.

---

[1] We define the Fourier transform for electrons as: $\mathcal{G}(\varepsilon) = \int_{-\infty}^{\infty} \mathcal{G}(t) e^{i\varepsilon t} dt$, or inversely, $\mathcal{G}(t) = \frac{1}{2\pi}\int_{-\infty}^{\infty} \mathcal{G}(\varepsilon) e^{-i\varepsilon t} d\varepsilon$.

Substituting Eqs. (2.91) and (2.95) into Eq. (2.90), as to the first term of Eq. (2.90) we have

$$\begin{aligned}\mathrm{Re}\Big[\sum_{\mathbf{k},nm}\varepsilon_{\mathbf{k}L}V_{\mathbf{k}L,n}V^{*}_{\mathbf{k}L,m}\mathcal{G}^{r}_{nm}(\varepsilon)g^{<}_{\mathbf{k}L}(\varepsilon)\Big] &= \mathrm{Re}\Big[\sum_{nm}\mathcal{G}^{r}_{nm}(\varepsilon)\frac{i}{\hbar}\varepsilon f(\varepsilon)\Gamma_{L,mn}\Big]\\ &= \frac{i}{2\hbar}\{\varepsilon f(\varepsilon)\Gamma_L(\varepsilon)[\mathcal{G}^{r}(\varepsilon)-\mathcal{G}^{a}(\varepsilon)]\},\end{aligned}\tag{2.96}$$

where the line-width function is defined as $\Gamma_{\mathbf{k}\alpha,mn}(\varepsilon) = 2\pi V_{\mathbf{k}\alpha,n}V^{*}_{\mathbf{k}\alpha,m}\delta(\varepsilon-\varepsilon_{\mathbf{k}\alpha})$. As to the second term of Eq. (2.90), we obtain

$$\mathrm{Re}\Big[\sum_{\mathbf{k},nm}\varepsilon_{\mathbf{k}L}V_{\mathbf{k}L,n}V^{*}_{\mathbf{k}L,m}\mathcal{G}^{<}_{nm}(\varepsilon)g^{a}_{\mathbf{k}L}(\varepsilon)\Big] = \frac{i}{2\hbar}\left[\varepsilon\Gamma_L(\varepsilon)\mathcal{G}^{<}(\varepsilon)\right].\tag{2.97}$$

The principal value of Eq. (2.97) is zero, because

$$\begin{aligned}&\mathrm{Re}\Big[2\sum_{\mathbf{k},nm}\varepsilon_{\mathbf{k}L}V_{\mathbf{k}L,n}V^{*}_{\mathbf{k}L,m}\mathcal{G}^{<}_{nm}(\varepsilon)\mathrm{P}\Big(\frac{1}{\varepsilon-\varepsilon_{\mathbf{k}L}}\Big)\Big]\\ &=\Big[\sum_{\mathbf{k},nm}\mathcal{G}^{<}_{nm}(\varepsilon)\mathrm{P}\Big(\frac{\varepsilon_{\mathbf{k}L}V_{\mathbf{k}L,n}V^{*}_{\mathbf{k}L,m}}{\varepsilon-\varepsilon_{\mathbf{k}L}}\Big)\Big]+\Big[\sum_{\mathbf{k},nm}\mathcal{G}^{<}_{nm}(\varepsilon)\mathrm{P}\Big(\frac{\varepsilon_{\mathbf{k}L}V_{\mathbf{k}L,n}V^{*}_{\mathbf{k}L,m}}{\varepsilon-\varepsilon_{\mathbf{k}L}}\Big)\Big]^{*}\\ &=0,\end{aligned}\tag{2.98}$$

where we have used $[\mathcal{G}^{<}(\varepsilon)]^{\dagger} = -\mathcal{G}^{<}(\varepsilon)$.

We now use Eqs. (2.96)-(2.98) and the energy current of Eq. (2.90) can then be rewritten as

$$I^{E}_{L} = \frac{i}{\hbar}\int_{-\infty}^{\infty}\frac{d\varepsilon}{2\pi}\varepsilon\mathrm{Tr}\{\Gamma_L(\varepsilon)\mathcal{G}^{<}(\varepsilon)+f_L(\varepsilon)\Gamma_L(\varepsilon)\left[\mathcal{G}^{r}(\varepsilon)-\mathcal{G}^{a}(\varepsilon)\right]\}.\tag{2.99}$$

The energy current from the right lead to the central region can be derived with the same process by starting from the time evolution of the Hamiltonian operator of the right lead. After some algebra, we can have

$$I^{E}_{R} = \frac{i}{\hbar}\int_{-\infty}^{\infty}\frac{d\varepsilon}{2\pi}\varepsilon\mathrm{Tr}\{\Gamma_R(\varepsilon)\mathcal{G}^{<}(\varepsilon)+f_R(\varepsilon)\Gamma_R(\varepsilon)\left[\mathcal{G}^{r}(\varepsilon)-\mathcal{G}^{a}(\varepsilon)\right]\}.\tag{2.100}$$

In steady state, the energy current flowing from the left lead to the central region should be equal to that flowing from the right lead to the central region except for a sign difference, *i.e.*, $I^{E}_{L} = -I^{E}_{R}$. This leads to

$$\begin{aligned}I^{E} &= \frac{I^{E}_{L}-I^{E}_{R}}{2}\\ &= \frac{i}{2\hbar}\int_{-\infty}^{\infty}\frac{d\varepsilon}{2\pi}\varepsilon\mathrm{Tr}\{[\Gamma_L(\varepsilon)-\Gamma_R(\varepsilon)]\mathcal{G}^{<}(\varepsilon)+\\ &\qquad [f_L(\varepsilon)\Gamma_L(\varepsilon)-f_R(\varepsilon)\Gamma_R(\varepsilon)][\mathcal{G}^{r}(\varepsilon)-\mathcal{G}^{a}(\varepsilon)]\}.\end{aligned}\tag{2.101}$$

Similar to the derivation of energy current, one can derive the electric current according to

$$J_L = -e\langle\dot{\hat{N}}_L\rangle = -\frac{ie}{\hbar}\langle[\hat{H},\hat{N}_L]\rangle,\tag{2.102}$$

where $\hat{N}_L = \sum_{\mathbf{k}} \hat{c}^{\dagger}_{\mathbf{k}L}\hat{c}_{\mathbf{k}L}$ is the occupation number operator. After some algebra, finally one can arrive at

$$J_L = \frac{ie}{\hbar}\int_{-\infty}^{\infty}\frac{d\varepsilon}{2\pi}\mathrm{Tr}\{\Gamma_L(\varepsilon)\mathcal{G}^<(\varepsilon) + f_L(\varepsilon)\Gamma_L(\varepsilon)[\mathcal{G}^r(\varepsilon) - \mathcal{G}^a(\varepsilon)]\}. \tag{2.103}$$

Taking into account the symmetric distribution of electric current in steady state as we mentioned before for energy current, one obtains

$$\begin{aligned} J &= \frac{J_L - J_R}{2} \\ &= \frac{ie}{2\hbar}\int_{-\infty}^{\infty}\frac{d\varepsilon}{2\pi}\mathrm{Tr}\{[\Gamma_L(\varepsilon) - \Gamma_R(\varepsilon)]\mathcal{G}^<(\varepsilon)+ \\ &\qquad [f_L(\varepsilon)\Gamma_L(\varepsilon) - f_R(\varepsilon)\Gamma_R(\varepsilon)][\mathcal{G}^r(\varepsilon) - \mathcal{G}^a(\varepsilon)]\}. \end{aligned} \tag{2.104}$$

Thus, the electric thermal current is defined according to the energy conservation law:

$$\begin{aligned} I^h &= I^E - \mu J \\ &= \frac{i}{2\hbar}\int_{-\infty}^{\infty}\frac{d\varepsilon}{2\pi}(\varepsilon-\mu)\mathrm{Tr}\{[\Gamma_L(\varepsilon) - \Gamma_R(\varepsilon)]\mathcal{G}^<(\varepsilon)+ \\ &\qquad [f_L(\varepsilon)\Gamma_L(\varepsilon) - f_R(\varepsilon)\Gamma_R(\varepsilon)][\mathcal{G}^r(\varepsilon) - \mathcal{G}^a(\varepsilon)]\}, \end{aligned} \tag{2.105}$$

where $\mu = (\mu_L + \mu_R)/2$ is the chemical potential and we take the energy current is the sum of heat current and charge current. The results are presented so far without any approximations.

Usually the energy-dependent line-width function is not very important and further simplification for Eqs. (2.101), (2.104), and (2.105) can be achieved by making assumptions on the Γ. We will have more discussions about this approximation in chapter 4. On the other hand if the left and right leads are constructed in the same way and thus their line-width functions are equal to each other, *i.e.*, $\Gamma_L(\varepsilon) = \Gamma_R(\varepsilon)$, in this case the energy, electric and heat currents can be expressed as

$$I^E = \frac{1}{\hbar}\int_{-\infty}^{\infty}\frac{d\varepsilon}{2\pi}\varepsilon[f_L(\varepsilon) - f_R(\varepsilon)]\mathcal{T}_e(\varepsilon), \tag{2.106}$$

$$J = \frac{e}{\hbar}\int_{-\infty}^{\infty}\frac{d\varepsilon}{2\pi}[f_L(\varepsilon) - f_R(\varepsilon)]\mathcal{T}_e(\varepsilon), \tag{2.107}$$

$$I^h = \frac{1}{\hbar}\int_{-\infty}^{\infty}\frac{d\varepsilon}{2\pi}(\varepsilon-\mu)[f_L(\varepsilon) - f_R(\varepsilon)]\mathcal{T}_e(\varepsilon), \tag{2.108}$$

where

$$\mathcal{T}_e(\varepsilon) = \mathrm{Tr}\left\{\frac{\Gamma_L(\varepsilon)\Gamma_R(\varepsilon)}{\Gamma_L(\varepsilon)+\Gamma_R(\varepsilon)}i[\mathcal{G}^r(\varepsilon) - \mathcal{G}^a(\varepsilon)]\right\}, \tag{2.109}$$

is the electronic transmission coefficient, which represents the transmission probability of particles from the left (right) lead to the right (left) lead through the quantum device in the central region. The above equations are widely used for quantum transport calculations and we will also use them in the following two chapters.

Based on the electric and thermal current formulas, we now derive the electrical conductance, Seebeck coefficient and electric thermal conductance. In the linear response regime where temperature gradient and bias between the two leads are small, we take a Taylor expansion up to first-order for the heat and electric currents with respect to the temperature and chemical potential, and we have

$$I^h = \frac{\partial I^h}{\partial T}\Delta T + \frac{\partial I^h}{\partial \mu}\Delta\mu, \tag{2.110}$$

$$J = \frac{\partial J}{\partial T}\Delta T + \frac{\partial J}{\partial \mu}\Delta\mu. \tag{2.111}$$

Then the electrical conductance is

$$G = \frac{J}{V}\bigg|_{\Delta T=0} = e\frac{\partial J}{\partial \mu} = \frac{e^2}{\hbar}\int_{-\infty}^{\infty}\frac{d\varepsilon}{2\pi}\mathcal{T}_e(\varepsilon)\Big(-\frac{\partial f(\varepsilon)}{\partial \varepsilon}\Big), \tag{2.112}$$

where $\Delta\mu = eV$. The Seebeck coefficient is

$$S = \frac{V}{\Delta T}\bigg|_{J=0} = -\frac{1}{e}\left(\frac{\partial J}{\partial T}\Big/\frac{\partial J}{\partial \mu}\right) = -\frac{1}{eT}\frac{\int_{-\infty}^{\infty}d\varepsilon\mathcal{T}_e(\varepsilon)(\varepsilon-\mu)\frac{\partial f(\varepsilon)}{\partial\varepsilon}}{\int_{-\infty}^{\infty}d\varepsilon\mathcal{T}_e(\varepsilon)\frac{\partial f(\varepsilon)}{\partial\varepsilon}}. \tag{2.113}$$

The electric thermal conductance is

$$\begin{aligned}\kappa_e &= \frac{I^h}{\Delta T}\bigg|_{J=0} = \frac{\partial I^h}{\partial T} - \frac{\partial I^h}{\partial \mu}\frac{\partial J}{\partial T}\Big/\frac{\partial J}{\partial \mu} \\ &= \frac{1}{T\hbar}\left\{\int_{-\infty}^{\infty}\frac{d\varepsilon}{2\pi}\mathcal{T}_e(\varepsilon)(\varepsilon-\mu)^2\Big(-\frac{\partial f(\varepsilon)}{\partial\varepsilon}\Big) - \frac{\left[\int_{-\infty}^{\infty}d\varepsilon\mathcal{T}_e(\varepsilon)(\varepsilon-\mu)\frac{\partial f(\varepsilon)}{\partial\varepsilon}\right]^2}{2\pi\int_{-\infty}^{\infty}d\varepsilon\mathcal{T}_e(\varepsilon)\Big(-\frac{\partial f(\varepsilon)}{\partial\varepsilon}\Big)}\right\}.\end{aligned} \tag{2.114}$$

In the above derivation, we have used the relations: $\frac{\partial f(\varepsilon,\mu,T)}{\partial\mu} = -\frac{\partial f(\varepsilon,\mu,T)}{\partial\varepsilon}$ and $\frac{\partial f(\varepsilon,\mu,T)}{\partial T} = -\frac{\varepsilon-\mu}{T}\frac{\partial f(\varepsilon,\mu,T)}{\partial\varepsilon}$. These equations are valid in linear response regime and provide a rigorous way to calculate the transport coefficients. The key quantity we found is the transmission probability function which depends on the Green's functions.

2.4.3 Landauer theory for electron transport

The above formulas are derived in terms of Green's functions based on the MB interaction Hamiltonian. For a non-interacting system, if one defines [30, 32]

$$\Sigma_\alpha^>(\varepsilon) = i(f_\alpha(\varepsilon)-1)\Gamma_\alpha(\varepsilon), \tag{2.115}$$

$$\Sigma_\alpha^<(\varepsilon) = if_\alpha(\varepsilon)\Gamma_\alpha(\varepsilon), \tag{2.116}$$

then the greater and lesser Green's functions are

$$\mathcal{G}^>(\varepsilon) = \mathcal{G}^r(\varepsilon)[\Sigma_L^>(\varepsilon)+\Sigma_R^>(\varepsilon)]\mathcal{G}^a(\varepsilon), \tag{2.117}$$

$$\mathcal{G}^<(\varepsilon) = \mathcal{G}^r(\varepsilon)[\Sigma_L^<(\varepsilon)+\Sigma_R^<(\varepsilon)]\mathcal{G}^a(\varepsilon), \tag{2.118}$$

where $\Sigma_\alpha^>(\varepsilon)$ and $\Sigma_\alpha^<(\varepsilon)$ are the non-interacting self energies of the lead α. The self-energy describes the coupling between the lead and the central region.

Considering the relation $\mathcal{G}^r - \mathcal{G}^a = \mathcal{G}^> - \mathcal{G}^<$, and substituting Eqs. (2.117) and (2.118) into Eqs. (2.101), (2.104), and (2.105), then the electrical conductance G, Seebeck coefficient S, and electric thermal conductance κ_e can be recast as

$$G(\mu,T) = e^2\mathcal{L}_0(\mu,T), \tag{2.119}$$

$$S(\mu,T) = -\frac{1}{eT}\frac{\mathcal{L}_1(\mu,T)}{\mathcal{L}_0(\mu,T)}, \tag{2.120}$$

$$\kappa_e(\mu,T) = \frac{1}{T}\left(\mathcal{L}_2(\mu,T) - \frac{\mathcal{L}_1(\mu,T)^2}{\mathcal{L}_0(\mu,T)}\right), \tag{2.121}$$

where

$$\mathcal{L}_n(\mu,T) = \frac{2}{h}\int_{-\infty}^{\infty} d\varepsilon \mathcal{T}_e(\varepsilon)(\varepsilon-\mu)^n\left(-\frac{\partial f(\varepsilon,\mu,T)}{\partial\varepsilon}\right), \tag{2.122}$$

is the Lorentz function and the pre-factor 2 is added by hand due to spin. $\mathcal{T}_e(\varepsilon)$ is the electronic transmission coefficient, which is given by

$$\mathcal{T}_e(\varepsilon) = \mathrm{Tr}[\mathcal{G}^r(\varepsilon)\Gamma_L(\varepsilon)\mathcal{G}^a(\varepsilon)\Gamma_R(\varepsilon)]. \tag{2.123}$$

In contrast to Eq. (2.109), Eq. (2.123) is valid for single particle approximation since the Green's functions here do not include the interacting effect. The explicit formulas for MB interacting and single-particle approximated Green's functions are shown in appendix B. As to the expressions of self-energies, one can find them in Ref. [30]. In the ballistic transport regime, for a periodic quasi-dimensional system the transmission coefficient is the same as the number of modes which can be easily captured from the band structure.

2.5 Bosonic Green's function

2.5.1 Modeling Hamiltonian of phonons

In this section we derive the lattice heat current formula for phonon transport in terms of the bosonic Green's functions. The system we modelled has been shown in Fig. 2.2. The left and right leads act as heat baths and their temperatures are T_L and T_R, respectively. The two heat baths are sufficiently large so that any finite energy transfer does not change its temperature. The heat can transport from left (or right) to right (or left) baths by crossing the central region if $T_L \neq T_R$. To keep the discussion simple, we employ a transformation of the atomic coordinates, *i.e.*, $\hat{u}_i = \sqrt{M_i}\Delta\hat{R}_i$, where u_i is the mass renormalized displacement and ΔR_i is the displacement for $i-th$ atom in contrast to its equilibrium position. In this way, the system Hamiltonian can be expressed as [33–35]

$$\begin{aligned}\hat{H} &= \sum_{\alpha=L,C,R}\hat{H}_\alpha + \hat{H}_{LC} + \hat{H}_{CR} + \hat{H}_n \\ &= \sum_{\alpha=L,C,R}\left[\frac{1}{2}(\dot{\hat{u}}^\alpha)^T\dot{\hat{u}}^\alpha + \frac{1}{2}(\hat{u}^\alpha)^T K^\alpha \hat{u}^\alpha\right] + (\hat{u}^L)^T V^{LC}\hat{u}^C \\ &\quad + (\hat{u}^C)^T V^{CR}\hat{u}^R + \sum_{ijk}\frac{1}{3}K_{ijk}\hat{u}_i^C\hat{u}_j^C\hat{u}_k^C,\end{aligned} \tag{2.124}$$

where the superscript T indicates the matrix transpose, $\hat{u}^\alpha$ is a column vector consisting of all the displacement variables in region α, K^α is the spring constant matrix, V^{LC} or

V^{CR} is the coupling matrix between the lead and the central region, and $\hat{H}_n$ describes the non-linear interaction. In Eq. (2.124) the cubic-order anharmonic interaction term is shown explicitly.

2.5.2 General expression of lattice heat current

Based on the lattice Hamiltonian, we define six Green's functions for bosons (phonons). They are

$$\mathcal{G}^r(t,t') = -\frac{i}{\hbar}\theta(t-t')\langle[\hat{u}(t)^T, \hat{u}(t')]\rangle, \tag{2.125}$$

$$\mathcal{G}^a(t,t') = \frac{i}{\hbar}\theta(t'-t)\langle[\hat{u}(t)^T, \hat{u}(t')]\rangle, \tag{2.126}$$

$$\mathcal{G}^>(t,t') = -\frac{i}{\hbar}\langle\hat{u}(t)^T\hat{u}(t')\rangle, \quad \mathcal{G}^<(t,t') = -\frac{i}{\hbar}\langle\hat{u}(t')^T\hat{u}(t)\rangle^T, \tag{2.127}$$

$$\mathcal{G}^t(t,t') = \theta(t-t')\mathcal{G}^>(t,t') + \theta(t'-t)\mathcal{G}^<(t,t'), \tag{2.128}$$

$$\mathcal{G}^{\bar{t}}(t,t') = \theta(t'-t)\mathcal{G}^>(t,t') + \theta(t-t')\mathcal{G}^<(t,t'), \tag{2.129}$$

where the notation $\langle[A^T, B]\rangle$ should be interpreted as $\langle A^T B\rangle - \langle B^T A\rangle^T$. In the above definitions, we did not illustrate the particular region, L or C or R, for the operator $\hat{u}$ since it could represent either the displacement variable of the leads or the displacement variable of the central region. Then the Green's function corresponds to the region as $\hat{u}$ specified and we shall see this clearly later. Similar to the fermionic Green's functions, Eqs. (2.125) to (2.129) are called the bosonic retarded, advanced, greater, lesser, time-ordered and anti-time-ordered Greens functions, respectively. For more detailed discussion about the bosonic Green's functions, one can find in Ref. [23]. From these definitions, we find that the following relations always hold:

$$\mathcal{G}^r(t,t') - \mathcal{G}^a(t,t') = \mathcal{G}^>(t,t') - \mathcal{G}^<(t,t'), \tag{2.130}$$

$$\mathcal{G}^t(t,t') + \mathcal{G}^{\bar{t}}(t,t') = \mathcal{G}^>(t,t') + \mathcal{G}^<(t,t'), \tag{2.131}$$

$$\mathcal{G}^t(t,t') - \mathcal{G}^{\bar{t}}(t,t') = \mathcal{G}^r(t,t') + \mathcal{G}^a(t,t'), \tag{2.132}$$

$$\mathcal{G}^r(t,t') = \mathcal{G}^t(t,t') - \mathcal{G}^<(t,t'), \quad \mathcal{G}^a(t,t') = \mathcal{G}^<(t,t') - \mathcal{G}^{\bar{t}}(t,t'). \tag{2.133}$$

Considering the mutual dependence of the above six Green's functions, we focus in the following mainly on the retarded and lesser Green's functions since the others can be derived easily from them. The bosonic Green's functions will be used to calculate the transmission probability of phonons and we shall introduce later.

Using these bosonic Green's functions, we now derive the lattice-vibrational heat current formula. The thermal flux out of the left lead is

$$\begin{aligned} I_L^{ph} &= -\Big\langle\frac{d\hat{H}_L}{dt}\Big\rangle = \frac{i}{\hbar}\langle[\hat{H}_L, \hat{H}_{LC}]\rangle \\ &= \frac{i}{2\hbar}\Big\langle\Big[\sum_{jk}\dot{\hat{u}}_j^L(t)\dot{\hat{u}}_j^L(t) + \hat{u}_j^L(t)K_{jk}^L\hat{u}_k^L, \sum_{j'k'}\hat{u}_{j'}^L(t)V_{j'k'}^{LC}\hat{u}_{k'}^C(t)\Big]\Big\rangle \\ &= \langle\dot{\hat{u}}^L(t)^T V^{LC}\hat{u}^C(t)\rangle, \end{aligned} \tag{2.134}$$

where we have used the commutation relations for the displacement variables, *i.e.*, $[\dot{\hat{u}}_j^\alpha(t), \hat{u}_{j'}^{\alpha'}(t)] = -i\hbar\delta_{jj'}\delta_{\alpha\alpha'}$ and $[\hat{u}_j(t), \hat{u}_{j'}(t)] = 0$. By defining

$$\tilde{\mathcal{G}}_{kj}^{CL,<}(t,t') = -\frac{i}{\hbar}\langle\dot{\hat{u}}_j^L(t')\hat{u}_k^C(t)\rangle, \tag{2.135}$$

we have

$$I_L^{ph} = i\hbar\mathrm{Tr}[\tilde{\mathcal{G}}^{CL,<}(t,t)V^{LC}], \tag{2.136}$$

where the lattice heat current is expressed in time space and for the frequency domain, a Fourier transform of Eq. (2.135) yields

$$\tilde{\mathcal{G}}_{kj}^{CL,<}(t,t') = \frac{d}{dt'}\mathcal{G}_{kj}^{CL,<}(t,t') = \frac{1}{2\pi}\int_{-\infty}^{\infty} i\omega\mathcal{G}_{kj}^{CL,<}(\omega)e^{-i\omega(t-t')}d\omega, \tag{2.137}$$

where $\mathcal{G}_{kj}^{CL,<}(t,t') = -\frac{i}{\hbar}\langle\hat{u}_j^L(t')\hat{u}_k^C(t)\rangle$ according to the definition of Eq. (2.127). Inserting Eq. (2.137) into Eq. (2.138), we obtain

$$I_L^{ph} = -\frac{1}{2\pi}\int_{-\infty}^{\infty}\hbar\omega\mathrm{Tr}[\mathcal{G}^{CL,<}(\omega)V^{LC}]d\omega. \tag{2.138}$$

The center-left Green's function $\mathcal{G}^{CL,<}(\omega)$ can be replaced by the center-center Green's function $\mathcal{G}^{CC}$ according to the Langreth theorem [34], *i.e.*,

$$\mathcal{G}_{CL}^<(\omega) = \mathcal{G}_{CC}^r(\omega)V^{CL}g_L^<(\omega) + \mathcal{G}_{CC}^<(\omega)V^{CL}g_L^a(\omega), \tag{2.139}$$

where we have moved the superscript CL to the subscript. $g_L^{<,a}(\omega)$ are the lesser or advanced Green's functions of the left lead, respectively. The detailed derivation of Eq. (2.139) coming from the equation of motion of the time-ordered Green's function can be found in appendix B. Substituting Eq. (2.139) into Eq. (2.138), we obtain

$$I_L^{ph} = -\frac{1}{2\pi}\int_{-\infty}^{\infty}\hbar\omega\mathrm{Tr}[\mathcal{G}_{CC}^r(\omega)V^{CL}g_L^<(\omega)V^{LC} + \mathcal{G}_{CC}^<(\omega)V^{CL}g_L^a(\omega)V^{LC}]d\omega. \tag{2.140}$$

If one defines

$$\Sigma_L^<(\omega) = V^{CL}g_L^<(\omega)V^{LC}, \tag{2.141}$$
$$\Sigma_L^a(\omega) = V^{CL}g_L^a(\omega)V^{LC}, \tag{2.142}$$

where $\Sigma_L^<$ and Σ_L^a are the lesser and advanced self-energies of the left lead, respectively, Eq. (2.140) turns into

$$I_L^{ph} = -\frac{1}{2\pi}\int_{-\infty}^{\infty}\hbar\omega\mathrm{Tr}[\mathcal{G}_{CC}^r(\omega)\Sigma_L^<(\omega) + \mathcal{G}_{CC}^<(\omega)\Sigma_L^a(\omega)]d\omega. \tag{2.143}$$

In the following we present the derivation of the Green's functions of the lead. According to the definition shown in Eq. (2.127), the lesser Green's function of the lead is

$$g^<(t,t') = -\frac{i}{\hbar}\langle\hat{u}(t')^T\hat{u}(t)\rangle^T = -\frac{i}{2\Omega}\left[e^{i\Omega(t-t')}(1+n(\Omega)) + e^{i\Omega(t'-t)}n(\Omega)\right], \tag{2.144}$$

where Ω is the intrinsic vibrational frequency and the following relations are used:

$$\hat{u} = \sqrt{\frac{\hbar}{2\Omega}}(\hat{a} + \hat{a}^\dagger), \tag{2.145}$$

$$\hat{a}(t) = \hat{a}e^{-i\Omega t}, \quad \hat{a}^\dagger(t) = \hat{a}^\dagger e^{i\Omega t}, \tag{2.146}$$

$$[\hat{a}, \hat{a}^\dagger] = 1, \quad \langle \hat{a}^\dagger \hat{a} \rangle = n(\Omega, T) = \frac{1}{e^{\hbar\Omega/k_B T} - 1}, \tag{2.147}$$

where $n(\Omega, T)$ is the Bose-Einstein distribution function. The Fourier transform of Eq. (2.144) gives

$$g^<(\omega) = -\frac{\pi i}{\Omega}\left[-\delta(\omega + \Omega)n(-\Omega) + \delta(\omega - \Omega)n(\Omega)\right], \tag{2.148}$$

where we have used the properties: $\delta(\Omega) = \frac{1}{2\pi}\int_{-\infty}^{\infty} e^{i\Omega t} dt$ and $n(-\Omega) = \frac{1}{e^{-\hbar\Omega/k_B T} - 1} = -\left(1 + \frac{1}{e^{\hbar\Omega/k_B T} - 1}\right) = -[1 + n(\Omega)]$. The retarded Green's function of the lead can be derived in a similar way and it is

$$\begin{aligned} g^r(t, t') &= -\frac{i}{\hbar}\theta(t - t')\langle[\hat{u}(t)^T, \hat{u}(t')]\rangle \\ &= -\frac{i}{2\Omega}\theta(t - t')\left[e^{i\Omega(t' - t)} - e^{i\Omega(t - t')}\right]. \end{aligned} \tag{2.149}$$

In the frequency domain, Eq. (2.149) becomes

$$\begin{aligned} g^r(\omega) &= \int_{\infty}^{\infty} g^r(t, t') e^{i\omega(t - t')} dt \\ &= \frac{1}{(\omega + i\zeta)^2 - \Omega^2}, \end{aligned} \tag{2.150}$$

where we have used $\int_{-\infty}^{\infty} g(\omega)\delta(\omega - \Omega)d\omega = g(\Omega)$. Therefore, the advanced Green's function of the lead is

$$g^a(\omega) = [g^r(\omega)]^\dagger = \frac{1}{(\omega - i\zeta)^2 - \Omega^2}. \tag{2.151}$$

Using the symbolic formula:

$$\frac{1}{\omega \pm i\zeta} = \mathrm{P}\left(\frac{1}{\omega}\right) \mp i\pi\delta(\omega), \tag{2.152}$$

Eq. (2.151) can be rewritten as

$$g^a(\omega) = \frac{1}{2\Omega}\left[\mathrm{P}\left(\frac{1}{\omega - \Omega}\right) + i\pi\delta(\omega - \Omega) - \mathrm{P}\left(\frac{1}{\omega + \Omega}\right) - i\pi\delta(\omega + \Omega)\right]. \tag{2.153}$$

We now substitute Eqs. (2.148) and (2.153) into Eq. (2.140). For the first term shown in Eq. (2.140), we have

$$\begin{aligned}
&-\frac{1}{2\pi}\int_{-\infty}^{\infty}\hbar\omega\mathrm{Tr}[\mathcal{G}^{r}_{CC}(\omega)V^{CL}g^{<}_{L}(\omega)V^{LC}]d\omega\\
&=\frac{i}{2\Omega}\int_{-\infty}^{\infty}\hbar\omega\mathrm{Tr}\{\mathcal{G}^{r}_{CC}(\omega)V^{CL}[-\delta(\omega+\Omega)n_L(-\Omega)+\delta(\omega-\Omega)n_L(\Omega)]V^{LC}\}d\omega\\
&=\frac{i}{\pi}\int_{0}^{\infty}\hbar\omega\mathrm{Tr}[\mathcal{G}^{r}_{CC}(\omega)\Gamma_L(\omega)n_L(\omega)]d\omega,
\end{aligned} \tag{2.154}$$

where $n_L(\omega)$ is the Bose-Einstein distribution of the left lead, and the line-width function is defined as $\Gamma_L(\omega)=iV^{CL}g^{<}_{L}(\omega)V^{LC}[n_L(\omega)]^{-1}=iV^{CL}[g^{r}_{L}(\omega)-g^{a}_{L}(\omega)]V^{LC}=i[\Sigma^{r}_{L}(\omega)-\Sigma^{a}_{L}(\omega)]$. For the second term of Eq. (2.140), it has

$$\begin{aligned}
&-\frac{1}{2\pi}\int_{-\infty}^{\infty}\hbar\omega\mathrm{Tr}[\mathcal{G}^{<}_{CC}(\omega)V^{CL}g^{a}_{L}(\omega)V^{LC}]d\omega\\
&=-\frac{1}{2\pi}\int_{-\infty}^{\infty}\hbar\omega\mathrm{Tr}\Big\{\mathcal{G}^{<}_{CC}(\omega)V^{CL}\frac{1}{2\Omega}\Big[\mathrm{P}\Big(\frac{1}{\omega-\Omega}\Big)+i\pi\delta(\omega-\Omega)-\\
&\qquad\mathrm{P}\Big(\frac{1}{\omega+\Omega}\Big)-i\pi\delta(\omega+\Omega)\Big]V^{LC}\Big\}d\omega,
\end{aligned} \tag{2.155}$$

where the principal part:

$$-\frac{1}{2\pi}\int_{-\infty}^{\infty}\hbar\omega\mathrm{Tr}\left\{\mathcal{G}^{<}_{CC}(\omega)V^{CL}\frac{1}{2\Omega}\left[\mathrm{P}\left(\frac{1}{\omega-\Omega}\right)-\mathrm{P}\left(\frac{1}{\omega+\Omega}\right)\right]V^{LC}\right\}d\omega=0, \tag{2.156}$$

because $[\mathcal{G}^{<}_{CC}(\omega)]^{\dagger}=-\mathcal{G}^{<}_{CC}(\omega)$. The proof is similar to the one we have shown in Eq. (2.98) for the electronic Green's functions in Sec. 2.4. Thus Eq. (2.155) becomes

$$-\frac{i}{2\pi}\int_{0}^{\infty}\hbar\omega\mathrm{Tr}[\mathcal{G}^{<}_{CC}(\omega)\Gamma_L(\omega)]d\omega. \tag{2.157}$$

Substituting Eqs. (2.154) and (2.157) into Eq. (2.140), finally we obtain the lattice thermal current:

$$I^{ph}_{L}=\frac{1}{2\pi}\int_{0}^{\infty}\hbar\omega\mathrm{Tr}\{[in_L(\omega)(\mathcal{G}^{r}_{CC}(\omega)-\mathcal{G}^{a}_{CC}(\omega))-i\mathcal{G}^{<}_{CC}(\omega)]\Gamma_L(\omega)\}d\omega, \tag{2.158}$$

where we have taken into account the fact that the current must be real. In the following we omit the subscript CC in the Green's functions.

With the same manipulation, one can also derive the heat current from the right lead and one can obtain

$$I^{ph}_{R}=\frac{1}{2\pi}\int_{0}^{\infty}\hbar\omega\mathrm{Tr}\{[in_R(\omega)(\mathcal{G}^{r}(\omega)-\mathcal{G}^{a}(\omega))-i\mathcal{G}^{<}(\omega)]\Gamma_R(\omega)\}d\omega, \tag{2.159}$$

where $n_R(\omega)$ is the Bose-Einstein distribution of the right heat bath. In steady state, the heat flux out of the left lead should be the same as the heat flux out of the right lead. Thus Eq. (2.158) can be written in a symmetric way as

$$
\begin{aligned}
I^{ph} &= \frac{I_L^{ph} - I_R^{ph}}{2} \\
&= \frac{1}{4\pi}\int_0^\infty \hbar\omega \mathrm{Tr}\{i[\mathcal{G}^r(\omega) - \mathcal{G}^a(\omega)][n_L(\omega)\Gamma_L(\omega) - n_R(\omega)\Gamma_R(\omega)] - \\
&\qquad i\mathcal{G}^<(\omega)[\Gamma_L(\omega) - \Gamma_R(\omega)]\}d\omega.
\end{aligned}
\tag{2.160}
$$

So far, we haven't made any approximations. Eq. (2.160) is a general expression for the lattice heat current. Comparing with the electric heat current [see Eq. (2.105)], there is no chemical potential in the lattice heat current. Moreover, the Green's functions here as a function of phonon frequency have completely different physical meaning with those of the fermionic system.

2.5.3 Landauer-like formula for phonon transport

In the above derivations, anharmonic effect is considered for the modelling of the Green's functions. While for a harmonic system, if one defines [33–35]

$$\Sigma_\alpha^<(\omega) = -in_\alpha(\omega)\Gamma_\alpha(\omega), \tag{2.161}$$

$$\Sigma_\alpha^>(\omega) = -i[n_\alpha(\omega) - 1]\Gamma_\alpha(\omega), \tag{2.162}$$

then the Green's functions become

$$\mathcal{G}^<(\omega) = \mathcal{G}^r(\omega)[\Sigma_L^<(\omega) + \Sigma_R^<(\omega)]\mathcal{G}^a(\omega), \tag{2.163}$$

$$\mathcal{G}^>(\omega) = \mathcal{G}^r(\omega)[\Sigma_L^>(\omega) + \Sigma_R^>(\omega)]\mathcal{G}^a(\omega), \tag{2.164}$$

where $\Sigma_\alpha^<$ and $\Sigma_\alpha^>$ are the lesser and greater self-energies, respectively. In this case, Eq. (2.160) can be recast as

$$I^{ph} = \frac{1}{2\pi}\int_0^\infty \hbar\omega\mathcal{T}_{ph}(\omega)[n_L(\omega) - n_R(\omega)]d\omega, \tag{2.165}$$

where we have used the relation shown in Eq. (2.130) and the transmission coefficient is

$$\mathcal{T}_{ph}(\omega) = \mathrm{Tr}[\mathcal{G}^r(\omega)\Gamma_L(\omega)\mathcal{G}^a(\omega)\Gamma_R(\omega)]. \tag{2.166}$$

$\mathcal{T}_{ph}$ is a probability function for phonons and we will use it to calculate the phonon thermal conductance. When the temperature difference between the two heat baths is sufficiently small, *i.e.*, $\Delta T (= T_L - T_R) \to 0$, the phonon thermal conductance can then be written as

$$\kappa_{ph} = \lim_{\Delta T \to 0}\frac{I^{ph}}{\Delta T} = \frac{1}{2\pi}\int_0^\infty \hbar\omega\mathcal{T}_{ph}(\omega)\frac{\partial n(\omega)}{\partial T}d\omega. \tag{2.167}$$

This equation is very similar to the formula of the electrical conductance we obtained from Landauer approach shown in Sec. 2.4 for electron transport [see Eq. (2.119)]. This Landauer-like formula, Eq. (2.167), for phonon transport is valid only in the linear response regime in harmonic approximation. And we will use this formula to calculate the lattice thermal conductance in the next chapter 3.

2.6 Boltzmann transport equation

Within linear response theory the electrical conductivity σ, Seebeck coefficient S and electronic thermal conductivity λ_e in the framework of Boltzmann transport equation can be written as [6, 36, 37]

$$\sigma(\mu, T) = e^2 \mathbf{K}_0(\mu, T), \tag{2.168}$$

$$S(\mu, T) = -\frac{1}{eT}\frac{\mathbf{K}_1(\mu, T)}{\mathbf{K}_0(\mu, T)}, \tag{2.169}$$

$$\lambda_e(\mu, T) = \frac{1}{T}\left(\mathbf{K}_2(\mu, T) - \frac{\mathbf{K}_1(\mu, T)^2}{\mathbf{K}_0(\mu, T)}\right), \tag{2.170}$$

where

$$\mathbf{K}_n(\mu, T) = \frac{1}{V}\sum_{i,\mathbf{k}} \tau_{i,e}(\mathbf{k})\mathbf{v}_i(\mathbf{k}) \otimes \mathbf{v}_i(\mathbf{k})[\varepsilon_i(\mathbf{k}) - \mu]^n \left(-\frac{\partial f(\varepsilon_i(\mathbf{k}), \mu, T)}{\partial \varepsilon_i(\mathbf{k})}\right). \tag{2.171}$$

In the above Eq. (2.171), $\otimes$ denotes a tensor product, $\mathbf{K}_n$ can be a tensor for two and three dimensional systems, $\tau_{i,e}(\mathbf{k})$ is the relaxation time of electrons corresponding to the energy band index i and momentum $\mathbf{k}$, $\mathbf{v}_i(\mathbf{k}) = \frac{1}{\hbar}\frac{\partial \varepsilon_i(\mathbf{k})}{\partial \mathbf{k}}$ is the group velocity for electrons, $\varepsilon_i(\mathbf{k})$ is the i-th band energy, μ is the chemical potential, V is the volume of the system, and $f(\varepsilon_i, \mu, T)$ is the Fermi-Dirac distribution function at a given temperature T.

For the quasi-one-dimensional system, the electrical conductivity, Seebeck coefficient and electric thermal conductivity can be expressed as scalars instead of tensors. Then $\mathbf{K_n}$ becomes

$$\mathcal{K}_n(\mu, T) = \frac{1}{V}\sum_{i,\mathbf{k}} \tau_{i,e}(\mathbf{k})\mathbf{v}_i(\mathbf{k}) \cdot \mathbf{v}_i(\mathbf{k})[\varepsilon_i(\mathbf{k}) - \mu]^n \left(-\frac{\partial f(\varepsilon_i(\mathbf{k}), \mu, T)}{\partial \varepsilon_i(\mathbf{k})}\right), \tag{2.172}$$

and in the energy domain,

$$\mathcal{K}_n(\mu, T) = \frac{1}{A}\sum_{i} \int_{-\infty}^{\infty} d\varepsilon D_{e,i}(\varepsilon)\tau_{i,e}(\varepsilon)\mathbf{v}_i(\varepsilon) \cdot \mathbf{v}_i(\varepsilon)[\varepsilon - \mu]^n \left(-\frac{\partial f(\varepsilon, \mu, T)}{\partial \varepsilon}\right), \tag{2.173}$$

where we have introduced the density of states:

$$D_{e,i}(\varepsilon) = \frac{1}{L}\sum_{\mathbf{k}} \delta(\varepsilon - \varepsilon_{i,\mathbf{k}}) = \frac{1}{2\pi\hbar|\mathbf{v}_i(\varepsilon)|}, \tag{2.174}$$

with A the cross-sectional area and L the length of the system in the longitudinal direction. The second step in Eq. (2.174) to obtain is considering the definition of the density of states which is given by

$$D_{e,i}(\varepsilon) = \frac{dk}{2\pi d\varepsilon_i} = \frac{1}{2\pi\hbar v_i(\varepsilon)}. \tag{2.175}$$

Then we obtain

$$\mathcal{K}_n(\mu, T) = \frac{1}{Ah}\sum_{i} \int_{-\infty}^{\infty} d\varepsilon \tau_{i,e}(\varepsilon)|\mathbf{v}_i(\varepsilon)|[\varepsilon - \mu]^n \left(-\frac{\partial f(\varepsilon, \mu, T)}{\partial \varepsilon}\right). \tag{2.176}$$

In the ballistic transport regime, the Boltzmann transport equation should be equivalent with the Landauer theory. Taking into account that $\Lambda_{i,e} = \tau_{i,e}|\mathbf{v}_i|$ is the mean free path of electrons, we have

$$\mathcal{K}_n(\mu, T) = \frac{1}{Ah}\int_{-\infty}^{\infty} d\varepsilon \Lambda_e N_e[\varepsilon - \mu]^n \left(-\frac{\partial f(\varepsilon, \mu, T)}{\partial \varepsilon}\right), \tag{2.177}$$

where N_e is the total number of opened transport channels which can be calculated directly from the energy bands. We will use the Boltzmann transport equation and the Landauer theory to calculate the thermoelectric coefficients in the next chapter.

On the other hand for phonon transport, the lattice thermal conductivity can be written as [38]

$$\tilde{\lambda}_{\mathbf{ph}}(T) = \frac{1}{V}\sum_{i,\mathbf{k}} \tau_{i,ph}(\mathbf{k})\mathbf{v}_i(\mathbf{k}) \otimes \mathbf{v}_i(\mathbf{k})\hbar\omega_i(\mathbf{k}) \left(\frac{\partial n(\omega_i(\mathbf{k}), T)}{\partial T}\right), \tag{2.178}$$

where $\tilde{\lambda}_{\mathbf{ph}}$ expresses the thermal conductivity as a tensor, $\tau_{i,ph}(\mathbf{k})$ is the relaxation time of phonons, $\mathbf{v}_i(\mathbf{k}) = \frac{\partial \omega_i(\mathbf{k})}{\partial \mathbf{k}}$ is the group velocity that can be calculated from the phonon dispersions, $\omega_i(\mathbf{k})$ is the vibrational frequency with respect to the band index i and momentum $\mathbf{k}$, and $n(\omega_i(\mathbf{k}), T)$ is the Bose-Einstein distribution function.

For the quasi-one-dimensional system, the phonon thermal conductivity in the frequency domain can be expressed as

$$\lambda_{ph}(T) = \frac{1}{A}\sum_i \int_0^{\infty} \hbar\omega D_{ph,i}(\omega)|\mathbf{v}_i(\omega)|\Lambda_{i,ph}(\omega) \left(\frac{\partial n(\omega, T)}{\partial T}\right) d\omega, \tag{2.179}$$

where we have taken into account that the actual phonons can have only positive frequency (otherwise the system is not stable). $D_{ph,i}(\omega)$ is the phonon density of states, which is defined as

$$D_{ph,i}(\omega) = \frac{1}{L}\sum_{\mathbf{k}} \delta(\omega - \omega_{i,\mathbf{k}}) = \frac{1}{2\pi|\mathbf{v}_i(\omega)|}, \tag{2.180}$$

and $\Lambda_{i,ph}(\omega) = \tau_{i,ph}|\mathbf{v}_i(\omega)|$ is the mean free path of phonons. The lattice thermal conductivity can then be rewritten as

$$\lambda_{ph}(T) = \frac{1}{2\pi A}\sum_i \int_0^{\infty} \hbar\omega \left(\frac{\partial n(\omega, T)}{\partial T}\right) \Lambda_{i,ph}(\omega) d\omega. \tag{2.181}$$

For the quasi-one-dimensional periodic system, phonons can transport perfectly without any scattering. The phonon thermal conductivity can be calculated by

$$\lambda_{ph}(T) = \frac{1}{2\pi A}\int_0^{\infty} \hbar\omega \Lambda_{ph} N_{ph} \left(\frac{\partial n(\omega, T)}{\partial T}\right) d\omega, \tag{2.182}$$

where N_{ph} is the total number of transport channels for phonons which can be obtained directly by counting the number of phonon modes from the dispersion.

Equations (2.177) and (2.182) give a simple method on how to utilize the energy bands and phonon dispersions which can be obtained from DFT calculations to calculate the thermoelectric coefficients in the ballistic transport regime for the quasi-one-dimensional periodic system.

2.7 Rate equation

In this section we briefly introduce the RE theory which will be used for the calculations of electrical conductance and Seebeck coefficient in the CB regime in the chapter 4 of this thesis. We recommend some references here if one has the interests to know the details of the RE (Refs. [39–41]). The formulas presented below are valid only in linear response regime for stationary state. The electric current and the heat flux are respectively given by

$$\begin{aligned} J = \frac{e}{\hbar k_B T}\sum_{p=1}^{\infty}\sum_{N=1}^{\infty}\frac{\Gamma_p^l\Gamma_p^r}{\Gamma_p^l+\Gamma_p^r}P_{eq}(N)F_{eq}(E_p/N)[1-f(\varepsilon_p-E_F)] \\ \times\left[eV-\frac{\Delta T}{T}(\varepsilon_p-E_F)\right], \end{aligned} \tag{2.183}$$

$$\begin{aligned} I^h = -\frac{1}{\hbar k_B T}\sum_{p=1}^{\infty}\sum_{N=1}^{\infty}\frac{\Gamma_p^l\Gamma_p^r}{\Gamma_p^l+\Gamma_p^r}P_{eq}(N)F_{eq}(E_p/N)[1-f(\varepsilon_p-E_F)] \\ \times(\varepsilon_p-E_F)\left[eV-\frac{\Delta T}{T}(\varepsilon_p-E_F)\right], \end{aligned} \tag{2.184}$$

where the first summation is over all the single particle energy levels and the second summation is over all the possible occupation numbers $N=\sum_i n_i$ with n_i the individual occupation number of the i-th level. n_i can take on only the values 1 and 0 corresponding to the occupied and unoccupied states, respectively. Γ_p^l and Γ_p^r denote the tunnelling rate from level p to the left and the right reservoirs, respectively. $\varepsilon_p \equiv E_p+U(N)-U(N-1)$, where E_p is the single particle energy of level p and $U(N)=N(N-1)e^2/2C+Nv$ is the charging energy with C the capacitance of the device and v the external potential applied on the quantum dot.

The equilibrium probability $P_{eq}(N)$ is defined as

$$P_{eq}(N)=\sum_{\{n_i\}}P_{eq}(\{n_i\})\delta_{N,\sum_i n_i}, \tag{2.185}$$

$$F_{eq}(E_p/N)=\frac{1}{P_{eq}(N)}\sum_{\{n_i\}}P_{eq}(\{n_i\})\delta_{n_p,1}\delta_{N,\sum_i n_i}, \tag{2.186}$$

where $\{n_i\}\equiv\{n_1,n_2,\cdots\}$ are all the possible combinations of occupation numbers.

$F_{eq}(E_p/N)$ is the conditional probability in equilibrium that level p is occupied given that the quantum dot contains N electrons. $P_{eq}(\{n_i\})$ is the Gibbs distribution in the grand canonical ensemble:

$$P_{eq}(\{n_i\})=Z^{-1}\exp\left[-\frac{1}{k_B T}\left(\sum_{i=1}^{\infty}E_i n_i+U(N)-NE_F\right)\right], \tag{2.187}$$

where Z is the partition function:

$$Z = \sum_{\{n_i\}} \exp\left[-\frac{1}{k_B T}\left(\sum_{i=1}^{\infty} E_i n_i + U(N) - NE_F\right)\right]. \tag{2.188}$$

Therefore according to the definitions shown in Eqs. (2.112)-(2.114) for conductance G, Seebeck coefficient S, and electric thermal conductance κ_e, one can obtain

$$G = \mathcal{L}^{(0)}, \tag{2.189}$$

$$S = -\frac{1}{eT}\frac{\mathcal{L}^{(1)}}{\mathcal{L}^{(0)}}, \tag{2.190}$$

$$\kappa_e = \frac{1}{e^2 T}\left[\mathcal{L}^{(2)} - \frac{[\mathcal{L}^{(1)}]^2}{\mathcal{L}^{(0)}}\right], \tag{2.191}$$

where

$$\begin{aligned}\mathcal{L}^{(n)} = \frac{e^2}{\hbar k_B T}\sum_{p=1}^{\infty}\sum_{N=1}^{\infty}\frac{\Gamma_p^l \Gamma_p^r}{\Gamma_p^l + \Gamma_p^r}[E_p + U(N) - U(N-1) - E_F]^n P_{eq}(N) F_{eq}(E_p/N) \\ \times \{1 - f[E_p + U(N) - U(N-1) - E_F]\}.\end{aligned} \tag{2.192}$$

When the coupling $\Gamma \to 0$, the RE becomes an *exact* theory which provides an alternative approach to calculate the transport coefficients of materials.

Chapter 3

Modeling and analysis of thermoelectric properties in nanostructures

3.1 Modeling of thermoelectric coefficients in SiGe nano membranes [⋆]

3.1.1 Introduction

Thermoelectric energy conversion is the ability of a device to convert a temperature gradient into an electrical current. One of the main advantages of this energy conversion is that the device can have a very long lifespan. Recently, the quest for a highly efficient thermoelectric energy material has attracted tremendous interests due to significant potential industrial applications [3, 5, 6, 42, 43]. Following the seminal work by Hicks and Dresselhaus [44, 45], a strong research activity has been focused on nanostructured materials. Graphene, a two-dimensional (2D) material, was first discovered experimentally in 2004 [46]. It exhibits exceptional properties such as high electron mobility as well as strongly mechanical characteristics. However, the extremely high thermal conductivity limits pristine graphene as an efficient thermoelectric material [47–49]. Nevertheless, it was shown that nanostructuring graphene with hexagonal boron-nitride in a nanoribbon increased the overall figure of merit by a factor 20 for a specific edge shape [50]. Notwithstanding its phenomenal properties, the integration of graphene with the current silicon-based technologies has proven to be a quite challenging task, whose solution would probably require the complete redesign of electronic devices. As our present technology is based on Si and Ge semiconductors, it thus appears natural to look at the thermoelectric properties of these materials, since the integration of a thermoelectric device based on them would be much simpler than the integration of carbon-based devices.

Silicene resembles graphene in the single atomic layered arrangements, *i.e.*, it forms a honeycomb lattice and shares with the carbon system similar electronic properties [51–55]. In particular, it is viewed as a new type of atomic-layered materials with outstanding

---

[⋆] This section is a part of the article **Phys. Rev. B** 89, 125403 (2014) by K. Yang, S. Cahangirov, A. Cantarero, A. Rubio, and R. D'Agosta.

properties such as the zero effective mass at the Dirac-point and infrared absorbance of optical spectra [56–58]. A free-standing 2D silicene is shown in Fig. 3.1. On the experimental side, single layered silicene (buckled) [37, 59–69] and silicene nanoribbons (SiNRs) [59, 61] have been synthesized on Ag substrate. In particular, SiNRs up to a narrow width of 1.6 nm have been produced, aligned parallel to each other in a well-distributed way [59]. From the experience gained with the current micro-electronics, we know that Ge is a good partner of Si since they share similar electronic properties and form bulk crystal with comparable lattice constant ($a_{\mathrm{Si}} = 0.5431$ nm and $a_{\mathrm{Ge}} = 0.5658$ nm) [70]. A single layered hexagonal lattice of Ge, called germanene, has been predicted from *ab-initio* calculations [56]. Theoretically, germanene presents a Dirac cone, and the electronic and structural properties of this material could be very similar to those of silicene. We will discuss some of them in more detail in the following. In particular, we will consider germanene nanoribbons (GeNRs) of different widths and consider the possibility of forming nanoribbons by alternating stripes of Si and Ge.

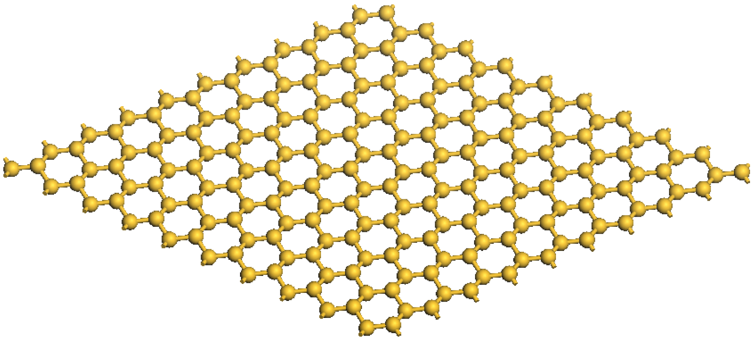

FIGURE 3.1: (Color) A schematics of 2D free-standing silicene. In contrast to graphene, silicene is not flat.

In this section, we systematically investigate with *ab-initio* technique combined with Landauer approach in the linear response regime the thermoelectric properties of both silicene and germanene nanosheets and one-dimensional (1D) Si and Ge nanoribbons. In Sec. 3.1.2 we will introduce the parameters we set in DFT calculations. In Sec. 3.1.3, we discuss the stability and study the transport properties of 2D silicene and germanene. In Sec. 3.1.4 we move the attention to the 1D systems. We focus mostly on the Ge system since the SiNRs have been investigated elsewhere [71]. From our calculations Si and Ge nanoribbons do share essentially similar properties. We find that the nanoribbons can have a quite large figure of merit, which is due to the fact that both Si and Ge nanoribbons have a finite electronic gap that leads to a high Seebeck coefficient. In Sec. 3.1.5 we consider nanoribbons created by alternating stripes of Si and Ge. By nanostructuring the system we would like to confine phonons and therefore decrease the thermal conductance. However, we find that the SiGeNRs show some analogous transport properties of pure Si or Ge nanoribbons. This is due to the limitations of our method of choice, namely, a full *ab-initio* study for the phonon transport. Indeed, within this technique we are limited to fairly small nanoribbons and therefore the long wavelength phonons are not quenched. We verified this point by using the nonequilibrium Green's function calculations within the tight-binding model. On the other hand, a classical technique based on molecular dynamics, would also allow us to calculate the thermal conductance of very larger systems. However, this technique does not recover the correct quantum limit of these 1D systems. And therefore we do expect that the molecular dynamics results give the incorrect thermal conductance at temperature below the Debye temperature, which for Si and Ge systems can be estimated to be about 640 K and 374 K [72], respectively.

3.1.2 Computational details

To obtain the energy bands of electrons and dispersions of phonons, we performed first principle calculations within local density approximation by using the projector augmented wave potentials as implemented in VASP [73]. The exchange correlation energy is chosen in the form of Ceperley-Alder which has been parameterized by Perdew and Zunger [74, 75]. For the self-consistent potential and the total energy calculations, the **k**-points of the Brillouin-zone in the reciprocal space are sampled by a (25×1×1) Monkhorst-Pack grid. The kinetic energy cut-off is set to 500 eV. After ionic relaxation, the Hellmann-Feynman forces acting on each atom are less than 0.01 eV/Å. We obtain the force constant matrix for the calculation of phonon dispersions through small displacement method [76]. We use a supercell technique with 15 Å of vacuum. In these calculations we have neglected both the phonon-phonon and the electron-phonon interactions. We expect that for the low energy phonons, mostly responsible for the thermal transport, the correction due to these interactions will be small, especially for the Seebeck coefficient.

Once we know the band structures of electrons and phonons, we can calculate their transmission coefficients immediately by counting the number of modes as we have discussed in chapter 2. Afterwards one can obtain the electrical conductance, Seebeck coefficient and thermal conductance by using the Landauer approach. This method is valid only in the ballistic transport regime for quasi-one-dimensional systems. For the 2D system, we use the Boltzmann transport equation to calculate the thermoelectric coefficients. The BTE theory has been implemented in BoltzTraP [77] and one can use the code simply.

3.1.3 Two-dimensional silicon and germanium

3.1.3.1 Geometrical structures of two-dimensional Si and Ge nanomembranes

We first investigate the structural stability of a single-layer of Si, *i.e.*, silicene. In trying to closely reproduce the experimental setup [63, 66, 67], we put one-layer of 3×3 silicene on top of five-layers of 4×4 Ag(111): According to experimental evidence, the two lattices should match, thus decreasing the total stress at the boundary and creating an ideal supercell for our calculations. The geometrical structure for silicene obtained after full relaxation is shown in Fig. 3.2 (a) and corresponds to the structure discussed in Ref. [69]. We have superimposed a Ag(111) layer to show the excellent structural matching, as highlighted by the boundary continuous line (red). Figure 3.2 (b) shows the silicene on Ag substrate in side view. Contrary to graphene, silicene is not a strict 2D system, in the sense that the atoms in silicene are arranged on two sub-layers with a fairly small buckling distance, which depends on the presence of the substrate. Indeed, it is found that the atomic arrangement is further distorted by the metallic substrate [69]. Starting from a single layer of Si, arranged in a plane on an hexagonal lattice without the Ag substrate, we would have obtained a system with a different buckling, where the atoms would divide equally between the upper and lower planes. The structure of the free standing silicene can be seen in Fig. 3.1. After the full relaxation, it is found that the buckling distance for the free standing silicene is about 0.43 Å. In our optimized structure, however, we observe that the silicene presents buckling forming two sub-layers with six atoms on top of the other twelve atoms which are therefore closer to the Ag surface. The buckling distance between these two sub-layers is about 0.79 Å.

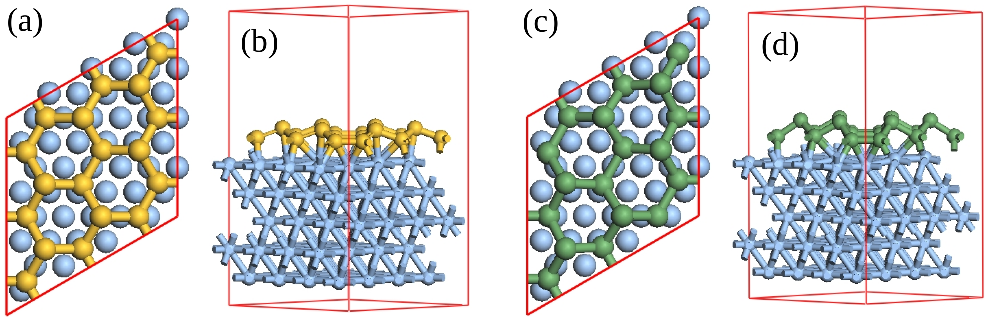

FIGURE 3.2: (Color) Geometrical structures of one-layer 3×3 silicene (yellow) (a) (top view) and (b) (side view) on top of five-layers 4×4 Ag(111) (white). Geometrical structures of one-layer 3×3 germanene (green) (c) (top view) and (d) (side view) on top of five-layers 4×4 Ag(111). The buckling distances for supported silicene and germanene are 0.79 Å and 1.42 Å, respectively.

Germanene is an analog of silicene, where Si is replaced by Ge. Here we study the structural properties of 2D germanene. Figure 3.2 (c) shows the atomic structure of one-layer 3×3 germanene on top of five-layers 4×4 Ag(111), and Figure 3.2 (d) shows the single-layered germanene on the Ag substrate with side view. The structure has been fully relaxed. It is found from Fig. 3.2 (d) that similar to silicene, two sub-layers are formed with six Ge atoms on the top sub-layer and the other twelve Ge atoms on the bottom sub-layer closer to the Ag surface. The buckling distance between the two sub-layers is about 1.42 Å. As to the free standing germanene, the buckling distance is found to be about 0.65 Å.

3.1.3.2 Energy Bands and electronic figure of merit

After the relaxation of silicene and germanene on Ag substrate, we now remove Ag and calculate the bands of these distorted silicene and germanene. For the band structures of supported silicene and germanene, more discussions can be found in Ref. [69]. In Fig. 3.3 (a) the electronic energy band for the distorted silicene is plotted along the high-symmetry points of the first Brillouin-zone, where the dotted blue line indicates the Fermi energy that we set for convenience at 0. It can be seen that a band gap about 0.3 eV crosses the Fermi energy, indicating semiconducting properties of the system. This must be compared with the flat silicene (unoptimized structure) and the silicene optimized without the Ag substrate, which both present a Dirac point at the K point of the first Brillouin-zone, therefore both showing metallic properties (see Fig. 3.4). Figure 3.3 (b) shows the band structure of the distorted germanene without the Ag substrate. It is found that there is no gap through the Fermi energy, indicating metallic properties. The zero gap observed in germanene originates from the larger buckling distance between the two atomic sub-layers.

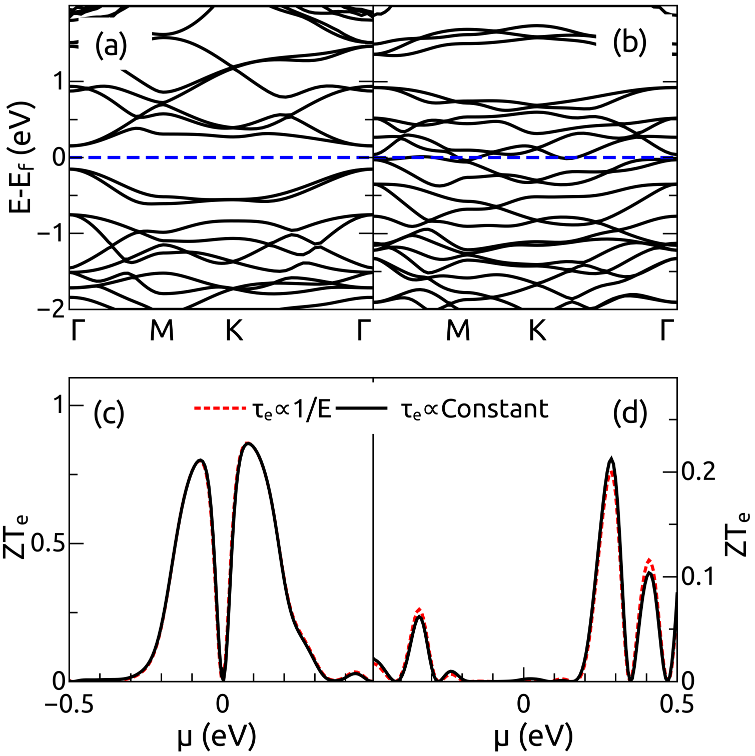

FIGURE 3.3: (Color) Electronic energy bands corresponding to the distorted (a) silicene and (b) germanene by removing the Ag substrate, respectively, where the dashed blue line denotes the Fermi energy position. (c) and (d) Dimensionless electronic figure of merit ZT_e at room temperature as a function of chemical potential μ corresponding to the distorted silicene and germanene, respectively. The black continuous and red dashed lines represent ZT_e evaluated at constant relaxation time approximation and $1/\tau_e \propto E$, respectively.

Based on the energy bands, we calculate the thermoelectric coefficients of the 2D silicene and germanene at room temperature, *i.e.*, $T = 300$ K. To perform the calculation of the figure of merit, we have evaluated the transport coefficients given in Eqs. (2.168)-(2.170) and Eq. (2.178). We have utilized the BoltzTraP-code [77] to perform the integration over the **k** points in momentum space in the first Brillouin-zone, using the data obtained from the VASP calculations. To calculate ZT, we have to estimate both the electron and phonon relaxation times $\tau_{i,e}(\mathbf{k})$ and $\tau_{i,p}(\mathbf{k})$ in λ_e and λ_{ph}, respectively (see Sec. 2.6 in chapter 2). However, for the electronic figure of merit ZT_e, which is defined as

$$ZT_e = \frac{S^2\sigma}{\lambda_e} T, \tag{3.1}$$

in the constant relaxation time approximation, ZT_e does not depend on $\tau_{i,e}$. We can calculate ZT_e independently without considering the phonon effect. Then ZT can be written according to (see chapter 1)

$$ZT = \frac{S^2\sigma}{\lambda_{ph} + \lambda_e} T = \frac{S^2\sigma}{\lambda_e} T \left(\frac{1}{1 + \lambda_{ph}/\lambda_e} \right) = \frac{ZT_e}{1 + \lambda_{ph}/\lambda_e}. \tag{3.2}$$

ZT_e does not include the phonon thermal contribution, but providing an upper limit for the total figure of merit ZT. A small ZT_e will therefore imply a small ZT.

Figures 3.3 (c) and (d) show the dimensionless electronic figure of merit, ZT_e, as a function of the chemical potential μ for the distorted silicene and germanene, respectively. It can be seen that the figure of merit for silicene exhibits two peaks in the left- and right-hand sides of $\mu = 0$, which separately correspond to the hole and electron transport. The maximum of the peak is about $ZT_e = 0.81$. While for the distorted germanene, it can be seen from Fig. 3.3 (d) that the peak of ZT_e is very small around $\mu = 0$, although some peaks appear at $\sim \pm 0.3$ eV. The reason is that the distorted germanene has a metallic character which leads to a very small Seebeck coefficient.

In Fig. 3.4 we show the electronic properties of the free standing silicene and germanene. For both the free standing silicene and germanene, from Figs. 3.4 (a) and (b) it can be seen that there is no gap at the Fermi energy. Indeed, at the high symmetric K point, a linear energy dispersion is shown in the band structures, indicating the massless Dirac fermions. This is similar to the 2D graphene system [51]. And our results agree with the previous work [56].

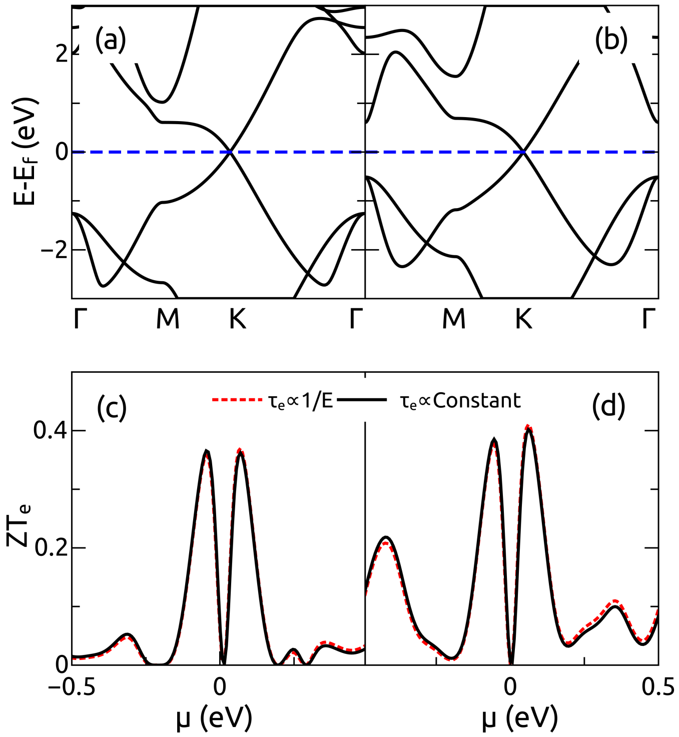

FIGURE 3.4: (Color) Electron energy bands of the free-standing (a) silicene and (b) germanene, respectively, where the dotted blue line denotes the Fermi energy. (c) and (d) Dimensionless electronic figure of merit ZT_e at room temperature as a function of chemical potential μ for the free-standing silicene and germanene, respectively. The black and red curves in (c) and (d) represent two different approximations of relaxation time.

Through the energy band structure calculations, in Figs. 3.4 (c) and (d) we investigate the dimensionless electronic figure of merit ZT_e for both free standing silicene and germanene, respectively. It is found that the figure of merit ZT_e for silicene and germanene shows two peaks near $\mu = 0$. The maximum value of ZT_e for silicene is 0.36 [see Fig. 3.4 (c)], and 0.41 for germanene [see Fig. 3.4 (d)]. We would point out here that the results obtained from BoltzTraP depend sensitively on the number of **k** points. One should sample the **k** points, in particular the **k** points around the Fermi energy, as much as possible to expect an accurate result. In our cases, we sampled $100 \times 100 \times 1$ $\mathbf{k}$ points in the whole first-Brillouin-zone for the calculation of the band structures.

To check the effect of the relaxation time on the electronic figure of merit, we have also performed the calculations by assuming $1/\tau_e$ to be proportional to the energy [54, 78]. The results are shown in Figs. 3.3 (c) and (d) and Figs. 3.4 (c) and (d) (see the red line). We found that both approximations give almost the same results. The continuous black line represents the results in the constant relaxation time approximation, and the dashed red line represents the results in the inverse energy dependence of relaxation time. The observation that the electronic figure of merit is independent from the relaxation time follows from the form of the Lorenz integral, where the derivative of the Fermi function is a strongly localized function around the Fermi energy. Therefore, the relaxation time is always evaluated around the Fermi energy and can be replaced with its value at that point.

Up to now we have shown that silicene and germanene crystal structures, similar to graphene where carbon has been replaced by either Si or Ge respectively, might possibly have a figure of merit of the order of 1. Our calculations provide an upper limit to the theoretical figure of merit since in these calculations we did not include the phonon thermal conductance and suggest that silicene might have a better thermoelectric properties than germanene in this 2D arrangement since distorted silicene does present a gap in the electronic energy spectrum and a larger Seebeck coefficient could occur.

3.1.4 Quasi-one-dimensional nanoribbons

We now consider quasi-one-dimensional systems, nanoribbons, made of stripes of germanene or silicene of finite width. We assume that it is possible to ”cut” those stripes from the respective crystal by removing the excess material. It has been reported that SiNRs can have a quite large figure of merit, up to 5 at 600 K [71]. Motivated by these results and by the expectation that GeNRs might perform better since their Debye temperature is lower, we have investigated the thermoelectric efficiency of GeNRs and, in the next section, nanoribbons obtained by alternating Si and Ge nanostructures or by incomplete randomising the Si and Ge arrangements. As standard with nanoribbons, there are two ways to terminate the edges of the ribbons (see Fig. 3.5), forming either zigzag or armchair edges. We identify the quantities associated with the zigzag with a Z and those of the armchair with a A. Because of the atomically thin structure, the cross-section and volume of these systems are not convenient to define. In the following we will use the concept of conductance instead of conductivity but ZT does not change as we have discussed in chapter 1 for the ballistic transport regime.

3.1.4.1 Germanene nanoribbons

Figures 3.5 (a) and (c) show the optimized structures of zigzag- and armchair-edged GeNRs (Z-GeNRs and A-GeNRs), respectively. To see the buckling more clearly, we have drawn the corresponding side views in (b) and (d). Hydrogen atoms are used to passivate the unsaturated bonds of the Ge atoms at the edges. W_Z and W_A identify the ribbon width. It can be seen from the top view that GeNRs form hexagonal ring as the union of two sublattices but, at odds with what happens for graphene nanoribbons, atoms in these two sublattices do not belong to the same plane: In the vertical direction there is some buckling, which is almost uniform for the atoms at the edge or in the center. Our calculations give for the Z-GeNRs a buckling distance of 0.62 Å, while for A-GeNRs they give 0.66 Å. For these nanoribbons, our total energy calculations show that the antiferromagnetic (AFM) state of Z-GeNRs is more stable than the ferromagnetic (FM) and nonmagnetic (NM) states counterparts. This is in agreement with other calculations performed for SiNRs [71] and theoretical predictions originally derived for graphene [79], which we expect to be valid for these systems. However, the energy difference between the different magnetic phases is small. This might be important for device stability, especially at temperatures higher than 300 K.

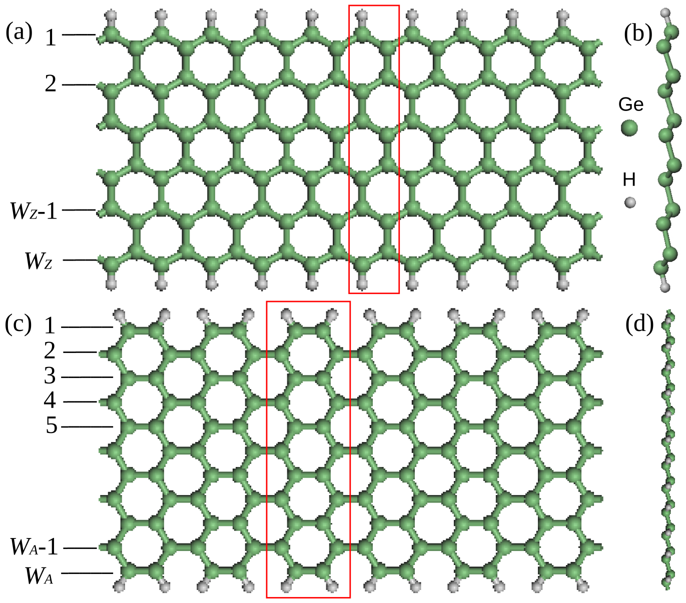

FIGURE 3.5: (Color) Optimized geometrical structures of (a) Z-GeNRs and (c) A-GeNRs and their lateral views. For the atoms at the edges, we passivate the unsaturated bonds with hydrogen atoms. W_Z and W_A denote the width of the nanoribbons for the zigzag and armchair terminated nanoribbons, respectively.

To further confirm the structural stability of the GeNRs, we have calculated the phonon dispersion relations. In Figs. 3.6 (a) and (b) we report the phonon dispersions for both Z-GeNR and A-GeNR with ribbon width 6, *i.e.*, $W_Z = W_A = 6$), respectively. We find that in the limit of phonon energy $\omega \to 0$, there are four acoustic phonon modes in the spectrum stemming from the lattice symmetry. In particular, no negative phonon mode is observed, which indicates that both Z-GeNRs and A-GeNRs passivated by hydrogen are structurally stable.

In Figs. 3.7 (a) and (b) the band structures of Z-GeNRs with AFM and FM states are calculated, respectively, where the dashed blue line corresponds to the Fermi energy. We can see that the AFM state exhibits a finite small gap: The bands for spin up and down are degenerate and the gap is about 0.1 eV. While for the FM state, it is found that spin up and down are nondegenerate, producing metallic properties, and similar properties are valid for the NM state (not shown). In the case of A-GeNR, our calculations indicate that the NM state is stable, indicating semiconducting properties as shown in Fig. 3.7 (c). Because the metallic system produces bad thermoelectric properties (generally ZT is smaller than 0.1), in the rest part of this work, we will put the attentions on the AFM state in the zigzag-edged nanoribbons and NM state in the armchair-edged nanoribbons.

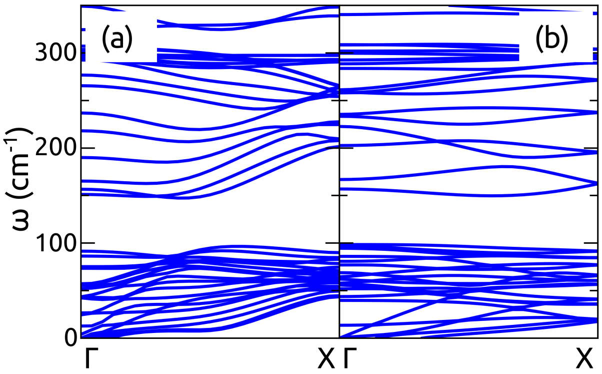

FIGURE 3.6: (Color) Phonon dispersions for (a) Z-GeNRs with $W_Z = 6$ and (b) A-GeNRs with $W_A = 6$, respectively.

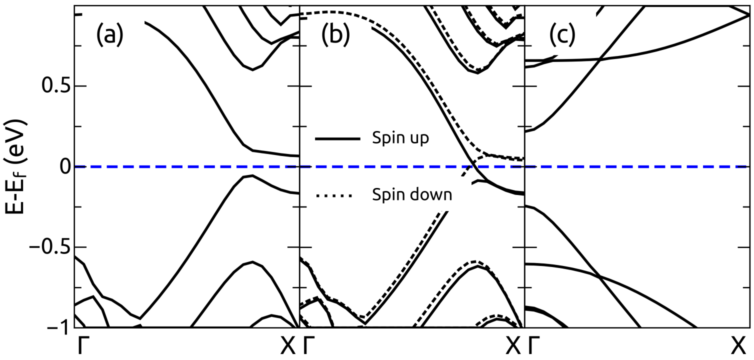

FIGURE 3.7: (Color) (a) Electron energy band of Z-GeNRs with $W_Z = 6$ for the AFM state: Notice the presence of a small electronic gap. (b) Electron energy band of Z-GeNRs with $W_Z = 6$ for the FM state. (c) Electron energy band of A-GeNRs with $W_A = 6$ corresponding to the NM state. In (a-c) the Fermi energy is chosen as the reference energy and set to 0.

In Fig. 3.8 we show the band gap of GeNRs as a function of ribbon width. It can be seen that the band gap of Z-GeNRs decreases monotonously with the increasing of the ribbon width. This must be compared with the oscillating behaviour we observe for the A-GeNRs [see Fig. 3.8 (b)]. For the A-GeNRs, for the ribbon widths $W_A = 3p$ and $3p + 1$ (where p is positive integer), the gap is larger than that of the ribbon with width $W_A = 3p + 2$. This width-dependent behavior of band gap is similar to that of the graphene nanoribbons.

To calculate the figure of merit ZT, we begin with the electronic transport properties. The upper panel in Fig. 3.9 corresponds to the results of Z-GeNRs, while the lower panel is for A-GeNRs. Figures 3.9 (a) and (b) show the transmission coefficients $\mathcal{T}_e$ as a function of the electron energy E for both Z-GeNRs and A-GeNRs, respectively. It can be seen that $\mathcal{T}_e$ exhibits a clear quantum stepwise structure, due to opening and closing of elastic transmission channels: Notice that the jumps are quantized and equal to 2 due to the electron spin. By making use of the transmission probability, we can calculate the electrical conductance G, Seebeck coefficient S and electron contributed thermal conductance κ_e. In Figs. 3.9 (c) and (d), the electrical conductance as a function of chemical potential is plotted for both Z-GeNRs and A-GeNRs, respectively. It can be seen that the electrical conductance for zigzag nanoribbons gradually increases with the ribbon width, and there is a peak corresponding the transmission step at $E \approx 0.5$

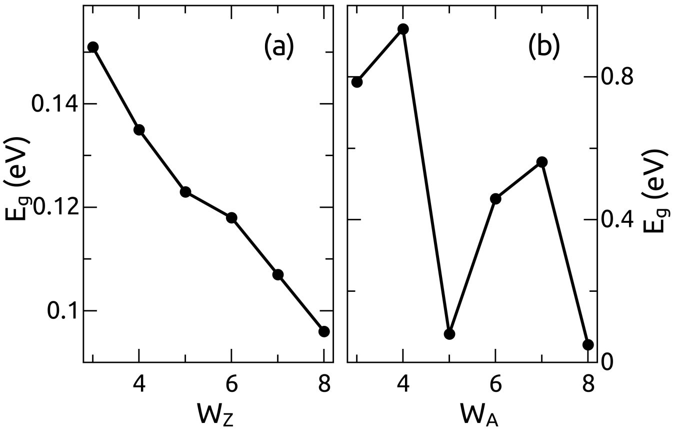

FIGURE 3.8: Band gap of (a) Z-GeNRs and (b) A-GeNRs as a function of the ribbon width W_Z and W_A, respectively.

eV. Around the Fermi energy, the conductance vanishes due to the finite gap. For the A-GeNRs, we find that the electrical conductance for the ribbon with width $3p$ or $3p+2$ vanishes, while for the ribbon with width $3p+2$, a non-zero dip is found. Interestingly, the conductance for all the curves of A-GeNRs exhibits quantized plateau-like characteristics.

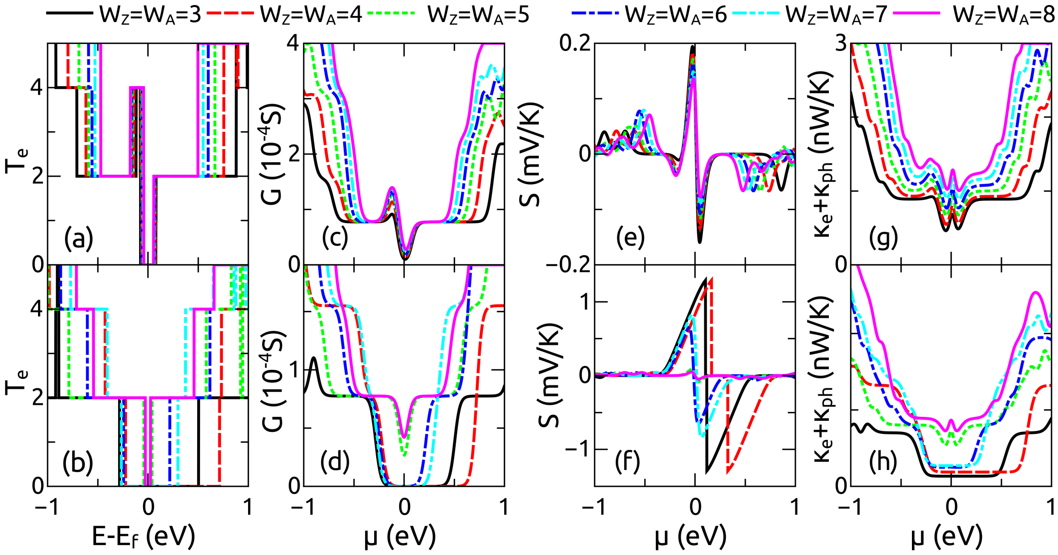

FIGURE 3.9: (Color) Electron transmission coefficient as a function of energy for (a) Z-GeNRs and (b) A-GeNRs with various ribbon widths, respectively. (c) and (d) Electrical conductance, (e) and (f) Seebeck coefficient, (g) and (h) electron and phonon thermal conductances for Z-GeNRs and A-GeNRs versus chemical potential μ, where the temperature is set to 300K.

In Figs. 3.9 (e) and (f) we report the Seebeck coefficient as a function of the chemical potential μ. It can be seen from Fig. 3.9 (e) that S presents two peaks around the position of the chemical potential needed to overcome the gap. Moreover the two peaks show different sign with positive and negative values. This behavior indicates the different carrier transport: The positive sign in the region of $\mu < 0$ corresponds to hole transport, while the negative at $\mu > 0$ corresponds to electron transport. In addition the absolute value of the peak of the Seebeck coefficient decreases with increasing W_Z. In the case of

A-GeNRs, it is found [see Fig. 3.9 (f)] that for the nanoribbons with width $3p$ and $3p+1$, the two Seebeck coefficient peaks with opposite sign can also be found centred around zero value of the chemical potential. We note that for the nanoribbons with width $3p+2$, the Seebeck coefficient is very small due to the small electronic gap. In Figs. 3.9 (g) and (h) the total thermal conductance, $\kappa_e + \kappa_{ph}$, for Z-GeNRs and A-GeNRs is depicted, respectively. It can be seen that the thermal conductance for Z-GeNRs increases with increasing the width of the nanoribbon. By checking the variation of the electrical and electric thermal conductances, G and κ_e, it is found that corresponding to the dip position of the electrical conductance, the electric thermal conductance (and therefore the total thermal conductance) shows a peak which becomes sharper with increasing W_A. Moreover, a similar effect can also be found in the A-GeNRs with width $3p+2$ as shown in Fig. 3.9 (h).

To understand the transport behavior, we plot the density of states $\mathcal{D}(E)$ around the Fermi energy in Fig. 3.10 for both Z-GeNRs and A-GeNRs. We can see that in the case of zigzag-edged nanoribbons, there are two peaks around the Fermi energy. In the case of armchair-edged nanoribbons with width $W_A = 3,\ 4$, $\mathcal{D}(E)$ is zero in the energy range from 0 to 0.5 eV. However, for the nanoribbons with width $W_A = 5$, $\mathcal{D}(E)$ around the Fermi energy shows a finite value, indicating the metallic properties which leads to the small Seebeck coefficient as we have seen in Fig. 3.9 (f).

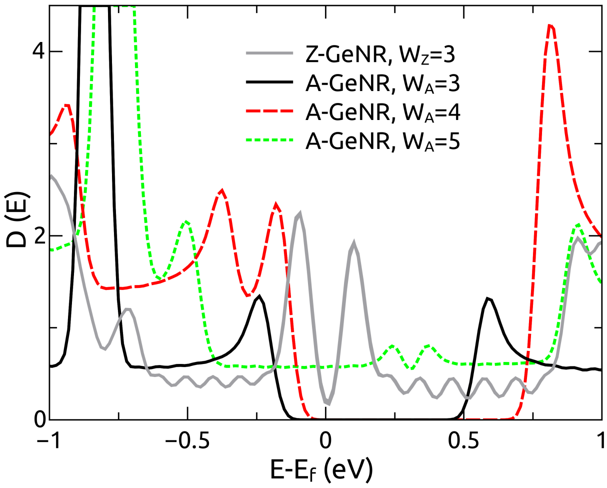

FIGURE 3.10: (Color) Density of states as a function of chemical potential μ for Z-GeNR with ribbon width $W_Z = 3$ and for A-GeNRs with ribbon width $W_A = 3,\ 4$ and 5.

To study the lattice thermal transport properties, the supercell approach is utilised to calculate the phonon force constant and then the dispersion relation is obtained by diagonalizing the corresponding dynamical matrix [76]. In Figs. 3.11 (a) and (b), the phonon thermal conductance κ_{ph} as a function of temperature T for both Z-GeNRs and A-GeNRs is plotted, respectively. It can be seen that the phonon thermal conductance increases with the increase of temperature, and finally reaches a constant value corresponding to the classical limit when $T > 400$ K. Moreover the thermal conductance for wide nanoribbons exhibits a higher value than that of the narrow nanoribbons. This can be simply explained by ”counting” the number of phonon modes, because the wide nanoribbons should have more phonon modes contributing to the thermal transport. To show the behaviour at low temperatures of the phonon thermal conductance, in Fig. 3.11 (c), we plot the logarithm of κ_{ph} versus the logarithm of T. It can be seen that κ_{ph}

shows a linear dependence on the temperature at low T, $T < 20$ K. At low temperature, for the one-dimensional systems, the lattice thermal conductance is dominated by the low-frequency acoustic phonons, which can be read as [80]

$$\kappa_{ph}(T) = \frac{4k_B^2 T}{h} \int_0^\infty d\xi\, \xi^2 \frac{e^\xi}{(e^\xi - 1)^2} = \frac{2\pi k_B^2 T}{3\hbar}, \tag{3.3}$$

where $\xi = \frac{\hbar\omega}{k_B T}$ and we have approximated the phonon transmission probability $\mathcal{T}_{ph}(\omega) = 4$ because of the sum rule. According to this approximation, it can be seen that the phonon thermal conductance exhibits a linear dependence on T in quasi-one-dimensional systems.

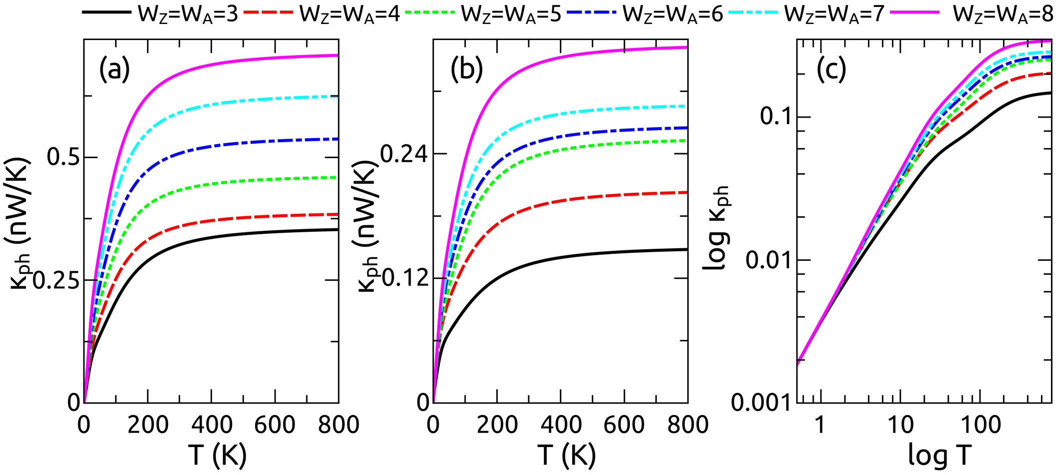

FIGURE 3.11: (Color) Phonon thermal conductance κ_{ph} of (a) Z-GeNRs and (b) A-GeNRs with different ribbon width as a function of temperature. (c) The logarithm of κ_{ph} for A-GeNRs as a function of logarithm of T, where the linear behavior is shown as we expect according to Eq. (3.3).

By combining the results of the electron and phonon calculations, we can finally investigate the thermoelectric efficiency of the GeNRs. Figures 3.12 (a) and (b) report the thermoelectric figure of merit ZT as a function of chemical potential μ for different ribbon width of both Z-GeNRs and A-GeNRs, respectively. We can see that there are two peaks around $\mu = 0$ for each curve in the case of Z-GeNRs. While for the A-GeNRs, the height of ZT peak for the ribbon width $W_A = 5, 8$ is much lower than that of the other ribbons. In Figs. 3.12 (c) and (d) we plot the figure of merit as a function of the ribbon width. Here ZT is chosen the maximum value of the figure of merit in (a) and (b) with respect to the chemical potential near the Fermi energy. It can be seen from Fig. 3.12 (c) that at narrow Z-GeNRs, ZT for electron and hole is about 0.35 and 0.61, and then it decreases with increasing the ribbon width. This effect can be explained by the lessening of the Seebeck coefficient and growing of the thermal conductance outweighing the increasing of the electrical conductance. Moreover, we observe from Fig. 3.12 (d) for the A-GeNRs, that ZT for both electron and hole transport coefficients show an oscillating behavior. In the case of the nanoribbons with width $W_A = 3p$ and $3p + 1$, ZT is larger than 1 for narrow nanoribbons. In particular for the ribbon width $W_A = 4$, ZT reaches 1.63, indicating a high thermoelectric conversion efficiency in these nanostructures.

We have also calculated the carrier density ρ at the chemical potential that gives the maximum efficiency for the GeNRs. To do that we used the formula valid for the electron

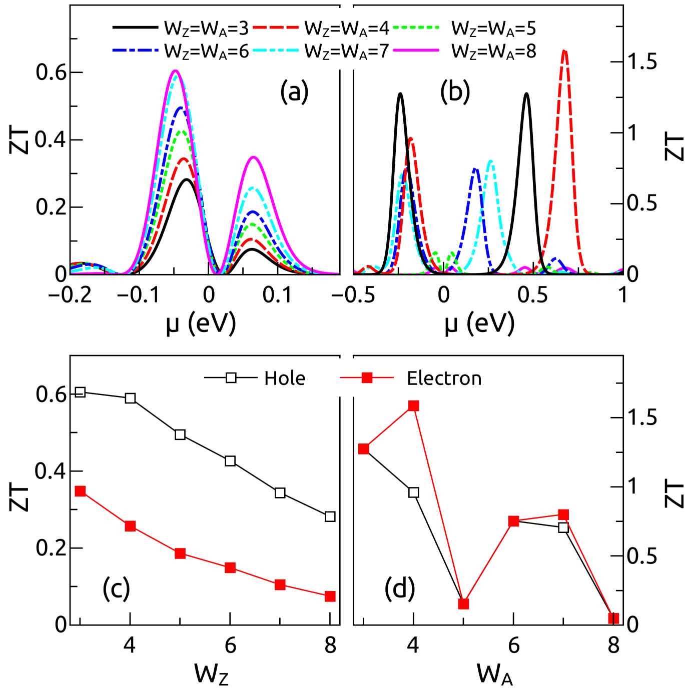

FIGURE 3.12: (Color) Figure of merit ZT at room temperature for (a) Z-GeNRs and (b) A-GeNRs as a function of chemical potential μ for different ribbon width W_Z and W_A, respectively. In (c) we report the peak value of ZT for Z-GeNRs at negative values of the chemical potential μ associated with the hole transport (square hollow points) and positive values μ associated with the electron transport (square full points). In (d) we pick out the peak value of ZT in (b) for A-GeNRs around $\mu = 0$ for both electron and hole transport.

TABLE 3.1: Carrier density for the Z-GeNRs as a function of the ribbon width calculated at the chemical potential that gives the maximum figure of merit, at $T = 300$ K. The e and h subscripts refer to the electrons or holes transport, respectively.

W_z	3	4	5	6	7	8
$\mu_{M,e}$ (meV)	32.5	32	32	31.5	31	31.5
ρ_e (10^{12} cm^{-2})	6.74	6.85	7.05	6.57	6.18	6.24
$\mu_{M,p}$ (meV)	-24	-22	-20	-19.5	-18	-16
ρ_p (10^{12} cm^{-2})	4.15	3.65	3.13	3.42	2.65	2.71

carrier density in an intrinsic semiconductor:

$$\rho_e = \int_{E_c}^{\infty} dE f(E, \mu, T)\mathcal{D}(E), \tag{3.4}$$

where $f(E, \mu, T)$ is the Fermi distribution, $\mathcal{D}(E)$ is the density of states, and E_c is the bottom energy of the conduction band. To calculate the hole carrier density we used

$$\rho_p = \int_{-\infty}^{E_v} dE \left[1 - f(E, \mu, T)\right] \mathcal{D}(E), \tag{3.5}$$

where E_v is the top of the valence band. We report our results for the electron and hole carrier densities for the Z-GeNRs in table 3.1, where μ_M is the chemical potential corresponding to the maximum figure of merit.

Table 3.2: Carrier density for the A-GeNRs as a function of the width calculated at the chemical potential that gives the maximum figure of merit, at $T = 300$ K. The e and h subscripts refer to the electrons or holes transport, respectively.

W_A	3	4	5	6	7	8
$\mu_{M,e}$ (meV)	231	337	22.5	90	131	20
ρ_e (10^{12} cm^{-2})	0.60	3.53	2.24	0.797	0.75	1.97
$\mu_{M,p}$ (meV)	-120	-91	-22	-102	-113	-20
ρ_p (10^{12} cm^{-2})	1.12	2.26	2.37	0.937	0.875	1.88

Similarly, we report our results for the electron and hole carrier densities in table 3.2 for the A-GeNRs.

Our results are consistent with what has been found for SiNRs [71]. However, we would like to point out that from our calculations the phonon thermal conductance of the small GeNR is never negligible with respect to the electronic thermal conductance, as instead has been argued for the SiNRs in Ref. [71]. We believe this is an artifact of the classical methods used in Ref. [71]. Unlike our quantum simulations, in these quasi-one-dimensional systems that are in the ballistic thermal transport regime, classical methods would not recover the linear dependence of phonon thermal conductance at low temperatures. Moreover, the classical calculations should be valid only for temperatures higher than the Debye temperature, which for these systems can be estimated to be about 600 K for SiNRs. In Ref. [71], the classical calculations are instead used to evaluate the phonon thermal conductance also below the Debye temperature, an assumption that would need an explanation. At the same time, the quantum technique does not include any inelastic effect and it is strongly limited in size, *i.e.*, we cannot consider a large supercell as instead is possible with classical methods [71].

3.1.4.2 Silicene nanoribbons

For completeness, and to have a direct comparison with the results available in the literature [71], we have calculated the figure of merit of SiNRs similar to the GeNRs that we have investigated in the previous section. Here we report only the phonon thermal conductance and the figure of merit. The electronic transport coefficients, G, S, and κ_e have shapes similar to those in Fig. 3.9 and we do not show them again. We plot in Figs. 3.13 (a) and (b) the phonon thermal conductance κ_{ph} for both zigzag- and armchair-edged SiNRs (Z-SiNRs and A-SiNRs) as a function of temperature T, respectively. It is seen that the phonon thermal conductance increases with the temperature, and finally reaches steady value. For the zigzag nanoribbons, the thermal conductance increases gradually with the ribbon width due to the increase of available phonon transport channels. As to the armchair nanoribbons, the thermal conductance also increases except for the ribbon width $W_A = 3,\ 4$ whose values are indeed close [see Fig. 3.13 (b)].

In Fig. 3.14 the figure of merit for SiNRs as a function of ribbon width is shown. It can be seen that the figure of merit for Z-SiNRs decreases with the increase of the ribbon width. Moreover ZT for the hole transport is larger than that contributed from the electron transport. The reason is due to the increased phonon thermal conductance and decreased electronic band gap. For the armchair nanoribbons, it is found from Fig. 3.14 (b) that the figure of merit at narrow ribbon is quite large, about 1.04. With the

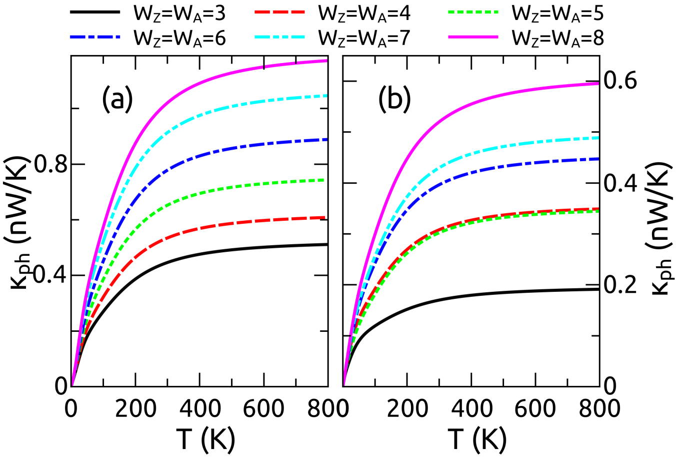

FIGURE 3.13: (Color) Phonon thermal conductance κ_{ph} of (a) Z-SiNRs and (b) A-SiNRs as a function of temperature, respectively.

increase of the ribbon width, ZT decreases overall and exhibits an oscillating behavior. We notice that, due to the larger thermal conductance, we obtain a figure of merit of the SiNRs that is smaller than the one reported in Ref. [71].

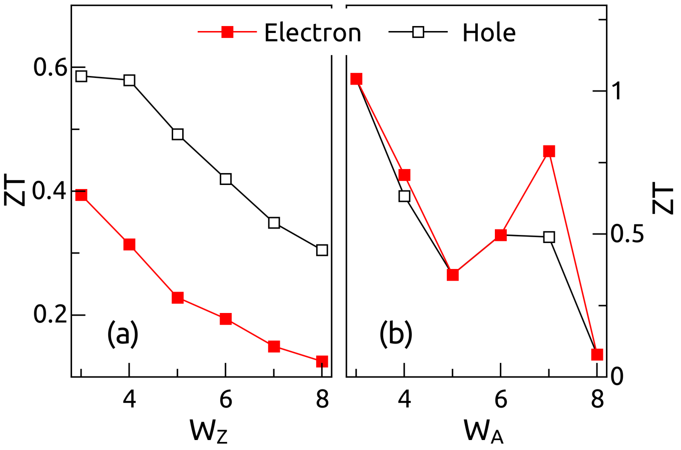

FIGURE 3.14: (Color) Figure of merit ZT at room temperature for (a) Z-SiNRs and (b) A-SiNRs as a function of ribbon width W_Z and W_A, where the black square hollow points and the red square full points correspond to the hole and electron transport, respectively.

3.1.5 Silicon-germanium heterostructures

We have shown that Si and Ge nanoribbons can have a substantial figure of merit, which is slightly above 1 for narrow ribbon with armchair edge. On the other hand, we would like to explore the possibility of improving on this result by mixing these nanoribbons. Since Si and Ge nanoribbons do share similar electronic properties, our first attempt is to investigate a nanoribbon created by alternating stripes of Si and Ge in the direction of the growth of the nanoribbon. Hopefully, their different masses would create a trap for the phonon modes, thus reducing the thermal conductance of the device and improving the overall figure of merit ZT. We will show in the following subsection that this idea is working partially and we do have a modest increasing of ZT. This is a limitation of our quantum method of calculating the thermal conductance. We are limited in the size of the supercell we can consider for our calculations. Indeed, the low energy phonons responsible primarily for the thermal transport have a wavelength that spans many supercells, thus making the chemical modulation ineffective as a phonon trap. To improve on this result, we have therefore investigated the case where we randomly substituted some Si atoms with Ge in the nanoribbon crystal. After fully relaxing the structure, we have, however, observed that also this nanoribbon with randomly distributed Si and Ge does not work too much as a phonon trap, for essentially the same reason of the perfect modulation: The Si and Ge randomly distributed supercell is not large enough to confine the low energy phonon modes.

3.1.5.1 Thermoelectric properties of hybrid silicene-germanene nanoribbons

In this subsection, we investigate the thermoelectric properties of orderly-distributed heterostructured silicene-germanene nanoribbons (SiGeNRs). After forming the structure, we have relaxed the atomic positions, without taking into account any substrate. Figure 3.15 shows the optimized geometrical structures of zigzag- and armchair-edged SiGeNRs (Z-SiGeNRs and A-SiGeNRs) passivated by hydrogen atoms, where the red line encloses a supercell along the ribbon axis. L_{Si} and L_{Ge} are the lengths of silicene and germanene stripes in the supercell, respectively.

(a) Zigzag-edge

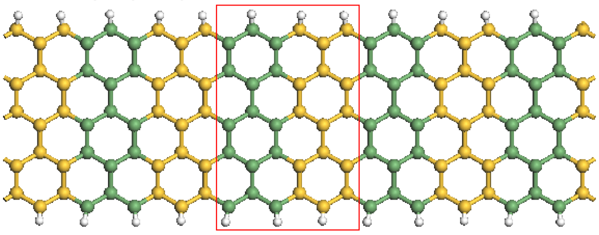

(b) Armchair-edge

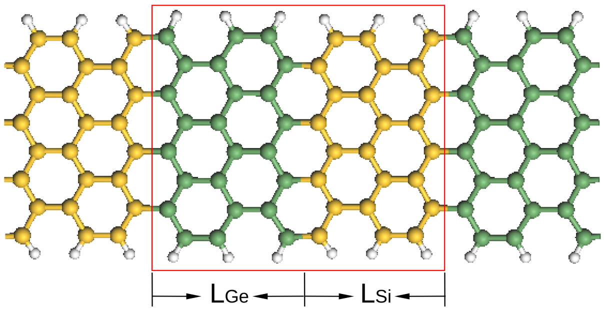

Figure 3.15: (Color) Geometrical structures of (a) Z-SiGeNRs and (b) A-SiGeNRs, where the red line encloses a supercell along the ribbon axis and L_{Si} and L_{Ge} are the lengths of silicene and germanene stripes in the supercell, respectively. We have chosen $L_{\mathrm{Si}} = L_{\mathrm{Ge}} = 3$ for this particular case and used the hydrogen to passivate the ribbon edges.

In Fig. 3.16 we plot the energy band gap for the hybrid silicene and germanene nanoribbons. Increasing the ribbon width, the band gap for Z-SiGeNRs decreases though the gap has a slight oscillation from $W_Z = 4$ to 7 [see Fig. 3.16 (a)], while the gap for A-SiGeNRs shows a strongly oscillating phenomenon as shown in Fig. 3.16 (b). When the ribbon width W_A satisfies either $3p$ or $3p+1$, a larger band gap appears than that of the nanoribbons with width $3p+2$. This width dependence of the band gap is similar to that of the A-GeNRs and A-SiNRs as we have discussed in Sec. 3.1.4.

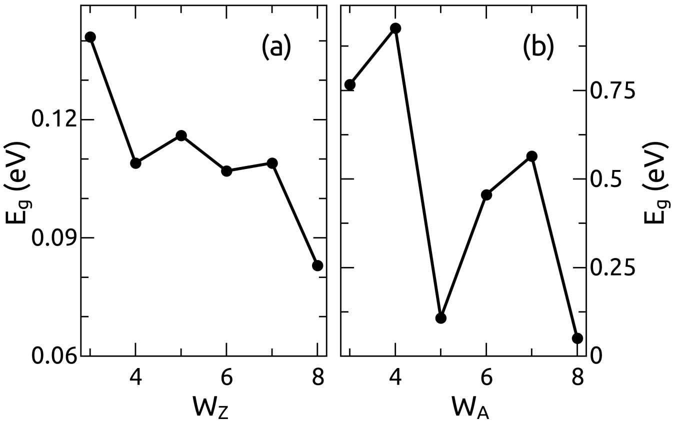

FIGURE 3.16: (a) and (b) Energy band gap as a function of ribbon width W_Z and W_A for Z-SiGeNRs and A-SiGeNRs, respectively.

We now investigate the transport properties and we start from the hybird nanoribbon with width $L_{\mathrm{Si}} = L_{\mathrm{Ge}} = 1$. In Figs. 3.17 (a) and (b) we report the transmission coefficients as a function of electronic energy for different width of the Z-SiGeNRs and A-SiGeNRs, respectively. It can be seen that the transmission probability exhibits characteristic quantized steps and a band gap is shown around the Fermi energy. Starting from this transmission function we can easily obtain the transport coefficients using the Landauer theory that we have discussed in Sec. 3.1.2. In Figs. 3.17 (c) and (d) we plot the electrical conductance in the linear response regime as a function of the chemical potential μ. It is found that the electrical conductance for Z-SiGeNRs exhibits a peak and a dip around $\mu = 0$. As for the A-SiGeNRs, we show that the electrical conductance at Fermi energy is zero for the nanoribbon with width $W_A = 3p$ and $3p+1$ due to the presence of the larger band gap as we have seen in Fig. 3.16 (b), while the conductance at $\mu = 0$ for the ribbon with width $W_A = 3p+2$ shows a dip where the conductance assumes a finite value.

In Figs. 3.17 (e) and (f), the Seebeck coefficient versus chemical potential is depicted. It is found that the Seebeck coefficient around $\mu = 0$ appears two peaks for both Z-SiGeNRs and A-SiGeNRs with width $W_A = 3p$ and $3p+1$. The absolute value of the peak for A-SiGeNRs is 1.4 mV/K, which is quite larger than the value of Z-SiGeNRs, indicating a high thermoelectric effect in this armchair edged nanoribbons. On the other hand, for the armchair nanoribbons with width $3p+2$, the Seebeck coefficient is very small due to the very small band gap presented in these systems. In Figs. 3.17 (g) and (h) the total thermal conductance $\kappa_e + \kappa_{ph}$ including electron and phonon contributions is plotted. It can be seen that $\kappa_e + \kappa_{ph}$ for Z-SiGeNRs exhibits a peak at $\mu = 0$, while for the A-SiGeNRs with widths $3p$ and $3p+1$, it has a plateau in the energy region around $\mu = 0$, mostly due to the phonon thermal transport. As for the nanoribbon with width $3p+2$, the thermal conductance reaches a local maximum on account of a local maximum of the electronic heat contribution at $\mu = 0$.

Figures 3.18 (a) and (b) show the phonon thermal conductance κ_{ph} for both Z-SiGeNRs and A-SiGeNRs as a function of temperature for different nanoribbon widths, respectively. It can be seen that the phonon thermal conductance κ_{ph} increases gradually

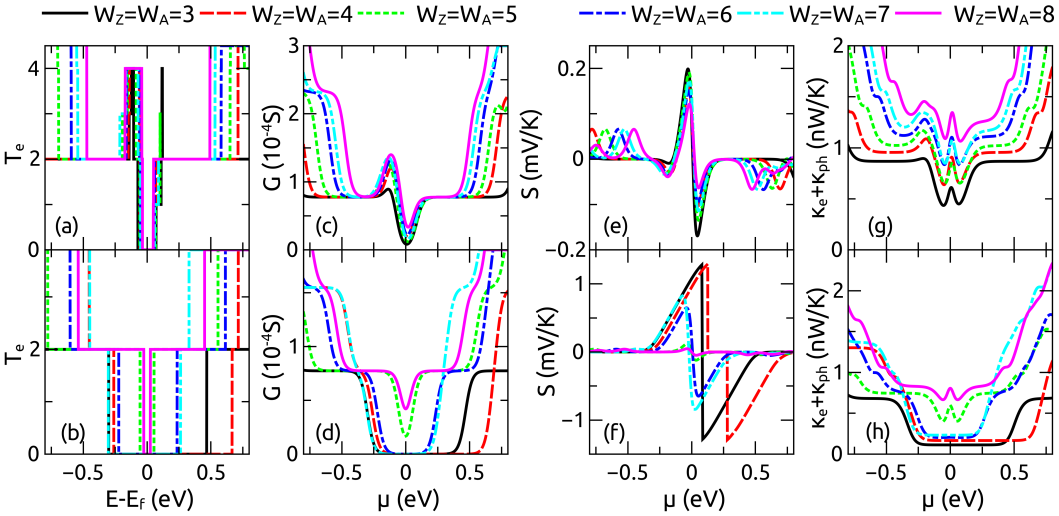

FIGURE 3.17: (Color) Electronic transmission coefficient as a function of energy for (a) Z-SiGeNRs and (b) A-SiGeNRs, respectively. (c) and (d) Electrical conductance, (e) and (f) Seebeck coefficient, (g) and (h) electron and phonon thermal conductances as a function of chemical potential μ for Z-SiGeNRs and A-SiGeNRs, respectively, where we have set the temperature $T = 300$ K.

with increasing temperature and finally reaches a plateau at $T > 400$ K. By comparing Fig. 3.18 with Figs. 3.11 and 3.13, we find that the thermal conductance of SiGeNRs is located between the value of GeNRs and SiNRs, *i.e.*, the thermal conductance of SiGeNRs is larger than that of GeNRs, but smaller than that of SiNRs. Similar to the case of GeNRs or SiNRs, at low temperature region, the linear dependence of the thermal conductance on the temperature is still observed, in agreement with Eq. (3.3).

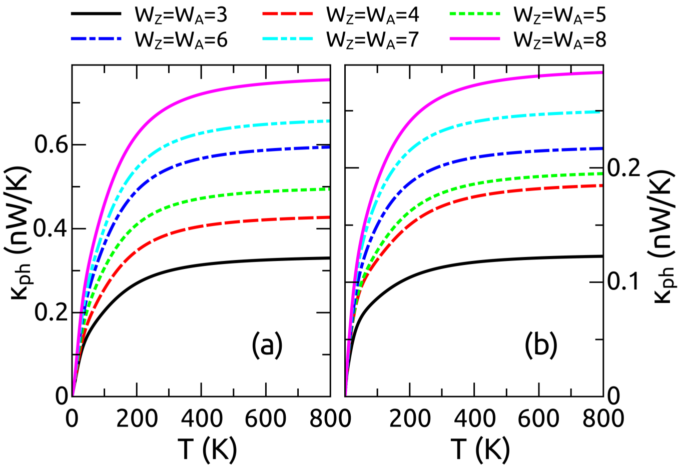

FIGURE 3.18: (Color) Phonon thermal conductance κ_{ph} of (a) Z-SiGeNRs and (b) A-SiGeNRs as a function of temperature, respectively.

In Figs. 3.19 (a) and (b), we report the figure of merit ZT for both Z-SiGeNRs and A-SiGeNRs as a function of ribbon widths W_Z and W_A, respectively. It is found that the maximum value of the figure of merit for Z-SiGeNRs appears in the narrowest nanoribbon, which is about 0.59 corresponding to the hole transport. While for the electron transport, the corresponding ZT is about 0.38. As to the armchair-edged nanoribbon with width $W_A = 3$, ZT is found to be 1.46 for both the hole and electron transport [see Fig. 3.19 (b)]. With the increase of the ribbon width, the figure of merit shows an oscillatory behavior reminiscent of the different properties of the nanoribbons with different widths. The amplitude of the "oscillation", however, decreases quite rapidly with increasing the ribbon width. This is mostly due to the rapid increasing of the phonon thermal conductance with W_A. In particular, ZT is very small in the case of nanoribbon with width $3p+2$ due to the small Seebeck coefficient as shown in Fig. 3.17 (f).

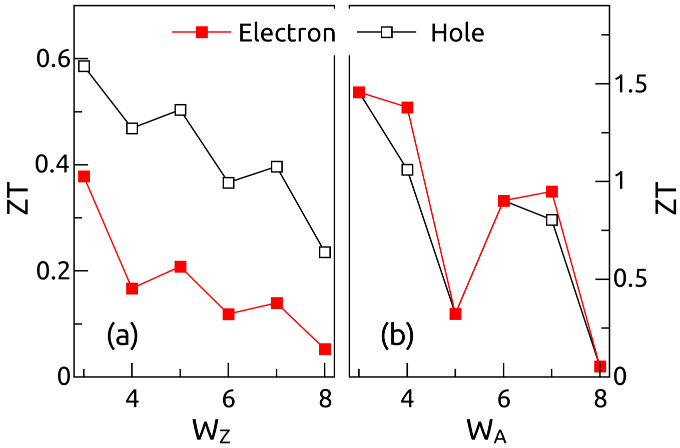

FIGURE 3.19: (Color) Figure of merit ZT at room temperature for (a) Z-SiGeNRs and (b) A-SiGeNRs as a function of nanoribbon with width W_Z and W_A, where the hollow and full points correspond to the hole and electron transport, respectively.

3.1.5.2 Component modulation on the figure of merit of hybrid silicene-germanene nanoribbons

In Fig. 3.20, we investigate the thermoelectric properties of SiGeNRs by modulating the component lengths of silicene and germanene stripes in the supercell. Figures 3.20 (a) and (b), (c) and (d), (e) and (f) show the figure of merit ZT at room temperature for Z-SiGeNRs and A-SiGeNRs as a function of ribbon width for $L_{\mathrm{Si}} = L_{\mathrm{Ge}} = 2$, 3 and 4, respectively. It is found that the maximum ZT for hole and electron transport in the case of Z-SiGeNRs is 0.85 and 0.42 for $L_{\mathrm{Si}} = L_{\mathrm{Ge}} = 2$, 0.87 and 0.53 for $L_{\mathrm{Si}} = L_{\mathrm{Ge}} = 3$, and 1.06 and 0.54 for $L_{\mathrm{Si}} = L_{\mathrm{Ge}} = 4$, respectively. As to the armchair nanoribbons, the maximum of ZT for $L_{\mathrm{Si}} = L_{\mathrm{Ge}} = 2$ is about 1.93, while the maximum ZT for $L_{\mathrm{Si}} = L_{\mathrm{Ge}} = 3$ and 4 is about 2.18 and 2.06, respectively. With the increase of the ribbon width, the overall figure of merit decreases for both Z-SiGeNRs and A-SiGeNRs with width $W_A = 3p$ and $3p+1$. Regarding the nanoribbon with width $3p+2$, the figure of merit is quite small compared to the ribbons with width $3p$ and $3p+1$. Through checking the Seebeck coefficient, it is found to be very small for nanoribbons with width $3p+2$ due to the small band gap, in agreement with our analysis of the system with $L_{\mathrm{Si}} = L_{\mathrm{Ge}} = 1$. Figures 3.20 (g) and (h) show the figure of merit as a function of temperature for Z-SiGeNRs with width $W_Z = 3,\ 4$ and A-SiGeNRs with width $W_A = 3,\ 4$, respectively. It can be seen that the figure of merit increases and then decreases with the increase of the temperature. The maximum ZT for Z-SiGeNRs is about 1.05 at $T \approx 200$ K, and the maximum ZT for A-SiGeNRs is about 3.91 at $T \approx 1000$ K. We will have more discussions about the temperature dependence of ZT in the forthcoming Sec. 3.2.

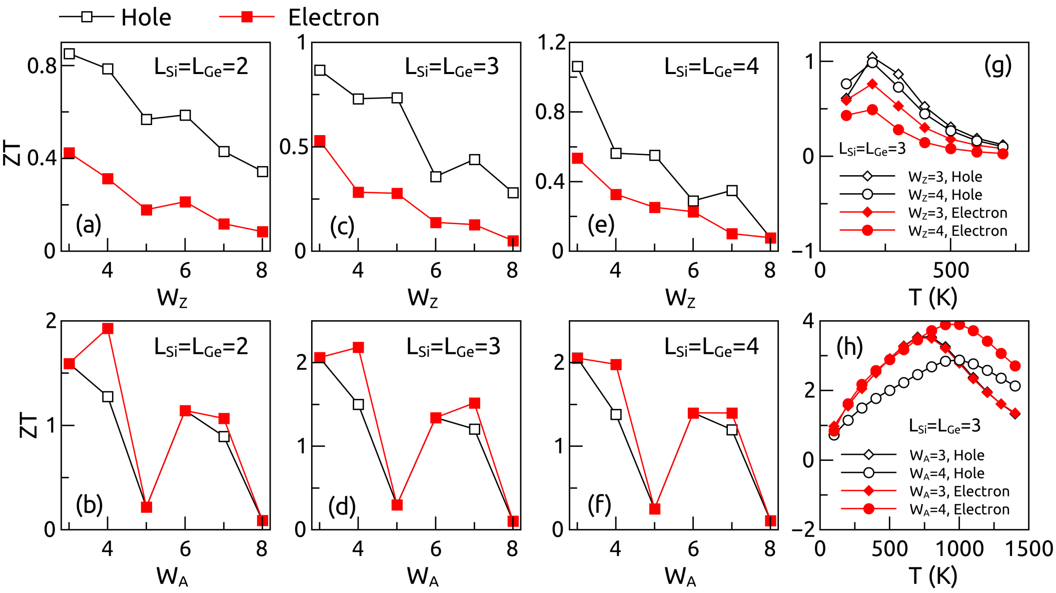

FIGURE 3.20: (Color) Figure of merit ZT at T=300K for Z-SiGeNRs and A-SiGeNRs as a function of ribbon width W_Z and W_A under different component lengths of silicene and germanene stripes: (a) and (b) $L_{\rm Si} = L_{\rm Ge} = 2$, (c) and (d) $L_{\rm Si} = L_{\rm Ge} = 3$, (e) and (f) $L_{\rm Si} = L_{\rm Ge} = 4$, respectively. (g) and (h) Figure of merit as a function of temperature for Z-SiGeNRs and A-SiGeNRs with the corresponding ribbon width 3 and 4, where the lengths of silicene and germanene stripes in the supercell are $L_{\rm Si} = L_{\rm Ge} = 3$. The hollow and full points correspond to the hole and electron transport, respectively

We wish to point out that ZT of these systems is larger than that for the pure A-GeNRs or A-SiNRs. This means that nanostructuring can improve the overall energy conversion efficiency. On the other hand, the modest increase in ZT for these nanoribbons shows how this nanostructuring is not effective in blocking the phonon modes. We should probably reach larger $L_{\rm Si}$ and $L_{\rm Ge}$, in order to achieve the trapping of the low energy phonon modes.

3.1.5.3 Disorder effect on the figure of merit of hybrid silicene-germanene nanoribbons

In the above discussions, the Si and Ge atoms in the nanoribbons are orderly distributed along the growth direction. Here we consider the case that Si and Ge atoms randomly occupy the site of the lattice in Fig. 3.15. The length of the supercell $L_S (= L_{\rm Si} + L_{\rm Ge}) = 6$ and the number of Si and Ge atoms in the supercell are taken the same. Since the armchair nanoribbons show the most promising values of the figure of merit, in Figs. 3.21 (a) and (b) we merely depict the figure of merit ZT as a function of chemical potential μ for disordered A-SiGeNRs under the ribbon width $W_A = 3$ and 4, respectively. As a comparison, we have also plotted the figure of merit for A-GeNRs, A-SiGRs and A-SiGeNRs. It can be seen that the maximum figure of merit for disordered A-SiGeNRs and ordered A-SiGeNRs is nearly twice of the value of clean A-GeNRs and A-SiGRs. The maximum ZT for disordered and ordered A-SiGeNRs with width $W_A = 3$ is about 2 for both electron and hole transport corresponding to the positive and negative chemical potentials, while the maximum ZT for the ribbon width $W_A = 4$ is 2.18 and 2.56 for electron transport and 1.5 and 1.8 for hole transport, respectively. The principal reason of the enhanced thermoelectric efficiency comes from the reduced phonon thermal conductance, since the electronic properties are slightly affected by the randomness of the atomic positions. Again, due to the small size of the supercell we can consider in *ab-initio* calculations, phonon confinement is not strong enough, and therefore the thermal conductance of disordered and ordered A-SiGeNRs is only slightly reduced with respect to the clean Si and Ge system. For the same reason, the thermal conductance of the random structure is similar to the one of the silicene-germanene heterostructures as expected.

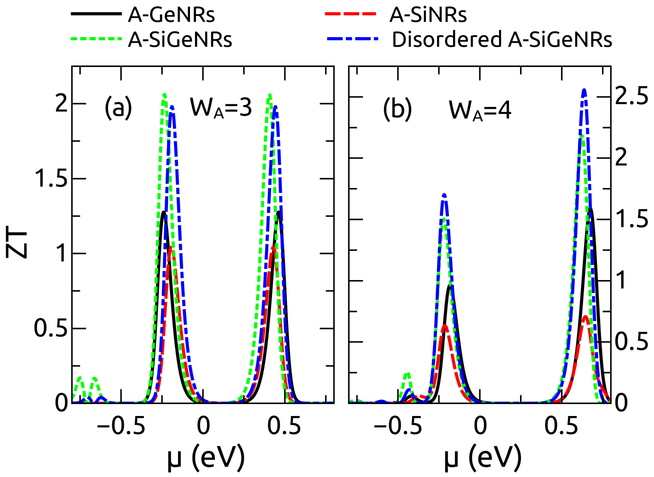

FIGURE 3.21: (Color) Figure of merit ZT at $T = 300$ K for A-GeNRs, A-SiNRs, A-SiGeNRs and disordered A-SiGeNRs with ribbon width (a) $W_A = 3$ and (b) $W_A = 4$ as a function of chemical potential μ, where we have taken the supercell length $L_S = 6$, respectively.

To present a proof that a large supercell can effectively reduce the phonon thermal conductance in the SiGe heterostructures as well as considering the computational time consuming in *ab-initio* calculations, here we employ the semiclassical tight-binding calculation to investigate the lattice thermal transport properties. To calculate the phonon Green's functions, we have to know the force constant firstly. In the following we use an empirical Keating potential [33, 70, 81] which has been widely applied in the SiGe nanowire systems [82, 83] and has been proved to provide a very good fit for the phonon dispersions [70, 84, 85]. The explicit expression of the Keating potential is

$$V = \frac{1}{2}k_r \sum_{i,j} \left(\mathbf{R}_{0,i,j}^2 - \mathbf{R}_{i,j}^2\right)^2 + \frac{1}{2}k_\theta \sum_{\substack{i,j,k \\ k\neq j}} \left(\mathbf{R}_{0,i,j}\cdot\mathbf{R}_{0,i,k} - \mathbf{R}_{i,j}\cdot\mathbf{R}_{i,k}\right)^2, \tag{3.6}$$

where $\mathbf{R}_{0,i,j}$ and $\mathbf{R}_{0,i,k}$ are the equilibrium position vectors connecting atom i with j and k, $\mathbf{R}_{i,j}$ and $\mathbf{R}_{i,k}$ are the corresponding position vectors after deformation, respectively. The bond stretching and bending force parameters, k_r and k_θ, for silicene in Eq. 3.6 are $7.2186{\times}10^{20}$ N/m^3 and $1.5225{\times}10^{20}$ N/m^3 [81]. As to the parameters of germanene, we roughly estimate $k_r = 5.3469 \times 10^{20}$ N/m^3 and $k_\theta = 1.2516 \times 10^{20}$ N/m^3 through comparing the force-constance ratio of this 2D system with that of the bulk Si and Ge crystals [70]. We have fine tuned these values to improve the agreement between *ab-initio* and tight-binding phonon spectra. For the force parameters between Si and Ge atoms in the hybrid structures, we take their average value. Regarding the Si-H and Ge-H interactions, we take 10% of the corresponding Si-Si and Ge-Ge interactions, accordingly. Based on the Keating model and combined with the nonequilibrium Green's function technique, we can calculate the phonon transmission probability and thus the thermal transport properties, using the theory we have described in detail in chapter 2.

Figures 3.22 (a) and (b) show the phonon thermal conductance calculated from tight-binding for A-GeNRs (continuous gray line), A-SiNRs(dashed gray line), A-SiGeNRs (dotted gray line) and disordered A-SiGeNRs (dash-dotted gray line), where the ribbon width $W_A = 3$. To check how reliable the tight-binding calculations are, we have also plotted the corresponding thermal conductance calculated from *ab-initio* [color lines in Fig. 3.22 (a)]. It can be seen that the thermal conductances obtained from tight-binding and *ab-initio* are quite close, especially in the low temperature region. In addition, it is found that the phonon thermal conductance in the case of A-SiGeNRs and disordered A-SiGeNRs is drastically decreased compared to the pure A-SiNRs and A-GeNRs. With further increasing the length of the supercell, the phonon thermal conductance still decreases as shown in Fig. 3.22 (b).

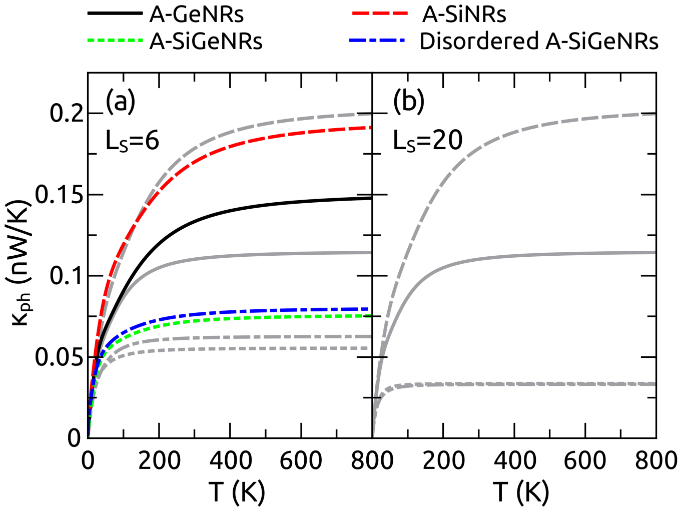

FIGURE 3.22: (Color) Phonon thermal conductance of various armchair nanoribbons with the ribbon width $W_A = 3$, where the supercell lengths L_S for A-SiGeNRs and disordered A-SiGeNRs are (a) $L_S = 6$ and (b) $L_S = 20$, respectively. The curves in color are calculated from *ab-initio* and the other curves in gray are calculated from tight-binding.

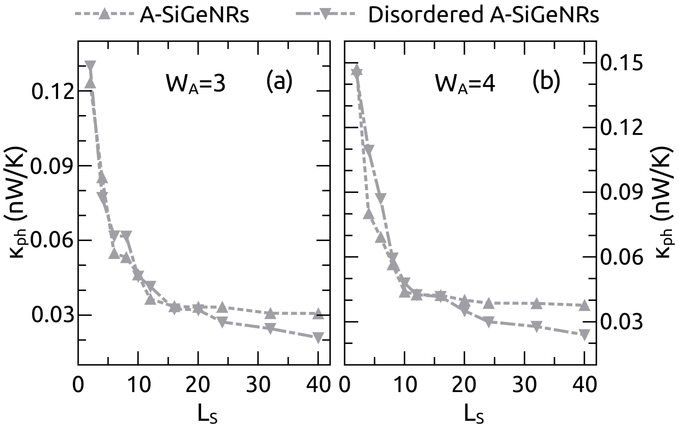

FIGURE 3.23: Phonon thermal conductance κ_{ph} at $T = 300$ K calculated from tight-binding as a function of supercell length L_S corresponding to the ribbon width (a) $W_A = 3$ and (b) $W_A = 4$, respectively.

In Fig. 3.23, the phonon thermal conductance at $T = 300$ K for both A-SiGeNRs and disordered A-SiGeNRs as a function of supercell length L_S is investigated, where L_S is defined as the sum of the lengths of silicene and germanene stripes. Because of the larger supercell size, here we employ the tight-binding method to calculate the thermal conductance. It can be seen that the phonon thermal conductance decreases largely with increasing the length of the supercell, and the decreased amplitude of κ_{ph} for both A-SiGeNRs and disordered A-SiGeNRs is close to each other. This indicates that the larger supercell in the silicene-germanene heterostructures can effectively constrain the phonon transport. Through checking the transmission probability, it is found that phonons gradually shift to the low frequency region (not shown).

3.2 Optimal figure of merit of SiGe core-shell nanowires [⋆]

3.2.1 Introduction

After the systematic studies of thermoelectric transport in the atomically thin 2D and 1D siliciene and germanene nanostructures, we put the attention here on the figure of merit of Si and Ge naonwires (NWs). It is well known that bulk Si is a poor thermoelectric material, while nanostructuring Si could possibly increase the figure of merit of this material [36, 44, 86–94]. Indeed, in a semiconducting nanostructure at room temperature, the electronic contribution to the thermal current around Fermi energy can be nearly neglected with respect to the lattice-vibrational contribution. In this way, confining or disrupting the lattice vibrations could lead to a reduction of the thermal conductance without a corresponding degradation of the electronic conductance due to the decoupling of degrees of freedom of electrons and phonons for ballistic transport. In this respect, Si NWs have been long studied as possible thermoelectric devices.

In the attempt to quench the phonon transport and then to improve the figure of merit, we propose the SiGe core-shell NWs and investigate how coating the Si NW with some Ge shells can influence ZT. Indeed, the presence of Ge shell creates an interface along the wire thus disrupting some of the vibrational modes. There is an optimal Ge shell depth after which the presence of the interface is not beneficial any more. We also investigate the case that the Ge NW is surrounded by Si atoms. We find that the figure of merit is a monotonously decreasing function of the radius of the NW. To further block the phonon transport, we consider the case in which the shell is an alloy of Si and Ge. We show that coating with such an alloy can increase the overall figure of merit. We find an empirical law that ZT follows by fitting the data. By changing the temperature, we find a relation between the band gap and the optimal working temperature at which ZT is maximized, verifying the Goldsmid-Sharp's rule. The results we present in this section are in good agreement with the experiment and we shall see later.

The theory we used for the calculations in this section is DFT and Landauer approach. We first use the VASP-code to calculate the band structures of electrons for the SiGe NW systems. Then we can extract the electronic transmission coefficient directly by counting the number of modes. Afterwards, one can obtain the electrical conductance, Seebeck coefficient, and electric thermal conductance easily using the theory we have described in chapter 2 or in Refs. [50, 95, 96]. For the phonon part, we discard the

---

[⋆] This section is a part of the article **Nano Res.** 8, 2611 (2015) by K. Yang, A. Cantarero, A. Rubio, and R. D'Agosta.

expensive and time-consuming DFT computations. Instead we employ the empirical Keating potential which has been shown in Sec. 3.1.5 to calculate the force constant and then we calculate the phononic transmission function as well as the lattice thermal conductance using the bosonic Green's functions [80, 97–101] as we have introduced in Sec. 2.5.

3.2.2 Details of electronic structure calculations

As to the prediction of electronic structural properties, we performed first-principle density functional theory calculations within the local density approximation by using the projector augmented wave potentials as implemented in VASP [73]. The exchange correlation energy is chosen in the form of Ceperley-Alder which has been parameterized by Perdew and Zunger [74, 75]. For the self-consistent potential and the total energy calculations, the **k**-points of the first Brillouin-zone are sampled by a $(15\times1\times1)$ Monkhorst-Pack grids. The kinetic energy cut-off for the plane wave basis set is chosen as 300 eV. We use a plane-wave representation of the wave-function which is most efficient with periodic boundary conditions. To avoid spurious interaction between the replica of the NW introduced by the periodic boundary conditions, we have included a vacuum gap larger than 13 Å in our supercell. We have therefore relaxed the ionic positions by minimising the forces and the total energy. After ionic relaxation, the force acting on each atom is smaller than 0.02 eV/Å. We have therefore calculated the electron energy bands, and the the structural stability of the NW is confirmed by checking the phonon dispersions.

3.2.3 Results and discussions

3.2.3.1 Geometries of SiGe nanowires

The geometrical structure of SiGe core-shell NW within a ball-stick representation can be seen in Fig. 3.24. Figure 3.24 (a) shows the clean Si or Ge core-shell NW, where we have either Si in the core and Ge in the shell, or vice-versa, Ge in the core and Si in the shell. Figure 3.24 (b) shows a NW with clean Si- or Ge-core but disordered shell where Si and Ge atoms are randomly distributed. The yellow and green could represent the Si or Ge atoms to build either Ge-core/Si-shell or Si-core/Ge shell NWs, respectively. The small grey balls on the NW surface represent hydrogen atoms which are used to passivate the unsaturated atomic-bonds. To denote the thickness of the NW, we introduce the parameters N_C (N'_C) to label the number of atomic layers in the Si-core (Ge-core) and N_S (N'_S) those in the Ge-shell (Si-shell). In the following we will adopt the notation of indicating the core atomic component before the shell component and separating them with a slash. Therefore a Si/Ge NW, is a nanowire with Si in the core and Ge in the shell. Analogously, a Si/SiGe NW has a core of Si and a shell of an alloy of Si and Ge.

To calculate the electronic energy bands, we first relax the structures by using density functional theory according to the methodology we have described above and in chapter 2 for details. The lattice constants we obtained are about 9.308 Å for Si NWs, 9.692 Å for Ge NWs, 9.4 Å for Si/Ge NWs and 9.6 Å for Ge/Si NWs, respectively, depending slightly on their diameters. These relaxed structural parameters are in agreement with those presented in some previous work [102, 103]. On the other hand, the atomic distances

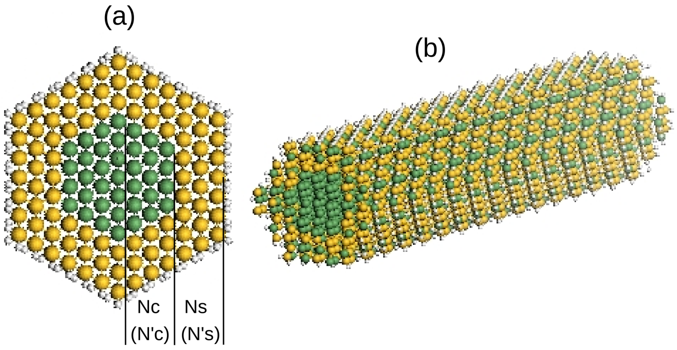

Figure 3.24: (Color) Schematic illustrations of (a) clean SiGe core-shell NW (top view) and (b) clean Si- or Ge-core but disordered SiGe-shell NW (tilted view). The yellow and green colors could represent either Si or Ge atoms. The grey atoms are hydrogen atoms used to saturate the dangling atomic-bonds at the surface. We have used N_C (or N'_C) and N_S (or N'_S) to indicate the thickness of core and shell layers, respectively, where for this particular case we have set $N_C = N_S = 3$.

between Si and Ge atoms depend on the NW diameter. For example, in considering clean Si/Ge NWs, after complete ionic relaxation the average SiSi distance for the smallest NW is equal to 2.33 Å, while the distance increases to 2.36 Å for the largest NW. Similar differences are observed for other interatomic distances (SiGe and GeGe) and other NWs. The diameters of the NWs we consider in the following range narrowly between 1 and 5 nm, varying with the number of layers in the core and in the shell.

3.2.3.2 Thermoelectric coefficients of pure Si and Ge nanowires

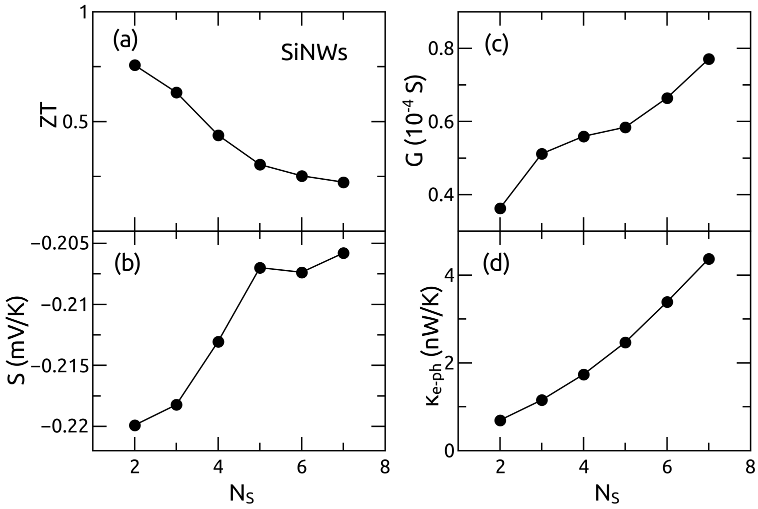

Figure 3.25: (a) Figure of merit, (b) Seebeck coefficient, (c) electrical conductance, and (d) total thermal conductance for pure Si NWs as a function of atomic layers N_S.

We first explore the thermoelectric properties of pure Si NWs. Figure 3.25 shows the thermoelectric coefficients as a function of atomic layers at room temperature. With increasing atomic layers, we can see from Fig. 3.25 (a) that the figure of merit decreases monotonously, while the Seebeck coefficient, electrical conductance and total thermal conductance increase with N_S [see Figs. 3.25 (b), (c) and (d)]. On the other hand, the absolute value of S actually decreases. Since we consider here only electron transport, the

Seebeck coefficient is negative according to the definition we have discussed in chapter 1. Therefore, the decreasing ZT can be attributed to the largely increased thermal conductance outweighing the increase of the electrical conductance.

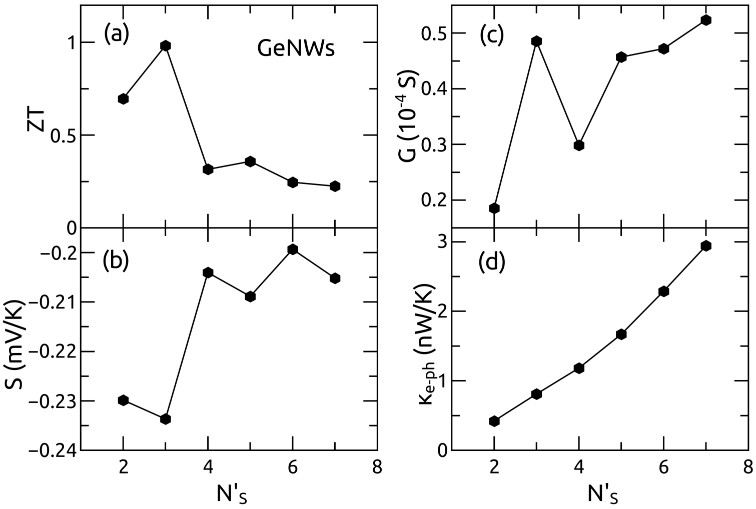

FIGURE 3.26: (a) Figure of merit, (b) Seebeck coefficient, (c) electrical conductance, and (d) total thermal conductance for pure Ge NWs as a function of atomic layers N'_S.

In Fig. 3.26 we investigate the thermoelectric properties of pure Ge NWs. Different from the Si NWs, we can see from Fig. 3.26 (a) that the figure of merit of Ge NWs increases at the beginning and then decreases with shell layer N'_S. This behavior can be understood from the Seebeck coefficient shown in Fig. 3.26 (b) and electrical conductance shown in Fig. 3.26 (c). The absolute value of S increases and the electrical conductance undergoes a sharp transition at $N'_S = 3$ varying from rising to ascending, although the thermal conductance increases slightly [see Fig. 3.26 (d)]. This shell layer dependent behavior of ZT for Ge NWs will impact the SiGe core-shell NWs as we will see in the following.

3.2.3.3 Figure of merit of clean SiGe core-shell nanowires

We explore here the thermoelectric properties of clean Si/Ge and Ge/Si NWs where Si and Ge atoms are arranged in a quasi-crystalline structure. Our results for the thermoelectric figure of merit ZT at room temperature are shown in Fig. 3.27. It can be seen that the figure of merit of the Si/Ge NWs increases initially and then decreases rapidly with the number of layers, N_S of the external shell. More interestingly, for these NWs the maximum ZT always appears at $N_S = 3$ whatever the N_C. The presence of the interface between the core and the shell localizes some of the vibrational modes thus reducing the total thermal conductance. On the other hand, the larger total cross section increases the electrical conductance bringing an increase of the figure of merit. For $N_S > 3$, however, the increase in the thermal conductance dominates again and the figure of merit is reduced. This behaviour is in striking contrast with that of the figure of merit of Ge/Si NWs which decreases monotonously with increasing the number of layers in the external shell. The largest figure of merits for Si/Ge and Ge/Si NWs are 1.117 at $N_S = 3$ and 1.582 at $N'_S = 1$, respectively. These values are much higher than that of pure Si and Ge NWs, where, by using the same steps as described above, we have obtained $ZT = 0.76$ for Si NW and $ZT = 0.98$ for Ge NW. With increasing the number of atomic layers in the core, the figure of merit generally decreases. This is due to the large increase of the phonon thermal conductance which outweighs the increase in the electrical conductance. Our results suggest that the best Si-based NW for thermoelectric application has a Si core covered by a thin layer of Ge.

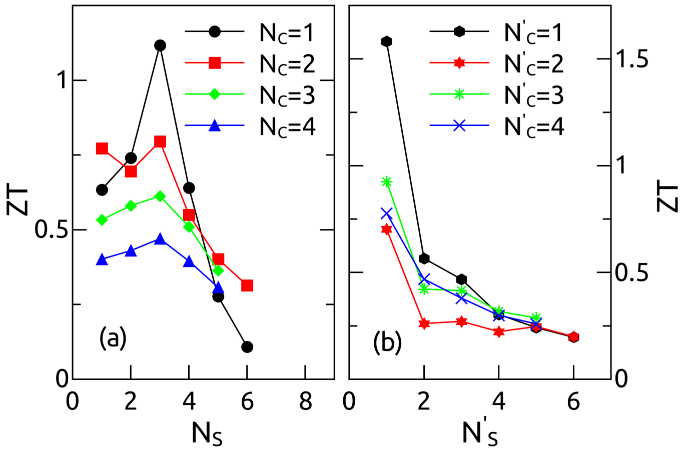

FIGURE 3.27: (Color) Thermoelectric figure of merit as a function of the number of atomic layers in the shell, N_S for (a) clean Si/Ge and N'_S for (b) clean Ge/Si NWs with different core sizes N_C and N'_C, respectively.

The thermoelectric behaviour of Si/Ge and Ge/Si NWs can be understood looking at their electron and phonon transport properties. We report them in table 3.3 for the case of a clean Si/Ge NW with core radius $N_C = 3$. For the other cases we get a similar behaviour of the transport coefficients. It can be seen from table 3.3 that the electrical conductance G for Si/Ge NWs increases very quickly with the radius N_S to reach a maximum value for $N_S = 4$, while the Seebeck coefficient does not show large variation oscillating around the value of 0.21 mV/K. Looking at the thermal transport coefficients, we can see that the phonon thermal conductance κ_{ph} keeps increasing with the number of shell layers due to the increased number of phonon modes which contribute to the heat energy transport.

TABLE 3.3: Electrical and thermal transport coefficients at the chemical potential for optimal ZT of the clean Si/Ge NWs with $N_C = 3$ for N_S between 1 and 5.

N_S	ZT	G (10^{-4} S)	S (mV/K)	κ_e (nW/K)	κ_{ph} (nW/K)
1	0.534	0.484	-0.21	0.145	1.06
2	0.58	0.588	-0.217	0.126	1.305
3	0.613	0.789	-0.2175	0.187	1.639
4	0.51	0.857	-0.216	0.201	2.14
5	0.364	0.83	-0.209	0.179	2.807

The electrical thermal conductance κ_e shows a non-monotonic behaviour, but in any case its value is about 10 times smaller than the phonon thermal conductance. It is important to point out that κ_e depends strongly on the value of the chemical potential μ. Here, we select the value that maximises the figure of merit ZT. In this system, the Wiedemann-Franz law is clearly not fulfilled for small diameters. This law is a phenomenological result, mostly valid for metal. The origin of this discrepancy can be understood via the Landauer theory of transport [50, 95]. Indeed, in this theory, κ_e is formed by two different contributions arising from different Lorentz integrals. For a metal, the Seebeck coefficient is nearly negligible, so this expression simplifies, leading to the Wiedemann-Franz law. For a semiconductor, the Seebeck coefficient is not small and we cannot expect a linear relation between the electrical and thermal conductances. Here again is the competition between the rapid increase in the electrical conductance G and the reduced growth of κ_{ph} that provides an optimal diameter for the shell in terms of the best figure of merit. By coating the NW with a thin layer of Ge, we have effectively reduced the rate of increasing of the thermal conductance with the NW radius. In the case of the Ge/Si NW, the electrical conductance does not show the same increasing trend, while the thermal conductance increase quickly with the number of Si layers in the shell, although these data are not reported here.

Our numerical calculations are in very good agreement with the experimental results, where the measured Seebeck coefficient at room temperature is about 0.22 mV/K for SiGe core-shell NWs [104]. Our thermal conductances are in qualitative agreement with the experiment [105], with the limit that the diameters of the NWs are quite larger than what we can reach with our numerical calculations, therefore making a direct quantitative comparison appears pointless at the moment.

3.2.3.4 Shell-disordered SiGe nanowires

Experimentally, fabricating NWs is unavoidably accompanied by some impurities. In addition, because these devices are meant for applications at finite, large temperatures (around 500 K), we investigate the NWs with pure Si or Ge-core and disordered SiGe shell in which Si and Ge atoms are randomly distributed. This might describe for example the diffusion of the atoms on the most external layer of the core into the layers of the shells, or some impurities present during the growing process. In this investigation, we have kept a 50/50 stoichiometric ratio between the total number of Si and Ge atoms present in the unit cell. This means that for a Si/SiGe, the shell is more rich in germanium, to compensate for the Si atoms in the core. To be accurate, we have performed the calculations for several different disordered geometrical structures by randomising the positions of Si and Ge atoms in the shell structures. In any case, a minimum of 5 different structures have been calculated. We have then considered the average over the realisation of the random positions. We report the values of the thermoelectric figure of merit ZT in Fig. 3.28: In the figure the vertical bar at each point indicates the range of variation of ZT with respect to the different realisation of the random structures.

It can be seen in Fig. 3.28 that the figure of merit for Si-core NWs increases at the beginning with the number of shell layers, and then decreases with further increasing N_S. Moreover, similarly to what happens in the clear Si/Ge NWs, there is always a peak of ZT around $N_S = 3$, and this value is independent of the number of the Si-core layers in the NWs. For Ge/SiGe NWs, ZT decreases gradually and monotonously with increasing the number of shell layers, regardless of the number of core layers.

Our numerical calculations can give access merely to small radius NWs. With the *ab-initio* techniques we are using, we are limited to a maximum system of 6 layers in the core and 6 layers in the shell. To understand what the thermoelectric properties are at the larger NW diameters, we have fitted the numerical data for the figure of merit. We have chosen

$$ZT = ZT_0 + A\mathrm{e}^{-2\left(\frac{D-D_C}{W}\right)^2}, \tag{3.7}$$

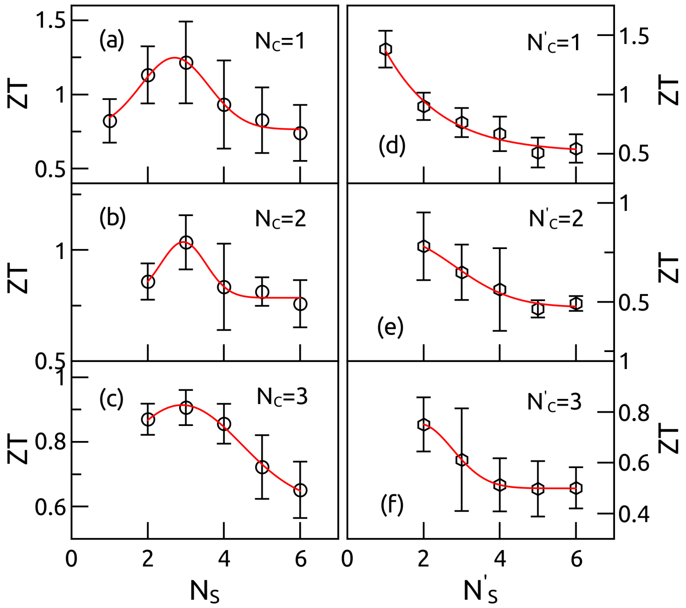

Figure 3.28: (Color) Thermoelectric figure of merit as a function of number of layers in the shell, (a-c) N_S for Si/disordered SiGe and (d-f) N'_S for Ge/disordered SiGe NWs at different core size N_C and N'_C, respectively. The vertical bars represent the range of variation of the figure of merit we have obtained from our calculations, and the solid lines represent the fitted curves [see Eqs. (3.7) for reference]. For each value of N_S or N'_S at least 5 different random structures have been calculated.

where ZT_0, A, W and D_C are then fitted against the available values of ZT. In Eq. 3.7, D is the total diameter of the NWs, ZT_0 will represent figure of merit in the limit of infinite diameter, W is an effective diameter, D_C an optimal NW diameter, and A the maximum amplitude of the figure of merit. The fitted parameters are shown in table 3.4 for Si core and Ge core/SiGe disordered NWs. The fit results allow the determination, for example, of ZT_0 for large diameter NWs. For Ge/SiGe disordered NWs, the parameters A, W, and D_C are quite sensitive to the number of points calculated. For now, a microscopic model does not exist that could justify Eq. (3.7) on a microscopic level.

Table 3.4: Fitted parameters of figure of merit ZT for both pure Si- and Ge-core with disordered SiGe shell NWs [explicit formula is presented in the text as Eq. (3.7)].

Si/disordered SiGe	ZT_0	A	W (nm)	D_C (nm)
$N_C = 1$	0.76±0.03	0.57±0.06	0.78±0.09	1.85±0.02
$N_C = 2$	0.79±0.03	0.25±0.05	0.43±0.09	2.46±0.06
$N_C = 3$	0.58±0.09	0.34±0.08	1.6±0.5	2.94±0.08
Ge/disordered SiGe	ZT_0	A	W (nm)	D_C (nm)
$N'_C = 1$	0.55±0.07	2.3±0.9	2.0±0.6	-0.4±0.5
$N'_C = 2$	0.47±0.03	0.5±1.4	1.5±2.0	1.2±2.8
$N'_C = 3$	0.498±0.004	0.4±0.2	1.2±0.4	1.7±0.5

The results we have presented address the case of having a global composition of 50% Si and 50% Ge in the whole structure. This implies that the shell contains a larger concentration of the species not in the shell. We have also investigated other case and different concentrations. Our results are in general good agreement with the one we have reported. Namely, the figure of merit is increased by the presence of a thin shell.

Moreover, a larger increase is achieved in the case of a Si core. We have reported the calculation for the figure of merit for an electron doped material or when the chemical potential is larger than the Fermi-energy. The figure of merit for holes, although sometimes larger than that for electrons in small diameter NWs, decays rapidly with increasing the diameter for both Si- and Ge-core NWs (results are not shown). We have considered disorder at a compositional level and we did not include any surface roughness or vacancies. These studies are left for future works.

3.2.3.5 Temperature effect on the figure of merit

So far the results we have presented were obtained at room temperature, $T = 300$ K. We examine in the following the effect of temperature on the thermoelectric figure of merit of SiGe core-shell NWs. Figures 3.29 (a) and (b) show ZT as a function of temperature for both clean and shell-disordered SiGe NWs, respectively. It can be seen that ZT shows a non-monotonic behaviour: There is an optimal working temperature T_C for the maximum efficiency [1]. When the temperature is below T_C, ZT increases almost linearly and then it decreases when $T > T_C$, a behaviour that has also been recently observed in experiment [106].

We attribute this behaviour to the bipolar effect. In the formulae for the electrical conductance, electronic thermal conductance and Seebeck coefficient, it enters the negative derivative of the Fermi-function with respect to the energy $f(E, \mu, T)$ [50, 95]. When the temperature is lower than T_C, the region of energies for which this negative derivative of the Fermi-function is not exponentially small is far from the valence band. The effective transport contribution to ZT comes mainly from the electron carriers in the conduction band. With increasing the temperature, $\partial f(E, \mu, T)/\partial E$ broadens gradually, and ZT also increases. When T is larger than T_C, the term $\partial f(E, \mu, T)/\partial E$ extends into the valence band. In this case, also the holes will start to contribute to the transport. Because the electrical conductance equals to the integral of the transmission probability times $-\partial f(E, \mu, T)/\partial E$ and G_0, where $G_0 = 2e^2/h$ is the quantized value of electrical conductance with e is the electron charge and h the Planck-constant (see Refs. [50, 95]), G would increase further. On the other hand according to the Wiedemann-Franz law [13] (although it is not fulfilled for NWs with small diameter), the electric thermal conductance κ_e will also increase, and the phonon thermal conductance κ_{ph} increases with T due to the phonon modes thawing. However, the Seebeck coefficient according to the derivation in chapter 2 is given by

$$S = \frac{2e}{ThG} \int_{-\infty}^{\infty} dE \mathcal{T}_e(E)(E - \mu) \frac{\partial f(E, \mu, T)}{\partial E}, \tag{3.8}$$

where $\mathcal{T}_e(E)$ is the electronic transmission probability at energy E. It can be seen from this relation that if $\partial f(E, \mu, T)/\partial E$ extends for energies going into the valence band, the value of $|S|$ is reduced since the integrand will have different signs around μ, thus reducing the power factor and the figure of merit. These results can be seen clearly in Fig. 3.30. Therefore the bipolar effect leads to the overall decrease of the figure of merit. Accordingly, the maximum ZT happens at the critical temperature T_C, when the electrons' response to the thermal gradient is not effectively neutralised by holes yet.

---

[1] We want to stress here that T_C is a working temperature. Since we are working in the linear response regime, the temperature gradient is negligible with respect to almost any other energy scale. In particular, the gradient is much smaller than the working temperature.

Furthermore through comparing Figs. 3.29 (a) and (b) we find that ZT of shell disordered SiGe core-shell NWs is much higher than that of the clean SiGe core-shell NWs. Indeed, the disorder in the shell largely suppresses the phonon transport, which can also be seen in Fig. 3.30.

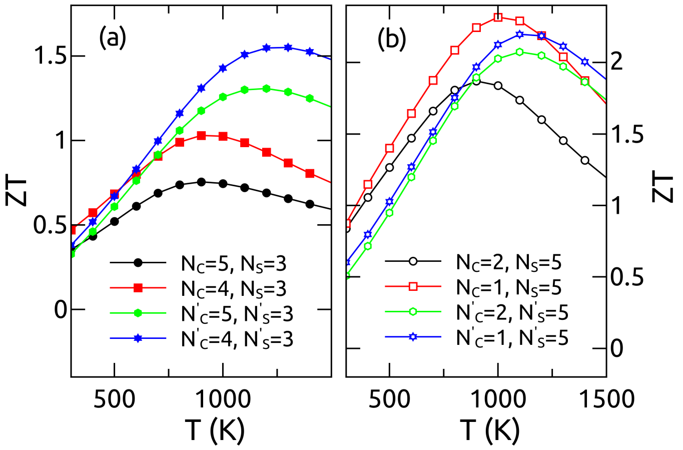

FIGURE 3.29: (Color) Thermoelectric figure of merit ZT as a function of temperature. (a) The ellipse in black and rectangle in red represent ZT of clean Si/Ge NWs with $N_C = 5$, $N_S = 3$ and $N_C = 4$, $N_S = 3$; the hexagon in green and star in blue represent ZT of clean Ge/Si NWs with $N'_C = 5$, $N'_S = 3$ and $N'_C = 4$, $N'_S = 3$, respectively. (b) The hollow ellipse and rectangle represent ZT of clean Si/disordered SiGe NWs with $N_C = 2$, $N_S = 5$ and $N_C = 1$, $N_S = 5$; the hollow hexagon and star represent ZT of clean Ge/disordered SiGe NWs with $N'_C = 2$, $N'_S = 5$ and $N'_C = 1$, $N'_S = 5$, respectively.

In Fig. 3.30, we plot the the electrical conductance G, Seebeck coefficient S, and thermal conductance κ_{e-ph}. It can be seen that G at low temperatures is almost constant and increases quickly when $T > 1000$ K. At the same time, the Seebeck coefficient has a minimum at about $800 - 900$ K. Indeed, for electrons, the minimum corresponds to a maximum for S^2. In the case of thermal transport, we can see that the total thermal conductance κ_{e-ph} increases slowly at the beginning and then increases quickly for $T > 1000$ K. On the other hand, the phonon thermal conductance κ_{ph} increases beginning with T, and then varies slowly approaching almost to a constant for $T > 600$ K [see the inset of Fig. 3.30]. Therefore for large temperatures, the ascending behaviour of κ_{e-ph} is dominated by the increase in the electronic thermal conductance.

In the range of temperatures we are considering here the Si/Ge and Ge/Si NWs are still stable against melting, since it has been predicted for them a melting temperature of about 2500 K (for Si NWs). To the best of our knowledge these results have not been yet confirmed by experiment.

To understand which factors dictate the transition temperature T_C in different systems, in Fig. 3.31 we plot the band gap E_g as a function of k_BT_C, where k_B is the Boltzmann-constant. We observe that for almost all the NWs we have considered in this section, there is a linear relation between E_g and T_C. We have therefore fitted E_g against

$$E_g = \Upsilon_0 + \Upsilon k_B T_C. \tag{3.9}$$

The values of Υ_0 and Υ from the fit can be found in table 3.5.

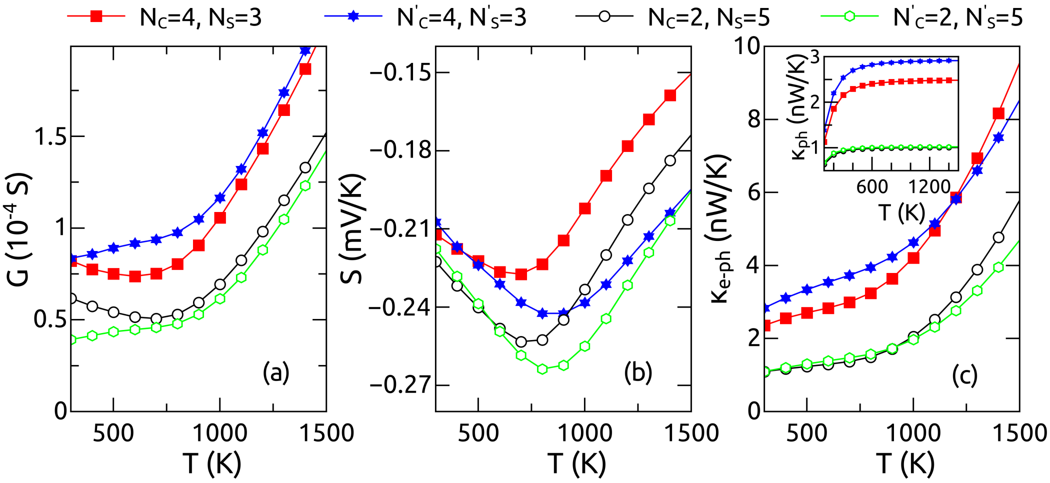

FIGURE 3.30: (Color) (a) Electrical conductance G, (b) Seebeck coefficient S and (c) total thermal conductance κ_{e-ph} as a function of temperature. The inset in (c) shows the corresponding phonon thermal conductance κ_{ph}. The curves with different symbols share the same structures as those in Fig. 3.29

TABLE 3.5: Fitted parameters of linear relation between E_g and k_BT_C in Fig. 3.31.

	Si/Ge	Ge/Si	Si/disordered SiGe	Ge/disordered SiGe
Υ_0 (eV)	-0.28±0.07	-1.4±0.3	-0.39±0.04	-0.94±0.13
Υ	10.9±0.6	17.2±2.7	13.2±0.4	17.0±1.2

In Fig. 3.31 the red and black solid lines are the linearly fitted curves for Si-core/clean Ge-shell and disordered SiGe-shell NWs, while the blue and green lines are the fitted curves for Ge-core/clean Si-shell and disordered SiGe-shell NWs, respectively. Interestingly, we found that the value of the slope Υ is essentially determined by the chemical element in the core: We calculated $\Upsilon \simeq 11$ for Si core NWs, and $\Upsilon \simeq 17$ for Ge-core NWs, independently of having a clean or disordered shell layer. This suggests an empirical method to determine the optimal working temperature for these NWs. It is sufficient to estimate or measure the electronic band gap, and then invert the linear relation in Eq. 3.9 to obtain T_C. As a rule-of-thumb, we found that $k_BT_C \simeq E_g/11$ for Si-core NWs ($k_BT_C \simeq E_g/17$ for Ge-core NWs) gives a good estimate of the optimal working temperature. In this way the thermoelectric enhancement due to the bipolar effect can thus be more easily realized in narrow band gap materials since there are many more carriers of both electrons and holes to contribute to the transport. This phenomenon was first observed in bismuth telluride [107]. Additionally we have also found that similar relations between the electronic band gap and the optimal working temperature for thermoelectric energy conversion exist in other materials, like for example monolayer molybdenum disulfide, silicene and germanene nanoribbons [96], though we didn't show here.

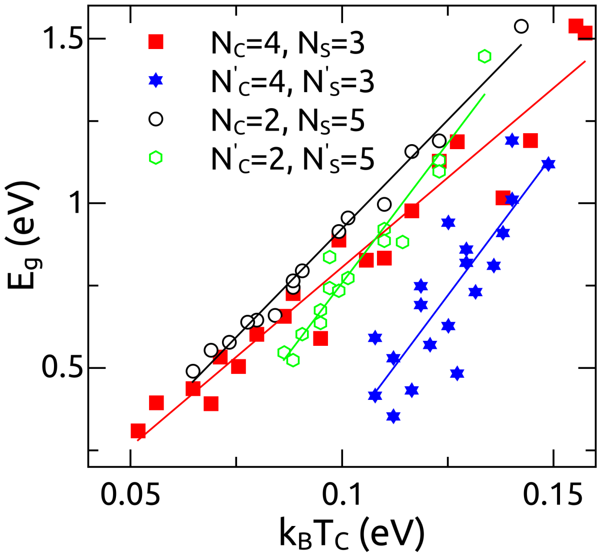

FIGURE 3.31: (Color) The electronic energy gap E_g versus the critical temperature k_BT_C for clean Si/Ge (rectangle) and Ge/Si NWs (star), Si/disordered SiGe (ellipse) and Ge/disordered SiGe NWs (hexagon). The red, blue, black and green lines are the linearly fitted curves.

3.3 Classical to quantum transition of heat transfer between silica nanoclusters *

3.3.1 Introduction

With the recent developments of nanotechnology, electronic devices continue to scale down in dimension and scale up in power density [108]. As a result, near-field radiation starts to play a notable role in the thermal design at nanoscales. Recently, it has been demonstrated both theoretically [109–114] and experimentally [115–117] that heat transfer through near-field radiation between two parallel plates or between a sphere and a plane can be several orders of magnitude larger than the black body limit over a limited range of frequency. This clearly corroborates the fact that when the gap between two objects is smaller than the characteristic photon wavelength, a different physical behavior emerges in which near-field radiation and phonon tunnelling significantly contribute to heat transfer [118, 119].

The first measurement of the radiative heat flux between two dielectric materials separated by a nanoscale gap distance has recently been performed by Narayanaswamy, Shen and Chen [115, 116]. Their results led them to conclude that the proximity-force approximation is not valid for near-field radiation heat transfer. Shortly after, Rousseau *et al.* [117] also measured the heat transfer in the near-field regime. Interestingly, and in contrast with Narayanaswamy's conclusions, these later results confirmed the proximity approximation. The difficulty in performing such experiments makes it probable that heat transfer at the nanoscale will continue to be debated, as commented by Kittel [120]. Near-field radiation under the dipole or multipole approximation has been extensively investigated on a theoretical basis. Nonetheless, mechanisms taking place for separation

---

[*] This section is a part of the article **Phys. Rev. Lett.** 112, 114301 (2014) by S. Xiong, K. Yang, Y. A Kosevich, Y. Chalopin, R. D'Agosta, P. Cortona, and S. Volz.

distances shorter than 10 nm remain unclear. This range of separation distances may not be directly accessible by experiments due to the difficulty in fabricating well-defined planes and spheres at those scales. At the same time, as modern nanostructures might be smaller than 10 nm and are separated in some cases by only a few fractions of a nanometer, this range of lengths is of great interest to those who design nanoscale devices [1, 120]. From a fundamental point of view, this domain is also involving the less understood transition from a classical charge-charge interaction, logically described as a radiation in the near-field, to a chemical bond interaction, yielding pure heat conduction.

By means of molecular dynamics simulations, Gilberto *et al.* [121] found a transition regime characterized by a thermal conductance larger than the contact thermal conductance. But the largest value exceeded the upper physical limit. Using ultra-high vacuum inelastic scanning tunnelling microscopy, a previously unknown mechanism of thermal transport (a field-induced phonon tunnelling) has been reported by Altfeder *et al.* [122]. The thermal energy transmitted through atomically narrow vacuum gap exceeds, by ten orders of magnitude, the one of black body thermal radiation. In fact, before these experimental findings, Kosevich [118] and Prunnila *et al.* [119] modelled how acoustic phonons can directly tunnel through vacuum by introducing a coupling mechanism, and both of them showed that phonons can travel through the vacuum gap with unitary transmission and thus can lead to significant thermal conductance and heat flux. Very recently, Chiloyan *et al.* [123] developed an atomistic framework based on microscopic Maxwell's equations and lattice dynamics to describe the convergence of heat transfer and the transition from near field radiation to phonon heat conduction. For gaps > 1 nm, they found the predicted conductance values are in good agreement with the continuum theory of fluctuating electrodynamics. However, for sub-nanometre gaps or near contact, the conductance is enhanced up to four times compared with the continuum approach due to the low-frequency acoustic phonons tunnelling through the vacuum gap.

In this section, we estimate the heat transfer through a chain composed by identical non-contacting silica nanoclusters by means of the phonon NEGF approach as we have discussed in chapter 2. We show that there are two critical vacuum gaps of about 4 Å and 3-5 times the cluster size. The first critical gap of 4 Å corresponds to a transition between the classical and the quantum regimes with strong interaction. Above this critical gap, *i.e.*, 4 Å, the thermal conductance decreases first according to a d^{-3} power law and then gradually changes to d^{-6} power law when the gap is larger than 5 times the cluster size. These power laws can be explained by classical charge-charge and dipole-dipole interactions, respectively. Below 4 Å, the thermal conductance shows a much stronger dependence on the gap thickness. The first critical gap is confirmed by *ab-initio* calculations showing that the electronic wave functions indeed merge when the gap becomes shorter than 4 Å.

3.3.2 Silica nanoclusters and computational details

We consider a periodic system composed of identical silica nanoclusters. The supercell length of the structure is denoted by d. Between two adjacent clusters there is a vacuum gap with distance l (see Fig. 3.32). A schematic illustration can be found in Fig. 3.32. We regard one cluster as the reference system and the clusters on its left and right sides as reservoirs. Since we are focused on the linear response regime, the temperatures T through the system are uniform. Then the thermal conductance for this quasi-one dimensional system is derived from the energy transmission coefficient $\mathcal{T}_{ph}(\omega)$ [50, 100, 124], *i.e.*,

$$\kappa_{ph}(T) = \frac{1}{2\pi}\int_0^{\omega_{max}} \mathcal{T}_{ph}(\omega)\frac{\partial}{\partial T}\left(\frac{1}{e^{\hbar\omega/k_BT}-1}\right)\hbar\omega d\omega, \tag{3.10}$$

where ω and ω_{max} are the phonon energy and the Debye frequency, respectively, k_B and $\hbar$ represent the Boltzmann and the reduced Planck's constants. The transmission coefficient $\mathcal{T}_{ph}(\omega)$ is obtained from the phonon Greens function approach as we have introduced in chapter 2:

$$\mathcal{T}_{ph}(\omega) = \mathrm{Tr}\left\{\Gamma_L\mathcal{G}^r(\omega)\Gamma_R[\mathcal{G}^r(\omega)]^\dagger\right\}, \tag{3.11}$$

where the retarded Green function can be deduced from

$$\mathcal{G}^r(\omega) = \left[(\omega+i\zeta)^2 - K_C - \Sigma_L - \Sigma_R\right]^{-1}, \tag{3.12}$$

where ζ is an infinitesimal positive value that maintains the causality of the Green's function, $\Sigma_L = K_{CL}g_L^rK_{LC}$ and $\Sigma_R = K_{CR}g_R^rK_{RC}$ are the self-energies of the left and the right leads, respectively, and the line width functions in Eq. (3.11) are defined as $\Gamma_L = i(\Sigma_L-\Sigma_L^\dagger)$ and $\Gamma_R = i(\Sigma_R-\Sigma_R^\dagger)$, g_L^r and g_R^r refer to the retarded Green's functions of the left and the right leads. K_C in Eq. (3.12) is the force constant matrix of the cluster, K_{CL} and K_{CR} are the coupling matrices between the clusters.

To calculate the Green's function, first we have to know the force constant matrix K. To do so we employ the van Beest, Kramer, and van Santen (BKS) potential [125], which can be expressed as

$$V_{ij} = q_iq_j/R_{ij} + A_{ij}\mathrm{e}^{-b_{ij}R_{ij}} - c_{ij}/R_{ij}^6, \tag{3.13}$$

where V_{ij} is the interaction energy of atoms i and j, which consists of a Coulomb term and a covalent contribution. In Eq. (3.13), q_i and q_j are the effective charges, R_{ij} is the inter-atomic distance, A_{ij}, b_{ij}, and c_{ij} are the fitted parameters as shown in table 3.6. The BKS potential provides the full physical picture of the long range electromagnetic and the short range repulsive-attractive interactions.

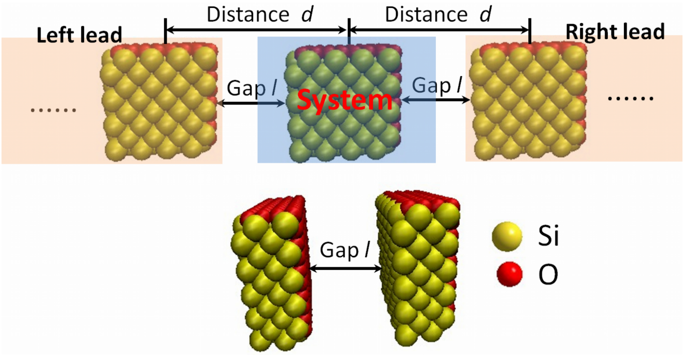

FIGURE 3.32: (Color) Schematics of the silica nanoclusters considered in the Greens function (top) and in the *ab-initio* (bottom) calculations. For the Greens function calculation, we use a cubic SiO_2 cluster with size $N \times N \times N$. For the *ab-initio* calculation, we use two parallel silica planes separated by a gap distance l. The lattice constant of SiO_2 is 4.52 Å.

On the other hand, according to the fluctuation-dissipation theorem, the thermal conductivity for the molecular dynamics simulation is calculated from the Green-Kubo

TABLE 3.6: Fitted parameters of BKS potential in Eq. (3.13).

$i-j$	A_{ij} (eV)	b_{ij} (Å^{-1})	c_{ij} (eV Å^6)	q_i (e)
$O-O$	1388.773	2.76	175.0	$q_O=-1.2$
$Si-O$	18003.7572	4.87318	133.5381	$q_{Si}=2.4$

formula, which is given by [126, 127]

$$\lambda_{ph} = \frac{1}{3k_B V T^2}\int_0^\infty \langle \mathbf{J}(0)\cdot\mathbf{J}(t)\rangle dt, \tag{3.14}$$

with

$$\mathbf{J} = \Big[\sum_i \varepsilon_i \mathbf{v}_i + \frac{1}{2}\sum_{\substack{i,j\\ i\neq j}}(\mathbf{F}_{ij}\cdot\mathbf{v}_i)\mathbf{R}_{ij}\Big], \tag{3.15}$$

where V represents the volume of the simulated supercell, $\mathbf{J}(0)$ and $\mathbf{J}(t)$ are the autocorrelation functions of heat flux, and t is the time. ε_i in Eq. (3.15) is the energy associated with atom i, $\mathbf{R}_{ij}=\mathbf{R}_i-\mathbf{R}_j$ is the displacement vector, and $\mathbf{F}_{ij}$ is the force exerted on atom i by atom j. $\mathbf{v}_i$ is the velocity vector of atom i. This formalism has been implemented in the LAMMPS-code and in the following we will use the code directly to calculate the thermal conductivity and accordingly the thermal conductance by $\kappa_{ph}=A\lambda_{ph}/L$, where A is the cross-section area and L is the length of the considered system.

3.3.3 Thermal conductance calculations and analyses

3.3.3.1 Lattice thermal conductance

The thermal conductance κ_{ph} for the quasi-one dimensional nanostructures obtained from Eq. (3.10) is reported in Fig. 3.33. We can see that the thermal conductance decreases very quickly with distance d in the short gap range. The power law in this range is estimated to be about d^{-12} and the absolute value of the power slightly increases with the increase of the particle diameter D. The thermal conductance per unit cross-section indeed increases with cross-section as the number of interacting pairs per atom increases. This latter number becomes larger at short distances and leads to a slight growth of the absolute exchanged power. This growth should however saturate to a maximum value as the number of interacting pairs per atom also saturates, but this limit remains beyond the maximum size under consideration here.

In the intermediate distance range, the thermal conductance decrease with distance turns to be smoother and follows the power law d^{-3}, which is expected in the framework of the non-piezoelectric interactions [118]. Silicon and oxygen atoms form a dipole as shown in the inset of Fig. 3.33 and each particle can be regarded as one macroscopic dipole, with bound charges of opposite sign at front and rear surfaces. When the distance between two nanoclusters is comparable with cluster size, the force between surface charges is proportional to A_2/d^2, where A_2 is the surface area of cluster 2. According to our previous model, the transmission of acoustic phonons through a vacuum gap can be written as

$$|\mathcal{T}_{aph}|^2 = \frac{1}{1+(\omega/\Omega)^2}, \tag{3.16}$$

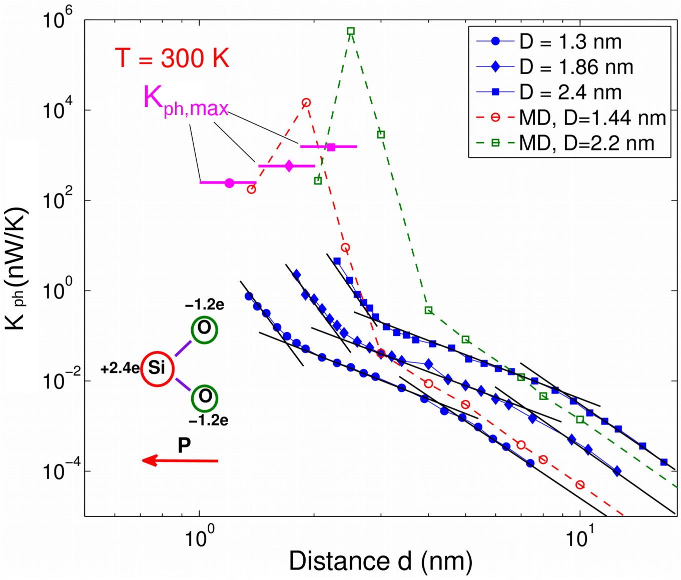

FIGURE 3.33: (Color) Thermal conductance κ_{ph} between two neighboring nanoclusters at $T = 300$ K for different cluster sizes versus the distance d indicated in Fig. 3.32. In our calculations, the cluster is a cube $N \times N \times N$ unit cells in volume. The diameter D is set in such a way that the sphere volume is equivalent to that of the simulated cube. The distance d is used as the abscissa instead of the gap distance l in order to discriminate the curves otherwise superimposed. The molecular dynamics (MD) results are taken from Ref. [1], where the same BKS potential parameters as those adopted in this work were used.

where Ω represents the effective width of the acoustic phonon pass band through the gap; Ω is proportional to the modulus of the derivative of the force per unit surface area with respect to the gap width, and as a result, $\Omega \propto A_2/d^3$. The total thermal conductance is given by the integral of the transmission over all frequencies times the surface area of cluster 1 A_1, and is proportional to $A_1\Omega$ and, hence is characterized by the scaling A_1A_2/d^3. This means that the thermal conductance in this range of distance d is performed mainly by acoustic phonons, which is in agreement with our results obtained from Greens function. Interestingly, the slope transition in the log scale occurs at the same gap distance $l = 4$ Å whatever the cluster diameter D.

When the gap distance increases further, *i.e.*, the distance between two neighboring clusters becomes much larger than the particle size, the energy transfer between two clusters is performed by optical phonon exchange through dipole-dipole interaction [121], following the Foerster energy transfer with a $1/d^6$ decay law [128]. The transition from charge-charge to dipole-dipole interaction occurs smoothly when d is around 3 to 5 times the cluster size. Furthermore, we also found that in charge-charge interaction region, the thermal conductance at a given gap width l follows a $D^{3.85}$ acaling law, while in the dipole-dipole interaction range, the thermal conductance varies with diameter according to $D^{6.5}$ for a given center of mass distance d. These findings further confirmed our proposed mechanism of surface charge-charge and volume dipole-dipole heat transfer, since the total thermal conductance is proportional to the product of clusters surface area A_1A_2, that is, to $D_1^2D_2^2/d^3$ for surface charge-charge interaction, while the thermal conductance is proportional to the product of clusters volume V_1V_2, that is, $D_1^3D_2^3/d^6$ for volume dipole-dipole interaction.

To validate our predictions, molecular dynamics (MD) simulation results as taken from Ref. [1] are plotted in Fig. 3.33 for comparison. A clear agreement between MD and Greens function predictions appears in the long distance range. But there is no intermediate region in MD predictions and the thermal conductance from Greens function is several orders of magnitude smaller than the one yielded from MD in the small gap range. Also in contrast to MD simulations, no thermal conductance decrease is found right before the contact in our Green's function calculations. Instead, the thermal conductance increases continually with the gap decrease. In fact, the maximum thermal conductance before contact predicted by MD simulations exceeds the physical upper-limit $\kappa_{ph,max}$ as shown in Fig. 3.33. This limit is calculated from the maximum energy $3Nk_B(T_1 - T_2)$ possibly transferred between two neighbor clusters of N atom each, set to temperature T_1 and T_2. Considering the fastest transfer characterized by the highest mode frequency ω_{max}, the maximum thermal conductance is obtained as $\kappa_{ph,max} = 3Nk_B\omega_{max}$. The MD predicted thermal conductance just before the contact is one or two orders of magnitude larger than the maximum value while the NEGF predictions give estimations below this limit.

3.3.3.2 Electronic density analysis

To understand the origin of the change in the dependence of the thermal conductance to the distance d, we performed *ab-initio* calculations (ABINIT-code) of the electronic densities for two silica planes schematically shown in the below panel of Fig. 3.32 and separated by vacuum gaps ranging from 0 to 6 Å. As each plane consists of a $1 \times 1 \times 2$ supercell, the two cells' axes are perpendicular to the interacting surfaces. Each unit cell contains twelve atoms and the simulation box includes four cells and 48 atoms. Experimental data for the atomic positions are used and the xc interaction is treated within the generalized gradient approximation with the Perdew-Burke-Ernzerhof functional [129]. Fritz-Haber Institute pseudopotentials [130] are adopted for Si and O atoms. The cut-off energy is set to 820 eV and the k-grid size to $4 \times 4 \times 1$.

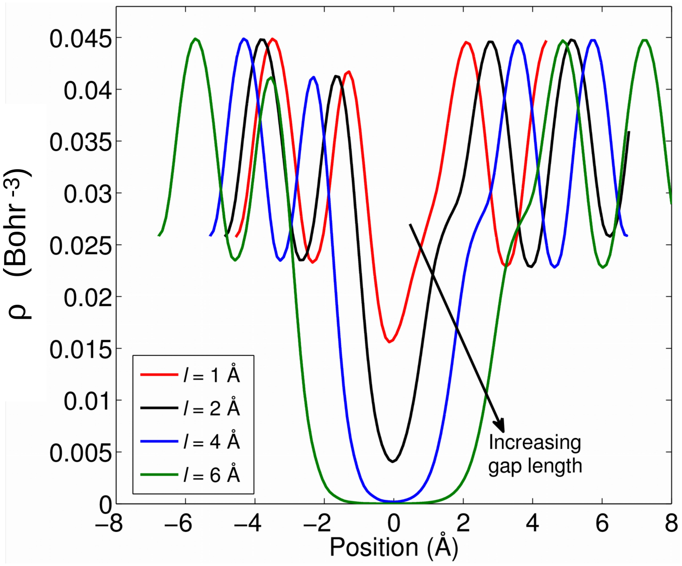

Figure 3.34: (Color) *Ab initio* computation of the electronic density ρ generated by two parallel silica films separated by different gap widths.

As revealed by Fig. 3.34, the electron density is non-zero in the middle of the gap, when the gap is smaller than 4 Å but decreases rapidly as the gap widens from 0 to 4 Å. The electron density reaches zero in the middle of the gap when l increases beyond 4 Å and the zero electron density domain extends when further increasing the gap. This indicates that the electron wave functions of both sides actually overlap in the short gap range when $l < 4$ Å to form a bond. In this region, the atoms of both sides are connected through a single electronic wave function instead of interacting through electromagnetic forces relating two separated wave functions. Beyond 4 Å, near-field radiative heat transfer can be described by Maxwell's equations while the quantum Schrödinger equation has to be considered when $l < 4$ Å. Since the bonds between atoms in silica nanoclusters are covalent, we call the bond at the contact as *pseudo-covalent*. With the formation of those latter bonds, the force between two neighbors dramatically increases beyond the force produced by electromagnetic waves. As a result, heat transfer shifts from radiative to conductive, also leading to a slope change of the thermal conductance in the small gap range.

3.3.3.3 Phonon transmission coefficient

To check the relative contribution of acoustic and optical phonons to heat conduction, we now turn to our previous modeling of the transmission of acoustic phonon modes through a vacuum gap as shown in Eq. (3.16). Since Ω represents the effective width of the acoustic phonon pass-band through the gap and it is proportional to the derivative of the force between clusters with respect to the gap width, it decreases with the increase of gap width. Consequently, the acoustic phonon cut-off frequency decreases when the gap widens and the frequency range of allowed transmission converges to zero.

Figure 3.35 reports the cumulative transmission coefficient from one cluster to its neighbor as a function of frequency and distance l. The cumulative transmission function increases continuously for the smallest gap of 1 Å (black line), reflecting a continuous dependence of the transmission to frequency. The continuous decrease of the transmission as the frequency Ω reduces to zero reveals that the modes involved are indeed acoustical ones.

When the gap width is slightly increased from 1 Å to 4 Å, the cumulative transmission function dramatically decreases and includes both a continuum at low frequencies and a set of jumps due to a discrete transmission at higher frequencies as highlighted by the inset of Fig. 3.35. In qualitative agreement with the model of Eq. (3.16), widening the gap indeed results in a decrease of the acoustic frequency pass band, which uncovers the presence of optical contributions appearing as peaks in the transmission spectrum. A careful analysis of our data shows that the frequency range of the acoustic phonons continuum reduces to zero as the gap width reaches 5 times the particles size and it accomplishes most of the heat transfer when the gap width is smaller than 3 times the particle size. The discrete set of modes also progressively disappear when the gap width is further increased and only the modes related to the force constants of long range interactions remain when the gap is enlarged and those also gradually disappear as those long range interactions vanish.

By considering the phonon-induced interactions of the gap edges, Kosevich [118] and Prunnila and Meltaus [119] have shown independently that acoustic phonons could transmit energy between separated bodies by tunnelling through vacuum gap, which

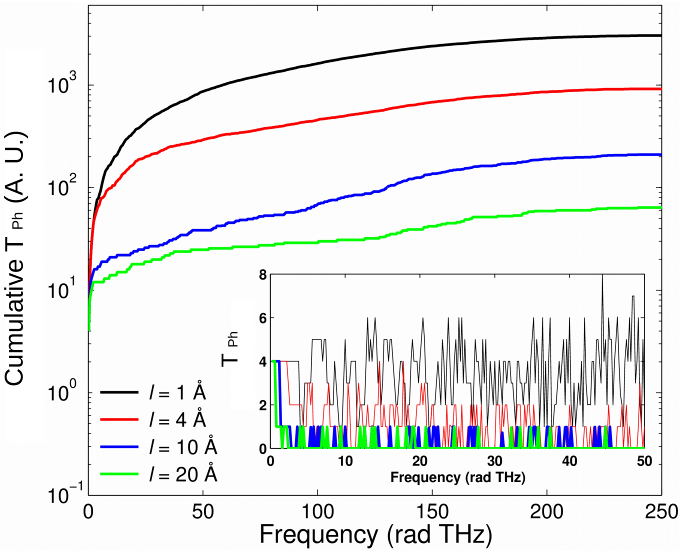

FIGURE 3.35: (Color) Angular frequency dependent cumulative phonon transmission coefficient $\mathcal{T}_{ph}$ for different gap distance l in the cluster of diameter D=1.3 nm. Inset: phonon transmission function versus angular frequency at low frequencies.

can lead to a significant thermal conductance enhancement and which is consistent with our findings. Accordingly, Altfeder *et al.* [122] observed phonon tunnelling from a sharp STM tip to a gold film at a vacuum gap distance of 3 Å. They have claimed that the tunnelling effect is driven by surface electronic-acoustic-phonon interactions. This result supports our argument stating that acoustic phonons are predominant in the phonon tunnelling through small gaps.

Chapter 4

Theory of thermoelectric coefficients and its application in the Coulomb blockade regime [⋆]

4.1 Introduction

In the previous chapter, we have utilized DFT combined with LB formalism (LB-DFT) to calculate the thermoelectric coefficients in the Si-Ge nanomembranes and nanowires as well as in the silica nanoclusters. LB-DFT is a method that is popularly used to investigate the transport properties of materials in the ballistic regime [32, 95]. However, an incautious use of LB-DFT in a confined quantum system as guide to material selection may point in the wrong direction. In fact, LB-DFT is unable to capture the ubiquitous CB phenomenon of quantum devices weakly coupled to leads, thereby overestimating the conductance [131] and, as we shall see, underestimating the Seebeck coefficient. In Refs. [131–133] it was shown that the erroneous high conductance at the particle-hole symmetric point predicted by LB-DFT stems from neglecting xc corrections to the bias [134–138]. According to a recently proposed DFT framework for thermal transport (and thus for the calculation of the Seebeck coefficient) [139, 140], xc corrections to the temperature gradient are also expected to occur.

In this chapter, we investigate the thermoelectric coefficients for quantum devices in the CB regime. We first show the analytical properties of density, conductance and Seebeck coefficient in the limit of coupling between the quantum dot (QD) and the lead goes to zero for single level system. Moreover, an *exact* expression of Hxc potential for this isolated single site is derived by reverse engineering procedure. We then show how to cure the KS conductance and Seebeck coefficient. Following a recent idea on the construction of xc corrections to the conductance [131], we propose an alternative DFT approach to the Seebeck coefficient well suited for quantum devices in the CB regime. We find a very simple xc correction to the LB-DFT Seebeck coefficient in terms of static DFT quantities. To illustrate the theory we consider the single impurity Anderson model, a paradigm for the CB effect [141, 142], and subsequently extend the analysis to multiple level systems. The proposed equations are validated by benchmarking the results against

---

[⋆] This chapter is a part of the article **Phys. Rev. Lett.**, (2016) (in review) by K. Yang, E. Perfetto, S. Kurth, G. Stefanucci, and R. D'Agosta.

those of the MB and the RE [39–41] calculations, demonstrating the crucial role of the xc correction. Finally, we apply the theory to single-wall carbon nanotubes and find good qualitative agreement with experiment.

4.2 Hamiltonian of the interacting system

Let us consider a system that includes a finite-sized QD which is coupled weakly to two semi-infinite leads. A schematic illustration of the system can be seen in Fig. 4.1. The two leads are metallic electrodes in which electrons are non-interacting, while for the QD, electrons are correlated and energy levels are discrete. The Hamiltonian of the MB interacting system is given by

$$\begin{aligned}\hat{H} = &\sum_{\mathbf{k},\alpha} \epsilon_{\mathbf{k}\alpha} \hat{c}^{\dagger}_{\mathbf{k}\alpha} \hat{c}_{\mathbf{k}\alpha} + \sum_{m} (\varepsilon_m + v_{\text{ext}}) \hat{d}^{\dagger}_m \hat{d}_m + \frac{1}{2} \sum_{m,n} U_{mn} \hat{d}^{\dagger}_m \hat{d}^{\dagger}_n \hat{d}_m \hat{d}_n \\ &+ \sum_{\mathbf{k},\alpha,n,} (\Gamma_{\mathbf{k}\alpha,n} \hat{c}^{\dagger}_{\mathbf{k}\alpha} \hat{d}_n + h.c.).\end{aligned} \tag{4.1}$$

For the KS system, the Hamiltonian is

$$\begin{aligned}\hat{H}_S = &\sum_{\mathbf{k},\alpha} \epsilon_{\mathbf{k}\alpha} \hat{c}^{\dagger}_{\mathbf{k}\alpha} \hat{c}_{\mathbf{k}\alpha} + \sum_{m} (\varepsilon_m + v_{\text{ext}} + v_{\text{Hxc}}) \hat{d}^{\dagger}_m \hat{d}_m \\ &+ \sum_{\mathbf{k},\alpha,n,} (\Gamma_{\mathbf{k}\alpha,n} \hat{c}^{\dagger}_{\mathbf{k}\alpha} \hat{d}_n + h.c.),\end{aligned} \tag{4.2}$$

where $\alpha = L, R$ represents the left (L) and right (R) leads, $\hat{c}^{\dagger}_{\mathbf{k}\alpha}$ and $\hat{c}_{\mathbf{k}\alpha}$ are the creation and annihilation operators in the leads for the state $\mathbf{k}$, $\hat{d}^{\dagger}_m$ and $\hat{d}_m$ are the creation and annihilation operators in the QD for the state m, $\epsilon_{\mathbf{k}\alpha}$ is the electronic energy dispersion of the leads, and ε_m describes the discrete energy levels of the QD. U_{mn} in Eq. (4.1) describes the interaction strength depending on the specific quantized energy levels, and v_{Hxc} in Eq. (4.2) represents the Hxc potential which is chosen such that the KS density is exactly the same as the one of the MB interacting system.

In the above two equations, we have used $\Gamma_{\mathbf{k}\alpha,m}$ to denote the coupling between the lead α and the QD, and v_{ext} to denote the external potential which can be, for example, the gate voltage applied on the QD. Comparing Eqs. (4.1) and (4.2) with Eq. (2.66) in chapter 2, we find that the only difference in Eq. (4.1) is the additional external potential v_{ext} applied on the QD, and for the KS system there is an additional term $v_{\text{ext}} + v_{\text{Hxc}}$ but no interaction term in the Hamiltonian. Therefore, one can derive the electric and heat current formulas in a very similar process as we have done in chapter 2. We skip the step-by-step derivation here and instead only show the final expressions in the following discussions.

4.3 Theory of thermoelectric coefficients for single level system

In this section we analyse the electrical conductance G and Seebeck coefficient S for strongly interacting electrons in the CB regime. The interacting G and S can be derived

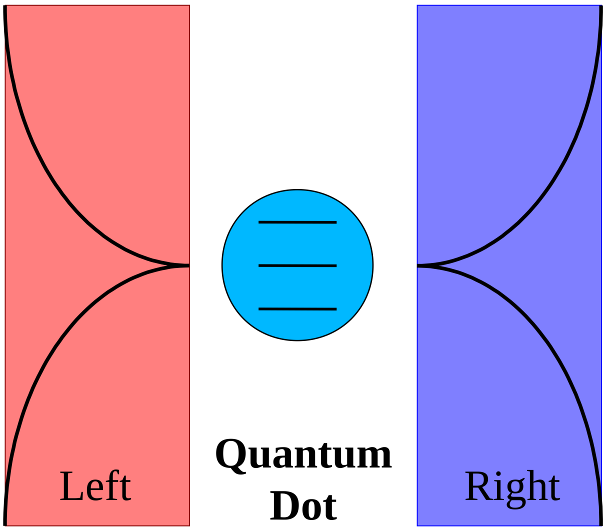

Figure 4.1: (Color) A schematic illustration of a finite-sized QD weakly coupled to two metallic leads, where the band width of the two leads are assumed to be much larger than the energy scale of the QD.

from the electric current by using the MB Hamiltonian [see Eq. (4.1)] and more information can be found in chapter 2. For the KS conductance G_S and Seebeck coefficient S_S, one can derive them based on the Hamiltonian of Eq. (4.2). For simplicity we shall start from a single level model system, and then we extend the theory to the multiple level systems.

4.3.1 Analytical properties for quantum dot weakly coupled to leads

Before we discuss the numerical results, let us first focus on the analytical properties of density, electrical conductance, and Seebeck coefficient in the limit $\gamma \to 0$, where γ describes the coupling between the dot and the lead. We have approximated $\Gamma(\varepsilon) = \gamma$ by taking into account the metallic electrodes in which the band-width of the lead is much larger than the energy scale of the QD, where γ is an energy independent constant and owns a real value. This approximation is called the wide-band limit approximation (WBLA) [30]. In this approximation we can express the line width functions of the leads as

$$\Gamma_L = \Gamma_R = \frac{\gamma}{2}, \tag{4.3}$$

accordingly the retarded self energies, based on the definition of chapter 2, are

$$\Sigma^r_L = \Sigma^r_R = -\frac{i}{4}\gamma, \tag{4.4}$$

where we assumed the QD is coupled equally to the left and right leads. The real part of Σ^r goes to zero within the WBLA and for the detailed explanation one can find in Ref. [30]. Using the above Hamiltonian of Eq. (4.1) and following the derivation we have shown in chapter 2, the electric current within the WBLA can be written as

$$J = \frac{i\gamma}{2} \int_{-\infty}^{\infty} \frac{d\varepsilon}{2\pi} \left[f_L(\varepsilon) - f_R(\varepsilon) \right] \left[\mathcal{G}^r(\varepsilon) - \mathcal{G}^a(\varepsilon) \right], \tag{4.5}$$

where $f_L(\varepsilon)$ and $f_R(\varepsilon)$ are the Fermi-Dirac distribution functions of the left and the right reservoirs, respectively. $\mathcal{G}^r(\varepsilon)$ and $\mathcal{G}^a(\varepsilon)$ are the retarded and the advanced Green's functions, respectively. For simplicity we have set $e = \hbar = 1$. For the KS system, one can simply replace the MB Green's functions with the KS Green's functions $\mathcal{G}_S^r$ and $\mathcal{G}_S^a$ to get the the current J_S, *i.e.*,

$$J_S = \frac{i\gamma}{2} \int_{-\infty}^{\infty} \frac{d\varepsilon}{2\pi} [f_L(\varepsilon) - f_R(\varepsilon)] \left[\mathcal{G}_S^r(\varepsilon) - \mathcal{G}_S^a(\varepsilon)\right]. \tag{4.6}$$

The retarded Green's function in Eq. (4.5) for the interacting system is

$$\begin{aligned} \mathcal{G}^r(\varepsilon) &= \frac{1-\rho/2}{\varepsilon - v - \Sigma_L^r - \Sigma_R^r} + \frac{\rho/2}{\varepsilon - v - U - \Sigma_L^r - \Sigma_R^r} \\ &= \frac{1-\rho/2}{\varepsilon - v + i\gamma/2} + \frac{\rho/2}{\varepsilon - v - U + i\gamma/2}, \end{aligned} \tag{4.7}$$

and for the KS system it is

$$\mathcal{G}_S^r(\varepsilon) = \frac{1}{\varepsilon - v - v_{\text{Hxc}} - \Sigma_L^r - \Sigma_R^r} = \frac{1}{\varepsilon - v - v_{\text{Hxc}} + i\gamma/2}, \tag{4.8}$$

where v and U are the external potential and charge energy, respectively. For the sake of clarity, we have omitted the subscripts [see Eqs. (4.1) and (4.2)]. The detailed derivation of the MB Green's function $\mathcal{G}^r$ can be found in appendix B. Using these Green's functions, we define two spectral functions for the MB and KS systems:

$$\begin{aligned} \mathcal{A}(\varepsilon) = i[\mathcal{G}^r(\varepsilon) - \mathcal{G}^a(\varepsilon)] &= \frac{\rho\gamma/2}{(\varepsilon - v - U)^2 + \gamma^2/4} + \frac{(1-\rho/2)\gamma}{(\varepsilon - v)^2 + \gamma^2/4} \\ &= \frac{\rho}{2}\mathcal{L}_r(\varepsilon - v - U) + \left(1 - \frac{\rho}{2}\right)\mathcal{L}_r(\varepsilon - v), \end{aligned} \tag{4.9}$$

and

$$\begin{aligned} \mathcal{A}_S(\varepsilon) = i[\mathcal{G}_S^r(\varepsilon) - \mathcal{G}_S^a(\varepsilon)] &= \frac{\gamma}{[\varepsilon - v - v_{\text{Hxc}}(\rho)]^2 + \gamma^2/4} \\ &= \mathcal{L}_r[\varepsilon - v - v_{\text{Hxc}}(\rho)], \end{aligned} \tag{4.10}$$

where the Lorentzian function is defined as

$$\mathcal{L}_r(\varepsilon) = \frac{\gamma}{\varepsilon^2 + \gamma^2/4}. \tag{4.11}$$

Moreover, $\mathcal{L}_r(\varepsilon) = 2\pi\delta(\varepsilon)$ when $\gamma \to 0$.

Therefore, the densities of the MB and KS systems are

$$\rho = 2\int_{-\infty}^{\infty} f(\varepsilon)\mathcal{A}(\varepsilon)\frac{d\varepsilon}{2\pi}, \tag{4.12}$$

$$\rho_s = 2\int_{-\infty}^{\infty} f(\varepsilon)\mathcal{A}_S(\varepsilon)\frac{d\varepsilon}{2\pi}, \tag{4.13}$$

where the pre-factor 2 is due to spin. Substituting Eq. (4.9) into Eq. (4.12), we have the MB density:

$$
\begin{aligned}
\rho &= 2\int_{-\infty}^{\infty} f(\varepsilon)\left[\frac{\rho\gamma/2}{(\varepsilon-v-U)^2+\gamma^2/4}+\frac{(1-\rho/2)\gamma}{(\varepsilon-v)^2+\gamma^2/4}\right]\frac{d\varepsilon}{2\pi} \\
&= \rho f(\varepsilon)|_{\varepsilon=v+U}+(2-\rho)f(\varepsilon)|_{\varepsilon=v}.
\end{aligned}
\tag{4.14}
$$

Therefore, if $\gamma \to 0$,

$$
\rho = \frac{2f(v)}{1+f(v)-f(v+U)}. \tag{4.15}
$$

With the same manipulation, inserting Eq. (4.10) into Eq. (4.13), we have the KS density:

$$
\begin{aligned}
\rho_s &= 2\int_{-\infty}^{\infty}\frac{d\varepsilon}{2\pi}f(\varepsilon)\frac{\gamma}{[\varepsilon-v-v_{\mathrm{Hxc}}(\rho)]^2+\gamma^2/4} \\
&= 2f(v+v_{\mathrm{Hxc}}).
\end{aligned}
\tag{4.16}
$$

Usually v_{Hxc} is a functional of the density, so Eq. (4.16) has to be solved self-consistently. In the next section we will derive the explicit formula of the Hxc potential. Combined Eqs. (4.5), (4.6), (4.9), and (4.10), the electrical conductance for the MB and KS systems can be respectively expressed as

$$
G = -\frac{\gamma}{2}\int_{-\infty}^{\infty}\frac{d\varepsilon}{2\pi}\frac{\partial f(\varepsilon)}{\partial\varepsilon}\mathcal{A}(\varepsilon), \tag{4.17}
$$

$$
G_S = -\frac{\gamma}{2}\int_{-\infty}^{\infty}\frac{d\varepsilon}{2\pi}\frac{\partial f(\varepsilon)}{\partial\varepsilon}\mathcal{A}_S(\varepsilon). \tag{4.18}
$$

Substituting Eq. (4.9) into Eq. (4.17), we have

$$
G = -\frac{\gamma}{2}\left[\frac{\rho}{2}\frac{\partial f(\varepsilon)}{\partial\varepsilon}\bigg|_{\varepsilon=v+U}+\left(1-\frac{\rho}{2}\right)\frac{\partial f(\varepsilon)}{\partial\varepsilon}\bigg|_{\varepsilon=v}\right], \tag{4.19}
$$

while substituting Eq. (4.10) into Eq. (4.18), we arrive at

$$
G_S = -\frac{\gamma}{2}\frac{\partial f(\varepsilon)}{\partial\varepsilon}\bigg|_{\varepsilon=v+v_{\mathrm{Hxc}}}. \tag{4.20}
$$

We notice from Eqs. (4.19) and (4.20) that the MB and KS conductances are proportional to the coupling γ. For the Seebeck coefficient,

$$
S = -\frac{1}{T}\frac{\int_{-\infty}^{\infty}\varepsilon d\varepsilon\frac{\partial f(\varepsilon)}{\partial\varepsilon}\mathcal{A}(\varepsilon)}{\int_{-\infty}^{\infty}d\varepsilon\frac{\partial f(\varepsilon)}{\partial\varepsilon}\mathcal{A}(\varepsilon)}, \tag{4.21}
$$

$$
S_S = -\frac{1}{T}\frac{\int_{-\infty}^{\infty}\varepsilon d\varepsilon\frac{\partial f(\varepsilon)}{\partial\varepsilon}\mathcal{A}_S(\varepsilon)}{\int_{-\infty}^{\infty}d\varepsilon\frac{\partial f(\varepsilon)}{\partial\varepsilon}\mathcal{A}_S(\varepsilon)}, \tag{4.22}
$$

where S and S_S are the MB and KS Seebeck coefficients, respectively. Substituting Eq. (4.9) into Eq. (4.21), we obtain

$$S = -\frac{1}{T}\frac{\left[\frac{\rho}{2}\varepsilon\frac{\partial f(\varepsilon)}{\partial\varepsilon}\Big|_{\varepsilon=v+U} + \left(1-\frac{\rho}{2}\right)\varepsilon\frac{\partial f(\varepsilon)}{\partial\varepsilon}\Big|_{\varepsilon=v}\right]}{\left[\frac{\rho}{2}\frac{\partial f(\varepsilon)}{\partial\varepsilon}\Big|_{\varepsilon=v+U} + \left(1-\frac{\rho}{2}\right)\frac{\partial f(\varepsilon)}{\partial\varepsilon}\Big|_{\varepsilon=v}\right]}. \tag{4.23}$$

Substituting Eq. (4.10) into Eq. (4.22), we obtain

$$S_S = -\frac{1}{T}\frac{\varepsilon\frac{\partial f(\varepsilon)}{\partial\varepsilon}}{\frac{\partial f(\varepsilon)}{\partial\varepsilon}}\Bigg|_{\varepsilon=v+v_{\rm Hxc}} = -\frac{v+v_{\rm Hxc}}{T}. \tag{4.24}$$

For the single level system within the WBLA, we can see that, distinct from the conductance, the MB and KS Seebeck coefficients are independent on the coupling γ, and S_S shows a linear dependence on gate v with a slope of $1/T$. We would point out that the KS conductance G_S and Seebeck coefficient S_S are exactly the coefficients predicted the LB-DFT approach as we have mentioned in the introduction. In the following we will see that the KS calculations miss the dynamical xc-correction which plays a significant role in the CB regime.

4.3.2 Hxc-potential of a single-site model

In this section we derive the Hxc potential for an isolated QD. The Hamiltonian for a single-site model in the presence of an on-site interaction is given by [143, 144]

$$\hat{H} = v(\hat{n}_\uparrow + \hat{n}_\downarrow) + U\hat{n}_\uparrow\hat{n}_\downarrow, \tag{4.25}$$

where $\hat{n}_\uparrow$ and $\hat{n}_\downarrow$ are the occupation number operators with spin up and down, respectively. For the non-interacting case, the single site Hamiltonian is

$$\hat{H}_S = v_s(\hat{n}_\uparrow + \hat{n}_\downarrow), \tag{4.26}$$

where v_s is the on-site energy. The complete Fock space of both Hamiltonians is spanned by the states $|0\rangle$, $|\uparrow\rangle$, $|\downarrow\rangle$, and $|\uparrow\downarrow\rangle$ with a particle occupation of zero, one, and two. These states are eigenstates of $\hat{H}$ with eigenvalues 0, v, v, and $2v+U$, as well as the eigenstates of $\hat{H}_S$ with eigenvalues 0, v_s, v_s, and $2v_s$, respectively. For the single site model, the density for the MB interacting case reads

$$\begin{aligned}\rho = \mathrm{Tr}[\hat{D}\hat{n}] &= \frac{\mathrm{Tr}\{\exp[-\beta(\hat{H}-\mu(\hat{n}_\uparrow+\hat{n}_\downarrow))](\hat{n}_\uparrow+\hat{n}_\downarrow)\}}{Z} \\ &= \frac{2\exp[-\beta(v-\mu)] + 2\exp\{-\beta[2(v-\mu)]+U\}}{Z},\end{aligned} \tag{4.27}$$

where $\hat{D}$ is the density matrix operator, β is the inverse temperature, *i.e.*, $\beta = 1/k_BT$, μ is the chemical potential, and

$$Z = 1 + 2\exp[-\beta(v-\mu)] + 2\exp\{-\beta[2(v-\mu)]+U\} \tag{4.28}$$

is the grand-canonical partition function. By inverting Eq. (4.27) we obtain

$$v = \mu - U - \frac{1}{\beta}\ln\left[\frac{\delta\rho + \sqrt{\delta\rho^2 + e^{-\beta U}(1-\delta\rho^2)}}{1-\delta\rho}\right]. \tag{4.29}$$

where $\delta\rho = \rho - 1$. Following the same lines for the non-interacting case, the density reads

$$\begin{aligned}\rho_s = \mathrm{Tr}[\hat{D}_S\hat{n}] &= \frac{\mathrm{Tr}\{\exp[-\beta(\hat{H}_S - \mu(\hat{n}_\uparrow + \hat{n}_\downarrow))](\hat{n}_\uparrow + \hat{n}_\downarrow)\}}{Z_S} \\ &= \frac{2\exp[-\beta(v_s-\mu)] + 2\exp\{-\beta[2(v_s-\mu)]\}}{Z_S},\end{aligned} \tag{4.30}$$

where $\hat{D}_S$ is the non-interacting density matrix operator and the non-interacting partition function is

$$Z_S = 1 + 2\exp[-\beta(v_s-\mu)] + 2\exp\{-\beta[2(v_s-\mu)]\}. \tag{4.31}$$

Again inverting Eq. (4.30), we obtain

$$v_s = \mu - \frac{1}{\beta}\ln\left(\frac{1+\delta\rho_s}{1-\delta\rho_s}\right), \tag{4.32}$$

where $\delta\rho_s = \rho_s - 1$. Therefore, the exact Hxc potential for the single site model can now be easily obtained by taking the difference of the two expressions of Eq. (4.29) and Eq. (4.32):

$$v_{\mathrm{Hxc}}^{\mathrm{imp}} = v_s - v = U + \frac{1}{\beta}\ln\left[\frac{\delta\rho + \sqrt{\delta\rho^2 + e^{-\beta U}(1-\delta\rho^2)}}{1+\delta\rho}\right], \tag{4.33}$$

where we have requested that the interacting density equals the non-interacting one, *i.e.*, $\rho = \rho_s$, and we find that $v_{\mathrm{Hxc}}^{\mathrm{imp}}$ is an explicit function of the density and the temperature. Eq. (4.33) is an *exact* result for the isolated single site QD.

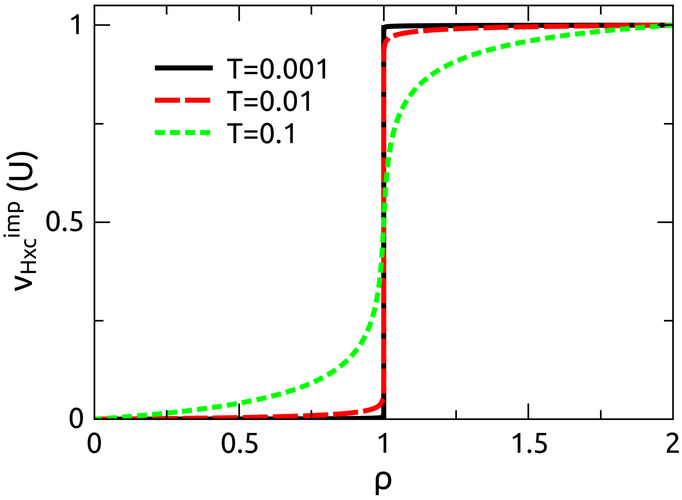

FIGURE 4.2: (Color) Hxc potential of single site impurity model for different temperatures as a function of density, where energies are give in units of U.

In Fig. 4.2 we plot the Hxc potential $v_{\mathrm{Hxc}}^{\mathrm{imp}}$ as a function of density ρ for different temperatures, where all the energies are given in units of U. At very low temperatures, it can be seen that $v_{\mathrm{Hxc}}^{\mathrm{imp}}$ becomes an extremely rapidly varying function of ρ in the vicinity of $\rho = 1$, approaching a step function with height U. With increasing the temperature, the curves become more and more smooth due to the thermal broadening. We will see in the following that the step feature of $v_{\mathrm{Hxc}}^{\mathrm{imp}}$ plays a dominant role in evaluating the conductance and Seebeck coefficient in the CB regime.

4.3.3 Dynamical xc-correction to the Kohn-Sham conductance

In the above discussions, we have shown how to calculate the conductance and Seebeck coefficient for the MB and KS systems. However, the KS calculation does not take into account the dynamical xc correction. We shall see in the following that at very high temperatures, the KS calculation has no problem since the xc-correction is negligible, but at low temperatures, in particular for $T \ll U$, the dynamical xc-correction becomes notable. Since the density of the KS system equals the density of the interacting system, we have

$$\frac{\partial \rho_s}{\partial \mu} = \frac{\partial \rho}{\partial \mu}, \tag{4.34}$$

where

$$\begin{aligned}\chi_s = \frac{\partial \rho_s}{\partial \mu} &= 2\int_{-\infty}^{\infty} \frac{\partial f(\varepsilon)}{\partial \mu} \mathcal{A}_S(\varepsilon) \frac{d\varepsilon}{2\pi} + 2\int_{-\infty}^{\infty} f(\varepsilon) \frac{\partial \mathcal{A}_S(\varepsilon)}{\partial \mu} \frac{d\varepsilon}{2\pi} \\ &= \frac{4}{\gamma} G_S - \chi_s \frac{\partial v_{\mathrm{Hxc}}}{\partial \rho_s} \frac{4}{\gamma} G_S,\end{aligned} \tag{4.35}$$

where we have used the relation: $\frac{\partial \mathcal{A}_S(\varepsilon)}{\partial \mu} = \frac{\partial \mathcal{A}_S(\varepsilon)}{\partial v_{\mathrm{Hxc}}} \frac{\partial v_{\mathrm{Hxc}}}{\partial \rho_s} \frac{\partial \rho_s}{\partial \mu} = -\frac{\partial \mathcal{A}_S(\varepsilon)}{\partial \varepsilon} \frac{\partial v_{\mathrm{Hxc}}}{\partial \rho_s} \frac{\partial \rho_s}{\partial \mu}$ by considering $\mathcal{A}_S$ as an explicit function of $(\varepsilon - v - v_{\mathrm{Hxc}})$. After some algebra, we get

$$\chi_s = \frac{4}{\gamma} G_S \frac{1}{1 + \frac{\partial v_{\mathrm{Hxc}}}{\partial \rho_s} \frac{4}{\gamma} G_S}. \tag{4.36}$$

On the other hand for the interacting system, we have

$$\begin{aligned}\chi = \frac{\partial \rho}{\partial \mu} &= 2\int_{-\infty}^{\infty} \frac{\partial f(\varepsilon)}{\partial \mu} \mathcal{A}(\varepsilon) \frac{d\varepsilon}{2\pi} + 2\int_{-\infty}^{\infty} f(\varepsilon) \frac{\partial \mathcal{A}(\varepsilon)}{\partial \mu} \frac{d\varepsilon}{2\pi} \\ &= \frac{4}{\gamma} G - \chi \mathcal{R},\end{aligned} \tag{4.37}$$

where we defined $\mathcal{R} = -2\int_{-\infty}^{\infty} f(\varepsilon) \frac{\partial \mathcal{A}(\varepsilon)}{\partial \rho} \frac{d\varepsilon}{2\pi}$. Therefore,

$$\chi = \frac{4}{\gamma} G \frac{1}{1 + \mathcal{R}}. \tag{4.38}$$

Combining Eqs. (4.36) and (4.38), we obtain

$$\frac{G}{G_S} = \frac{1 + \mathcal{R}}{1 + \frac{\partial v_{\mathrm{Hxc}}}{\partial \rho} \frac{4}{\gamma} G_S}. \tag{4.39}$$

Eq. (4.39) is an *exact* result for single level system and its r.h.s. is the dynamical correction term, although the quantity $\mathcal{R}$ remains unknown. In the following we approximate

$\mathcal{R}$ as a function of density:

$$\begin{aligned}\mathcal{R} &= -2\int_{-\infty}^{\infty} f(\varepsilon)\frac{\partial\mathcal{A}(\varepsilon)}{\partial\rho}\frac{d\varepsilon}{2\pi} \\ &= -2\int_{-\infty}^{\infty} f(\varepsilon)\left[\frac{\gamma/2}{(\varepsilon-v-U)^2+\gamma^2/4}-\frac{\gamma/2}{(\varepsilon-v)^2+\gamma^2/4}\right]\frac{d\varepsilon}{2\pi} \\ &= \mathcal{I}(v)-\mathcal{I}(v+U),\end{aligned} \tag{4.40}$$

where we have defined

$$\mathcal{I}(x)=\int_{-\infty}^{\infty} f(\varepsilon)\frac{\gamma}{(\varepsilon-x)^2+\gamma^2/4}\frac{d\varepsilon}{2\pi}=\int_{-\infty}^{\infty} f(\varepsilon)\mathcal{L}_r(\varepsilon-x)\frac{d\varepsilon}{2\pi}. \tag{4.41}$$

For the density, we have

$$\rho=2\int_{-\infty}^{\infty} f(\varepsilon)\mathcal{A}(\varepsilon)\frac{d\varepsilon}{2\pi}=\rho\mathcal{I}(v+U)-\rho\mathcal{I}(v)+2\mathcal{I}(v). \tag{4.42}$$

Accordingly,

$$\rho=\frac{2\mathcal{I}(v)}{1+\mathcal{I}(v)-\mathcal{I}(v+U)}. \tag{4.43}$$

The combination of Eqs. (4.40) and (4.43) yields

$$1+\mathcal{R}=\frac{2\mathcal{I}(v)}{\rho}. \tag{4.44}$$

In the case of $\rho<1$ and $v+U>0$, we have $\mathcal{I}(v)\gg\mathcal{I}(v+U)$ and then

$$\rho\approx\frac{2\mathcal{I}(v)}{1+\mathcal{I}(v)}, \tag{4.45}$$

namely,

$$\mathcal{I}(v)\approx\frac{\rho}{2-\rho}, \tag{4.46}$$

thus,

$$1+\mathcal{R}\approx\frac{2}{2-\rho}. \tag{4.47}$$

Taking into account the particle-hole symmetric property, we approximate

$$1+\mathcal{R}=\begin{cases}\frac{1}{1-\left|\frac{\rho}{2}-\mathrm{Int}\left(\frac{\rho}{2}\right)\right|} & \text{if } \left|\frac{\rho}{2}-\mathrm{Int}\left(\frac{\rho}{2}\right)\right|<\frac{1}{2} \\ \frac{1}{\left|\frac{\rho}{2}-\mathrm{Int}\left(\frac{\rho}{2}\right)\right|} & \text{if } \left|\frac{\rho}{2}-\mathrm{Int}\left(\frac{\rho}{2}\right)\right|\geq\frac{1}{2},\end{cases} \tag{4.48}$$

where the function $\mathrm{Int}(x)$ is defined as the integer value of x and one should abandon all the fractional parts. Substituting Eq. (4.48) into Eq. (4.39), we obtain

$$G=\begin{cases}\frac{1}{1-\left|\frac{\rho}{2}-\mathrm{Int}\left(\frac{\rho}{2}\right)\right|}\frac{G_S}{1+\frac{\partial v_{\mathrm{Hxc}}}{\partial\rho}\frac{4}{\gamma}G_S} & \text{if } \left|\frac{\rho}{2}-\mathrm{Int}\left(\frac{\rho}{2}\right)\right|<\frac{1}{2} \\ \frac{1}{\left|\frac{\rho}{2}-\mathrm{Int}\left(\frac{\rho}{2}\right)\right|}\frac{G_S}{1+\frac{\partial v_{\mathrm{Hxc}}}{\partial\rho}\frac{4}{\gamma}G_S} & \text{if } \left|\frac{\rho}{2}-\mathrm{Int}\left(\frac{\rho}{2}\right)\right|\geq\frac{1}{2},\end{cases} \tag{4.49}$$

In the following we will use this expression to calculate the electrical conductance and show how significant the dynamical xc-correction is.

4.3.4 Dynamical xc-correction to the Kohn-Sham Seebeck coefficient

We now derive the xc-correction for the KS Seebeck coefficient. Let me first define

$$\frac{\partial J}{\partial T} = \frac{\gamma}{2}\int_{-\infty}^{\infty} \frac{\partial f(\varepsilon)}{\partial T}\mathcal{A}(\varepsilon)\frac{d\varepsilon}{2\pi}, \tag{4.50}$$

$$\frac{\partial J_S}{\partial T} = \frac{\gamma}{2}\int_{-\infty}^{\infty} \frac{\partial f(\varepsilon)}{\partial T}\mathcal{A}_S(\varepsilon)\frac{d\varepsilon}{2\pi}. \tag{4.51}$$

In this case the Seebeck coefficient for the interacting and KS systems can be respectively expressed as

$$S = -\left(\frac{\partial J}{\partial T}\right)\Big/ G, \tag{4.52}$$

$$S_S = -\left(\frac{\partial J_S}{\partial T}\right)\Big/ G_S, \tag{4.53}$$

because $\frac{\partial f(\varepsilon)}{\partial T} = -\frac{\varepsilon}{T}\frac{\partial f(\varepsilon)}{\partial \varepsilon}$ and we have set the chemical potential as zero. To find out the connection between S and S_S, we have to know the relation between $\partial J/\partial T$ and $\partial J_S/\partial T$. In the derivation of the conductance, we obtain the relation between G and G_S by taking a derivative of the density with respect to chemical potential. Here, we take a derivative of the density with respect to temperature. For the KS system,

$$\begin{aligned} \varphi_s = \frac{\partial \rho_s}{\partial T} &= 2\int_{-\infty}^{\infty} \frac{\partial f(\varepsilon)}{\partial T}\mathcal{A}_S(\varepsilon)\frac{d\varepsilon}{2\pi} + 2\int_{-\infty}^{\infty} f(\varepsilon)\frac{\partial \mathcal{A}_S(\varepsilon)}{\partial T}\frac{d\varepsilon}{2\pi} \\ &= \frac{4}{\gamma}\frac{\partial J_S}{\partial T} - \left(\varphi_s\frac{\partial v_{\mathrm{Hxc}}}{\partial \rho_s} + \left.\frac{\partial v_{\mathrm{Hxc}}}{\partial T}\right|_{\rho_s}\right)\frac{4}{\gamma}G_S, \end{aligned} \tag{4.54}$$

where we have used the relation $\frac{\partial \mathcal{A}_S(\varepsilon)}{\partial T} = \frac{\partial \mathcal{A}_S(\varepsilon)}{\partial v_{\mathrm{Hxc}}}\left[\frac{\partial v_{\mathrm{Hxc}}}{\partial \rho_s}\frac{\partial \rho_s}{\partial T} + \left.\frac{\partial v_{\mathrm{Hxc}}}{\partial T}\right|_{\rho_s}\right]$ by taking into account that v_{Hxc} is an explicit function of ρ_s and T and ρ_s also is a function of T, *i.e.*, $v_{\mathrm{Hxc}}[\rho_s(T), T]$. Therefore we obtain

$$\varphi_s = \frac{4}{\gamma}\left(\frac{\partial J_S}{\partial T} - G_S\left.\frac{\partial v_{\mathrm{Hxc}}}{\partial T}\right|_{\rho_s}\right)\frac{1}{1 + \frac{\partial v_{\mathrm{Hxc}}}{\partial \rho}\frac{4}{\gamma}G_S}. \tag{4.55}$$

For the interacting system,

$$\begin{aligned} \varphi = \frac{\partial \rho}{\partial T} &= 2\int_{-\infty}^{\infty} \frac{\partial f(\varepsilon)}{\partial T}\mathcal{A}(\varepsilon)d\varepsilon + 2\int_{-\infty}^{\infty} f(\varepsilon)\frac{\partial \mathcal{A}(\varepsilon)}{\partial T}\frac{d\varepsilon}{2\pi} \\ &= \frac{4}{\gamma}\frac{\partial J}{\partial T} - \mathcal{R}\varphi. \end{aligned} \tag{4.56}$$

Therefore we have

$$\varphi = \frac{4}{\gamma}\frac{\partial J}{\partial T}\frac{1}{1+\mathcal{R}}. \tag{4.57}$$

Since, by hypothesis,

$$\varphi = \varphi_s, \tag{4.58}$$

we obtain by combining Eqs. (4.55) and (4.57)

$$\frac{\partial J}{\partial T} = \left(\frac{\partial J_S}{\partial T} - G_S \frac{\partial v_{\rm Hxc}}{\partial T}\bigg|_{\rho_s} \right) \frac{1 + \mathcal{R}}{1 + \frac{\partial v_{\rm Hxc}}{\partial \rho} \frac{4}{\gamma} G_S}. \tag{4.59}$$

Using Eq. (4.49), finally we can get

$$S = -\frac{\partial J / \partial T}{G} = -\frac{\partial J_S / \partial T}{G_S} + \frac{\partial v_{\rm Hxc}}{\partial T}\bigg|_{\rho} = S_S + \frac{\partial v_{\rm Hxc}}{\partial T}\bigg|_{\rho}, \tag{4.60}$$

where the first term is the KS Seebeck coefficient and the second term shows the dynamical xc-correction to the S_S. In the following, we will evaluate both terms on the r.h.s. of Eq. (4.60), *i.e.*, S_S and $\frac{\partial v_{\rm Hxc}}{\partial T}$.

Our theory, *i.e.*, Eqs. (4.49) and (4.60), provides a rigorous route to cure the LB-DFT calculations while still remaining in a pure DFT framework.

4.4 Numerical calculations of thermoelectric coefficients for single impurity Anderson model

At temperatures $T \gg \gamma$, but still $T \ll U$ where U is the on-site repulsion energy, the CB phenomenon leaves clear fingerprints on the conductance and Seebeck coefficient. Nevertheless, these are only partially captured by G_S and S_S, even when the *exact* $v_{\rm Hxc}$ is used. We will see the difference between G and G_S as well as the difference between S and S_S clearly in the following calculations.

We start from the single impurity Anderson model since this model is particularly instructive allowing us to disentangle the coordinated actions of the CB effect on G_S and S_S and of the xc correction in reproducing the interacting G and S. In the calculations we assume that γ is the smallest energy scale and we approximate $v_{\rm Hxc}$ by the *exact* Hxc potential of the isolated ($\gamma = 0$) QD [143, 145] as we have derived in Sec. 4.3.2. The Eq. (4.33) can be reformulated as

$$v_{\rm Hxc}[\rho] \approx v_{\rm Hxc}^{\rm imp}[\rho] = \frac{U}{2} + g_U(\rho - 1), \tag{4.61}$$

where $g_U(x) = \frac{U}{2} + \frac{1}{\beta} \ln \left(\frac{x + \sqrt{x^2 + \exp(-\beta U)(1 - x^2)}}{1 + x} \right)$. At very low temperatures ($T > 0$), the Hxc potential exhibits a sharp (but continuous) step of size U at occupation $\rho = 1$ [143, 146, 147] (see Fig. 4.2).

With an analytic expression for $v_{\rm Hxc}$, we can evaluate G and G_S in Eq. (4.49) and both terms on the r.h.s. of Eq. (4.60) for the Seebeck coefficient. Before doing so, let us first look at the density. It can be found from Fig. 4.3 that the density obtained from our DFT approach is exactly the same as the one calculated from MB and RE [40]. The RE is *exact* in the limit of $\gamma \to 0$ and its detailed formalism has been introduced in chapter 2. The MB result is calculated by using the Eq. (4.15) [31].

In Fig. 4.4 (a) we plotted the electrical conductance as a function of gate v. We can see that the conductances calculated from DFT, MB and RE are the same, while the KS conductance is very different in contrast to the other three curves. The G_S completely

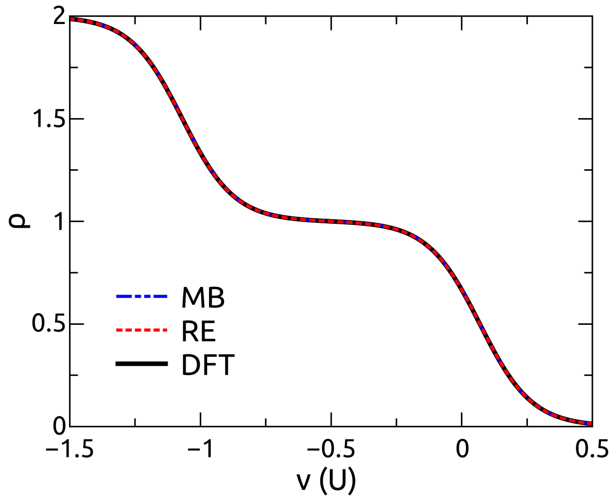

FIGURE 4.3: (Color) Density ρ versus gate v for our xc corrected DFT (black), MB (blue), and RE (red). The parameters are $T = 0.1$ and $\gamma = 0.01$, where energies are given in units of U.

fails to capture the CB peaks and instead shows a plateau in the gate range $(-U, 0)$. The behavior of the conductance can be easily understood. The first electron comes the quantum dot at $v \simeq 0$, and then the second electron can enter into the quantum dot only when the charging energy U is paid effectively by an external potential. So we observe a peak of G at $v \simeq -U$. The broadening of the peaks in Fig. 4.4 (a) is due to the finite temperature. As to the Seebeck coefficient, in Fig. 4.4 (b) we show S calculated from our DFT equation (black) versus the gate v. To demonstrate the accuracy of the result we also show the Seebeck coefficient calculated from MB (blue) as well as the one calculated using the RE approach (red). We find all three approaches give the same Seebeck coefficient.

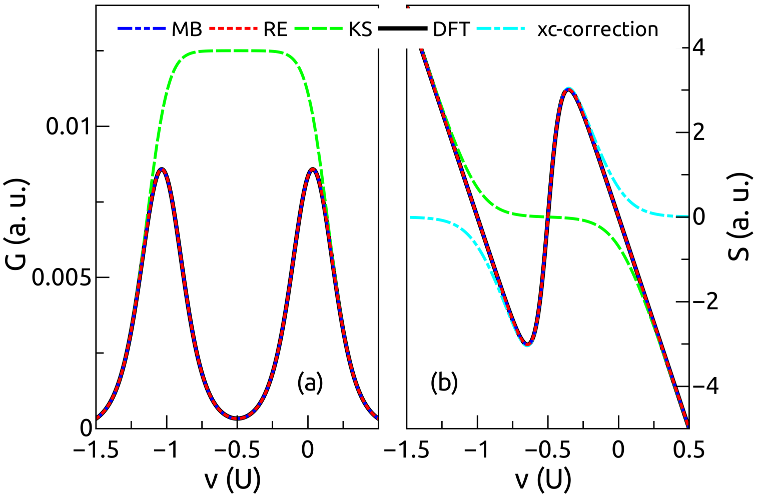

FIGURE 4.4: (Color) (a) Conductance G and (b) Seebeck coefficient S versus gate v for our xc corrected DFT (black), MB (blue) and RE (red). The G_S, S_S (KS, green) and the xc correction $\partial v_{\mathrm{Hxc}}/\partial T$ (cyan) of the Seebeck coefficient are also displayed. The parameters are $T = 0.1$ and $\gamma = 0.01$, where energies are given in units of U.

Let us now discuss how the two terms in Eq. (4.60) contribute. The KS Seebeck coefficient S_S (green) accounts for the correct linear behavior (with slope proportional to T^{-1}) at large values of $|v|$. In fact, for $\gamma \to 0$ the KS spectral function becomes $\mathcal{A}_S(\varepsilon) = 2\pi\delta(\varepsilon - v - v_{\rm Hxc})$ and consequently $S_S = -(v + v_{\rm Hxc})/T$ as we have seen in Eq. (4.24). The linear behavior at large $|v|$ is not surprising since the non-interacting Seebeck coefficient behaves in the same way. Noteworthy is instead the plateau of S_S for $v \in (-U, 0)$. This is a direct consequence of the step in $v_{\rm Hxc}$ which pins the KS level to the chemical potential thereby blocking electrons with energy below $v+U$ from entering the impurity site. The CB-induced plateau in S_S opens a gap in the non-interacting straight line $-v/T$, shifting it leftward by U for $v < -U$ and generating the correct behavior at large negative values of v. However, S_S misses entirely the oscillation of S for $\rho \approx 1$, thus severely underestimating the true Seebeck coefficient. Remarkably, this deficiency is exactly cured by the xc correction $\partial v_{\rm Hxc}/\partial T$ [see the cyan line of Fig. 4.4 (b)]. The temperature variation of $v_{\rm Hxc}$ is the key ingredient for the nonvanishing Seebeck coefficient in the CB regime [40, 148–150].

4.5 Generalization to multiple levels

We now extend the DFT approach to junctions with more than one level. For $T \gg \gamma$ the Seebeck coefficient exhibits a sawtooth behavior as a function of v, with ”jumps” occurring when the number of electrons crosses an integer. Furthermore, if the level spacing $\Delta\varepsilon^0$ is much larger than T, a superimposed fine structure of wiggles spaced by $\Delta\varepsilon_0$ emerges (see Ref. [40]). The wiggles originate from excitations that bring the system in ground state to an excited state according to the discussions by Beenakker in Ref. [40].

The physics of the Seebeck coefficient in a multiple level junction is well captured by the constant interaction model (CIM). The CIM Hamiltonian reads $\hat{H} = \sum_{i\sigma} \varepsilon_i \hat{n}_{i\sigma} + \frac{1}{2}\sum_{i\sigma \neq j\sigma'} U_{ij} \hat{n}_{i\sigma}\hat{n}_{j\sigma'}$, where $\hat{n}_{i\sigma}$ is the occupation operator of the i-th level with spin σ. The indices i, j run over M levels and for $M = 1$ we are back to the impurity Anderson model. For simplicity we assume that each level is equally coupled to the left and right leads with tunnelling rate $\gamma/2$. In this case the derivation of Eq. (4.21) can be repeated step by step by replacing the spectral function $\mathcal{A}$ with its trace $\mathrm{Tr}[\mathcal{A}]$. Consequently, we can again express S in a pure DFT framework by calculating the derivatives of the total number of electrons from the KS expression $\rho_s = 2\int_{-\infty}^{\infty} \frac{d\epsilon}{2\pi} f(\epsilon)\mathrm{Tr}[\mathcal{A}_S(\epsilon)]$. The KS spectral function $[\mathcal{A}_S]_{ij} = \delta_{ij}\mathcal{A}_{S,i}$ is diagonal in the level basis and reads $\mathcal{A}_{S,i}(\epsilon) = \mathcal{L}_r(\epsilon - \varepsilon_i - v_{{\rm Hxc},i})$, where the Hxc potential of level i depends on the occupations $\{\rho_1, \rho_2, \cdots\}$ of all the levels. It is straightforward to show that

$$S = S_S + \sum_j \frac{\int_{-\infty}^{\infty} d\epsilon f'(\epsilon) A_{S,j}(\epsilon)}{\int_{-\infty}^{\infty} d\epsilon f'(\epsilon)\mathrm{Tr}[A_S(\epsilon)]} \left(\left. \frac{\partial v_{{\rm Hxc},j}}{\partial T} \right|_{\rho} \right). \tag{4.62}$$

As to the conductance for multiple level system, one only needs to replace the spectral functions in Eqs. (4.17) and (4.18) by their traces $\mathrm{Tr}[\mathcal{A}]$ and $\mathrm{Tr}[\mathcal{A}_S]$, respectively, and one can still get Eq. (4.49) but using the multiple level Hxc potential.

In Ref. [151] it was proved that at zero temperature the Hxc potential of the isolated ($\gamma = 0$) CIM Hamiltonian is uniform and depends only on ρ, *i.e.*, $v_{{\rm Hxc},i}[\{\rho_1, \rho_2, \cdots\}] = v_{\rm Hxc}[\rho]$, where $\rho = \sum_i \rho_i$. The zero-th order approximation at finite temperatures and weak coupling to the leads therefore consists in neglecting the nonuniformity and the local dependence on the $\{\rho_1, \rho_2, \cdots\}$. In this approximation Eq. (4.62) reduces to Eq. (4.60).

The interacting Seebeck coefficient then follows once we specify the functional form of $v_{\rm Hxc}$. Following Ref. [131] we construct $v_{\rm Hxc}[\rho]$ as the sum of single-impurity Hxc potentials according to

$$v_{\rm Hxc}[\rho] = \sum_{K=1}^{2M-1} \left[\frac{U_K}{2} + g^{\rm ext}_{U_K}(\rho - K) \right], \tag{4.63}$$

where M is the number of the spin-degenerated levels of the QD, U_K is the charging energy needed for adding one electron to the system with K electrons, and the extended $g^{\rm ext}_U$ function is defined according to

$$g^{\rm ext}_U(\rho - 1) = \begin{cases} -U/2 & \rho < 0 \\ g_U(\rho - 1) & 0 \le \rho \le 2 \\ U/2 & \rho > 2 \end{cases}, \tag{4.64}$$

with g_U given below Eq. (4.61). The Hxc potential in Eq. (4.63) has a staircase behavior with steps of width U_K between two consecutive integers.

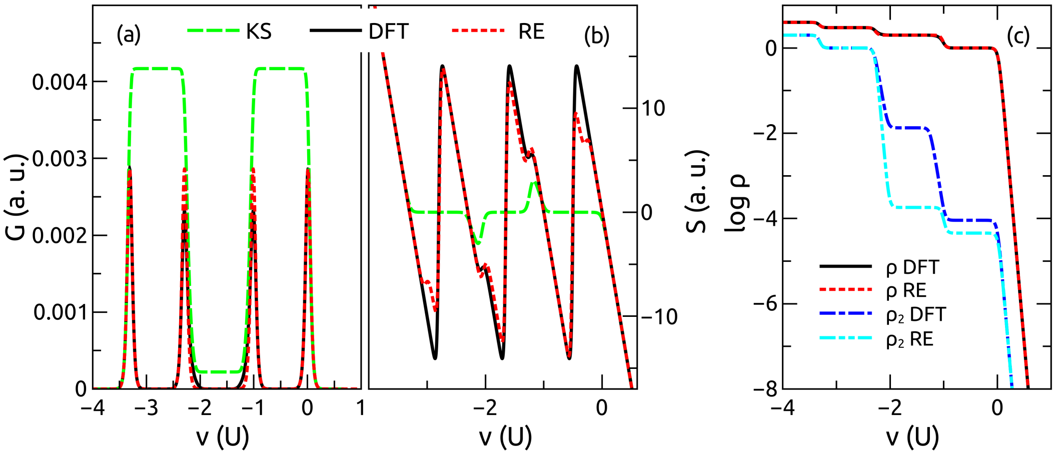

FIGURE 4.5: (Color) (a) Conductance, (b) Seebeck coefficient and (c) density of CIM with two spin-degenerate levels computed from RE and DFT using the approximate functional of Eq. (4.63). The KS conductance and Seebeck coefficient are also shown.

To assess the quality of our approximate Hxc potential we first consider a two-level CIM with $U_{ij} = U$. In Fig. 4.5 we display the results at temperature $T = 0.03$, coupling $\gamma = 0.001$ and $\varepsilon_i = \varepsilon_i^0 + v$ where $\varepsilon_1^0 = 0$ and $\varepsilon_2^0 = 0.3$ (energies in units of U). The right panel (c) shows the total occupation ρ as well as the occupation $\rho_2 = \sum_\sigma \rho_{2\sigma}$ of the highest level calculated using both DFT and RE. Although a perfect agreement is found for ρ, exponentially small discrepancies are seen for the local occupation. In fact, the uniformity (*i.e.*, level independence) of our zero-th order approximation $v_{\rm Hxc}$ of Eq. (4.63) neglects thermal excitations, which correspond to mixing only ground states of different ρ. These thermal excitations could induce additional wiggles in the Seebeck coefficient as we have mentioned previously, and the number of the wiggles depends on the level spacing and thermal energy. Accordingly, the DFT Seebeck coefficient is expected to exhibit only those wiggles associated with the addition of one electron in the lowest available level. This is confirmed by the middle panel of Fig. 4.5 (b) where the wiggles associated to the addition energies of excited states are captured by the RE (red) but missed by DFT (black). As well the DFT conductance shows small difference compared with the RE results [see Fig. 4.5 (a)]. For improving the agreement between

DFT and RE one should abandon the zero-th order uniform approximation and consider a level-dependent Hxc potential which correctly reproduces the level occupations.

To further support this analysis on the relation between the nonuniformity of v_{Hxc} and physical excitations we show in Fig. 4.6 the Seebeck coefficient for the Anderson model with broken spin degeneracy (a) and for a three-level CIM (b). In the first case DFT agrees with RE since there exists only one addition energy, whereas in the second case DFT misses the wiggles of excited-state addition energies. We emphasize that the wiggles stem from S_S (green line), and are not due to the xc correction. The latter is responsible for the large sawtooth oscillations and, as Figs. 4.5 and 4.6 clearly show, it is the dominant contribution to S.

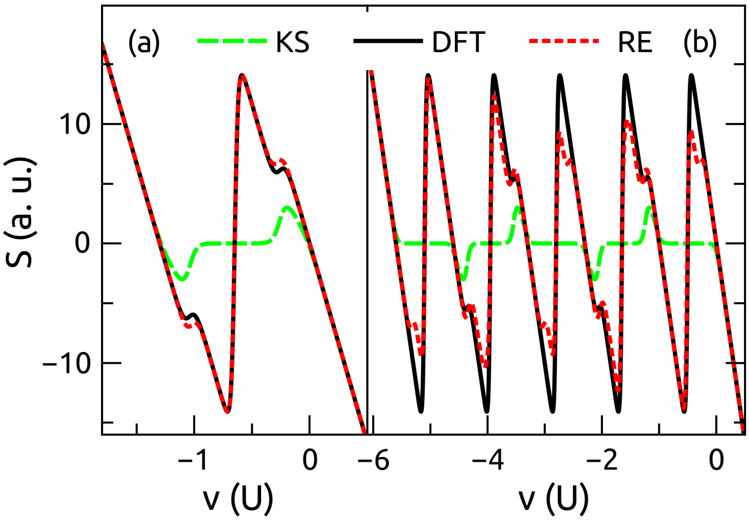

FIGURE 4.6: (Color) Seeebeck coefficient for the Anderson model with non-degenerate single-particle levels (left) and for three spin-degenerate levels (right). The parameters are $\varepsilon_\uparrow^0 = 0$, $\varepsilon_\downarrow^0 = 0.3$ (left panel) and $\varepsilon_1^0 = 0$, $\varepsilon_2^0 = 0.3$, $\varepsilon_3^0 = 0.6$ (right panel). In both panels $T = 0.03$ and $\gamma = 0.001$ (all energies in units of U).

4.6 Application to carbon nanotubes

Recently experimental measurements of the Seebeck coefficient and the electrical conductance in the CB regime have been reported for an individual single-wall carbon nanotube [2] as well as for QDs [149, 150]. For the transport properties of nanotubes, we can extract from the experimental results both single-particle energies and charging energies which are then used to calculate both G and S with our DFT scheme. Based on the CIM Hamiltonian for multiple level system, it is straightforward to have

$$\varepsilon_1^0 = E_1,\ U_1 = dE_{12}, \tag{4.65}$$

$$\varepsilon_2^0 - \varepsilon_1^0 + U_2 = dE_{23}, \quad \varepsilon_2^0 - \varepsilon_1^0 = \delta\mathcal{E}_{12}, \tag{4.66}$$

$$\varepsilon_3^0 - \varepsilon_2^0 + U_3 = dE_{34}, \quad \varepsilon_3^0 - \varepsilon_2^0 = \delta\mathcal{E}_{23}, \tag{4.67}$$

$$\varepsilon_4^0 - \varepsilon_3^0 + U_4 = dE_{45}, \quad \varepsilon_4^0 - \varepsilon_3^0 = \delta\mathcal{E}_{34}, \tag{4.68}$$

$$\cdots, \qquad \cdots, \tag{4.69}$$

where E_1 is the first peak position of the conductance versus gate for the 1-st electron entering into the QD, $dE_{K(K+1)}$ is the energy distance between the K-th and the (K+1)-th conductance peak coordinates, $\delta\mathcal{E}_{K(K+1)}$ is the distance between two wiggles which could show in the Seebeck coefficient, and U_K is the changing energy. Comparing with the model calculations described previously, here the charging energies U_K depend on the charging state K. In the above expressions, $dE_{K(K+1)}$ and $\delta\mathcal{E}_{K(K+1)}$ can be measured directly from the experimental results. Then the single particle energies ε_K^0 and charging energies U_K can be calculated by solving the serial Eqs. (4.65-4.69) systematically, and the results are shown in table 4.1. We will still use Eq. (4.63) to construct the Hxc potential, and the coupling for each level to the leads is assumed to be the same.

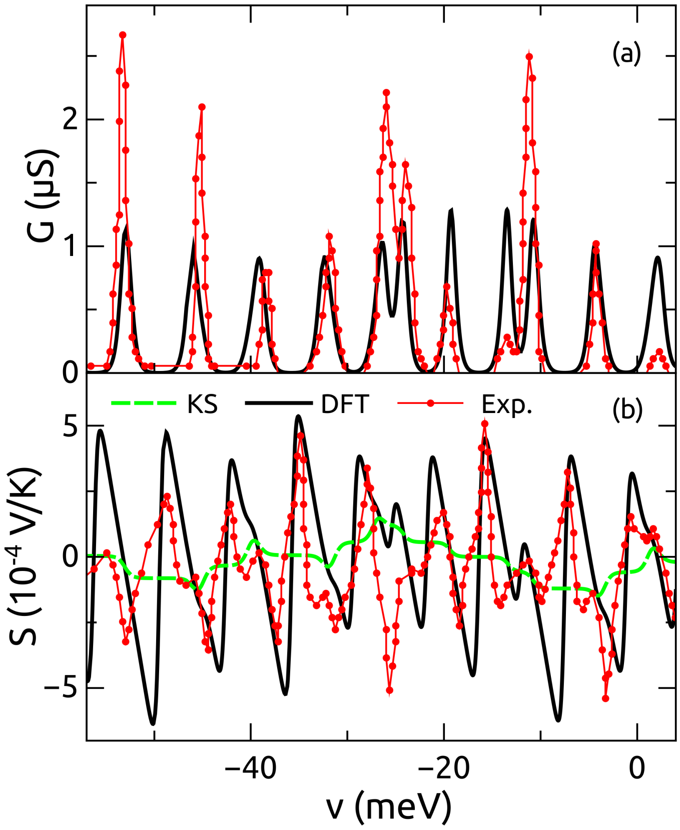

FIGURE 4.7: (Color) Conductance (a) and Seebeck coefficient (b) of a single-wall carbon nanotube from our DFT (black) and experiment (red, data from Ref. [2]). Also shown is the KS Seebeck coefficient (dashed green). The single particle and charging energies are given in table 4.1. The other parameters are $T = 4.5$ K and $\gamma = 0.02$ meV.

TABLE 4.1: Single-particle energies ε_K^0 and charging energies U_K (in meV), for modelling the calculation of Fig. 4.7.

ε_K^0	-6.0	-3.75	-3.75	-3.75	-1.5	0.75
K, U_K	1, 3.75	2, 5.0	4, 2.25	6, 4.5	8, 4.5	10, 5.25
		3, 6.25	5, 5.75	7, 2.0	9, 6.5	11, 6.75

In Fig. 4.7 we present both the electrical conductance G (upper panel), and the Seebeck coefficient (lower panel) S as a function of gate voltage v calculated with the parameters listed in table 4.1 and for temperature $T = 4.5$ K and $\gamma = 0.02$ meV. For comparison we also report the Seebeck coefficient as calculated from the LB-DFT formalism (dashed green line) with the same parameters. LB-DFT fails in reproducing the characteristic sawtooth behaviour of the experimental results. Instead, the Seebeck coefficient calculated with our DFT scheme clearly shows the peak and valley structures observed in experiment, confirming again the crucial role of the xc correction. Also, all the fine structure wiggles (kinks in some cases) are correctly captured.

Chapter 5

Conclusions

In this thesis, we used DFT calculations combined with LB formalism to investigate the transport properties of nanostructured materials and in particular the efficiency of thermoelectric energy conversion in the silicene and germanene nanomembranes, the Si and Ge nanowires, and the silica nanoclusters. We calculated the figure of merit of these systems and found ZT can be remarkably enhanced in contrast to their counterparts of bulk crystals. We also calculated the thermoelectric coefficients for quantum devices in the CB regime and found the dynamical xc-correction plays a key role in evaluating the conductance and Seebeck coefficient. We expect our results are useful for designing future nanodevices and we summarize as follows.

(1) We first performed first-principle calculations of the thermoelectric coefficients for both two-dimensional silicene and germanene nanosheets as well as for one-dimensional silicene and germanene nanoribbons [96]. We also considered the heterostructures of Si and Ge stripes to form a nanoribbon in the attempt to quench phonon dynamics and thus increasing the figure of merit. We found the figure of merit ZT for Si and Ge low dimensional systems is quite high, in the range 1 to 3 at room temperature. These systems can be good thermoelectric materials if they can be reliably produced. We expect these devices based on Si and Ge to be easily interfaced with the modern electronic systems, a distinct advantage with respect to other materials which have shown poor integrability with the current technology.

(2) We then investigated the thermoelectric efficiency of SiGe core-shell NWs along (111) direction [152]. We found that coating a Si core NW with a thin atomic layer of Ge or an alloy of Si and Ge provides the highest figure of merit. This result is stable over the range of core diameters we have been able to investigate with the *ab-initio* technique and it should be possible for an experimental group to test this prediction. We do not expect this enhancement of the figure of merit due to the coating to depend strongly on the growing direction of the NW. Moreover, we provided a simple rule-of-thumb for the NWs we considered here to determine the optimal working temperature at which ZT is maximized, verifying the Goldsmid-Sharps's formula [6]. We expect this rule to be applicable also in other systems.

(3) We investigated the heat transfer between two silica nanoclusters using NEGF approach [153]. We found that the studied gap range can be divided into three regimes with two critical gap distances of 4 Å and 3-5 times the cluster size, and they follow different decay power laws of d^{-12}, d^{-3} and d^{-6}, respectively. The critical gap of 4 Å corresponds

to the classical to quantum transition beyond which heat transfer between neighboring clusters follows the classical law prescribed by the charge-charge (intermediate range) and dipole-dipole (long range) interactions, while the heat flux drastically increases with the gap distance below 4 Å. Near-field radiation clearly captures the thermal interaction above 4 Å, but the heat transfer below this distance is dominated by heat conduction as we showed that electrons are actually forming a chemical bond in the gap. Our results hence provide a deeper insight to understand the behaviour of the transition between radiation and heat conduction in gaps smaller than a few nanometers.

(4) We proposed an alternative DFT scheme for the calculation of thermoelectric coefficients, in particular the Seebeck coefficient, which corrects the deficiencies of the canonical LB approach in the CB regime [154]. We found that two ingredients in the Hxc potential are essential for Seebeck coefficient: (i) the step feature at integer particle number opens a gap in the linear dependence on gate voltage and (ii) the temperature derivative generates the sawtooth behaviour in this gap region. Remarkably, the xc correction represents the dominant contribution to the Seebeck coefficient just as the xc correction to the electrical conductance dominates in the CB regime [131]. We compared our theory with both RE and experimental results on a carbon nanotube, and found good quantitative agreement in all cases. The present approach is valid in the linear response regime, where the applied voltage and thermal gradient between the two leads are small. Going beyond the linear response would pave the way for a deeper understanding of the thermoelectric effect and allow to study materials for extreme applications. The recently proposed DFT framework for thermal transport by Eich *et al.* [139, 140] appears a promising starting point for this purpose.

Appendix A

Relations of Seebeck, Peltier and Thomson coefficients

In this appendix we derive the relations among Seebeck, Peltier and Thomson coefficients according to the thermodynamical laws [155]. We use the same notation of Fig. 1.1 and assume the temperatures at the interfaces A and B of the two metals are T_1 and T_2, respectively, (see the main text of chapter 1). When a current flows through the ring, it will take place heat absorption or generation processes which are found to be reversible as we have discussed before. Taking into account the first law of thermodynamics, the absorbed heat energy after a cycle could be fully transferred into the work, while the inner-energy of the system does not change, *i.e.*,

$$\sum \Delta U = \sum (Q + W) = 0, \tag{A.1}$$

where ΔU represents the change of inner-energy of the system in each step of the cycle process, W is the work produced by the system, and Q is the summation of Peltier heat and Thomson heat in the ring. Supposing that there is a charge q moving along the direction from conductor a to b by crossing the interface A with temperature T_1, and then back to a by crossing the interface B with temperature T_2, in this process the work produced by the system is qV_{ab}. For the first step that the charge q crosses the interface A, the absorbed Peltier heat is

$$q[\Pi_b(T_1) - \Pi_a(T_1)] = q\Pi_{ab}(T_1), \tag{A.2}$$

where we have defined $\Pi_{ab}(T) = \Pi_b(T) - \Pi_a(T)$ and for the absorbed Thomson heat it is

$$q \int_{T_1}^{T_2} \Theta_b(T) dT, \tag{A.3}$$

where the charge q moves in conductor b from interface A to B.

Similarly for the second step that the charged particle goes back to a from conductor b at the r.h.s., the absorbed Peltier heat through the interface B is

$$q\Pi_{ba}(T_2) = -q\Pi_{ab}(T_2), \tag{A.4}$$

and the absorbed Thomson heat in conductor a going from B to A is

$$q\int_{T_2}^{T_1}\Theta_a(T)dT = -q\int_{T_1}^{T_2}\Theta_a(T)dT. \tag{A.5}$$

Using Eq. (A.1), therefore we have

$$qV_{ab} + q\Pi_{ab}(T_1) - q\Pi_{ab}(T_2) + q\int_{T_1}^{T_2}[\Theta_b(T) - \Theta_a(T)]dT = 0, \tag{A.6}$$

namely,

$$V_{ab} = \Pi_{ab}(T_2) - \Pi_{ab}(T_1) - \int_{T_1}^{T_2}\Theta_{ab}(T)dT, \tag{A.7}$$

where $\Theta_{ab}(T) = \Theta_b(T) - \Theta_a(T)$.

In the above equation, if we take T_1 as a constant and do a derivative of Eq. (A.7) with respect to T, we obtain

$$S_{ab} = \frac{dV_{ab}}{dT} = \frac{d\Pi_{ab}}{dT} - \Theta_{ab}(T). \tag{A.8}$$

Considering the change of entropy should equal zero always for a reversible process from the second law of thermodynamics, *i.e.*,

$$\sum\frac{Q}{T} = 0, \tag{A.9}$$

so

$$\frac{\Pi_{ab}(T_2)}{T} - \frac{\Pi_{ab}(T_1)}{T} - \int_{T_1}^{T_2}\frac{\Theta_{ab}(T)}{T}dT = 0, \tag{A.10}$$

where we have used the Eq. (A.6).

Taking a derivation of Eq. (A.10) with respect to temperature T, one obtains

$$\frac{d}{dT}\left[\frac{\Pi_{ab}(T)}{T}\right] - \frac{\Theta_{ab}(T)}{T} = 0. \tag{A.11}$$

Combination of Eqs. (A.8) and (A.11) gives

$$\Pi_{ab} = S_{ab}T. \tag{A.12}$$

Substituting Eq. (A.12) into Eq. (A.11) we obtain

$$\frac{dS_{ab}}{dT} = \frac{\Theta_{ab}(T)}{T}. \tag{A.13}$$

Therefore once we know the Seebeck coefficient, we can immediately obtain the Peltier and Thomson coefficients.

Appendix B

Time-ordered Green's functions

In this appendix, we present the derivation of the equation of motion for both fermionic and bosonic time-ordered Green's functions [33–35]. And also we will derive the many body spectral function for interacting system [31], which could be used in chapter 4.

B.1 Fermionic Green's function

B.1.1 Equation of motion of time-ordered Green's function

We start from the Heisenberg equation using the Hamiltonian we have described in chapter 2. The time-ordered Green's function of fermionic system is defined as

$$\begin{aligned}\mathcal{G}^t_{n,\mathbf{k}\alpha}(t,t') &= -\frac{i}{\hbar}\langle \hat{T}[\hat{c}^\dagger_{\mathbf{k}\alpha}(t')\hat{d}_n(t)]\rangle \\ &= -\frac{i}{\hbar}\theta(t'-t)\langle \hat{c}^\dagger_{\mathbf{k}\alpha}(t')d_n(t)\rangle + \frac{i}{\hbar}\theta(t-t')\langle \hat{d}_n(t)\hat{c}^\dagger_{\mathbf{k}\alpha}(t')\rangle.\end{aligned} \tag{B.1}$$

where $\hat{T}$ is the time-ordered operator.
Taking a derivative of the above Green's function with respect to t', it yields

$$\begin{aligned}i\hbar\frac{\partial}{\partial t'}\mathcal{G}^t_{n,\mathbf{k}\alpha}(t,t') &= \delta(t'-t)\langle \hat{c}^\dagger_{\mathbf{k}\alpha}(t')\hat{d}_n(t)\rangle + \delta(t'-t)\langle \hat{d}_n(t)\hat{c}^\dagger_{\mathbf{k}\alpha}(t')\rangle + \\ &\quad \theta(t'-t)\langle \dot{c}^\dagger_{\mathbf{k}\alpha}(t')\hat{d}_n(t)\rangle - \theta(t-t')\langle \hat{d}_n(t)\dot{c}^\dagger_{\mathbf{k}\alpha}(t')\rangle \\ &= \theta(t'-t)\langle \dot{\hat{c}}^\dagger_{\mathbf{k}\alpha}(t')\hat{d}_n(t)\rangle - \theta(t-t')\langle \hat{d}_n(t)\dot{\hat{c}}^\dagger_{\mathbf{k}\alpha}(t')\rangle \\ &= -i\theta(t'-t)\langle [\hat{c}^\dagger_{\mathbf{k}\alpha}(t'), \hat{H}(t')]\hat{d}_n(t)\rangle + i\theta(t-t')\langle \hat{d}_n(t)[\hat{c}^\dagger_{\mathbf{k}\alpha}(t'), \hat{H}(t')]\rangle \\ &= -i\theta(t'-t)\langle [\hat{c}^\dagger_{\mathbf{k}\alpha}(t'), \sum_{\mathbf{k}',\alpha'=L,R} \varepsilon_{\mathbf{k}'\alpha'}\hat{c}^\dagger_{\mathbf{k}'\alpha'}(t')\hat{c}_{\mathbf{k}'\alpha'}(t) + \\ &\quad \sum_m \varepsilon_m \hat{d}^\dagger_m(t')\hat{d}_m(t') + U\sum_m \hat{n}_{m\uparrow}\hat{n}_{m\downarrow} + \\ &\quad \sum_{\mathbf{k}",\alpha"=L,R,m} (V_{\mathbf{k}"\alpha",m}\hat{c}^\dagger_{\mathbf{k}",\alpha"}(t')\hat{d}_m(t') + V^*_{\mathbf{k}"\alpha",m}\hat{d}^\dagger_m(t')\hat{c}_{\mathbf{k}"\alpha"}(t'))]\hat{d}_n(t)\rangle +\end{aligned} \tag{B.2}$$

$$
\begin{aligned}
& i\theta(t-t')\langle \hat{d}_n(t)[\hat{c}^{\dagger}_{\mathbf{k}\alpha}(t'), \sum_{\mathbf{k}'\alpha'=L,R} \varepsilon_{\mathbf{k}'\alpha'}\hat{c}^{\dagger}_{\mathbf{k}'\alpha'}(t')\hat{c}_{\mathbf{k}'\alpha'}(t')+ \\
& \sum_m \varepsilon_m \hat{d}^{\dagger}_m(t')\hat{d}_m(t') + U\sum_m \hat{n}_{m\uparrow}\hat{n}_{m\downarrow} + \sum_{\mathbf{k}",\alpha"=L,R,m} (V_{\mathbf{k}"\alpha",m}\hat{c}^{\dagger}_{\mathbf{k}"\alpha"}(t')\hat{d}_m(t')+ \\
& V^{*}_{\mathbf{k}"\alpha",m}\hat{d}^{\dagger}_m(t')\hat{c}_{\mathbf{k}"\alpha"}(t'))]\rangle \\
= & -i\theta(t'-t)\langle[\hat{c}^{\dagger}_{\mathbf{k}\alpha}(t'), \sum_{\mathbf{k}',\alpha'=L,R} \varepsilon_{\mathbf{k}'\alpha'}\hat{c}^{\dagger}_{\mathbf{k}'\alpha'}(t')\hat{c}_{\mathbf{k}'\alpha'}(t')+ \\
& \sum_{\mathbf{k}",\alpha"=L,R,m} (V_{\mathbf{k}"\alpha",m}\hat{c}^{\dagger}_{\mathbf{k}"\alpha"}(t')\hat{d}_m(t') + V^{*}_{\mathbf{k}"\alpha",m}\hat{d}^{\dagger}_m(t')\hat{c}_{\mathbf{k}"\alpha"}(t'))]\hat{d}_n(t)\rangle+ \\
& i\theta(t-t')\langle \hat{d}_n(t)[\hat{c}^{\dagger}_{\mathbf{k}\alpha}(t'), \sum_{\mathbf{k}',\alpha'=L,R} \varepsilon_{\mathbf{k}'\alpha'}\hat{c}^{\dagger}_{\mathbf{k}'\alpha'}(t')\hat{c}_{\mathbf{k}'\alpha'}(t')+ \\
& \sum_{\mathbf{k}",\alpha"=L,R,m} (V_{\mathbf{k}"\alpha",m}\hat{c}^{\dagger}_{\mathbf{k}"\alpha"}(t')\hat{d}_m(t') + V^{*}_{\mathbf{k}"\alpha",m}\hat{d}^{\dagger}_m(t')\hat{c}_{\mathbf{k}"\alpha"}(t'))]\rangle \\
= & -i\theta(t'-t)\langle[\hat{c}^{\dagger}_{\mathbf{k}\alpha}(t'), \varepsilon_{\mathbf{k}\alpha}\hat{c}^{\dagger}_{\mathbf{k}\alpha}(t')\hat{c}_{\mathbf{k}\alpha}(t') + \sum_m (V_{\mathbf{k}\alpha,m}\hat{c}^{\dagger}_{\mathbf{k}\alpha}(t')\hat{d}_m(t')+ \\
& V^{*}_{\mathbf{k}\alpha,m}\hat{d}^{\dagger}_m(t')\hat{c}_{\mathbf{k}\alpha}(t'))]\hat{d}_n(t)\rangle+ \\
& i\theta(t-t')\langle \hat{d}_n(t)[\hat{c}^{\dagger}_{\mathbf{k}\alpha}(t'), \varepsilon_{\mathbf{k}\alpha}\hat{c}^{\dagger}_{\mathbf{k}\alpha}(t')\hat{c}_{\mathbf{k}\alpha}(t') + \sum_m (V_{\mathbf{k}\alpha,m}\hat{c}^{\dagger}_{\mathbf{k}\alpha}(t')\hat{d}_m(t')+ \\
& V^{*}_{\mathbf{k}\alpha,m}\hat{d}^{\dagger}_m(t')\hat{c}_{\mathbf{k}\alpha}(t'))]\rangle \\
= & -i\theta(t'-t)\langle[-\varepsilon_{\mathbf{k}\alpha}\hat{c}^{\dagger}_{\mathbf{k}\alpha}(t') - \sum_m V^{*}_{\mathbf{k}\alpha,m}\hat{d}^{\dagger}_m(t')]\hat{d}_n(t)\rangle+ \\
& i\theta(t-t')\langle \hat{d}_n(t)[-\varepsilon_{\mathbf{k}\alpha}\hat{c}^{\dagger}_{\mathbf{k}\alpha}(t') - \sum_m V^{*}_{\mathbf{k}\alpha,m}\hat{d}^{\dagger}_m(t')]\rangle \\
= & i\theta(t'-t)\langle \varepsilon_{\mathbf{k}\alpha}\hat{c}^{\dagger}_{\mathbf{k}\alpha}(t')\hat{d}_n(t)\rangle - i\theta(t-t')\langle \varepsilon_{\mathbf{k}\alpha}\hat{d}_n(t)\hat{c}^{\dagger}_{\mathbf{k}\alpha}(t')\rangle+ \\
& i\theta(t'-t)\langle \sum_m \hat{d}^{\dagger}_m(t')\hat{d}_n(t)V^{*}_{\mathbf{k}\alpha,m}\rangle - i\theta(t-t')\langle \sum_m \hat{d}_n(t)\hat{d}^{\dagger}_m(t')V^{*}_{\mathbf{k}\alpha,m}\rangle \\
= & -\varepsilon_{\mathbf{k}\alpha}\hbar\mathcal{G}^{t}_{n,\mathbf{k}\alpha}(t,t') - \hbar\sum_m \mathcal{G}^{t}_{n,m}(t,t')V^{*}_{\mathbf{k}\alpha,m},
\end{aligned}
\tag{B.3}
$$

where we have used the anti-commutate relation for Fermi particles.

Therefore we have

$$
[-i\frac{\partial}{\partial t'} - \varepsilon_{k\alpha}]\mathcal{G}^{t}_{n,k\alpha}(t,t') = \sum_m \mathcal{G}^{t}_{n,k\alpha}(t,t')V^{*}_{k\alpha,m}. \tag{B.4}
$$

If one defines

$$
(-i\frac{\partial}{\partial t'} - \varepsilon_{k\alpha})g^{t}_{k\alpha}(t,t') = \delta(t,t'), \tag{B.5}
$$

we can finally get

$$
\mathcal{G}^{t}_{n,k\alpha}(t,t') = \sum_m \int_{-\infty}^{\infty} dt_1 \mathcal{G}^{t}_{nm}(t,t_1)V^{*}_{k\alpha,m}g^{t}_{k\alpha}(t_1,t'). \tag{B.6}
$$

This is called the equation of motion for the time-ordered Green's function $\mathcal{G}^{t}_{n,k\alpha}$ and it will be used for the derivation of electric and energy current formulas in chapter 2.

B.1.2 Spectral function of many body interacting system with single level

We start from an isolated quantum dot, and then add the coupling effect to the Green's function in terms of a self-energy based on the Dyson equation [31]. We assume that there is only one level in the central region for simplicity, and the equilibrium counterpart of the time-ordered Green's function for the dot is $g^{\sigma\sigma,t}(t,t') = -\frac{i}{\hbar}\langle \hat{T}\hat{d}_\sigma(t)\hat{d}_\sigma^\dagger(t')\rangle$, where σ denotes the spin up or spin down. Then the equation of motion for $g^{\sigma\sigma,t}(t,t')$ in the time space is

$$i\frac{\partial}{\partial t}g^{\sigma\sigma,t}(t,t') = \delta(t-t') + \varepsilon_\sigma g^{\sigma\sigma,t}(t,t') + Ug^{(2),t}(t,t'), \tag{B.7}$$

and in the energy space it can be

$$(\varepsilon - \varepsilon_\sigma)g^{\sigma\sigma,t}(\varepsilon) = 1 + Ug^{(2),t}(\varepsilon), \tag{B.8}$$

where we have used the relation $i\hbar\dot{\hat{d}}_\sigma = \varepsilon_\sigma\hat{d}_\sigma + U\hat{d}_\sigma\hat{n}_{\bar{\sigma}}$ and $\bar{\sigma} = -\sigma$. The minus sign indicates the opposite spin polarization direction. The second term in the relation for $\hat{d}_\sigma$, which is due to the on-site interaction, generates a higher order Green's function $g^{(2),t}$:

$$g^{(2),t}(t,t') = -\frac{i}{\hbar}\langle \hat{T}\{\hat{d}_\sigma(t)\hat{n}_{\bar{\sigma}}(t)\hat{d}_\sigma^\dagger(t')\}\rangle. \tag{B.9}$$

The next step is to derive the equation of motion for $g^{(2),t}$. Since $[\hat{n}_{\bar{\sigma}}, \hat{H}] = 0$, one only has to consider the time derivative of $\hat{d}_\sigma$. The result is

$$i\frac{\partial}{\partial t}g^{(2),t}(t,t') = \delta(t,t')\langle\hat{n}_{\bar{\sigma}}\rangle + \varepsilon_\sigma g^{(2),t}(t,t') + Ug^{(2),t}(t,t')\rangle. \tag{B.10}$$

After a Fourier transformation, we have

$$(\varepsilon - \varepsilon_\sigma - U)g^{(2),t}(\varepsilon) = \langle\hat{n}_{\bar{\sigma}}\rangle. \tag{B.11}$$

Inserting Eq. (B.11) into Eq. (B.8), we find

$$\begin{aligned} g^{\sigma\sigma,t}(\varepsilon) &= \frac{\varepsilon - \varepsilon_\sigma - (1-\langle\hat{n}_{\bar{\sigma}}\rangle)U}{(\varepsilon-\varepsilon_\sigma-U)(\varepsilon-\varepsilon_\sigma)} \\ &= \frac{\langle\hat{n}_{\bar{\sigma}}\rangle}{\varepsilon-\varepsilon_\sigma-U} + \frac{1-\langle\hat{n}_{\bar{\sigma}}\rangle}{\varepsilon-\varepsilon_\sigma}, \end{aligned} \tag{B.12}$$

where the second line shows that the Green's function has two resonances, at $\varepsilon = \varepsilon_\sigma + U$ and $\varepsilon = \varepsilon_\sigma$, with weights $\langle\hat{n}_{\bar{\sigma}}\rangle$ and $1 - \langle\hat{n}_{\bar{\sigma}}\rangle$, respectively.

Eq. (B.12) can be used to determine the density $\langle\hat{n}_{\bar{\sigma}}\rangle$ and hence $g^{\sigma\sigma,t}(\varepsilon)$ by self-consistent calculation. In equilibrium according to the fluctuation-dissipation theorem, we have

$$\langle\hat{n}_\sigma\rangle = -i\int_{-\infty}^{\infty}\frac{d\varepsilon}{2\pi}g^{\sigma\sigma,<}(\varepsilon) = \int_{-\infty}^{\infty}\frac{d\varepsilon}{2\pi}[-2\ \mathrm{Im}\ g^{\sigma\sigma,r}(\varepsilon)f(\varepsilon)], \tag{B.13}$$

where the retarded Green's function $g^{\sigma\sigma,r}$ is obtained from Eq. (B.12) with the replacement $\varepsilon = \varepsilon + i\zeta$. For single degenerated level system, the density $\langle\hat{n}_\sigma\rangle$ should be equal to $\langle\hat{n}_{\bar{\sigma}}\rangle$. For non-degenerated system, one has to self-consistently calculate the spin up and spin down densities by combining Eqs. (B.12) and (B.13).

Using the Dyson equation, we can finally obtain

$$\mathcal{G}^{\sigma\sigma,r}(\varepsilon) = \frac{\langle \hat{n}_{\bar{\sigma}} \rangle}{\varepsilon - \varepsilon_\sigma - U - \Sigma^r} + \frac{1 - \langle \hat{n}_{\bar{\sigma}} \rangle}{\varepsilon - \varepsilon_\sigma - \Sigma^r}, \tag{B.14}$$

where Σ^r is the related self energy.
Therefore the interacting spectral function is

$$\mathcal{A}(\varepsilon) = i[\mathcal{G}^{\sigma\sigma,r}(\varepsilon) - \mathcal{G}^{\sigma\sigma,a}(\varepsilon)], \tag{B.15}$$

where $\mathcal{G}^a$ is the advanced Green's function: $\mathcal{G}^a = [\mathcal{G}^r]^\dagger$. For the non-interacting Green's function and spectral function, one can easily obtain, by setting $U = 0$,

$$\mathcal{G}_S^{\sigma\sigma,r}(\varepsilon) = \frac{1}{\varepsilon - \varepsilon_\sigma - \Sigma^r}, \tag{B.16}$$

$$\mathcal{A}_S(\varepsilon) = i[\mathcal{G}_S^{\sigma\sigma,r}(\varepsilon) - \mathcal{G}_S^{\sigma\sigma,a}(\varepsilon)]. \tag{B.17}$$

These expressions will be used in the derivation of chapter 4.

B.2 Time-ordered bosonic Green's function

In this section, we derive the equation of motion for bosonic time-ordered Green's function. The center-left time-ordered Green's function is defined as [33–35]

$$\begin{aligned}
\frac{\partial}{\partial t'}\mathcal{G}_{jk}^{CL,t}(t,t') &= -\frac{i}{\hbar}\frac{\partial}{\partial t'}\langle \hat{T}\hat{u}_k^L(t')\hat{u}_j^C(t)\rangle \\
&= -\frac{i}{\hbar}\frac{\partial}{\partial t'}\langle \theta(t'-t)\hat{u}_k^L(t')\hat{u}_j^C(t) + \theta(t-t')\hat{u}_j^C(t)\hat{u}_k^L(t')\rangle \\
&= -\frac{i}{\hbar}\langle \delta(t'-t)[\hat{u}_k^L(t'),\hat{u}_j^C(t)]\rangle - \frac{i}{\hbar}\langle \hat{T}\dot{\hat{u}}_k^L(t')\hat{u}_j^C(t)\rangle \\
&= -\frac{i}{\hbar}\langle \hat{T}\dot{\hat{u}}_k^L(t')\hat{u}_j^C(t)\rangle,
\end{aligned} \tag{B.18}$$

where the first term in the second line from bottom equals zero since the two elements commute. The second derivative can be derived in a similar way as Eq. (B.18), and it yields

$$\frac{\partial^2}{\partial t'^2}\mathcal{G}_{jk}^{CL,t}(t,t') = -\frac{i}{\hbar}\langle \hat{T}\ddot{\hat{u}}_k^L(t')\hat{u}_j^C(t)\rangle, \tag{B.19}$$

where

$$\begin{aligned}
\ddot{\hat{u}}_k^L(t') &= -\frac{i}{\hbar}e^{i\hat{H}t'}[\dot{\hat{u}}_k^L,\hat{H}]e^{-i\hat{H}t'} \\
&= -\frac{i}{\hbar}e^{i\hat{H}t'}[\dot{\hat{u}}_k^L,\hat{H}_L + \hat{H}_{LC}]e^{-i\hat{H}t'} \\
&= -\frac{i}{\hbar}e^{i\hat{H}t'}[\dot{\hat{u}}_k^L,\sum_{lm}(\frac{1}{2}(\dot{\hat{u}}_l^L)^T\dot{\hat{u}}_m^L + \frac{1}{2}\hat{u}_l^L K_{lm}^L\hat{u}_m^L + \hat{u}_l^L V_{lm}^{LC}\hat{u}_m^C)]e^{-i\hat{H}t'} \\
&= -\frac{i}{\hbar}e^{i\hat{H}t'}[-i\hbar\sum_l(K_{kl}^L\hat{u}_l^L + V_{kl}^{LC}\hat{u}_l^C)]e^{-i\hat{H}t'} \\
&= -\sum_l[K_{kl}^L\hat{u}_l^L(t') + V_{kl}^{LC}\hat{u}_l^C(t')].
\end{aligned} \tag{B.20}$$

So Eq. (B.19) becomes

$$\begin{aligned}\frac{\partial^2}{\partial t'^2}\mathcal{G}^{CL,t}_{jk}(t,t') &= -\frac{i}{\hbar}\langle\hat{T}[-\sum_l(K^L_{kl}\hat{u}^L_l(t')+V^{LC}_{kl}\hat{u}^C_l(t'))]\hat{u}^C_j(t)\rangle \\ &= -\langle -\frac{i}{\hbar}[\sum_l \hat{T}K^L_{kl}\hat{u}^L_l(t')\hat{u}^C_j(t)+\hat{T}V^{LC}_{kl}\hat{u}^C_l(t')\hat{u}^C_j(t)]\rangle \\ &= -\sum_l[K^L_{kl}\mathcal{G}^{CL,t}_{jl}(t,t')+\mathcal{G}^{CC,t}_{jl}(t,t')V^{LC}_{kl}].\end{aligned} \tag{B.21}$$

We now omit the subscript and express in a more compact matrix form:

$$\frac{\partial^2}{\partial t'^2}\mathcal{G}^t_{CL}(t,t') + K^L\mathcal{G}^t_{CL}(t,t') = -\mathcal{G}^t_{CC}(t,t')V^{CL}. \tag{B.22}$$

This is the equation of motion for the bosonic Green's function. If one defines a time-ordered Green's function for the left lead, *i.e.*,

$$\frac{\partial^2}{\partial t'^2}g^t_L(t,t') + K^L g^t_L(t,t') = -\delta(t,t'), \tag{B.23}$$

the combination of Eqs. (B.22) and (B.23) will yield

$$\mathcal{G}^t_{CL}(t,t') = \int_{-\infty}^{\infty} dt_1 \mathcal{G}^t_{CC}(t,t_1)V^{CL}g^t_L(t_1,t'). \tag{B.24}$$

This expresses the center-left time-ordered Green's function in terms of the center-center time-ordered Green's function, and we will use this equation for the derivation of the heat current for bosons in chapter 2.

Bibliography

[1] Y. Ni, H. Le Khanh, Y. Chalopin, J. Bai, P. Lebarny, L. Divay, and S. Volz. Highly efficient thermal glue for carbon nanotubes based on azide polymers. *Appl. Phys. Lett.*, 100:193118, 2012.

[2] J. P. Small, K. M. Perez, and P. Kim. Modulation of Thermoelectric Power of Individual Carbon Nanotubes. *Phys. Rev. Lett.*, 91:256801, 2003.

[3] F. J. DiSalvo. Thermoelectric Cooling and Power Generation. *Science*, 285:703, 1999.

[4] C. B. Vining. Thermoelectrics: Half-full glasses. *Nat. Mater.*, 7:765, 2008.

[5] C. B. Vining. An inconvenient truth about thermoelectrics. *Nat. Mater.*, 8:83, 2009.

[6] H. J. Goldsmid. *Introduction to Thermoelectricity.* Springer Berlin Heidelberg, Berlin, Heidelberg, 2010.

[7] C. M. Jaworski, J. Yang, S. Mack, D. D. Awschalom, J. P. Heremans, and R. C. Myers. Observation of the spin-Seebeck effect in a ferromagnetic semiconductor. *Nat. Mater.*, 9:898, 2010.

[8] H. Adachi, K. Uchida, E. Saitoh, and S. Maekawa. Theory of the spin Seebeck effect. *Reports Prog. Phys.*, 76:036501, 2013.

[9] S. M. Rezende, R. L. Rodríguez-Suárez, and A. Azevedo. Theory of the spin Seebeck effect in antiferromagnets. *Phys. Rev. B*, 93:014425, 2016.

[10] S. M. Wu, W. Zhang, A. KC, P. Borisov, J. E. Pearson, J. S. Jiang, D. Lederman, A. Hoffmann, and A. Bhattacharya. Antiferromagnetic spin Seebeck Effect. *Phys. Rev. Lett.*, 116:097204, 2016.

[11] D. Nemir and J. Beck. On the Significance of the Thermoelectric Figure of Merit Z. *J. Electron. Mater.*, 39:1897, 2010.

[12] R. Venkatasubramanian, E. Siivola, T. Colpitts, and B. O'Quinn. Thin-film thermoelectric devices with high room-temperature figures of merit. *Nature*, 413:597, 2001.

[13] N. W. Ashcroft and N. D. Mermin. *Solid State Physics.* Saunders College Publishing, Philadelphia, 1976.

[14] Y. Dubi and M. Di Ventra. Colloquium : Heat flow and thermoelectricity in atomic and molecular junctions. *Rev. Mod. Phys.*, 83:131, 2011.

[15] L. D. Zhao, S. H. Lo, Y. Zhang, H. Sun, G. Tan, C. Uher, C. Wolverton, V. P. Dravid, and M. G. Kanatzidis. Ultralow thermal conductivity and high thermoelectric figure of merit in SnSe crystals. *Nature*, 508:373, 2014.

[16] G. Onida, L. Reining, and A. Rubio. Electronic excitations: density-functional versus many-body Green's-function approaches. *Rev. Mod. Phys.*, 74:601, 2002.

[17] K. Capelle. A bird's-eye view of density-functional theory. *arXiv:cond-mat/0211443*, 2002.

[18] M. A. L. Marques, C. A. Ullrich, F. Nogueira, A. Rubio, K. Burke, and E. K. U. Gross. *Time-Dependent Density Functional Theory.* Springer Berlin Heidelberg, Berlin, Heidelberg, 2006.

[19] X. D. Xie and D. Lu. *Energy Band Theory of Solids.* Fudan University Press, Shanghai, 2007.

[20] E. Engel and R. M. Dreizler. *Density Functional Theory.* Springer Berlin Heidelberg, Berlin, Heidelberg, 2011.

[21] M. A. L. Marques, N. T. Maitra, F. M. S. Nogueira, E. K. U. Gross, and A. Rubio. *Fundamentals of Time-Dependent Density Functional Theory.* Springer Berlin Heidelberg, Berlin, Heidelberg, 2012.

[22] J. J. Sakurai. *Modern Quantum Mechanics.* Addison-Wesley Publishing Company, New York, 1995.

[23] G. D. Mahan. *Many-Particle Physics.* Springer US, Boston, MA, 2000.

[24] L. H. Thomas. The calculation of atomic fields. *Math. Proc. Cambridge Philos. Soc.*, 23:542, 1927.

[25] E. Fermi. Un Metodo Statistico per la Determinazione di alcune Prioprietà dell'Atomo. *Rend. Accad. Naz. Lincei*, 6:602, 1927.

[26] C. A. Ullrich. *Time-Dependent Density-Functional Theory.* Oxford University Press, New York, 2012.

[27] W. Kohn and L. J. Sham. Self-Consistent Equations Including Exchange and Correlation Effects. *Phys. Rev.*, 140:A1133–A1138, 1965.

[28] L. W. Wang and M. P. Teter. Kinetic-energy functional of the electron density. *Phys. Rev. B*, 45:13196, 1992.

[29] R. M. Dreizler and E. K. U. Gross. *Density Functional Theory.* Springer Berlin Heidelberg, Berlin, Heidelberg, 1990.

[30] G. Stefanucci and R. van Leeuwen. *Nonequilibrium Many-Body Theory of Quantum Systems.* Cambridge University Press, Cambridge, 2013.

[31] H. Haug and A. P. Jauho. *Quantum Kinetics in Transport and Optics of Semiconductors.* Springer Berlin Heidelberg, Berlin, Heidelberg, 2008.

[32] M. Di Ventra. *Electrical Transport in Nanoscale Systems.* Cambridge University Press, Cambridge, 2008.

[33] J. S. Wang, J. Wang, and J. T. Lü. Quantum thermal transport in nanostructures. *Eur. Phys. J. B*, 62:381, 2008.

[34] N. Zeng. *Thermal conduction in nanoscale systems.* PhD thesis, National University of Singapore, 2008.

[35] J. S Wang, B. K. Agarwalla, H. Li, and J. Thingna. Nonequilibrium Green's function method for quantum thermal transport. *Front. Phys.*, 9:673, 2014.

[36] J. H. Lee, G. A. Galli, and J. C. Grossman. Nanoporous Si as an Efficient Thermoelectric Material. *Nano Lett.*, 8:3750, 2008.

[37] M. X. Chen and R. Podloucky. Electronic thermal conductivity as derived by density functional theory. *Phys. Rev. B*, 88:045134, 2013.

[38] X. Wang and M. Z. Wang. *Nanoscale Thermoelectrics.* Springer International Publishing, Cham, 2014.

[39] C. W. J. Beenakker. Theory of Coulomb-blockade oscillations in the conductance of a quantum dot. *Phys. Rev. B*, 44:1646, 1991.

[40] C. W. J. Beenakker and A. A. M. Staring. Theory of the thermopower of a quantum dot. *Phys. Rev. B*, 46:9667, 1992.

[41] X. Zianni. Theory of the energy-spectrum dependence of the electronic thermoelectric tunneling coefficients of a quantum dot. *Phys. Rev. B*, 78:165327, 2008.

[42] D. D. Pollock. *Thermoelectricity : theory, thermometry, tool.* ASTM, Philadelphia, 1985.

[43] G. S. Nolas, J. Sharp, and H. J. Goldsmid. *Thermoelectrics: Basic Principles and New Materials Developments.* Cambridge University Press, Cambridge, 2001.

[44] L. D. Hicks and M. S. Dresselhaus. Effect of quantum-well structures on the thermoelectric figure of merit. *Phys. Rev. B*, 47:12727, 1993.

[45] L. D. Hicks and M. S. Dresselhaus. Thermoelectric figure of merit of a one-dimensional conductor. *Phys. Rev. B*, 47:16631, 1993.

[46] K. S. Novoselov, A. Geim, S. V. Morozov, D. Jiang, Y. Zhang, S. V. Dubonos, I. V. Grigorieva, and A. A. Firsov. Electric Field Effect in Atomically Thin Carbon Films. *Science*, 306:666, 2004.

[47] A. A. Balandin, S. Ghosh, W. Bao, I. Calizo, D. Teweldebrhan, F. Miao, and C. N. Lau. Superior Thermal Conductivity of Single-Layer Graphene. *Nano Lett.*, 8:902, 2008.

[48] J. H. Seol, I. Jo, A. L. Moore, L. Lindsay, Z. H. Aitken, M. T. Pettes, X. Li, Z. Yao, R. Huang, D. Broido, N. Mingo, R. S. Ruoff, and L. Shi. Two-Dimensional Phonon Transport in Supported Graphene. *Science*, 328:213, 2010.

[49] R. Prasher. Graphene Spreads the Heat. *Science*, 328:185, 2010.

[50] K. Yang, Y. Chen, R. D'Agosta, Y. Xie, J. Zhong, and A. Rubio. Enhanced thermoelectric properties in hybrid graphene/boron nitride nanoribbons. *Phys. Rev. B*, 86:045425, 2012.

[51] A. H. Castro Neto, F. Guinea, N. M. R. Peres, K. S. Novoselov, and A. K. Geim. The electronic properties of graphene. *Rev. Mod. Phys.*, 81:109, 2009.

[52] N. M. R. Peres. Colloquium: The transport properties of graphene: An introduction. *Rev. Mod. Phys.*, 82:2673, 2010.

[53] P. Ayala, R. Arenal, A. Loiseau, A. Rubio, and T. Pichler. The physical and chemical properties of heteronanotubes. *Rev. Mod. Phys.*, 82:1843, 2010.

[54] S. Das Sarma, S. Adam, E. H. Hwang, and E. Rossi. Electronic transport in two-dimensional graphene. *Rev. Mod. Phys.*, 83:407, 2011.

[55] V. N. Kotov, B. Uchoa, V. M. Pereira, F. Guinea, and A. H. Castro Neto. Electron-Electron Interactions in Graphene: Current Status and Perspectives. *Rev. Mod. Phys.*, 84:1067, 2012.

[56] S. Cahangirov, M. Topsakal, E. Aktürk, H. ahin, and S. Ciraci. Two- and One-Dimensional Honeycomb Structures of Silicon and Germanium. *Phys. Rev. Lett.*, 102:236804, 2009.

[57] L. Chen, C. C. Liu, B. Feng, X. He, P. Cheng, Z. Ding, S. Meng, Y. Yao, and K. Wu. Evidence for Dirac Fermions in a Honeycomb Lattice Based on Silicon. *Phys. Rev. Lett.*, 109:056804, 2012.

[58] F. Bechstedt, L. Matthes, P. Gori, and O. Pulci. Infrared absorbance of silicene and germanene. *Appl. Phys. Lett.*, 100:261906, 2012.

[59] P. De Padova, C. Quaresima, C. Ottaviani, P. M. Sheverdyaeva, P. Moras, C. Carbone, D. Topwal, B. Olivieri, A. Kara, H. Oughaddou, B. Aufray, and G. Le Lay. Evidence of graphene-like electronic signature in silicene nanoribbons. *Appl. Phys. Lett.*, 96:261905, 2010.

[60] B. Lalmi, H. Oughaddou, H. Enriquez, A. Kara, S. Vizzini, B. Ealet, and B. Aufray. Epitaxial growth of a silicene sheet. *Appl. Phys. Lett.*, 97:223109, 2010.

[61] P. De Padova, O. Kubo, B. Olivieri, C. Quaresima, T. Nakayama, M. Aono, and G. Le Lay. Multilayer Silicene Nanoribbons. *Nano Lett.*, 12:5500, 2012.

[62] A. Kara, H. Enriquez, A. P. Seitsonen, L. C. Lew Yan Voon, S. Vizzini, B. Aufray, and H. Oughaddou. A review on silicene-New candidate for electronics. *Surf. Sci. Rep.*, 67:1, 2012.

[63] B. Feng, Z. Ding, S. Meng, Y. Yao, X. He, P. Cheng, L. Chen, and K. Wu. Evidence of Silicene in Honeycomb Structures of Silicon on Ag(111). *Nano Lett.*, 12:3507, 2012.

[64] H. Enriquez, S. Vizzini, A. Kara, B. Lalmi, and H. Oughaddou. Silicene structures on silver surfaces. *J. Phys. Condens. Matter*, 24:314211, 2012.

[65] H. Jamgotchian, Y. Colignon, N. Hamzaoui, B. Ealet, J. Y. Hoarau, B. Aufray, and J. P. Bibérian. Growth of silicene layers on Ag(111): unexpected effect of the substrate temperature. *J. Phys. Condens. Matter*, 24:172001, 2012.

[66] P. Vogt, P. De Padova, C. Quaresima, J. Avila, E. Frantzeskakis, M. C. Asensio, A. Resta, B. Ealet, and G. Le Lay. Silicene: Compelling Experimental Evidence for Graphenelike Two-Dimensional Silicon. *Phys. Rev. Lett.*, 108:155501, 2012.

[67] C. L. Lin, R. Arafune, K. Kawahara, M. Kanno, N. Tsukahara, E. Minamitani, Y. Kim, M. Kawai, and N. Takagi. Substrate-Induced Symmetry Breaking in Silicene. *Phys. Rev. Lett.*, 110:076801, 2013.

[68] L. Meng, Y. Wang, L. Zhang, S. Du, R. Wu, L. Li, Y. Zhang, G. Li, H. Zhou, W. A. Hofer, and H. J. Gao. Buckled Silicene Formation on Ir(111). *Nano Lett.*, 13:685, 2013.

[69] S. Cahangirov, M. Audiffred, P. Tang, A. Iacomino, W. Duan, G. Merino, and A. Rubio. Electronic structure of silicene on Ag(111): Strong hybridization effects. *Phys. Rev. B*, 88:035432, 2013.

[70] H. Rücker and M. Methfessel. Anharmonic Keating model for group-IV semiconductors with application to the lattice dynamics in alloys of Si, Ge, and C. *Phys. Rev. B*, 52:11059, 1995.

[71] L. Pan, H. J. Liu, X. J. Tan, H. Y. Lv, J. Shi, X. F. Tang, and G. Zheng. Thermoelectric properties of armchair and zigzag silicene nanoribbons. *Phys. Chem. Chem. Phys.*, 14:13588, 2012.

[72] http://www.ioffe.ru/SVA/NSM/Semicond/SiGe/basic.html, where we obtained the basic parameters of bulk Si and Ge crystals.

[73] G. Kresse and J. Furthmüller. Efficient iterative schemes for ab initio total-energy calculations using a plane-wave basis set. *Phys. Rev. B*, 54:11169, 1996.

[74] D. M. Ceperley and B. J. Alder. Ground state of the electron gas by a stochastic model. *Phys. Rev. Lett.*, 45:566, 1980.

[75] J. P. Perdew and A. Zunger. Self-interaction correction to density-functional approximations for many-electron systems. *Phys. Rev. B*, 23:5048, 1981.

[76] D. Alfè. PHON: A program to calculate phonons using the small displacement method. *Comput. Phys. Commun.*, 180:2622, 2009.

[77] G. K. H. Madsen and D. J. Singh. BoltzTraP. A code for calculating band-structure dependent quantities. *Comput. Phys. Commun.*, 175:67, 2006.

[78] E. H. Hwang and S. Das Sarma. Acoustic phonon scattering limited carrier mobility in two-dimensional extrinsic graphene. *Phys. Rev. B*, 77:115449, 2008.

[79] J. Jung, T. Pereg-Barnea, and A. H. MacDonald. Theory of Interedge Superexchange in Zigzag Edge Magnetism. *Phys. Rev. Lett.*, 102:227205, 2009.

[80] T. Yamamoto and K. Watanabe. Nonequilibrium Green's Function Approach to Phonon Transport in Defective Carbon Nanotubes. *Phys. Rev. Lett.*, 96:255503, 2006.

[81] S. Y. Davydov. Third-order elastic moduli of single-layer graphene. *Phys. Solid State*, 53:665, 2011.

[82] J. Chen, G. Zhang, and B. Li. Tunable thermal conductivity of Si(1-x)Ge(x) nanowires. *Appl. Phys. Lett.*, 95:073117, 2009.

[83] W. Wan, B. Xiong, W. Zhang, J. Feng, and E. Wang. The effect of the electronphonon coupling on the thermal conductivity of silicon nanowires. *J. Phys. Condens. Matter*, 24:295402, 2012.

[84] H. R. Shanks, P. D. Maycock, P. H. Sidles, and G. C. Danielson. Thermal Conductivity of Silicon from 300 to 1400K. *Phys. Rev.*, 130:1743, 1963.

[85] T. Thonhauser and G. D. Mahan. Phonon modes in Si [111] nanowires. *Phys. Rev. B*, 69:075213, 2004.

[86] A. I. Hochbaum, R. Chen, R. D. Delgado, W. Liang, E. C. Garnett, M. Najarian, A. Majumdar, and P. Yang. Enhanced thermoelectric performance of rough silicon nanowires. *Nature*, 451:163, 2008.

[87] A. I. Boukai, Y. Bunimovich, J. T. Kheli, J. K. Yu, W. A. Goddard III, and J. R. Heath. Silicon nanowires as efficient thermoelectric materials. *Nature*, 451:168, 2008.

[88] T. T. M. Vo, A. J. Williamson, V. Lordi, and G. Galli. Atomistic Design of Thermoelectric Properties of Silicon Nanowires. *Nano Lett.*, 8:1111, 2008.

[89] J. Tang, H. T. Wang, D. H. Lee, M. Fardy, Z. Huo, T. P. Russell, and P. Yang. Holey Silicon as an Efficient Thermoelectric Material. *Nano Lett.*, 10:4279, 2010.

[90] X. Chen, Y. Wang, and Y. Ma. High Thermoelectric Performance of Ge/Si Core-Shell Nanowires: First-Principles Prediction. *J. Phys. Chem. C*, 114:9096, 2010.

[91] M. Amato, S. Ossicini, and R. Rurali. Band-Offset Driven Efficiency of the Doping of SiGe CoreShell Nanowires. *Nano Lett.*, 11:594, 2011.

[92] E. K. Lee, L. Yin, Y. Lee, J. W. Lee, S. J. Lee, J. Lee, S. N. Cha, D. Whang, G. S. Hwang, K. Hippalgaonkar, A. Majumdar, C. Yu, B. L. Choi, J. M. Kim, and K. Kim. Large Thermoelectric Figure-of-Merits from SiGe Nanowires by Simultaneously Measuring Electrical and Thermal Transport Properties. *Nano Lett.*, 12:2918, 2012.

[93] T. Markussen. Surface Disordered GeSi CoreShell Nanowires as Efficient Thermoelectric Materials. *Nano Lett.*, 12:4698, 2012.

[94] B. M. Curtin, E. A. Codecido, S. Krämer, and J. E. Bowers. Field-Effect Modulation of Thermoelectric Properties in Multigated Silicon Nanowires. *Nano Lett.*, 13:5503, 2013.

[95] R. D'Agosta. Towards a dynamical approach to the calculation of the figure of merit of thermoelectric nanoscale devices. *Phys. Chem. Chem. Phys.*, 15:1758, 2013.

[96] K. Yang, S. Cahangirov, A. Cantarero, A. Rubio, and R. D'Agosta. Thermoelectric properties of atomically thin silicene and germanene nanostructures. *Phys. Rev. B*, 89:125403, 2014.

[97] P. N. Keating. Effect of Invariance Requirements on the Elastic Strain Energy of Crystals with Application to the Diamond Structure. *Phys. Rev.*, 145:637, 1966.

[98] N. Mingo. Anharmonic phonon flow through molecular-sized junctions. *Phys. Rev. B*, 74:125402, 2006.

[99] J. S. Wang, J. Wang, and N. Zeng. Nonequilibrium Green's function approach to mesoscopic thermal transport. *Phys. Rev. B*, 74:033408, 2006.

[100] J. S. Wang, N. Zeng, J. Wang, and C. K. Gan. Nonequilibrium Green's function method for thermal transport in junctions. *Phys. Rev. E*, 75:061128, 2007.

[101] X. W. Wang, H. Lee, Y. C. Lan, G. H. Zhu, G. Joshi, D. Z. Wang, J. Yang, A. J. Muto, M. Y. Tang, J. Klatsky, S. Song, M. S. Dresselhaus, G. Chen, and Z. F. Ren. Enhanced thermoelectric figure of merit in nanostructured n-type silicon germanium bulk alloy. *Appl. Phys. Lett.*, 93:193121, 2008.

[102] M. Shelley and A. A. Mostofi. Prediction of high zT in thermoelectric silicon nanowires with axial germanium heterostructures. *Europhys. Lett.*, 94:67001, 2011.

[103] R. Rurali. Colloquium : Structural, electronic, and transport properties of silicon nanowires. *Rev. Mod. Phys.*, 82:427, 2010.

[104] J. Moon, J. H. Kim, Z. C. Y. Chen, J. Xiang, and R. Chen. Gate-Modulated Thermoelectric Power Factor of Hole Gas in GeSi CoreShell Nanowires. *Nano Lett.*, 13:1196, 2013.

[105] M. C. Wingert, Z. C. Y. Chen, E. Dechaumphai, J. Moon, J. Kim, J. Xiang, and R. Chen. Thermal Conductivity of Ge and GeSi CoreShell Nanowires in the Phonon Confinement Regime. *Nano Lett.*, 11:5507, 2011.

[106] B. Yu, M. Zebarjadi, H. Wang, K. Lukas, H. Wang, D. Wang, C. Opeil, M. Dresselhaus, G. Chen, and Z. Ren. Enhancement of Thermoelectric Properties by Modulation-Doping in Silicon Germanium Alloy Nanocomposites. *Nano Lett.*, 12:2077, 2012.

[107] H. J. Goldsmid. The Thermal Conductivity of Bismuth Telluride. *Proc. Phys. Soc. Sect. B*, 69:203, 1955.

[108] C. Cheng, W. Fan, J. Cao, S. G. Ryu, J. Ji, C. P. Grigoropoulos, and J. Wu. Heat Transfer across the Interface between Nanoscale Solids and Gas. *ACS Nano*, 5:10102, 2011.

[109] D. Polder and M. Van Hove. Theory of Radiative Heat Transfer between Closely Spaced Bodies. *Phys. Rev. B*, 4:3303, 1971.

[110] A. I. Volokitin and B. N. J. Persson. Near-field radiative heat transfer and non-contact friction. *Rev. Mod. Phys.*, 79:1291, 2007.

[111] K. Joulain, J. P. Mulet, F. Marquier, R. Carminati, and J. J. Greffet. Surface electromagnetic waves thermally excited: Radiative heat transfer, coherence properties and Casimir forces revisited in the near field. *Surf. Sci. Rep.*, 57:59, 2005.

[112] P. O. Chapuis, M. Laroche, S. Volz, and J. J. Greffet. Radiative heat transfer between metallic nanoparticles. *Appl. Phys. Lett.*, 92:201906, 2008.

[113] P. O. Chapuis, S. Volz, C. Henkel, K. Joulain, and J. J. Greffet. Effects of spatial dispersion in near-field radiative heat transfer between two parallel metallic surfaces. *Phys. Rev. B*, 77:035431, 2008.

[114] P. O. Chapuis, M. Laroche, S. Volz, and J. J. Greffet. Near-field induction heating of metallic nanoparticles due to infrared magnetic dipole contribution. *Phys. Rev. B*, 77:125402, 2008.

[115] A. Narayanaswamy, S. Shen, and G. Chen. Near-field radiative heat transfer between a sphere and a substrate. *Phys. Rev. B*, 78:115303, 2008.

[116] S. Shen, A. Narayanaswamy, and G. Chen. Surface Phonon Polaritons Mediated Energy Transfer between Nanoscale Gaps. *Nano Lett.*, 9:2909, 2009.

[117] E. Rousseau, A. Siria, G. Jourdan, S. Volz, F. Comin, J. Chevrier, and J. J. Greffet. Radiative heat transfer at the nanoscale. *Nat. Photonics*, 3:514, 2009.

[118] Y. A. Kosevich. Van der Waals coupled surface waves in nonpiezoelectric crystals and thin films. *Phys. Lett. A*, 155:295, 1991.

[119] M. Prunnila and J. Meltaus. Acoustic Phonon Tunneling and Heat Transport due to Evanescent Electric Fields. *Phys. Rev. Lett.*, 105:125501, 2010.

[120] A. Kittel. Nanophotonics: Probing near-field thermal radiation. *Nat. Photonics*, 3:492, 2009.

[121] G. Domingues, S. Volz, K. Joulain, and J. J. Greffet. Heat Transfer between Two Nanoparticles Through Near Field Interaction. *Phys. Rev. Lett.*, 94:085901, 2005.

[122] I. Altfeder, A. A. Voevodin, and A. K. Roy. Vacuum Phonon Tunneling. *Phys. Rev. Lett.*, 105:166101, 2010.

[123] V. Chiloyan, J. Garg, K. Esfarjani, and G. Chen. Transition from near-field thermal radiation to phonon heat conduction at sub-nanometre gaps. *Nat. Commun.*, 6:6755, 2015.

[124] N. Mingo and L. Yang. Phonon transport in nanowires coated with an amorphous material: An atomistic Green's function approach. *Phys. Rev. B*, 68:245406, 2003.

[125] B. W. H. van Beest, G. J. Kramer, and R. A. van Santen. Force fields for silicas and aluminophosphates based on ab initio calculations. *Phys. Rev. Lett.*, 64:1955, 1990.

[126] S. Stackhouse and L. Stixrude. Theoretical Methods for Calculating the Lattice Thermal Conductivity of Minerals. *Rev. Mineral. Geochemistry*, 71:253, 2010.

[127] http://lammps.sandia.gov/doc/compute_heat_flux.html.

[128] T. Förster. Zwischenmolekulare Energiewanderung und Fluoreszenz. *Ann. Phys.*, 437:55, 1948.

[129] J. P. Perdew, K. Burke, and M. Ernzerhof. Generalized Gradient Approximation Made Simple. *Phys. Rev. Lett.*, 77:3865, 1996.

[130] M. Bockstedte, A. Kley, J. Neugebauer, and M. Scheffler. Density-functional theory calculations for poly-atomic systems: electronic structure, static and elastic properties and ab initio molecular dynamics. *Comput. Phys. Commun.*, 107:187, 1997.

[131] S. Kurth and G. Stefanucci. Dynamical Correction to Linear Kohn-Sham Conductances from Static Density Functional Theory. *Phys. Rev. Lett.*, 111:030601, 2013.

[132] Z. F. Liu and K. Burke. Density functional description of Coulomb blockade: Adiabatic versus dynamic exchange correlation. *Phys. Rev. B*, 91:245158, 2015.

[133] G. Stefanucci and S. Kurth. Steady-State Density Functional Theory for Finite Bias Conductances. *Nano Lett.*, 15:8020, 2015.

[134] G. Stefanucci and C. O. Almbladh. Time-dependent partition-free approach in resonant tunneling systems. *Phys. Rev. B*, 69:195318, 2004.

[135] G. Stefanucci and C. O. Almbladh. Time-dependent quantum transport: An exact formulation based on TDDFT. *Europhys. Lett.*, 67:14, 2004.

[136] N. Sai, M. Zwolak, G. Vignale, and M. Di Ventra. Dynamical Corrections to the DFT-LDA Electron Conductance in Nanoscale Systems. *Phys. Rev. Lett.*, 94:186810, 2005.

[137] M. Koentopp, K. Burke, and F. Evers. Zero-bias molecular electronics: Exchange-correlation corrections to Landauer's formula. *Phys. Rev. B*, 73:121403, 2006.

[138] G. Vignale and M. Di Ventra. Incompleteness of the Landauer formula for electronic transport. *Phys. Rev. B*, 79:014201, 2009.

[139] F. G. Eich, A. Principi, M. Di Ventra, and G. Vignale. Luttinger-field approach to thermoelectric transport in nanoscale conductors. *Phys. Rev. B*, 90:115116, 2014.

[140] F. G. Eich, M. Di Ventra, and G. Vignale. Density-Functional Theory of Thermoelectric Phenomena. *Phys. Rev. Lett.*, 112:196401, 2014.

[141] R. Bulla, T. A. Costi, and T. Pruschke. Numerical renormalization group method for quantum impurity systems. *Rev. Mod. Phys.*, 80:395, 2008.

[142] T. A. Costi and V. Zlatić. Thermoelectric transport through strongly correlated quantum dots. *Phys. Rev. B*, 81:235127, 2010.

[143] G. Stefanucci and S. Kurth. Towards a Description of the Kondo Effect Using Time-Dependent Density-Functional Theory. *Phys. Rev. Lett.*, 107:216401, 2011.

[144] G. Xianlong, A. H. Chen, I. V. Tokatly, and S. Kurth. Lattice density functional theory at finite temperature with strongly density-dependent exchange-correlation potentials. *Phys. Rev. B*, 86:235139, 2012.

[145] E. Perfetto and G. Stefanucci. Missing derivative discontinuity of the exchange-correlation energy for attractive interactions: The charge Kondo effect. *Phys. Rev. B*, 86:081409, 2012.

[146] P. Tröster, P. Schmitteckert, and F. Evers. Transport calculations based on density functional theory, Friedel's sum rule, and the Kondo effect. *Phys. Rev. B*, 85:115409, 2012.

[147] J. P. Bergfield, Z. F. Liu, K. Burke, and C. A. Stafford. Bethe Ansatz Approach to the Kondo Effect within Density-Functional Theory. *Phys. Rev. Lett.*, 108:066801, 2012.

[148] A. A. M. Staring, L. W. Molenkamp, B. W. Alphenaar, H. Van Houten, O. J. A. Buyk, M. A. A. Mabesoone, C. W. J. Beenakker, and C. T. Foxon. Coulomb-Blockade Oscillations in the Thermopower of a Quantum Dot. *Europhys. Lett.*, 22:57, 1993.

[149] A. S. Dzurak, C. G. Smith, M. Pepper, D. A. Ritchie, J. E. F. Frost, G. A. C. Jones, and D. G. Hasko. Observation of Coulomb blockade oscillations in the thermopower of a quantum dot. *Solid State Commun.*, 87:1145, 1993.

[150] A. S. Dzurak, C. G. Smith, C. H. W. Barnes, M. Pepper, L. Martín-Moreno, C. T. Liang, D. A. Ritchie, and G. A. C. Jones. Thermoelectric signature of the excitation spectrum of a quantum dot. *Phys. Rev. B*, 55:R10197, 1997.

[151] G. Stefanucci and S. Kurth. Kondo effect in the Kohn-Sham conductance of multiple-level quantum dots. *Phys. status solidi*, 250:2378, 2013.

[152] K. Yang, A. Cantarero, A. Rubio, and R. D'Agosta. Optimal thermoelectric figure of merit of Si/Ge core-shell nanowires. *Nano Res.*, 8:2611, 2015.

[153] S. Xiong, K. Yang, Y. A. Kosevich, Y. Chalopin, R. D'Agosta, P. Cortona, and S. Volz. Classical to Quantum Transition of Heat Transfer between Two Silica Clusters. *Phys. Rev. Lett.*, 112:114301, 2014.

[154] K. Yang, E. Perfetto, S. Kurth, G. Stefanucci, and R. D'Agosta. Density Functional Theory of the Seebeck coefficient in the Coulomb blockade regime. *arXiv:1512.07540*, 2015.

[155] E. K. Liu, B. S. Zhu, and J. S. Luo. *Semiconductor Physics.* Publishing House of Electronics Industry, Beijing, 2006.